SAPIENZA
UNIVERSITÀ DI ROMA

PH.D. IN ASTRONOMY, ASTROPHYSICS
AND SPACE SCIENCE

CYCLE XXX

The Most Luminous Quasars of the Universe: Probing the AGN/galaxy Co-evolution at its extremes

Giustina Vietri
A.Y. 2016/2017

Supervisor: Prof. Fabrizio Fiore

Co-supervisor: Dr. Enrico Piconcelli

Coordinator: Prof. Roberto Capuzzo Dolcetta

Deputy Coordinator: Prof. Pasquale Mazzotta

ONCE UPON A TIME.....

Inizierei con una frase di Baricco, «non è che la vita vada come tu te la immagini. Fa la sua strada. E tu la tua», ed un bel giorno scopri di dover lasciare Bologna per andare a Roma, per tre anni.

Da lì i tre anni son volati, iniziati in solitaria...città nuova, istituto nuovo, persone nuove...chissà come mi troverò... (Paolo, in questo momento ci sei tu nella mia testa che ridi e fai paragoni tra Bologna e Roma ahahah...non ti preoccupare da te torno tra poco!!).

Inizierei dicendo che la fortuna, caso o chiamatelo come volete, mi ha dato la possibilità di poter lavorare assieme al prof. Fabrizio Fiore, un supervisor dalla cultura ed un sapere infiniti, un punto fondamentale e di riferimento senza il quale il mio dottorato non avrebbe avuto lo stesso successo e per questo lo ringrazierò infinitamente. Sì, concedetemelo perchè credo che questo dottorato sia stato un successo per me. In che senso? Una conquista del sapere, ho avuto la possibilità di crescere scientificamente e tutto questo grazie al prof. Fiore ed al gruppo di cui ho fatto parte.

Vorrei ringraziare in particolar modo il Dr. Enrico Piconcelli, mio insostituibile co-supervisor, con cui sono stata più a stretto contatto in questi tre anni. Sempre presente in ogni fase del mio lavoro e sempre pronto ad aiutarmi, spronarmi a dare il meglio. Ho potuto "usufruire" della sua passione per la ricerca e voglia di conoscenza, che hanno condizionato in modo fondamentale il mio percorso di questi anni.

Ma il gruppo non finisce qua....ci sono i Dr Angela Bongiorno e Dr Luca Zappacosta che hanno reso il mio lavoro migliore, grazie ai loro suggerimenti costruttivi.

Grazie anche a Fede e Silvia, per il bel gioco di squadra e l'aiuto indispensabile! Andrea...l'ultimo arrivato della combriccola, ma con cui ho condiviso dei momenti magnifici. Il tuo arrivo ha reso le ore e le giornate in ufficio colorate e gioiose!!! Tralascio i mal di testa causati dal profumo..... povera Manu, non sa cosa le aspetta.....

La Manuuuuuu....che posso dire, secondo me ci abbiamo messo un po' per intenderci però poi è stato l'inizio della fine...in senso buono! Le riunioni più divertenti....per motivi ovvi! Compagna di conferenze, di bevute e di cibo! e amica, perchè ho la fortuna di poterti dire amica e non solo collega....e poi....ormai mio idolo per sempre, tu sola hai raggiunto il vero obiettivo del dottorato!!! e lo sai!!!!

Ma al di fuori di questo gruppo magnifico, ho conosciuto persone altrettanto fantastiche. Flavia, Marco e Paola...persone amiche con cui ho condiviso dei bellissimi momenti e risate...povero Marco che si trovava tra tre fuochi!!! A me non piacciono gli inizi e faccio fatica ad adattarmi, ma voi tre avete addolcito e reso meno traumatico tutto questo...non per nulla la vostra partenza è stato un dramma!!!

E Mattia, con le sue 50 sfumature di colori nei plot ed una risata contagiosa! Ho avuto la fortuna di condividere con te questo percorso e di conoscerti anche al di fuori del lavoro.

Marco Castellani con i numerosi pranzi assieme, ed i racconti che ti vedevano protagonista assieme a Paolo, che più di una volta ci hanno fatto sorridere!

E poi Paolo, ecco sì Paolo. Una delle poche persone che conosca che ha sempre cercato di fare da ponte tra il mondo degli studenti ed il mondo dei ricercatori/professori. Potrei scrivere all'infinito. Ho avuto la fortuna di essere tra i pochi eletti, di poterti conoscere. Non saprei da dove inizia-

re.....Mi hai fatto conoscere Roma, quella purtroppo forse meno nota ai più, la Roma del Cavallini e dei mosaici, che sembrano dipinti con i loro colori vivaci. Suonare ad un campanello di una piccola porta, dietro cui mai penseresti ci possano essere delle suore che custodiscono gelosamente opere del Cavallini (gli affreschi...i dipinti..quelli sul muro....scusa ma non potevo non scriverlo!!!!). I mosaici di Santa Prassede o il Barocci (di cui ignoravo l'esistenza). Che dire...le risate? le imitazioni? le pause caffè? le piacevolissime cene? Artena? i fantastici pranzi? le uscite? l'amicizia?...la Roma???? ahahah ....direi che ti ringrazio per tutto questo e per i meravigliosi tre anni resi tali dalla tua presenza.

Un ringraziamento va anche ad Erendira e a tutti i miei colleghi con cui ho condiviso questo folle dottorato romano.

Cos'altro dire....ho trascorso tre anni meravigliosi e devo tutto questo non solo alle persone conosciute durante questo percorso, ma anche e soprattutto a quelle che già conoscevo. Grazie ai miei zii ed ai miei cugini che sono riusciti a rendere le giornate, le domeniche (quelle libere, poche..lo so) meno lavorative e più in famiglia, come se fossi a casa.

Nicola....sei riuscito ad annullare le distanze e seguirmi in ogni dove. Nonostante il tuo odio per il mio computer e per il mio lavoro "senza orari", hai sempre accettato tutto, supportandomi nelle mie scelte, anche se questo significava essere ancora più lontani. Una fortuna unica nella mia vita avere accanto una persona come te.

Permettetemi di concludere con le persone che più amo al mondo, i miei genitori e le mie sorelle. Le mie rocce! Scontato dire che non sono mai stata sola, ho sempre avuto il vostro supporto ed incoraggiamento, no...forse non è così scontato e va detto! Non voglio far piangere nessuno, tantomeno me che sto scrivendo, ma credo che vada detto che i sacrifici ci son stati e sono stati tanti. Mi avete permesso di arrivare fino al dottorato, e nessuno sa meglio di noi le 1000 vite e 1000 situazioni assurde che siamo ...anzi direi... siete riusciti a fronteggiare a testa alta e a superare brillantemente! Grazie di tutto!!!!

Stai per cominciare a leggere il nuovo romanzo (..). Rilassati. Raccogliti. Allontana da te ogni altro pensiero. Lascia che il mondo che ti circonda sfumi nell'indistinto. La porta è meglio chiuderla; di là c'è sempre la televisione accesa. Dillo subito, agli altri: «No, non voglio vedere la televisione!» Alza la voce, se no non ti sentono: «Sto leggendo! Non voglio essere disturbato!» Forse non ti hanno sentito, con tutto quel chiasso; dillo più forte, grida: «Sto cominciando a leggere il nuovo romanzo (..)!» O se non vuoi non dirlo; speriamo che ti lascino in pace.

(Italo Calvino, Se una notte d'inverno un viaggiatore)

Contents

List of Figures

List of Tables

Overview

The discovery of supermassive black hole (SMBH) in the center of most local massive galaxies and theoretical and observational motivations lead to the idea that BHs and their host galaxies co-evolve regulating each other. The so-called AGN feedback mechanism is invoked to explain the correlation between the BH mass and the velocity dispersion of the bulge (Silk & Rees 1998, Kormendy & Ho 2013 and reference therein), the bimodality in the colours of galaxies and it can suppress the excessive growth of massive galaxies and drive their evolution from gas-rich starburst galaxies to red and dead ellipticals (Hopkins *et al.* 2008).

Furthermore, the energy released by accretion in building a SMBH considerably exceeds the binding energy of the bulge. Powerful AGN-driven outflows are routinely invoked as a viable mechanism for kinetic energy injection into the ISM which can affect the evolution of their host galaxies (Zubovas & King 2012 and reference therein). Indeed they are thought to be powerful enough to swept up the cold gas reservoir of the host galaxy, affecting both BH growth and regulating star formation.

Compelling evidence of kpc-scale, powerful outflows in local and distant AGN host galaxies have been collected over the past few years (Fabian 2012; Fiore *et al.* 2017 and reference therein), such as in molecular and atomic gas phase (both neutral and ionized) with large kinetic power that only quasar activity can account for them. The first pieces of evidence of outflowing gas in AGNs have been historically derived by the detection of blueshifted and highly asymmetrical emission profiles of [OIII]λ5007 Å and CIVλ1549 Å (also in absorption in this case).

More specifically, the [OIII]λ5007 Å emission line is used to trace AGN-driven outflow at large-scale in the Narrow Line Region (NLR), which usually shows broad blueward profile with the receding gas likely obscured by the host galaxy. The CIVλ1549 Å emission line is usually used to reveal the presence of outflows in the Broad Line Region (BLR), by its asymmetric profiles towards the blue-side with the peak of the emission line blueshifted with respect to the low ionization lines, such as MgIIλ2797 Å or Hβ (e.g. Gaskell 1982; Sulentic *et al.* 2000; Richards *et al.* 2011).

This co-evolutionary scenario is expected to be more significant in the redshift interval $1 < z < 3$, i.e. the golden epoch of AGN and galaxy evolution (e.g. Madau & Dickinson 2014; Merloni & Heinz 2013). Moreover since physical models of AGN outflows suggest that the efficiency of driving powerful outflows increases with AGN luminosity (Menci *et al.* 2008; Faucher-Giguère & Quataert 2012), the most

luminous quasars are potentially the best objects to hunt for AGN-driven outflows, especially at high z.

In order to search for these hyper-luminous rare objects, sensitive wide-area surveys are required. The mid-IR range is particularly indicated to collect AGNs because of the advantage to be not biased against dust obscured sources. By combining optically discovered quasars in the SDSS with the all-sky WISE survey, which observed the entire sky in the mid-IR, the most luminous Type 1 quasars were found in the Universe up to z∼5, with $L_{7.8\mu m} > 10^{47}$ erg s^{-1} . In addition to these optically bright QSOs, WISE allowed to discover a population of red (i.e. very extincted) quasars, as common as the blue QSOs. These sources are believed to undergo the brief evolutionary phase that traces the transition from a heavily enshrouded phase of SMBH growth to the blue unobscured quasars (Glikman *et al.* 2012).

My PhD thesis is part of a project led at Observatory of Rome, i.e. the so-called WISE/SDSS selected hyper luminous (WISSH) quasars project. This project aims to probe the widespread presence of outflows at different gas phases and distances, constrain the properties of the central engine and study the interstellar medium (ISM) and star-formation rate (SFR) of the quasars host galaxies of the most luminous quasars in the universe. In this framework, the main goals of my Thesis are: (1) to measure the mass and accretion rate of the SMBHs of these hyper-luminous QSOs, (2) to search for powerful ionized outflows in the NLR and BLR, whereas the theory predicts the maximum efficiency of the AGN-galaxy feedback mechanism.

For these purposes the rest-frame Optical of thirteen WISSH quasars and Ultra-Violet (UV) spectra of eighteen WISSH quasars at redshift z ∼ 2–3 have been analyzed. The rest-frame Optical observations have been performed by near-IR spectrographs LUCI at the Large Binocular Telescope and SINFONI at Very Large Telescope, and the rest-frame UV spectra have been collected from the public Sloan Digital Sky Survey (SDSS). We adopted the Hβ emission line to obtain the most accurate estimates of the SMBH masses and [OIII]λ5007 Å and CIVλ1549 Å emission line profiles as tracers of the NLR and BLR outflows, respectively.

The thesis is organized as follows:

- **Chapter 1**. The general properties of AGN are presented, with a description of the AGN emission mechanism. Theoretical models of AGN outflows and observations of outflows at different scales are reviewed in Sect. 1.3 and Sect. 1.4. Specifically I present the best evidence of outflows in the nuclear region in Sect. 1.4.a and at kpc-scale in Sect. 1.4.b. The outflows driving mechanisms are presented in Sect. 1.5. A brief review about the influence and the role of AGNs on the evolution of their host galaxy is also discussed.

- **Chapter 2** I present here the selection criteria, general properties and the goals of the WISSH survey. Specifically, in Sect. 2.2 I discuss about the discovery of powerful ionized winds in WISSH QSOs.

- **Chapter 3** I present details about LBT/LUCI and VLT/SINFONI spectrographs, observations and data reduction of the proprietary data analyzed in this Thesis. A section dedicated to SDSS archival data is also provided.

- **Chapter 4** In this chapter I outline the models used in the analysis of the LBT/SINFONI and SDSS spectra of the WISSH quasars.

- **Chapter 5** The properties of the [OIII] and Hβ emission lines in the context of a scenario based on the orientation of our line of sight, the Hβ-based SMBH mass and Eddington ratio are reported. I also discuss about the properties of the CIV emission line, with particular emphasis on the blueshifted component and the mass outflow rate and kinetic power of the associated BLR winds in the WISSH quasars, and their relation with NLR winds traced by [OIII]. I also investigate the dependence of the CIV velocity shifts with fundamental AGN parameters such as L_{Bol}, λ_{Edd} and αox.

- **Chapter 6** This chapter is dedicated to the SUPER survey and the preliminary results about the discovery of extended NLR outflow in the WISSH quasar J1549+1245 at z = 2.365.

- **Chapter 7** This chapter summarizes the results presented in this Thesis about the study of the UV/optical properties of the WISSH quasars. Our findings reveals the presence of different ionized winds acting on different spatial scales, exhibiting extreme properties in terms of outflow rate and velocity. This confirms hyper-luminous QSOs, such as WISSH sources, being ideal target to accurately study the AGN-driven feedback process.

Chapter 1

Physics of Active Galactic Nuclei: accretion and ejection

1.1 The central engine: the SMBH paradigm

Active Galactic Nuclei (AGN) are known to be powered by accretion of nearby matter onto Supermassive Black Holes (SMBHs) at the center of galaxies. A fraction of the gravitational potential of the accreted mass is converted into radiation, which covers the full electromagnetic spectrum from γ to the radio wavelengths. The rate at which the energy is emitted by the nucleus, i.e. the AGN bolometric luminosity (L_{Bol}), is given by:

$$L_{Bol} = \eta \dot{m} c^2 \tag{1.1}$$

where $\dot{m} = dm/dt$ is the mass accretion rate of a mass m, η is the mass-to-energy conversion efficiency and c is the speed of light.

The accretion process as a viable mechanism to convert gravitational potential into radiation depends on the η factor. Considering that the potential energy U of a mass m at a distance r from the central source of mass M_{BH} is given by:

$$U = \frac{GM_{BH}m}{r} \tag{1.2}$$

where G is the gravitational constant, we can derive the rate at which the potential energy of infalling material is converted into radiation as follows:

$$L_{Bol} \approx \frac{dU}{dt} = \frac{GM_{BH}}{r}\frac{dm}{dt} = \frac{GM_{BH}\dot{m}}{r} \tag{1.3}$$

The characteristic scale of the BH is the Schwarzschild radius $R_S = 2GM/c^2$. Since the most of the optical/UV continuum radiation is expected to originate at $5R_S$ (Peterson 1997), from 1.3 we derived:

$$L_{Bol} = \frac{GM_{BH}\dot{m}}{5R_S} = \frac{GM_{BH}\dot{m}}{10GM_{BH}/c^2} = 0.1\dot{m}c^2 \tag{1.4}$$

which leads to a mass-to-energy conversion efficiency η of 0.1, much higher than that of the nuclear fusion process [1]. For instance, for an AGN with $L_{Bol} = 10^{47}$ erg s^{-1} the accretion rate is $\dot{m} \approx 20\ M\odot\ yr^{-1}$.

The accretion onto a BH suffers from the effects of the radiation pressure acting on the infalling matter. This leads to a limit on the luminosity and mass accretion rate of a BH, which was first pointed out by Arthur Eddington in the 1920s. This so-called Eddington limit depends on the mass of the central source and the opacity of the infalling material, i.e. on the fraction of the radiation absorbed. If we supposed that the accreting material is fully ionized hydrogen, the opacity is given by σ_T/m_p, where σ_T is the Thomson scattering and m_p is the proton mass. Assuming a spherical symmetry, the Eddington luminosity is obtained by equating the outward radiation force defined as follows:

$$F_{rad} = \frac{L_{bol}\sigma_T}{4\pi r^2 c} \tag{1.5}$$

to the inward force due to the gravity defined as follows:

$$F_{grav} = \frac{GM_{BH}m_p}{r^2} \tag{1.6}$$

By equating 1.5 and 1.6, the Eddington luminosity is therefore:

$$L_{Edd} = \frac{4\pi GM_{BH}m_p c}{\sigma_T} \simeq 1.3\ 10^{38}\frac{M_{BH}}{M_\odot}\ \text{erg}\ s^{-1} \tag{1.7}$$

which is the maximum luminosity of a source with mass M_{BH}, under the conditions mentioned above. The Eddington accretion rate is defined as:

$$\dot{M}_{Edd} = L_{Edd}/\eta c^2 \tag{1.8}$$

which is the maximum accretion rate to sustain the Eddington luminosity. For instance, a BH mass of at least $M_{BH} \sim 10^{6-9}\ M\odot$ is required, in order to produce an AGN with the observed luminosity of $L_{Bol} \sim 10^{44-47}$ erg s^{-1}.

A useful quantity used to compare the BHs accretion rates over a wide range of masses is the so-called Eddington ratio λ_{Edd}, defined as follows:

$$\lambda_{Edd} = \frac{L_{bol}}{L_{Edd}} \tag{1.9}$$

The limit on the accretion is reached when $\lambda_{Edd} = 1$. It is possible to distinguish between low and high accretion rate AGNs usually defining the $\lambda_{Edd} \leq$ and ≥ 0.1, respectively.

Angular momentum considerations must be taken into account, whereas the major problem for the accretion process is the mechanism which allows to transport outward the angular momentum, as matter falls onto the center from host-galaxy

[1] The efficiency depends on the spin of the BH. η=0.057 is valid for the case of a Schwarzschild BH (spin=0). For a Kerr BH the spin=1 and η ~0.42.

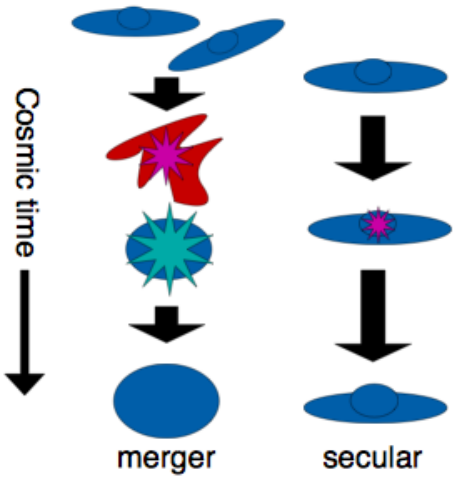

Figure 1.1. Schematic diagram in which is illustrated the large-scale processes likely responsible for the angular momentum transport, such as merger and secular processes (Alexander & Hickox 2012).

scales down to the parsec scales. Various mechanisms are likely responsible for the angular momentum transport at different scales. At large distance (> 100 pc), mechanisms such as interactions between galaxies, major and minor mergers or galaxy bars on galactic scale are involved (Barnes & Hernquist 1992; García-Burillo *et al.* 2005) (see Fig. 1.1). At small distance (< 1pc) the magneto-rotational instability (MRI) seems to be the best candidate (Balbus & Hawley 1991), where local turbulent viscosity is produced by a magnetic field, which transports angular momentum outwards.

An approximate solution to the angular momentum transport problem was proposed by Shakura & Sunyaev 1973 in the so-called α- disc model. They assumed that the origin of viscosity is related to turbulence and the kinematic viscosity v has the following form:

$$v = \alpha c_s h \tag{1.10}$$

where c_s is the sound speed, h is the disk semi-thickness and $0 < \alpha < 1$ is a constant dimensionless coefficient.

This α disc model was developed for a geometrically thin ($h / r \ll 1$, where h is the height above the disk midplane and r is the radius) optically thick accretion disks and assumed that the accretion is radiatively efficient with energy dissipated in a small region at distance *r* from the central BH.

Disk geometry. Considering the gas at a radius r and the height z above the disk midplane, the gravitational acceleration g in the vertical direction is given by:

$$g = \frac{GM_{BH}}{r^2}\frac{z}{r} \sim \frac{GM_{BH}}{r^3}z \tag{1.11}$$

In the vertical direction the gas is in hydrostatic equilibrium, which is determined by the balance between the gravitational force and the pressure gradient:

$$\frac{\delta P}{\delta z} = -\rho g = -\rho \frac{GM_{BH} z}{r^3} \tag{1.12}$$

where P is the pressure equal to $\rho\, c_s^2$ assuming an isothermal disk (c_s is the speed of sound).

The Eq. 1.12 can be rewritten in the form

$$\frac{1}{\rho}\frac{\delta \rho}{\delta z} \approx -\frac{GM}{r^3 c^2} z = -\Omega^2 z \tag{1.13}$$

where Ω is the angular velocity in the disk ($= \frac{v_\phi}{r} = \sqrt{\frac{GM_{BH}}{r^3}}$ i.e. the Keplerian angular velocity, where v_ϕ is the tangential velocity of the gas in the disk). This lead to a density ρ defined as follows:

$$\rho = \rho_{z=0} e^{-\frac{\Omega^2 z^2}{2c_s^2}} \tag{1.14}$$

where $\rho_{z=0}$ is the density in the disk midplane. Considering $h^2 \equiv \frac{2c_s^2}{\Omega^2} = \frac{c_s^2 r^2}{v_\phi^2}$ with h the vertical scale height of the disk, we can write:

$$\frac{h}{r} \approx \frac{c_s}{v_\phi} \tag{1.15}$$

This implies that the thickness of the disk as a fraction of the radius is given by the ratio of the sound speed and the tangential velocity. For thin disks ($h / r \ll 1$) it is equivalent to saying that the disk rotation is supersonic.

The characteristic temperature of the gas. The characteristic spectrum of a thin accretion disk is that of a black body with a temperature T as a function of radius r. Gravitational potential energy is released at the rate as defined in Eq. 1.3 and according to the virial theorem, half of this energy heats the gas and the other half is radiated away at the rate L defined as:

$$L = \frac{GM\dot{m}}{2r} = 2 \times\ 2\pi r^2 \sigma T^4 \tag{1.16}$$

where σT^4 is the Stefan-Boltzmann law for a black body radiation and $2\,\pi r^2$ is the disk area (the extra factor of 2 in Eq. 1.16 takes into account the two sides of the disk). This leads to a temperature T at r:

$$T = \left(\frac{GM_{BH}\dot{m}}{8\pi\sigma r^3}\right)^{1/4} \tag{1.17}$$

An expression for the temperature can be also derived considering how the energy is dissipated in the disk through viscosity and can be rewritten as follows:

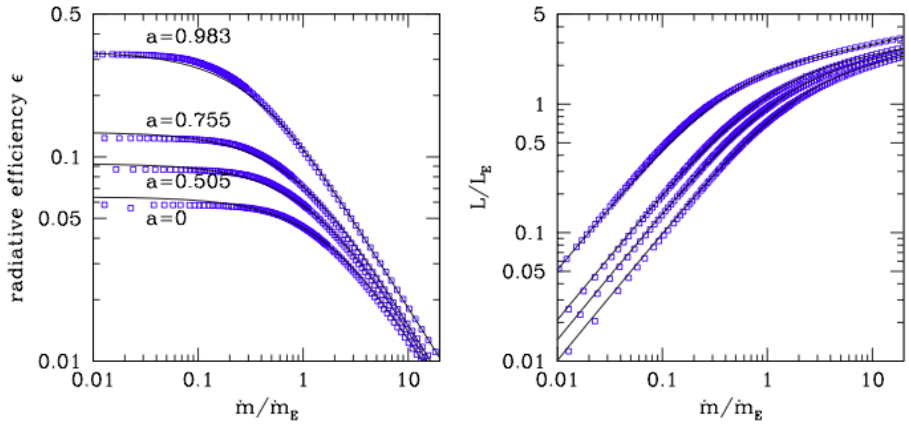

Figure 1.2. The radiative efficiency (left panel) and the Eddington ratio (right panel) of an accreting black hole as a function of the accretion rate $\dot{m}$ in units of Eddington rate $\dot{m}_E$, obtained from numerical integration of the relativistic slim disk equations. The solid curves are the best-fit to the data for different spin parameters (Madau *et al.* 2014).

$$T(r) = 6.3\ 10^5 (\dot{m}/\dot{M}_{Edd})^{1/4}\ M_8^{-1/4} (\frac{r}{R_S})^{-3/4}\ K \tag{1.18}$$

where R_S is the Schwarzschild radius and M_8 is the mass of the central source in units of 10^8 $M_\odot$ (Peterson 1997). From Eq. 1.18 it is expected that the peak temperature of the accretion disk is lower for more massive BHs. The thermal emission from an AGN accretion disk is expected to be prominent in the UV spectrum with a temperature peak T$\sim 10^5$ K.

Slim disk. The α-disc assumes a thermal equilibrium determined by the balance of viscous heating and radiative cooling, which is valid for small accretion rates. At high accretion rates or similarly at high luminosity ($L_{Bol} \approx 0.3\ L_{Edd}$), the disk is not consistent with the standard thin disk assumption but with a "slim" (not thin) disk in which an additional source of cooling is triggered: the advection (Abramowicz *et al.* 1988).

The thickness of the disk increases with the accretion rate, up to the maximum value of h/r $\sim$ 0.3. In case of a slim disk the flux emerging from the disk depends on the advection, which influences the efficiency of transforming the gravitational energy to radiative flux. Indeed slim disks are radiatively inefficient and the accretion energy is advected close to the BH rather than radiated. In Fig. 1.2 it is shown the radiative efficiency (left panel) and the Eddington ratio (right panel) of an accreting black hole as a function of the accretion rate $\dot{m}$ in units of Eddington rate $\dot{m}_E$ (Madau *et al.* 2014).

1.2 Main components of an AGN

As already mentioned in Sect 1.1, the basic idea is that the BH is surrounded by an accretion disk (R < 0.01 pc) and an optically thick torus is also present, consisting of gas and dust. At distance of the order of 1 pc from the AGN, there is the so-called BLR, where the clouds produce broad emission lines seen in the AGN spectrum. A hot corona close to the BH could be present, where the hot electrons scatter the cooled accretion disk photons. Far from the nucleus there is the so-called NLR, where narrow emission lines are produced. Bi-directional strong relativistic jets could be also present, which emit radiation via synchrotron and inverse Compton mechanisms.

A large diversity of observed AGNs properties leads to different classification schemes. Specifically, according to radio properties an AGN can be classified as radio-loud and radio-quiet, if the source produce or not jets and lobes, respectively. More recently, a revisited classification was presented by Padovani (2017), according to which an AGN is jetted or non-jetted if strong jets are present or not, respectively. In particular jetted AGNs are characterized by strong relativistic jets and non-jetted can also show the presence of jets but with different characteristic in terms of size (small), strength (weak) and velocity (low).

From the optical point of view AGNs can be divided in Type 1, characterized by narrow permitted and forbidden lines produced by clouds situated in the NLR and broad permitted lines such as Balmer lines, mainly Hα, Hβ, Hγ and Lyα, CIV, MgII which are produced by clouds located in the BLR, and Type 2 showing narrow permitted and forbidden lines such as Balmer lines and [OIII], [OII], [NII] and [SII], produced by clouds situated in the NLR.

An example of the composite UV/optical spectrum of a quasar, created from over 2200 QSOs spectra from SDSS, is shown in Fig. 1.3 (Vanden Berk *et al.* 2001). It is shown the UV power-law continuum with index α_ν = -0.46 and an optical power-law with index α_ν = -1.58. It is evident a lack of emission line free region across the entire UV/optical wavelength range, which it makes difficult the fitting of the continuum over a small wavelength range.

In the 90s, a unified model of AGN classification was proposed by Antonucci 1993 and Urry & Padovani 1995. This model is based on the idea that the observing angle has a role in the AGN classification. As a consequence the AGNs are classified as Type 1 or Type 2 sources if the observer is looking face-on or through the torus (edge-on) at the AGN, respectively. In Fig. 1.4 a schematic description of the unified model from Urry & Padovani (1995) is shown.

1.2.a Typical spectral energy distribution of an AGN

AGNs emit radiation over a wide range of wavelength. Over the past decades this leads to multi-wavelength observations with different telescopes in order to have a complete picture of the spectral shape of these sources. The spectral energy

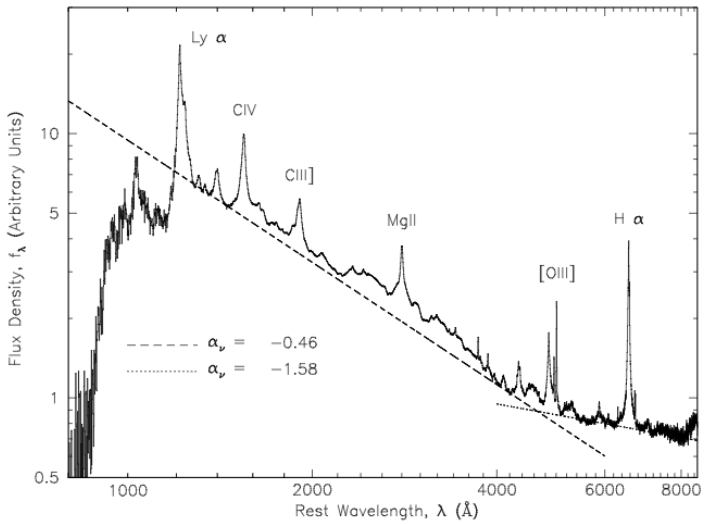

Figure 1.3. Composite quasar spectrum from Vanden Berk *et al.* (2001).

distribution (SED) of an AGN shows the following features:

- Big blue bump (BBB), which covers the wavelength range from 4000 Å to 1000 Å and typically dominates the SED of an unobscured AGN. As already mentioned in Sect. 1.1, the thermal emission from the accretion disk is expected to be prominent in the UV spectrum. This explains the observed bump.

- The infrared bump: it is a broad feature with a peak at 10 μm. This emission is due to the hot dust emission. The dust grains present in the torus surrounding the accretion disk reprocess the BBB emission, which is re-emitted at infrared wavelengths. At longer wavelengths (> 100μm) the IR emission is mostly due to the cold dust heated by star formation in the AGN host galaxy.

- The near-infrared inflection at 1-2 μm, which appears as a dip between the two bumps, corresponds to the dust sublimation temperature and may vary according to the dust composition.

- The submillimeter break: it marks a sharp drop in emission, which location and size is different within the AGN population. In radio-loud objects the drop ranges $\sim$ 2 orders of magnitude, while for the radio-quiet objects it may be $\sim$ 5 or 6 orders of magnitude (Elvis *et al.* 1994). The synchrotron radiation from powerful jets in radio-loud AGN is responsible for this emission feature.

- X-ray region: it can be divided in soft (< 2 keV) and hard X-ray bands.

  In the soft region there is the soft X-ray excess with respect to the primary continuum that may be related to the comptonisation and/or reflection occurring on the accretion disk surface. The hard X-ray band is characterized by a power

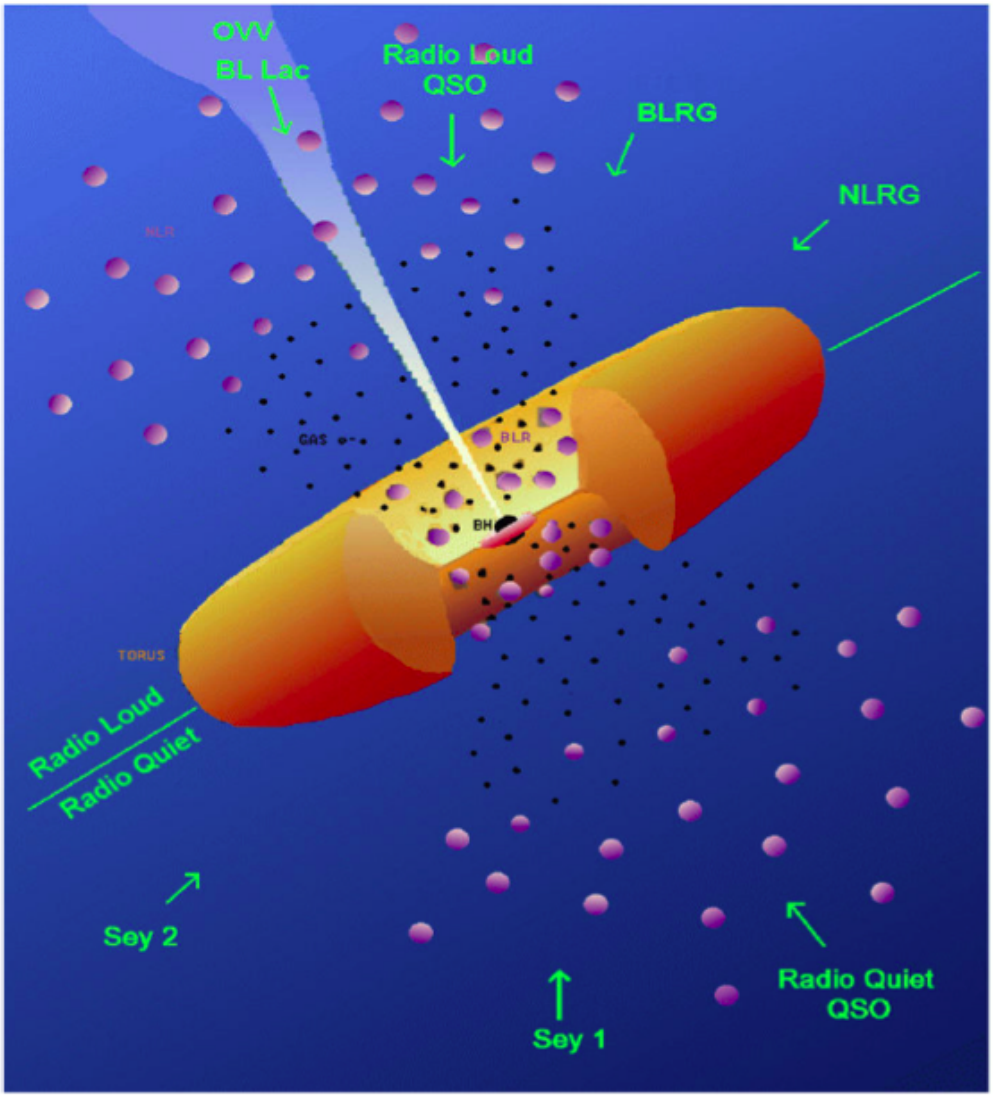

Figure 1.4. Schematic description of the Unified AGN model, according to different viewing angles (Urry & Padovani 1995).

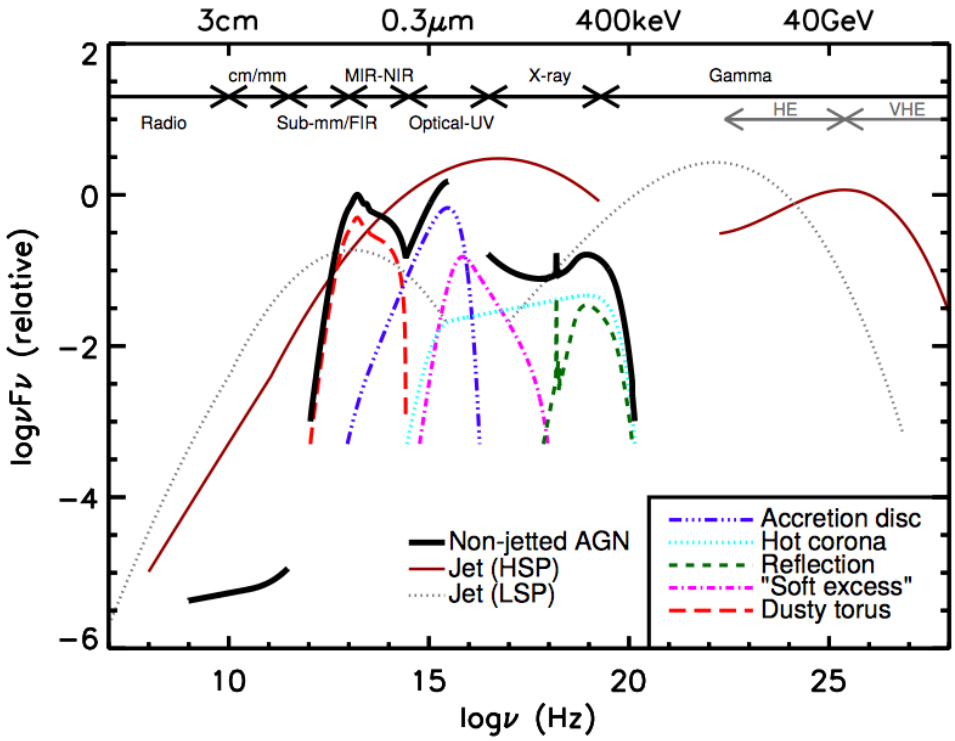

Figure 1.5. Scheme of an AGN continuum spectrum that ranges from radio to hard X-ray based on non-jetted quasars (Elvis *et al.* 1994; Richards *et al.* 2006). The black solid curve refer to the total emission. The red curve represent the dusty torus contribution. The blue curve refers to the emission from the accretion disc. The pink curve refers to the soft X-ray excess. The cyan curve indicates the emission from the hot corona. The SED of high synchrotron peaked blazar is shown in brown solid curve and low synchrotron peaked blazar is shown in brown dashed curve (Padovani *et al.* 2017).

law spectrum, likely due to the Compton up-scattering of Optical/UV photons from the accretion disk by the hot or non-thermal electrons of the corona. Fe Kα emission line at 6.4 keV and a Compton reflection hump above 10 keV are also present. These two features are thought to be due to fluorescence and reflection from both the accretion disk and the torus.

In Fig. 1.5 a schematic representation of the broad-band continuum spectral energy distribution, based on the observed SEDs of non-jetted AGNs is shown (Padovani *et al.* 2017).

1.2.b Properties of the BLR region

As mentioned previously, close to the AGN is located the BLR, which consists on a set of clouds producing broad emission lines with a Full Width at Half Maximum (FWHM) of the order of 10^3 km s^{-1} to a few of 10^4 km s^{-1}. A typical temperature of the BLR is of 10^4 K, which corresponds to a thermal line width of the order of 10 km s^{-1} , according to the following formula:

$$\mathrm{v} \approx \left(\frac{\mathrm{kT}}{\mathrm{m}}\right)^{1/2} \tag{1.19}$$

where k is the Boltzmann constant, T is the temperature and m is the mass of a particle. This means that the widths of the BLR emission lines do not reflect purely thermal motions, which required $\mathrm{T} > 10^9$ K according to 1.19, but they are the result of Doppler broadening due to the supersonical orbital motion around the BH.

The absence of forbidden lines such as [OIII]λ4363,4959,5007 suggests that the BLR clouds are characterized by electron density $\mathrm{n}_e > 10^9$ cm^{-3} (Ferland & Elitzur 1984), since these emission lines are suppressed in high density region by collisional de-excitation process. The presence of the semiforbidden line CIII]λ1909 Å instead gives an upper limit of $\mathrm{n}_e = 10^{10}$ cm^{-3}, since its radiative transition probability is higher than a true forbidden line and, as a consequence, its critical density is higher.

The size of the BLR can be measured using a technique called reverberation mapping, which uses the time-domain to resolve the BLR. The emission lines from the BLR are variable and the variation corresponds to a UV/optical continuum variation. The time delay between the continuum and the line variations is due to light travel time delay, by which it is possible to estimate the distance of the BLR as follows:

$$\mathrm{R_{BLR}} = \tau_{\mathrm{BLR}}\, \mathrm{c} \tag{1.20}$$

where τ_{BLR} is the time delay between the changes in the continuum and the emission line in the BLR and c is the speed of light.

The reverberation mapping experiments demonstrate that this delay is short and it is different from lines to lines. We can infer that the gas is photoionized and optically thick to ionizing radiation, the emitting region is small and the emission lines come from different radii. In particular Gaskell & Sparke (1986) show that the

BLR is stratified with the high ionization lines (such as CIV) coming from smaller radii than the low-ionization lines (such as Hβ).

The radius of the BLR inferred by the reverberation mapping is:

$$R_{BLR} = 0.1\ {L_{Bol,46}}^{1/2}\ \mathrm{pc} \tag{1.21}$$

where R_{BLR} depends on the bolometric luminosity L_{Bol} (in units of 10^{46} erg/s).

The outer radius of the BLR may be set by the dust sublimation due to bolometric luminosity, since the presence of dust in the BLR will suppress the line emission (Netzer & Laor 1993) when the ionization parameter U > 0.01. Specifically, considering the column of the photoionized HII layer as $\Sigma_{ion} \sim 10^{23}$ U cm^{-2} and the UV dust optical depth $\tau_{dust} \sim \Sigma/10^{21}$ this implies $\tau_{dust}(HII) \sim 100$U, i.e. when U > 0.01 the ionizing radiation is absorbed by dust which re-emits at IR emission, implying a decreasing of the line emission which is further reduce by dust destruction of the line photons. The outer radius set by the dust sublimation predicted by Netzer & Laor (1993) is:

$$R_{out} = 0.2\ L_{Bol,46}^{1/2}\ \mathrm{pc} \tag{1.22}$$

The typical radius of the BLR for an AGN of $L_{Bol} \sim 10^{47}$ erg s^{-1} is $\sim$ 1 pc.

The geometry of the BLR is still debated, with two main options for the configuration: quasi-spherically symmetric or flattened. Several works have found evidences for a disk-like, flattened configuration rather than a spherical one (Wills & Browne 1986; Murray & Chiang 1997, Elvis 2000). From radio observations, Wills & Browne 1986 showed that the FWHM of Hβ is correlated with the orientation, favoring the flattened scenario.

Furthermore, the covering factor of the clouds of the BLR, which is the fraction of the sky covered by the gas clouds, is high ($\sim$ 50%) and imply that the line of sight would intercept the BLR clouds (at least in the $\geq$ 50% of the cases). But the absence of a sharp Lyman absorption edge in the spectra is indicative of a flattened geometry (Gaskell *et al.* 2007; Gaskell 2009). This means that at the equatorial plane there is the ~100% probability to intersect a BLR cloud. Moreover the clouds will be self-shielding along this plane and the radiation will be diluted, instead it can freely escape along the axis of symmetry.

Flattened geometry is also supported by the detection of double-peaked Balmer lines in AGNs (Perez *et al.* 1988; Eracleous & Halpern 1994), where single peaked broad line emission also observed are thought to be the result of emitting disk viewed at low inclination (Popović *et al.* 2004). A schematic representation of two major options of the BLR configuration is shown in Fig. 1.6 (Gaskell *et al.* 2007).

The structure of the BLR can be also infer using gravitational microlensing. Hutsemekers *et al.* (2017) have found different microlensing effects in the high-ionization lines, such as CIV and low ionization lines, such as Hα. For a quasar at z $\sim$ 2, they found that the microlensing magnifies the continuum source and can deform the line profiles, exhibiting symmetric and asymmetric distortions in both high and low ionization emission lines (Richards *et al.* 2004; Braibant *et al.*

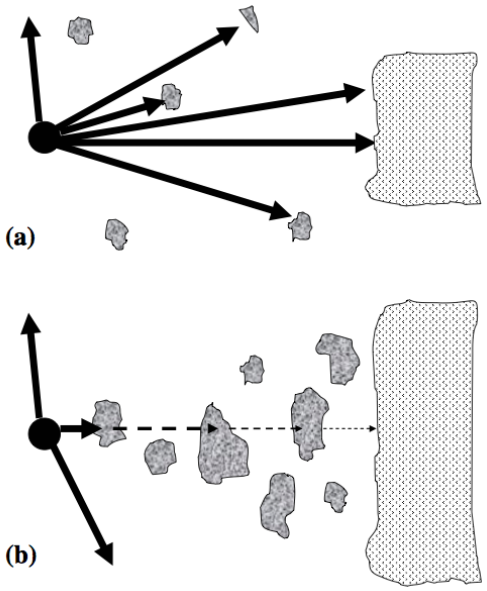

Figure 1.6. Schematic representation of the geometry of the BLR. (a) The BLR clouds are distributed quasi-spherically and do not shield distant clouds or torus. (b) The BLR clouds are distributed in a flattened geometry, where the torus and the distant clouds are shielded by clouds closer to the BH (Gaskell *et al.* 2007).

2014; Motta *et al.* 2017). In particular in the CIV emission line the microlensing results symmetric, where the wings are more magnified than the core, instead in the Hα emission line is more asymmetric, where the red wing is more magnified than the blue wing. This implies different kinematical properties for high and low ionization lines: the asymmetry in Hα is likely due to different location of red and blue wings, suggesting that the low ionization lines are situated in a Keplerian disk. The symmetric distortion found in the CIV line can be reproduced by assuming a polar outflow model for the CIV emission line (see Fig. 1.7).

FWHM of the Broad emission lines as a proxy of the SMBH mass. Assuming that the BLR is virialized and the clouds are dominated by gravitational motions, it is possible to estimate the mass of the central source M_{BH}, using the reverberation mapping, as follows:

$$M_{BH} = \frac{f\, R_{BLR}\, V_{BLR}^2}{G} \tag{1.23}$$

where G is the gravitational constant and f is a factor which depends on the BLR geometry and kinematics (Peterson *et al.* 2004), V is the velocity of the BLR clouds measured from the width of a specific line emission and R_{BLR} is the BLR size found from reverberation mapping.

This technique is limited by the large amount of telescope time required. Indeed considering a luminous quasar and its typical BLR radius of $\sim$ 100 light-days, the monitoring of a period of several years is required to obtain reverberation

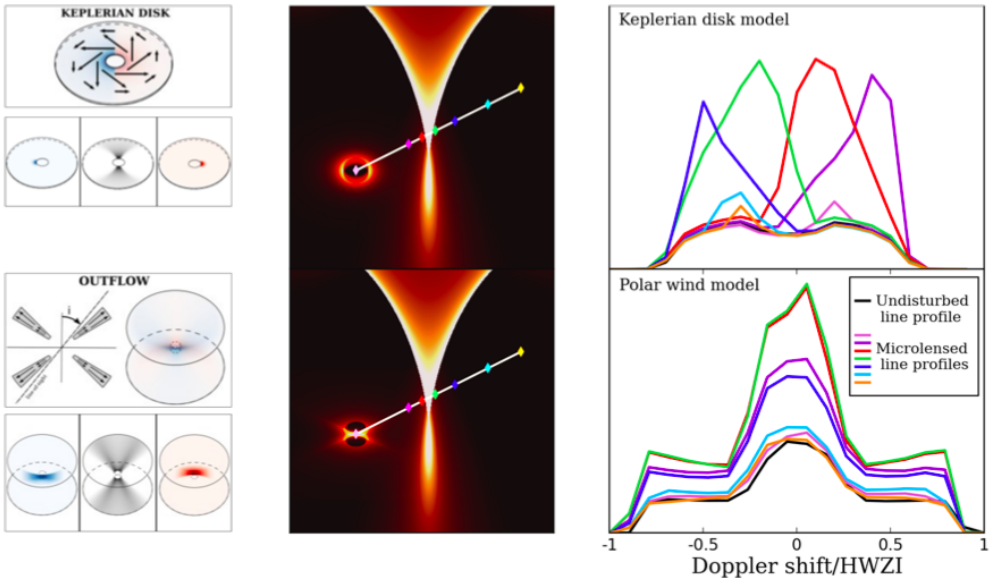

Figure 1.7. Microlensing of different BLR structures and the resulting line profile distortions. Two models are represented in the left panel: a rotating Keplerian disk and a biconical outflow, both seen at intermediate inclination. The location of the approaching and receding gas is indicated in blue and red, respectively. The middle panel shows the BLR superimposed on a typical caustic. At the different positions indicated by colored diamonds, different subregions of the BLR are magnified by the caustic. The right panel illustrates the line profiles corresponding to the different positions of the BLR onto the caustic pattern. Microlensing of the Keplerian disk is characterized by asymmetric red/blue line profile distortions while microlensing of the biconical outflow is characterized by symmetric wings/core distortions. (Hutsemekers *et al.* 2017)

measurements.

In case of no reverberation-mapped data, another method is used for the black hole mass estimation, i.e. the so-called single epoch method (Vestergaard 2002).

By using the radius-luminosity relation (Eq. 1.21) and substituting the R_{BLR} in 1.21, the black hole mass can be derived as follows:

$$M_{BH} = \frac{f\,(KL^{\alpha}_{AGN})\,V^2_{BLR}}{G} \tag{1.24}$$

This relation must be calibrated by comparing with the BH masses measured directly from reverberation mapping or from M_{BH}-σ relation. The calibration leads to the following formula:

$$Log(M_{BH}/M_{\odot}) = a + b \times Log\left(\frac{\Delta V}{10^3\ km\ s^{-1}}\right) + c \times Log\left(\frac{L}{10^{44}\ erg\ s^{-1}}\right) \tag{1.25}$$

where L is the monochromatic continuum or line luminosity and ΔV is the measure of the line width for a specific line and a, b, c are the calibration coefficients.

Different lines have been used to estimate the BH mass, depending on the redshift, i.e. Hβ, Hα, MgII and the CIV with different measures of the line width, i.e. FWHM or line dispersion (Vestergaard 2002, McLure & Jarvis 2002, Wang *et al.* 2009).

The Hβ emission line is widely used since it is the best studied line in the reverberation mapping. The MgII is usually used for intermediate redshift and for a few cases the time-lag of MgII have been measured (Reichert *et al.* 1994), with consistent results with what is found using the Hβ line (McLure & Dunlop 2004; Shen *et al.* 2008; Shen & Liu 2012). At high redshift the CIV line is usually adopted, and its single-epoch estimation is calibrated with Hβ reverberation-mapped AGNs.

As earlier studies have been confirmed, a strong correlation among the widths of Hα, Hβ and MgII is present (Greene & Ho 2005; Shen *et al.* 2008). However, the CIV line width poorly correlates with the Hβ line width as shown in Fig. 1.8 (Shen & Liu 2012). This finding suggests a different kinematics of the CIV and Hβ, likely due to the different origin of the high-ionization emission lines with respect to the low-ionization lines, as previously discussed. Furthermore the CIV emission line is more asymmetric than MgII or Balmer lines and shows prominent blueshift with respect to the low-ionization lines (Gaskell 1982). This suggests that the CIV emission line profile is not only the result of virial motions but it is also driven by outflowing motions (Shen *et al.* 2008, Richards *et al.* 2011, see Sect. 1.4.a for a discussion about CIV winds), and therefore the CIV line would be a biased virial mass estimator.

An empirical correction of the BH mass based on CIV line was developed by Denney (2012), using the shape of the CIV itself, in order to improve the consistency between the CIV- and Hβ-based virial BH mass estimates. Coatman *et al.* (2017), analyzing a sample of high-luminosity quasars in the redshift bin $1.5 < z < 4.0$ having both CIV and Hα coverage, found that in the presence of large blueshifts of

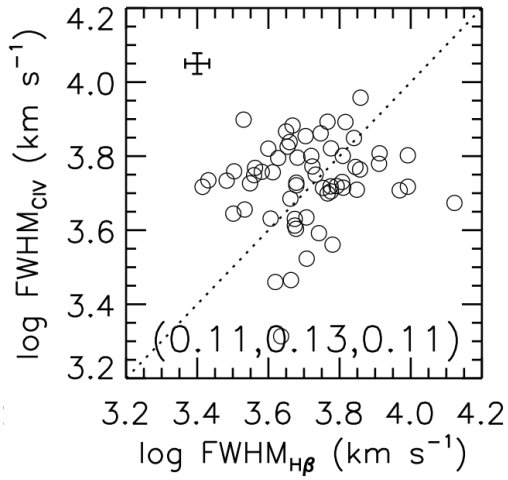

Figure 1.8. Comparison between the FWHM of CIV and the Hβ emission lines. The uncertainties are indicated in the top-left corner. The dotted line indicates the unity relation. In the panel is also shown the result from the best-fit linear regression using the Bayesian method in Kelly (2007). In particular the best-fit slope, the uncertainty of the slope and the intrinsic random scatter about the regression is labeled (Shen & Liu 2012).

the CIV the BH mass derived from the CIV emission line tends to be a factor of five larger than those measured by the Hα line and even larger at higher blueshifts, as shown in Fig. 1.9. As a consequence, they estimate a correction factor from the relationship between the CIV blueshift and the BH mass ratio based on CIV and Hα, leading to a scatter between the corrected CIV-based masses and Hα-based massed of 0.24 and 0.1 dex at low and high blueshifts, respectively, i.e. much lower than that observed for uncorrected CIV-based BH mass (~0.4 dex).

The Baldwin effect. As found by Baldwin (1977) analyzing a sample of 20 quasars (mostly radio-loud) with two orders of magnitude in continuum luminosity in the redshift range $1.24 \leq z \leq 3.53$, a relation exists between the equivalent width of the CIV emission line and the continuum luminosity at 1450 Å, the so-called Baldwin effect, i.e. at increasing luminosities the equivalent width of the CIV decreases (see Fig. 1.10). This effect has been confirmed in much larger samples (Wu *et al.* 2009) and also discovered for MgII and other UV/optical emission lines with different slopes for different lines: higher ionization species display steeper slopes in the equivalent width - luminosity plane (e.g. Dietrich *et al.* 2002). In particular the Balmer lines show no Baldwin effect. However multiple studies have been demonstrated that the equivalent width of N V λ1240 Å shows little/absent dependence on luminosity despite the large ionization potential (Dietrich *et al.* 2002 and reference therein). This is likely due to metallicity effect, where an increasing metallicity with luminosity compensates for the decreasing in the NV producing photons at increasing luminosity (the SED becomes softer).

Several studies have investigated the Eddington ratio and the black hole mass

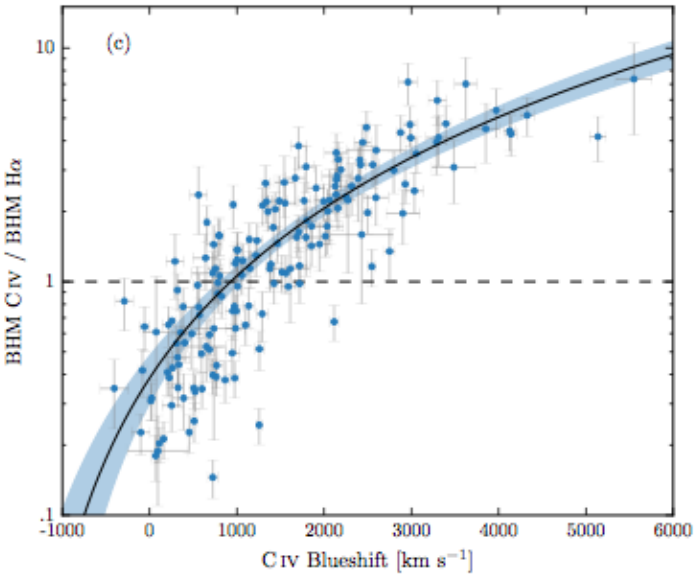

Figure 1.9. CIV-based BH mass compared to Hα-based mass as a function of the CIV blueshift (Coatman *et al.* 2017).

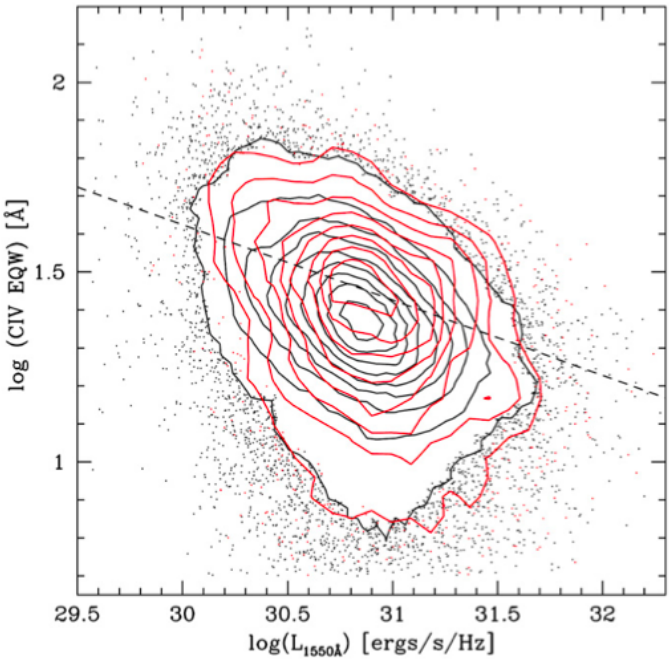

Figure 1.10. The CIV equivalent width as a function of the luminosity at 1550 Å, the so-called Baldwin Effect. Red contours refer to radio-loud and black contours to radio-quiet samples. The dashed line shows the best-fit to the data from Wu *et al.* (2009) (Richards *et al.* 2011).

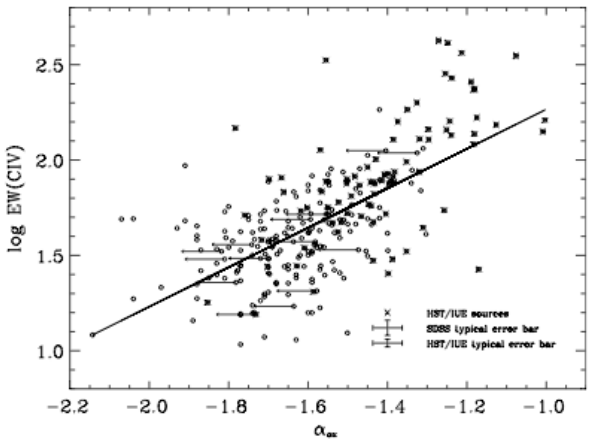

Figure 1.11. Equivalent width of the CIV emission line as a function of αox. The solid line corresponds to the best fit relation (Wu *et al.* 2009).

(Boroson & Green 1992, Baskin & Laor 2004) as physical drivers of the Baldwin effect. Specifically Baskin & Laor (2004) found for the PG quasars a tight relation between the EW of the CIV and the Eddington ratio than the luminosity. Recently Bian *et al.* (2012) found a strong correlation between the CIV equivalent width and the CIV-based BH mass using a sample of ∼35000 QSOs at redshift $1.9 \leq z < 5$ and a weaker correlation between CIV equivalent width and MgII-based BH mass for QSOs at $1.5 \leq z < 1.9$, as a result of the bias CIV-based BH mass. Indeed applying a correction factor for the CIV-based BH mass the relation becomes weaker. They also found a stronger correlation with the Eddington ratio, considering MgII-based BH mass.

The Baldwin effect may also depends on the softening of the X-ray spectrum at high luminosities, as found by Wu *et al.* (2009). Wu *et al.* (2009) investigated the CIV Baldwin effect for a sample of radio-quiet Type 1 AGNs, having both UV/optical and X-ray observations. They found that the EW of the CIV is correlated with both the shape of the Optical-to-X-ray continuum αox (Fig. 1.11) [2] and luminosity at 2500 Å (Fig. 1.12). This finding may suggest that more CIV ions are produced when the spectrum is harder, whereas in case of softer spectrum it is expected a deficit of the ionizing photons having high potentials to ionize the CIV emission line (Netzer *et al.* 1992).

The properties of the FeII emission. The FeII emission lines are low excitation lines, with uncertain location. It is likely mainly emitted in the BLR clouds since they have the same width as the broad Hβ lines in both the optical and in the

[2] The α_{OX} is defined as :

$$\alpha_{OX} = \frac{\mathrm{Log}(L_{2keV}/L_{2500Å})}{\mathrm{Log}(\nu_{2keV}/\nu_{2500Å})} \tag{1.26}$$

where L_{2keV} and $L_{2500Å}$ are the luminosities at 2 keV and 2500 Å, respectively.

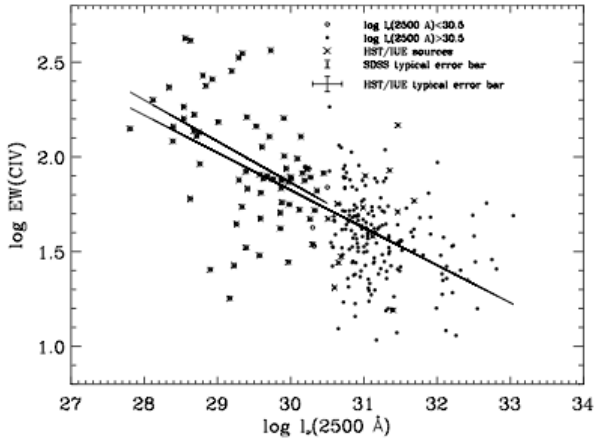

Figure 1.12. The CIV equivalent width as a function of luminosity at 2500 Å. Different symbols correspond to different luminosities. The short solid line is the best linear fit to low-luminosity points and the long one is the best linear fit to the entire sample (Wu *et al.* 2009).

ultraviolet. But other solutions have been proposed for their location as (i) the accretion disk close to the black hole (Zhang *et al.* 2006); (ii) region which can be heated by shocks in a intermediate line region between the BLR and NLR (Marziani & Sulentic 1993; Hu *et al.* 2008) and (iii) shielded, neutral outer region of the BLR (Gaskell 2009).

Strong FeII emission requires density $n_e \gg 10^9$ cm^{-3}, high column density and temperature T $\sim$ 5000 K (Collin-Souffrin *et al.* 1980). These features are too strong to be produced by photoionization and an additional excitation mechanism is required such as: continuum fluorescence (Phillips 1979); collisional excitation (Véron-Cetty *et al.* 2006); self-fluorescence among FeII transitions (Netzer & Wills 1983) and fluorescent excitation by the Lyα and Lyβ lines (Verner *et al.* 1999).

The iron emission is important for the BLR since it is an efficient coolant and emits ~25% of the total energy of the BLR (Wills *et al.* 1985). The numerous multiplets form a pseudo-continuum, which extends from the UV to NIR with the deblending of over 344000 transitions (Bruhweiler & Verner 2008). Several distinct bands can be identify with permitted UV lines at 2200-2600 Å, permitted optical lines at 3000-3400 Å, 4500-4600 Å and 5250-5350 Å (between odd parity and even parity levels as shown in Fig. 1.13).

The FeII emission is highly variable and the ratio between the FeII and Hβ is usually used to quantify the weakness or the strongness of this feature, i.e. the range varies from 0 < FeII/Hβ < 10. In a few cases the FeII emission is the strongest contributor to the line spectrum as found for the ULIRG IRAS 07598+6508 (Véron-Cetty *et al.* 2006).

The FeII emission is usually modeled with observational templates, such as the ones of Boroson & Green (1992), Véron-Cetty *et al.* (2004) and Tsuzuki *et al.* (2006) for the optical region, which are based on the FeII emission of the spectrum of

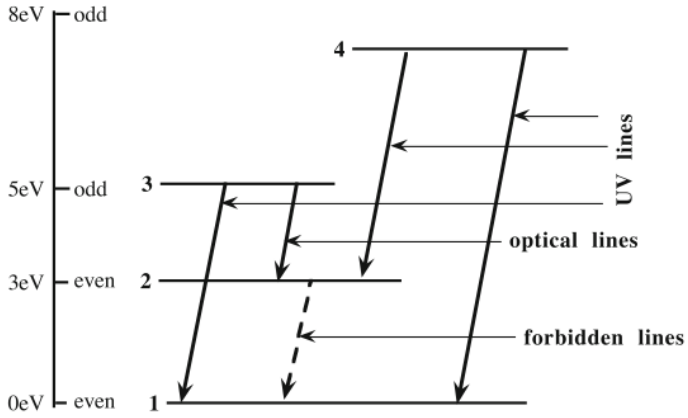

Figure 1.13. Grotrian diagram of Fe II emission.

I Zw 1, a well-known Narrow Line Seyfert 1 showing strong FeII emission. Models from Cloudy simulation are also used in order to match the observed FeII emission and the BLR features (Ferland *et al.* 2013). Vestergaard & Wilkes (2001) extended the FeII template of I ZW 1 in the UV band, using Hubble Space Telescope and FOS spectra, providing the first UV template for the FeII.

The FeII emission correlates with other emission lines such as [OIII] and Hβ, as found by Boroson & Green (1992). In particular the equivalent width of the FeII anti-correlates with the ratio of the equivalent width of the [OIII] and with the FWHM of the Hβ, i.e strong [OIII] corresponds to weak FeII objects and viceversa, a trend known to be a part of the Eigenvector 1. The physics underlying these correlations is still unclear but several works point towards the Eddington ratio as the responsible for this behaviour (Boroson & Green 1992; Marziani *et al.* 2003).

1.2.c NLR region

The NLR exhibits emission line narrower than those of the BLR, with typical widths of a few hundred km/s. A narrow width and the lack of variability indicate that they are originated far from the nucleus. As a consequence it is possible to see narrow lines in both face-on and edge-on view.

The emission lines emitting in the NLR are typically the Balmer lines and forbidden lines such as [O III]$\lambda\lambda$4959,5007, [N II]$\lambda\lambda$6548,6583, [O I]$\lambda\lambda$6300,6364, [S II]$\lambda\lambda$6716,6731, which are photoionized by the UV/X-ray continuum radiation emitted by the central source. The presence of forbidden lines implies a NLR density of the order of $\sim 10^{3-5}$ cm^{-3}, since these lines are not collisionally suppressed.

The NLR is spatially extended and can reach up to kpc scale, with a morphology usually described with an ionizing bicone. In Fig. 1.14 the NLR biconical morphology in NGC5728 is shown, traced by the [OIII]λ5007 Å emission line.

Several studies leads to the idea that the NLR extension seems to be proportional to the [OIII] luminosity, i.e. $R_{NLR} \propto L^{0.5}_{[OIII]}$, as found by Bennert *et al.* (2002),

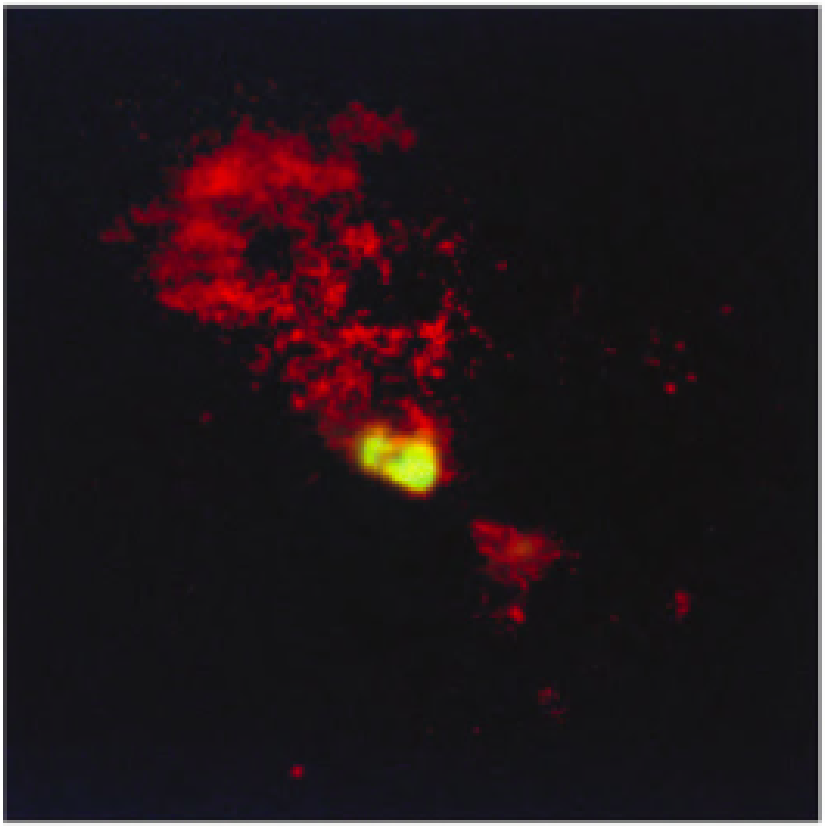

Figure 1.14. HST image of NGC5728 showing the bi-conical emission morphology in the NLR as traced by [OIII]λ5007 emission line. Image Credit: Andrew S. Wilson (STScI)/NASA/ESA, James A. Braatz (Univ. Of Maryland), Timothy M. Heckman (STScI), Julian H. Krolik (JHU), George K. Miley (Leiden Observatory), and Allan Sandage (Carnegie Observatories)

analyzing a sample of luminous radio-quiet PG quasars or $R_{NLR} \propto L_{[OIII]}^{0.33}$, as found by Schmitt *et al.* (2003), studying a large sample of Seyfert-1 and Seyfert-2. The increasing in size of the NLR with luminosity may partially explain the Baldwin effect observed by Croom *et al.* (2002) in the $EW_{[OIII]}$ of ∼ 22000 AGNs. Indeed the galactic scale dimension of the NLR in the most luminous objects are likely to escape the system leading to AGNs with weak or no NLR emission. This is also suggested by Netzer *et al.* (2004), which presented results about a sample of 29 high-luminosity high-redshift AGNs. They found two distinct classes of sources according to different [OIII]λ5007 Å properties, specifically one-third of the total sample exhibits a strong [OIII]λ5007 Å emission line and the remaining objects show no or a weak [OIII] emission. They claimed that the AGNs with weak [OIII] have lost their very large, dynamically unbound NLR, whereas the sources showing strong [OIII] emission are likely in a phase of violent star-forming events where a large quantity of gas is produced in their nuclear region and ionized by the central source.

The presence of ionization cones indicate that the AGN radiation can escape along the polar axis of the torus. As the [OIII] emission lines are located well outside the torus, the [OIII] observed flux is little affected by viewing angle and can be seen in similar strengths in Type-1 and Type-2 AGNs. The luminosity of the [OIII]λ5007 Å emission line can be therefore considered as a proxy of the intrinsic luminosity of the AGNs. In Fig. 1.15 it is shown the comparison between the [OIII] luminosity and the IR luminosity for Seyfert 1 and Seyfert 2 from Mulchaey *et al.* (1994), where the IR emission can be also considered as an indicator of the intrinsic AGN luminosity. As already discussed in Sect. 1.2.a the IR emission is produced by the dust located in the obscuring torus and represent the reprocessed optical-UV-X-ray emission from the accretion disk. For the Seyfert-1 the correlation between IR and [OIII] emission is stronger than that of Seyfert 2, which in this case is likely contaminated by the contribution in the IR of the host-galaxy and star-formation, instead the [OIII] emission is the least contaminated emission lines by the contribution from HII regions associated with the star formation.

As a consequence to be a good indicator of the intrinsic luminosity, the [OIII] emission line, i.e its equivalent width, is expected to be a function of the inclination angle θ between the disc axis and the line of sight, if the continuum emission is due to an optically thick disc, as found by Risaliti *et al.* (2011) and Bisogni *et al.* (2017). They analyzed a large sample of SDSS DR7 AGN with $0.001 < z < 0.8$, considering the observed equivalent width $EW_{[OIII]} = EW_{intrinsic}/cos(\theta)$, where $EW_{intrinsic}$ is the intrinsic equivalent width as measured in a face-on disc. They showed that the distribution of the observed $EW_{[OIII]}$, which exhibits a power-law tail with $\Gamma \sim -3.5$ at the largest $EW_{[OIII]}$ values, is well reproduced by assuming an isotropic [OIII] emission (as stressed it is proportional to the intrinsic disc luminosity) and a random inclination of the disc with respect to the line of sight (see Fig. 1.16). As a result, the $EW_{[OIII]}$ can be used as a proxy of the inclination, which is likely responsible of the large-$EW_{[OIII]}$ power-law tail observed in the distribution, where the higher $EW_{[OIII]}$

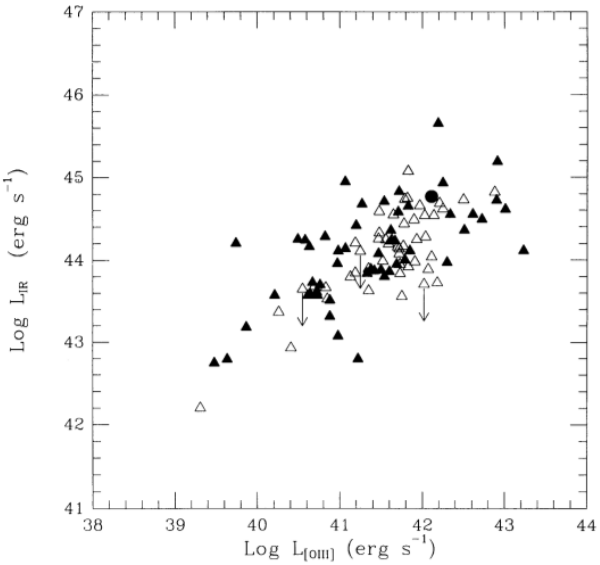

Figure 1.15. IR luminosity as a function of [OIII] luminosity in the log-space for Seyfert-1 (open triangles) and Seyfert-2 (filled triangles) from Mulchaey *et al.* (1994). A correlation is present for both Seyfert-1 and Seyfert-2, but the relation is much weaker for the Seyfert-2 due to the contribution in the IR of the star-formation in the host galaxy.

the higher inclination. The peak of the distribution is $\sim$ 10 Å and the orientation effect dominates at $EW_{[OIII]} \geq$ 25-30 Å . At lower $EW_{[OIII]}$ the distribution resembles the intrinsic distribution of the equivalent width, which is expected to depend on the spectral characteristic of the continuum emission and the dimension and shape of the NLR.

By using forbidden emission lines it is possible to derive physical quantities of the NLR. The electron temperature can be measured from the line ratios [OIII] λ4363Å/λ5007Å and it is found in the range of 10000–25000 K.

The metallicity can be measured from a direct method such as the conversion of electron temperature in metallicity or empirical methods based on the optical ratios [NII]λ6584/Hα (Pettini & Pagel 2004), ([OII]/Hβ)/([NII]/Hα) (Pettini & Pagel 2004) and [OII]λ3727+[OIII]$\lambda\lambda$4959,5007/Hβ.

The density is derived from the [OII] doublet, but it is a very weak line, or [SII]λ6716/6731Å (Osterbrock 1978) and it is in the range 80–1000 cm^{-3} (Genzel *et al.* 2014; Peterson 1997).

1.3 Theoretical model of AGN outflows

Observational evidences of outflows have been observed in several AGNs, at both pc and kpc scales and gas with different ionization states (Fiore *et al.* 2017 and reference therein).

A theoretical model was developed by King & Pounds (2003) to explain the

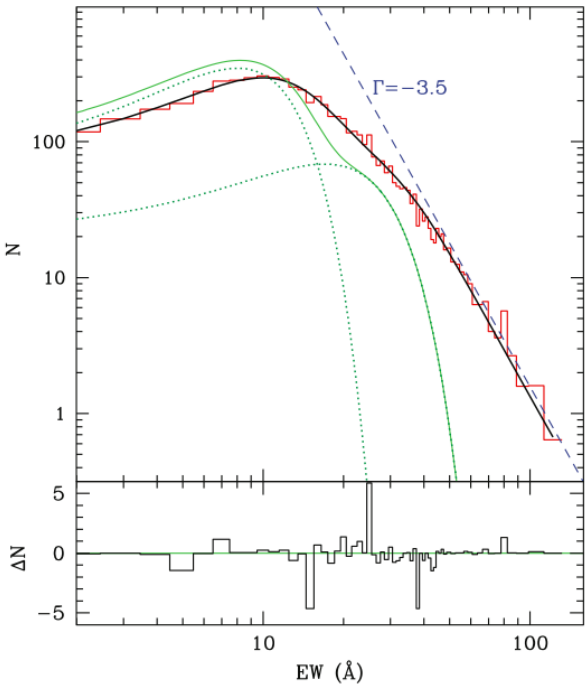

Figure 1.16. Distribution of the $EW_{[OIII]}$ (red histogram) and best-fit model (black line) for a sample of SDSS quasars studied by Risaliti *et al.* (2011). The dashed blue line is a power law with a slope Γ = -3.5. The solid green curve is the total intrinsic distribution, as a result of the combination of two Gaussian components (dotted green curves). Inclinations effect are likely responsible for the power law tail at high $EW_{[OIII]}$.

detection of the X-ray absorption lines in the quasar PG 1211+143 by Pounds *et al.* (2003), characterized by high column density ($N_H \sim 10^{24}$ cm^{-2}) and velocity (v ∼ 0.1 c). They showed that these features are expected for an optically thick wind driven by continuum radiation pressure from a black hole accreting at rate comparable to the Eddington value.

King & Pounds (2003) assumed a radial outflow in a double cone which occupies a solid angle 4πb, where b is the covering factor of the outflow which is assumed to be ∼ 1, and with an outflow velocity v constant for larger radial distance R.

Considering the mass conservation equation, the mass outflow rate ($\dot{M}_{out} = dM_{out}/dt$) is:

$$\dot{M}_{out} = 4\pi b R^2 v \rho(R) \tag{1.27}$$

with ρ(R) is the mass density. The electron scattering optical depth through the wind is defined as:

$$\tau = \int_{inf}^{R} \kappa \rho dr = \frac{\kappa \dot{M}_{out}}{4\pi v b R} \tag{1.28}$$

where κ is the electron scattering opacity ($= \sigma_T/\sigma_p$). By combining Eq. 1.27 and 1.28, the electron scattering optical depth can be rewritten as:

$$\tau = \frac{1}{2\eta b} \frac{R_S}{R} \frac{c}{v} \frac{\dot{M}_{out}}{\dot{M}_{Edd}} \tag{1.29}$$

where R_S is the Schwarzschild radius, and defining the photospheric radius R_{ph} as the distance at which $\tau \sim 1$

$$\frac{R_{ph}}{R_S} = \frac{1}{2\eta b} \frac{c}{v} \frac{\dot{M}_{out}}{\dot{M}_{Edd}} \tag{1.30}$$

As derived from Eq. 1.28 considering $\eta = 0.1$(see Chapter 5.2), a covering factor b ∼ 1, a mass outflow rate close to the Eddington rate, the wind is Compton thick at radius $> R_S$. This implies that each photon scatters about once before escaping to infinity, giving up all of its momentum to the wind. At distance larger than R_{ph} the photons decouple from the matter with resulting no more acceleration, which justified the constant velocity assumption at large distance. In order to reach the escape velocity for the matter, the R_{ph} have to lie close to the escape radius $R_{esc} = (\frac{c}{v})^2 R_S$. Rewriting Eq. 1.30, substituting Eq. 1.8 and imposing $R_{ph} = R_{esc}$:

$$\frac{v}{c} = \frac{2\eta b \dot{M}_{Edd}}{\dot{M}_{out}} = \frac{2\ b L_{Edd}}{\dot{M}_{out}\ c^2} \tag{1.31}$$

From Eq. 1.31 it is possible to estimate the momentum flux of the outflow $\dot{P}_{out}$:

$$\dot{P}_{out} = \dot{M}_{out}\ v \sim \frac{L_{Edd}}{c} \tag{1.32}$$

which is of the same order as that in the Eddington-limited radiation field. The kinetic energy flux is:

$$\dot{E}_{out} = \frac{1}{2}\dot{M}_{out} v^2 \sim \frac{L_{Edd} v}{2c} \sim 0.05 L_{Edd} \tag{1.33}$$

the kinetic energy of the outflow is a few percent lower of the energy of a Eddington-limited radiation field.

From Eq. 1.27 and 1.31, it is possible to estimate the ionization parameter of the outflow which determines the spectral lines observed (King 2010):

$$\xi = \frac{L_i}{NR^2} \tag{1.34}$$

where $L_i = \lambda_{\rm Edd}\, L_{\rm Edd}$ is the ionizing luminosity ($\lambda_{\rm Edd}$ <1 is the dimensionless parameter called Eddington ratio) and N is the number density ($= \rho/\mu m_p$). Considering for instance a quasar luminosity of $0.3L_{\rm Edd}$, ξ corresponds to a photon energy threshold for highly ionized iron, in agreement with the observed blueshifted iron absorption lines (Ultra-fast outflows) (Cappi *et al.* 2006,Tombesi *et al.* 2010).

How efficiently the wind energy is transmitted to large scale outflows depends on how the winds interacts with the ISM. The way by which the interstellar gas is swept up was investigated by Zubovas & King (2012). They proposed a two-phase mechanism by which the large-scale outflows are driven by wide-angle high-velocity winds expelled by radiation pressure from the center (Pounds *et al.* 2003). In this model they assumes with the term *wind* the mildly relativistic ejection of accretion disk gas near the BH and with the term *outflow* the large-scale non relativistic flows due to interaction between the wind and the host-galaxy gas.

In their model these winds are moving at hypersonic speed and impact against the host galaxy gas, producing reverse and forward shocks, which slows the wind and accelerates the swept-up gas respectively. If the shocked wind gas cools on a short timescale shorter than the flow time, then flow is momentum-driven and the kinetic energy is lost and the drop of pressure results in a compression of the shocked wind gas towards high density. In this phase the wind kinetic energy is radiated away and $\dot{E}_{out} \ll \dot{E}_w$ (Eq. 1.33) where $\dot{E}_{out}$ is the kinetic energy of the large scale outflow and $\dot{E}_w$ is the wind kinetic energy. Only the ram pressure is conserved, which pushes at the large distance. The cooling process is the inverse Compton effect (Ciotti & Ostriker 1997) and implies that the momentum-driven flows occur when shocks happen within $\sim$ 1 kpc of the AGN. When SMBH accretes at near Eddington accretion rate, the momentum flow rate of the wind is:

$$\dot{\rm P}_{\rm w} = \dot{\rm M}_{\rm w} {\rm v} \sim \frac{{\rm L}_{\rm Edd}}{\rm c} \tag{1.35}$$

If the wind gas is not efficiently cooled, thus the energy injected by the wind is fully conserved throughout the outflow:

$$\frac{1}{2}\dot{\rm M}_{\rm w} {\rm v}_{\rm w}^2 \sim \frac{1}{2}\dot{\rm M}_{\rm out} {\rm v}_{\rm out}^2 \tag{1.36}$$

$\dot{E}_{out} \sim \dot{E}_w \sim 0.05\ L_{Edd}$ and the flow expands adiabatically. This phase is called energy-driven. The momentum flow rate of the outflow is given by rewriting the Eq. 1.36:

$$\dot{\rm P}_{\rm out} = \dot{\rm P}_{\rm w}\left(\frac{\dot{\rm M}_{\rm out}}{\dot{\rm M}_{\rm w}}\right)^{1/2} \sim 20\sigma_{200}^{-2/3}\lambda_{\rm Edd}^{1/6}\frac{{\rm L}_{\rm Edd}}{\rm c} \tag{1.37}$$

where σ_{200} is the velocity dispersion in unit of 200 km s^{-1} and $\lambda_{\rm Edd}$ is the Eddington ratio. Eq. 1.37 show that in energy-driven outflows the momentum flow rate increases proportionally to the AGN bolometric luminosity. Values of $\dot{P}_{out}$ of $\sim$ 10-20 $\frac{L_{Edd}}{c}$ have been measured for kpc-scale outflows (Cicone *et al.* 2014)

A diagram of these two different outcomes is represented in Fig. 1.17.

An alternative way of driving large-scale outflows is by direct radiation pressure on dust as proposed by Ishibashi & Fabian (2015). They found that shells driven by radiation pressure on dust can reach high velocities and large values of the momentum flux under certain physical conditions. Large values of the momentum flux consistent with the observed ones can be obtained, if the shell is initially optically thick to its own reprocessed IR radiation. Such high values of the IR optical depth can be easily found in the central regions of ULIRGs and gas-rich AGN, where kpc-scale outflows are indeed detected.

1.4 Observations of outflows from nuclear to kpc-scales

Evidences of radiatively-driven winds are observed at sub-pc scale, in the innermost regions of the AGNs through the detection of blueshifted highly ionized Fe K-shell transitions, i.e. Ultra Fast Outflows (UFOs), with velocities $\sim$ 0.1c (King & Pounds 2015; Tombesi *et al.* 2010, 2014; Gofford *et al.* 2013); at pc scale via warm absorbers and broad absorption lines (BAL), moving at velocities up to 10,000 km s^{-1} (King & Pounds 2015; Tombesi *et al.* 2013a) and via the blueshift of the CIV emission line (Gaskell 1982); at kpc-scale through different gas phases such as ionized gas, i.e. broad asymmetric blueward [OIII] emission lines (Harrison *et al.* 2012, 2014; Cano-Díaz *et al.* 2012; Brusa *et al.* 2015 Carniani *et al.* 2015); neutral atomic as NaID (Rupke & Veilleux 2015), and molecular gas with velocities up to a few thousands km s^{-1} (Feruglio *et al.* 2010; Cicone *et al.* 2014; Spoon *et al.* 2013).

At the present day, enormous observational efforts have been made to constrain the incidence, kinematics and energetics of powerful outflows. While a lot of progress has happened we still face several observational and conceptual issues, such as the outflows morphology, the timescales involved and the spatial extension. In this section i will discuss about the different outflow types at different regions: nuclear and kpc-scale winds.

1.4.a Nuclear winds

CIV outflows

The high ionization lines, such as CIVλ1549 Å, are known to exhibit asymmetric profiles towards the blue-side, with the peak of the emission line blueshifted with respect to the low ionization lines, such as MgII or Hβ (Gaskell 1982; Sulentic *et al.* 2000 and Richards *et al.* 2011). As an example, in Fig. 1.18 it is shown part of the

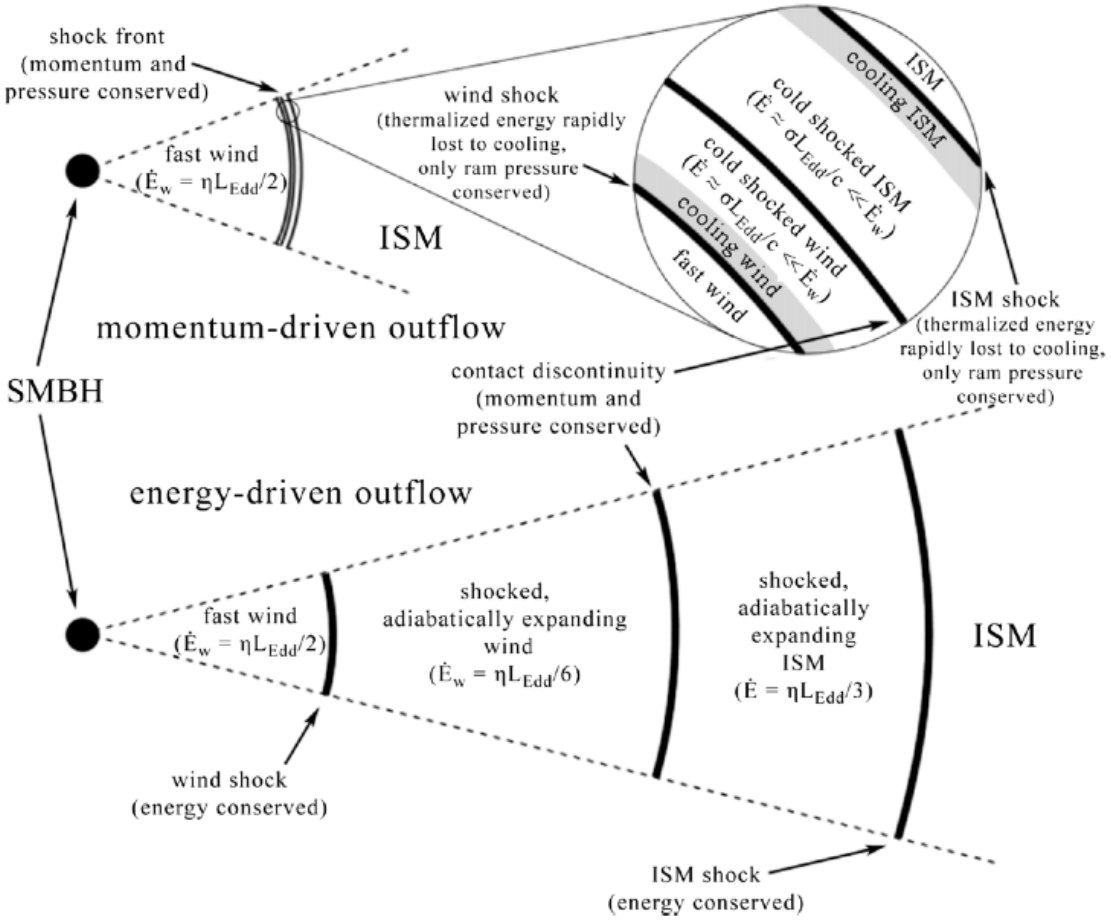

Figure 1.17. Schematic representation of momentum-driven (*top*) and energy-driven (*bottom*) outflows. In both cases a fast wind impacts the interstellar gas of the host galaxy, producing an inner reverse shock slowing the wind, and an outer forward shock accelerating the swept-up gas. In the momentum-driven case, the shocks cool to become isothermal. Only the ram pressure is communicated to the outflow, leading to very low kinetic energy. In an energy-driven outflow, the shocked regions do not cool. They expand adiabatically, communicating most of the kinetic energy of the wind to the outflow (Zubovas & King 2012),

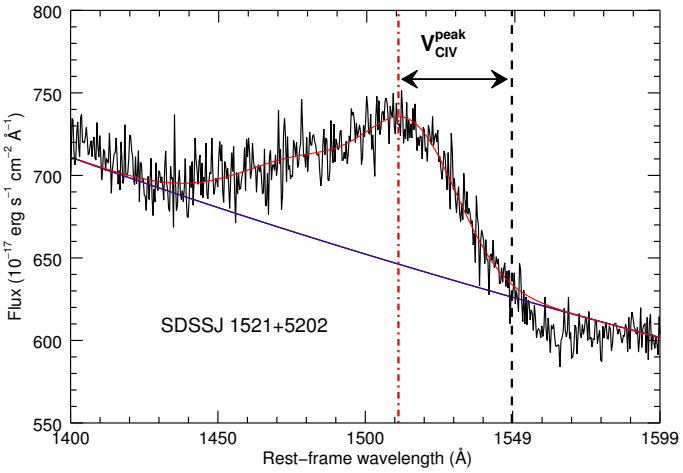

Figure 1.18. Rest-frame UV spectrum in the region of the CIV emission line of the WISSH QSO J1521+5202. The peak of the CIV emission line is blueshifted (v_{CIV}^{peak}) with respect to the systemic redshift (black dashed line). The red dot-dashed line denotes the peak of the CIV emission line. The solid red curve indicates the best-fit to the data.

UV spectrum of the WISSH QSO J1521+5202, in the region of CIV emission line, which exhibits a strong blueshift of the peak with respect to the systemic redshift.

This behaviour cannot be ascribed to virialized motions but it can be interpreted in terms of outflowing gas, which likely result from the presence of a radiation line-driven accretion-disc wind, whereas low ionization lines are gravitationally bounded and likely emitted in a flattened configuration. The presence of these outflows possibly leads to biased BH mass estimates derived from the entire CIV emission line (Denney 2012; Coatman *et al.* 2017), as already discussed in Sect. 5.2.

The blueshift of the CIV emission line can be a valuable tool to trace the winds in the BLR. The CIV emission line typically shows a blueshift ~ 600 km s^{-1} up to 2000 km s^{-1} (Shen *et al.* 2011; Richards *et al.* 2002), with a mean shift of ~ 810 km s^{-1} for radio-quiet quasars and ~ 360 km s^{-1} for radio-loud quasars (Richards *et al.* 2011). As discussed in Richards *et al.* 2011, the blueshift are luminosity-dependent (see Fig. 1.19). Specifically in Fig. 1.19, the blueshift of the CIV as a function of luminosity at 1550 Å is shown for radio quiet and radio loud quasars. A trend exists for both types of quasars, although the radio loud has a shallower slope. Despite the large scatter, luminous quasars are more likely to have larger CIV blueshifts.

Furthermore, AGNs with large blueshifts of the CIV emission line tend to have small CIV equivalent width, as shown in Fig. 1.20. In particular this plot shows a missing quadrant rather than a correlation between the two parameters. As discussed in Sect. 1.2.b, a correlation between the equivalent width of the CIV and αox

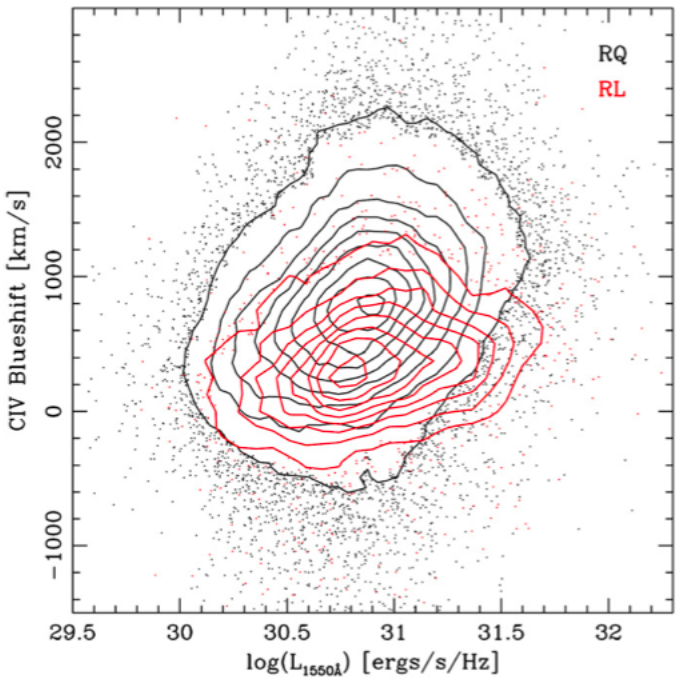

Figure 1.19. CIV blueshift as a function of the luminosity at 1550 Å for radio loud (red) and radio quiet (black) quasars, from Richards *et al.* (2011). The radio loud have a shallower trend than the radio quiet, but despite the large scatter both types of quasars have larger blueshifts at higher luminosities.

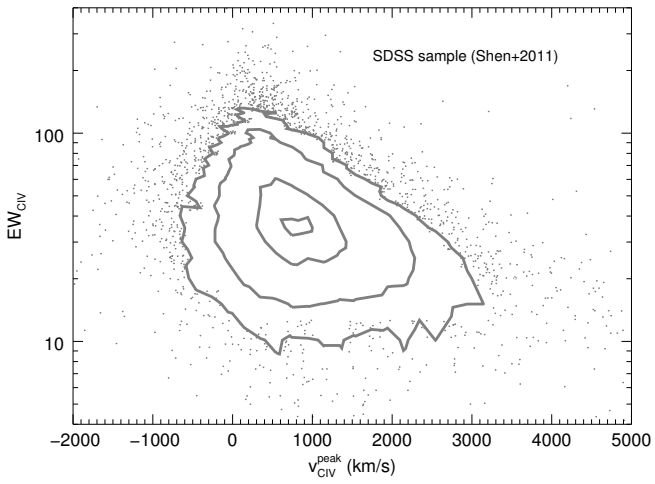

Figure 1.20. Rest-frame equivalent width of the CIV emission line (EW_{CIV}) as a function of its velocity shift (v_{CIV}^{peak}) for the SDSS sample from Shen *et al.* (2011).

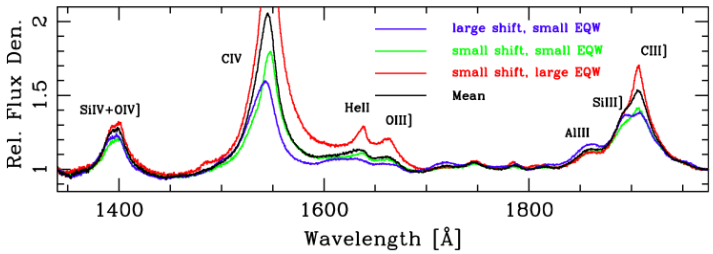

Figure 1.21. Composite UV spectra for four different regions of CIV equivalent width - blueshift plane. Red curve indicates objects with large EW_{CIV} and small blueshifts, blue curve indicates those with small EW_{CIV} and large blueshifts, green curve represents objects with small blueshifts and small EW_{CIV} and black curve refers to a mean spectrum of objects exhibiting intermediate properties (Richards *et al.* 2011).

is present and from the sample compiled by Wu *et al.* (2009), Richards *et al.* (2011) found a correlation between the velocity shift of the CIV and the αox, i.e. quasars with larger blueshifts are weaker in the X-ray (have steeper αox) as show in Fig. 1.22, and have lower equivalent width of the CIV. A steep αox consists on a SED weak in X-rays, which suggests a strong radiation line-driving, whereby the UV luminosity which drives the wind, is high relative to the X-ray luminosity. Indeed strong X-ray radiation can overionize the material and hamper an efficient line-driving mechanism. This can be also seen from the composite UV spectra built by Richards *et al.* (2011) and shown in Fig. 1.21. Here different quadrants of the EW(CIV) - blueshift plane of Fig. 1.20 are shown in terms UV emission lines. They noted that the CIV emission line exhibits large blueshift when the Si III] 1892/CIII] 1909 ratio is large, which is indicative of an X-ray weak spectrum. A similar behavior is also present when comparing the CIV with HeII emission lines, with a stronger HeII in the presence of a strong soft-X-ray spectrum.

The largest blueshifts have been discovered in an extreme quasar population at $2.2 \lesssim z \lesssim 5.9$, the so-called Weak Line Quasars (hereafter WLQs). These objects exhibit weak/undetectable UV emission lines and are defined as quasars with rest-frame equivalent width of the CIV emission line of less than 10 Å (Fan *et al.* 1999; Diamond-Stanic *et al.* 2009; Plotkin *et al.* 2010; Wu *et al.* 2011).

The velocity shift of the CIV emission line is part of the 4D Eigenvector 1 parameter space (Boroson & Green 1992; Sulentic *et al.* 2000) and correlates with parameters of characterizing the optical emission lines. The 4D Eigenvector 1 also involves the broad Fe II emission, the equivalent width of the narrow [OIII] component, the width of Hβ emission line and the X-ray photon index.

As found by Marziani *et al.* 2016, these winds occurring in the BLR may affect the host galaxy. They studied a sample of quasars with $L_{Bol} = 10^{45-48.2}$ erg s^{-1} at $0.9 < z < 3$ and found that the outflow kinetic power of these winds traced by CIV emission line is comparable to the binding energy of the gas in a massive spheroid, underlying the importance of considering these winds in the feedback scenario. In the Chapter 2 a detailed discussion will be presented about the CIV winds.

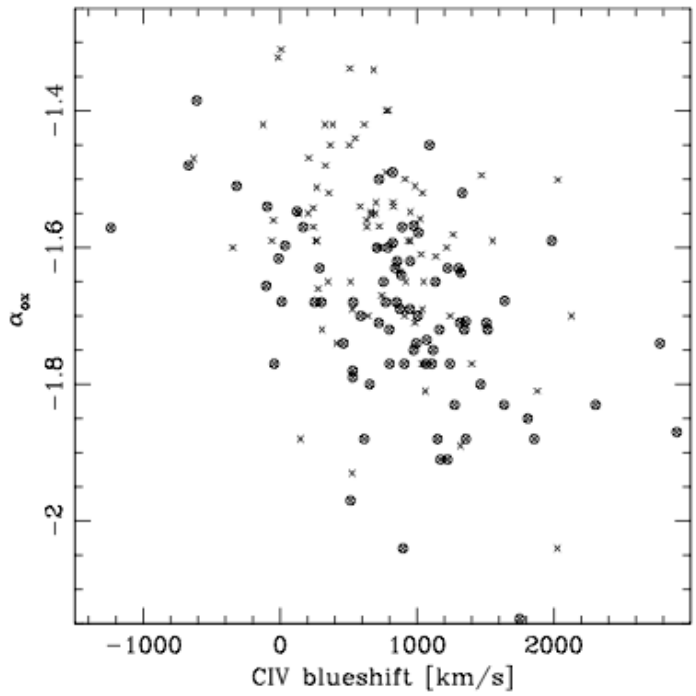

Figure 1.22. αox as a function of the velocity shift of the CIV emission line (Richards *et al.* 2011). Quasars with more negative values of αox are weaker in X-rays and have larger blueshifts.

Broad Absorption lines

In the UV part of the spectrum of QSOs a manifestation of outflows is also observed through the Broad absorption lines (BALs) (Weymann *et al.* 1991; Gibson *et al.* 2009 and reference therein). Absorptions in a spectrum can be caused by (i) an intrinsic material which is accelerated by the AGN, (ii) a material in the host galaxy not related to the AGN, (iii) absorbing material along the line of sight not related to the AGN or host galaxy. But the velocity width of the absorptions observed in BAL QSOs are indicative of their intrinsic nature. Indeed these blueshifted lines with respect to the system reference are indicating of the presence of outflows with velocities up to 50000 km s^{-1}, only achievable if the material is accelerated by an AGN.

BAL QSOs are classified according to the material which produces the BAL troughs. The typical lines observed are resonance transitions of L$\alpha\lambda$1216 Å and moderate/high ionization metals such as CIVλ1549 Å , SiIVλ1393,1404 Å, NVλ1239,1243 Å and OVIλ1032,1038 Å. In these cases the BAL systems are called High-ionization BAL QSOs (HiBALs). Lower ionization lines in absorption are also observed such as Mg IIλ2796,2804 Å and Al IIIλ1855,1863 Å and in this case the BAL QSOs are called Low-ionization BALs (LoBALs), which can also contain HiBAL features in their spectra.

In Fig. 1.23 the SDSS DR12 rest-frame UV spectrum of the BAL quasar

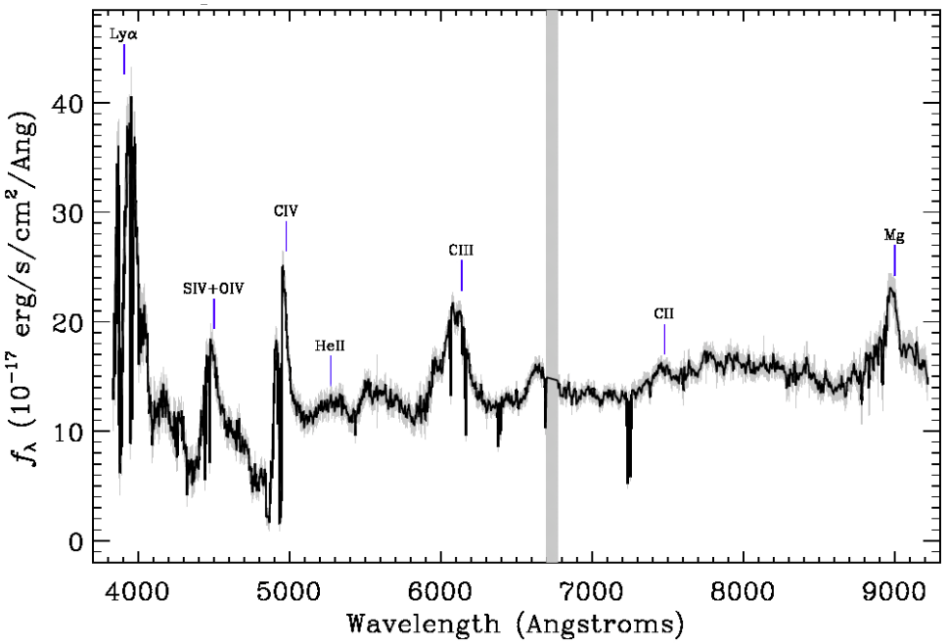

Figure 1.23. SDSS rest-frame UV spectrum of the BAL quasar J1157+2724 from the WISSH sample.

J1157+2724 from the WISSH sample is shown as an example of BAL QSO.

The absorption features are P Cygni like, i.e. characterized by a broad emission peak with a superimposed absorption feature at wavelengths blueward with respect to the line center, due to the approaching gas intercepting radiation coming from the central source. Furthermore for the high ionization species involved and the high velocities reached, a nuclear region system is suggested for the BALs.

To quantify the broad absorption, Weymann *et al.* (1991) proposed the so-called Balnicity index (BI), which accounts only for dip width of 2000 km s^{-1} and blueshifted more than 3000 km s^{-1}. The BI is defined as :

$$BI = -\int_{3000 kms^{-1}}^{25000 kms^{-1}} [1 - \frac{f(v)}{0.9}]C(v)dv \tag{1.38}$$

where f(v) is the normalized flux as a function of the velocity shift of 3000 km s^{-1} up to 25000 km s^{-1} blueward of 1549 Å, C is a constant equal to 1 if the dip exceeds 2000 km s^{-1} or 0 otherwise. A more relaxed BI definition was suggested by Hall *et al.* (2002) in order to include dip width smaller than 1000 km s^{-1} (i.e mini-BALs), the so-called absorption index (AI).

$$AI = -\int_{0 kms^{-1}}^{25000 kms^{-1}} [1 - \frac{f(v)}{0.9}]C(v)dv \tag{1.39}$$

Because of the two different definitions, the fraction of BAL quasars may vary from 15% to 26% (Hewett & Foltz 2003, Gibson *et al.* 2009).

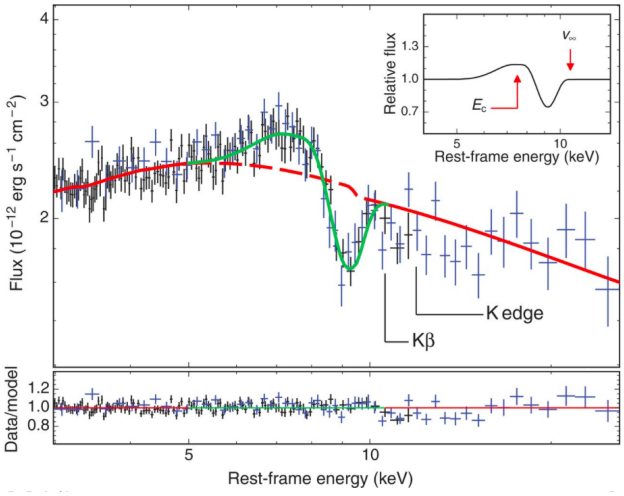

Figure 1.24. X-ray spectrum of PDS 456 with the typical P-Cygni profile in Fe XXVI Kα. The green curve represent the fit obtained using a model of P-Cygni profile due to a spherically symmetric outflow and the red curve indicate the continuum emission (Nardini *et al.* 2015).

UFOs and Warm absorbers

As predicted by theoretical models, we expect to see winds launched by the intense radiation field of accreting AGN near the Eddington rate, moving at hypersonic velocities and emitting in the X-ray band. These winds are observed in the innermost regions of the AGNs through the detection of blueshifted highly ionized Fe K-shell transitions, i.e. Ultra Fast Outflows (UFOs), with velocities ~ 0.1c (King & Pounds 2015; Tombesi *et al.* 2010, 2014; Gofford *et al.* 2013; Feruglio *et al.* 2015).

In Fig. 1.24 the X-ray spectrum of the radio-quiet quasar PDS 456 is shown (Nardini *et al.* 2015). The typical P Cygni feature in Fe XXVI Kα is present as a result of a spherically symmetric outflow, with a bulk velocity of 0.25c, a mass outflow rate $\dot{M}_{out} \sim 10$ M$\odot$/year and a kinetic power $E_{kin} \sim 2 \times 10^{46}$ erg/s, corresponding to 20% of the bolometric luminosity of the quasar, in agreement with theoretical model about an efficient feedback mechanism.

Based on a large number of X-ray observations over the last decade of the luminous QSO PDS 456 at $z = 0.184$, Matzeu *et al.* (2017) report the existence of a correlation between the velocity of the UFO and the X-ray luminosity, i.e. the centroid energy of the blueshifted Fe K absorption profile increases with luminosity $v_{UFO}/c \propto L^{\gamma}_{7-30keV}$ where $\gamma = 0.22 \pm 0.04$ (see Fig. 1.25). This is consistent with a wind that is predominately radiatively driven, possibly resulting from the high Eddington ratio of PDS 456, whereby higher luminosities helping to accelerate the wind to higher terminal velocities.

The soft X-ray spectral region reveals the presence of absorption by warm gas, i.e. warm absorbers, which location is still debated, from the BLR up to 10 pc or even more. These features are seen in about half of the all Type-1 Seyfert galaxies

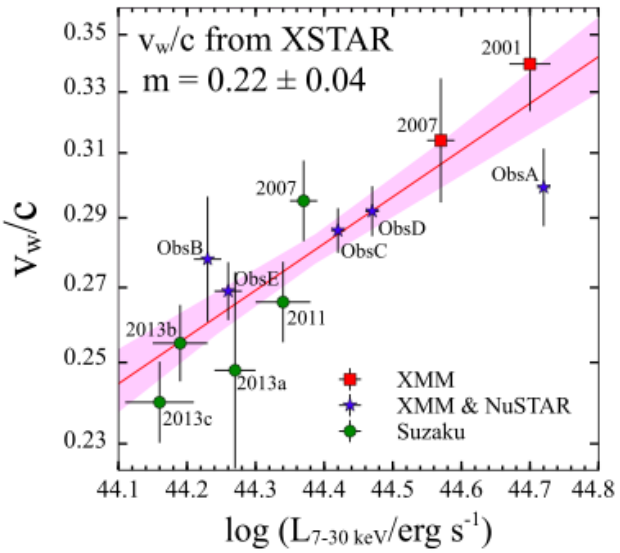

Figure 1.25. The outflow velocity as a function of the intrinsic 7-30 keV continuum luminosity. The red line shows the linear regression fitted to the data with 1σ uncertainty shaded. The slope 0.22±0.04 is consistent with a wind that is predominately radiatively driven, when the source is more luminous the disc-wind is faster (Matzeu *et al.* 2017).

and quasars (Piconcelli *et al.* 2005) and they are always blueshifted, suggesting an outflow from the central source with typical velocities of 10^{2-3} km s^{-1} and column density of $n_H \sim 10^{20-23}$ cm^{-2}. Accordingly, their impact on the ISM of the host galaxies is believed to be negligible.

1.4.b Kpc-scale winds

[OIII] outflows

A typical diagnostic tool used to search for kpc-scale outflows is the broad, asymmetric and high-velocity [OIII]λ5007 emission line profile. Indeed as a forbidden line, [OIII] outflows can only be produced in the NLR due to the low density of the gas, whereas collisional de-excitation takes place in more dense region such as BLR.

The [OIII]λ5007 arises through collisional excitation to the $^1D_2$ level, located 2.51 eV above the ground level, with a critical density for collisional de-excitation of 7×10^5 cm^{-3}. The FWHM of the emission line is of the order of a few km s^{-1}. In presence of outflows, the [OIII] profile is asymmetric blue/redwards with respect to the core component. An example of integrated spectra in the region of the [OIII] emission line is shown in Fig. 1.26 (from Harrison *et al.* 2012). The spectra show a core component (FWHM~ few hundred km s^{-1}) in blue, which likely traces the host galaxy dynamics and broad component (FWHM ~ 900-1500 km s^{-1}) in green, which can be redshifted (upper panel) or blueshifted (lower panel) with respect to

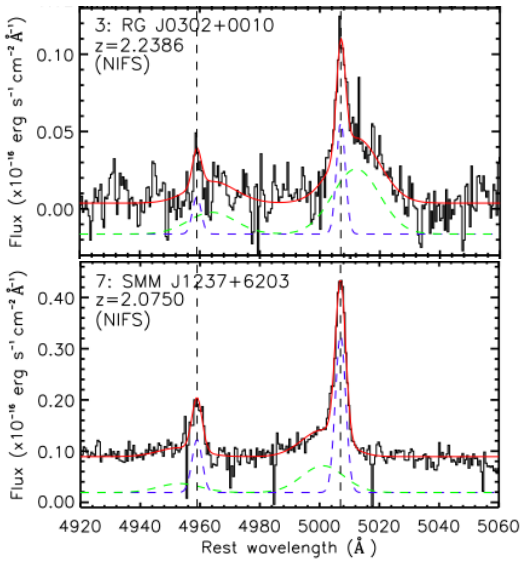

Figure 1.26. Integrated spectra in the region of [OIII] emission line from Harrison *et al.* (2012). (*Top panel*) RG J0302+0010 exhibits a redshifted component with respect to the core component. (*Bottom panel*) SMM J1237+6203 exhibits a blueshifted component with respect to the core component. In both panels the red lines represent the best-fit to the data, blue dashed lines represent the core component and green dashed lines represent the broad component.

the core emission, and it is most likely due to energetic outflows. The velocity shift of the [OIII] emission line is defined as the velocity offset of the broad component with respect to the core [OIII] component.

As illustrated in Fig. 1.27 the velocity offsets and observed spatial extension depends on the orientation with respect to the line of sight: if the outflow is oriented along the line of sight, we expect to see high velocity offset and small spatial extent, instead if the outflow is in the plane of the sky then small velocities offset and large spatial extent are observed; in both cases broad emission lines are always observed. The broad redshifted [OIII] emission lines can be also associated to outflows in the far-side and explained by the orientations of the AGN and obscuring material in the host galaxy (Crenshaw *et al.* 2010).

Thanks to the SDSS large-area survey, Shen & Ho (2014) analyzed a large (~20000) samples of Type I AGN at z < 0.9 with Hβ-[OIII] region covered to study their [OIII] properties. In the upper panel of Fig. 1.28 the FWHM of the broad Hβ emission (from BLR) as a function of the FeII strength (R_{FeII}=EW_{FeII}/$EW_{H\beta}$) is shown. Large values of R_{FeII} are indicative of high Eddington ratio. Each point is color-coded according to the strength of the [OIII]λ5007 (i.e. $EW_{[OIII]}$). The $EW_{[OIII]}$ decreases with increasing of the FeII strength, which is the well known Eigenvector 1 correlation, i.e. lower BH mass or higher Eddington ratio leads to weaker [OIII]. The total SDSS sample was divided in bins in order to study the

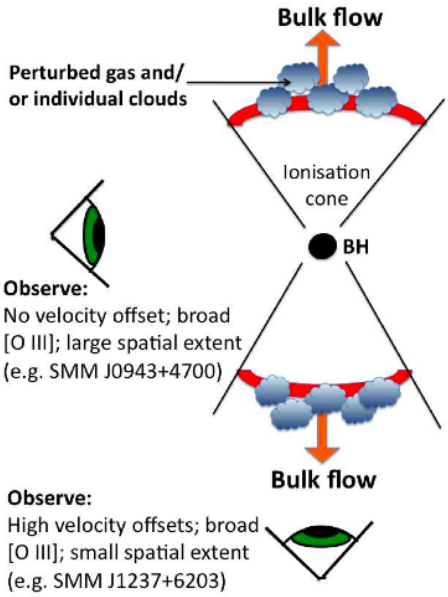

Figure 1.27. Scheme of a possible interpretation of the observations of the broad [OIII] emission lines. If the outflow is oriented along the line of sight, we expect to see high velocity offset and small spatial extent, instead if the outflow is in the plane of the sky then small velocities offset and large spatial extent are observed; in both cases broad emission lines are always observed (Harrison *et al.* 2012).

average [OIII] properties in each bin. In particular they focused on the [OIII] line profiles as a function of the continuum luminosity at 5100 Å , as shown in the bottom panel of Fig. 1.28. The [OIII] strength decreases with luminosity (i.e. the well-know Baldwin effect) and the [OIII] wings, associated with the outflowing gas, becomes more prominent. This suggests that at increasing luminosity the core component is photoionized by the continuum emission from the accretion disk, whereas the blueshifted wings are likely excited by others mechanisms.

With the advent of spatially resolved spectroscopy, step forwards have been made about our knowledge on the extension of ionized outflows. Cano-Díaz *et al.* (2012) studied the luminous quasar 2QZJ002830.4-281706 at z = 2.4 using VLT/SINFONI integral field spectroscopy. They revealed a powerful outflow on several kpc scales, traced by the [OIII]λ5007 line, with a high outflow velocity ($>$ 1000 km s^{-1}) and an outflow rate of 200 M$\odot$/yr. They also revealed the presence of a narrow Hα component which traces star formation in the host galaxy on kpc scales and with a SFR $\sim$ 100 M$\odot$/yr. The star formation is not distributed uniformly, found in the regions not directly invested by the outflow and heavily suppressed in the region where the strongest outflow is detected (see Fig. 1.29), supporting the negative feedback scenario.

Another example of spatially resolved spectroscopy is shown in Fig. 1.30, found by Cresci *et al.* (2015). They presented SINFONI IFU spectra of the obscured,

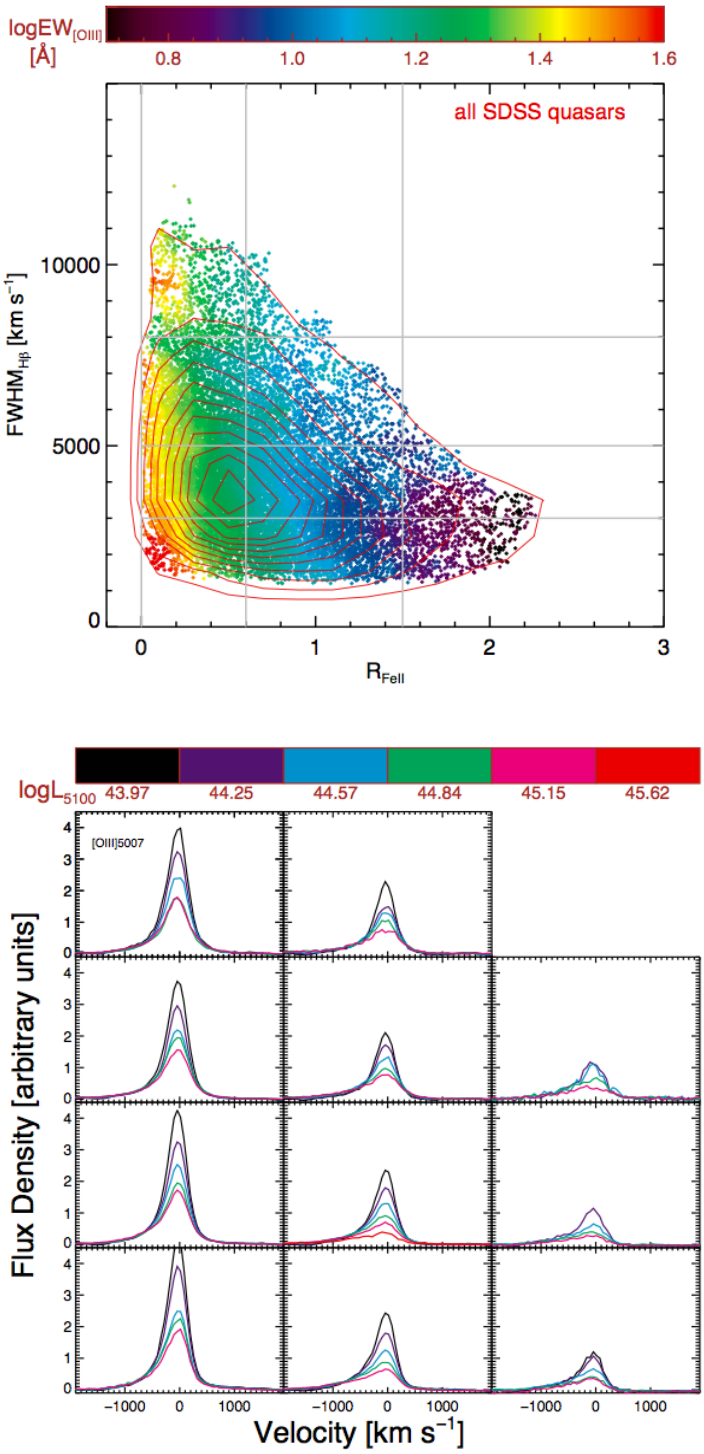

Figure 1.28. (upper panel) FWHM of the Hβ emission line as a function of the FeII strength (= EW$_{FeII}$/EW$_{H\beta}$). Red contours show the distribution of the SDSS quasar sample. The points, which represent the individual sources, are color-coded by the [OIII]λ5007 Å strength. The FWHM of the Hβ and the strength of FeII are divided into bins denoted by gray grids. (lower panel) The average [OIII] profiles in each different bin along the gray grid. In each bin it is shown the [OIII] profile as a function of the quasar luminosity L$_{5100}$ (Shen & Ho 2014).

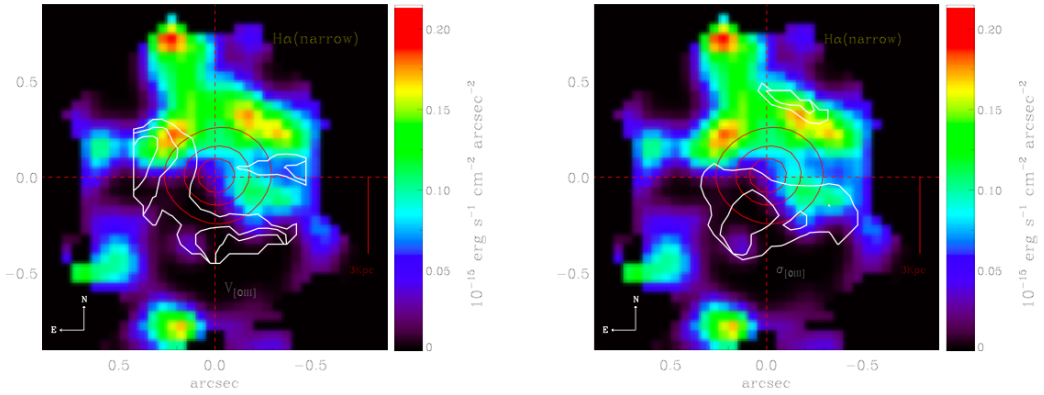

Figure 1.29. Map of the core component of Hα. *(left)* The white contours identify the strongest gas outflow traced by the highly blueshifted [OIII] line. *(right)* The white contours identify the highest velocity dispersion region, which is likely the region where the strong outflow interacts with the host galaxy disk (Cano-Díaz *et al.* 2012).

radio-quiet QSO XID2028 at z=1.59. They found a fast (1500 km s^{-1}) and extended (up to ~13 projected kpc from the QSO position) outflow in the [OIII] emission line, driven by the AGN. In Fig. 1.30 the integrated SINFONI spectrum of XID2028 is shown, where the blue shaded area denotes the blue wing associated to outflowing material and the red shaded area refers to the systemic [OIII] emission. In the bottom panel the continuum subtracted [OIII] images corresponding to the core component (left) and the blue wing (right) are shown.

They also mapped the on-going star formation in the host galaxy using Hα emission. As shown in Fig. 1.31 the outflow position lies in the center of an empty cavity surrounded by star forming regions. In this case the outflow is both removing gas from the host galaxy and triggering star formation, which makes XID2028 the first example of QSO supporting both negative and positive feedback.

Molecular outflows

The first discovery of molecular outflow was in Mrk 231 observed with IRAM Plateau de Bure Interferometer, with the detection of broad wings of CO(1-0) as shown in Fig. 1.32, with v ~ 1000 km s^{-1} (Feruglio *et al.* 2010, Feruglio *et al.* 2015) spatially resolved on the kpc scale and with a mass outflow rate ~ 700 M$\odot$/yr much higher than the ongoing SFR (~200 M$\odot$/yr) observed in the host galaxy. It is possible to use the CO detection in order to constrain the abundance of H_2, which is the most abundance molecular gas. H_2 has no permanent electric dipole moment, but it can be traced via CO (Scoville *et al.* 1991) using a conversion factor $\alpha_{CO} = M_{H_2}/L_{CO}$, where M_{H_2} is the mass of H_2 and L_{CO} is the CO luminosity. This leads to a mass of the outflowing H_2 molecular gas for Mrk 231 of 5.8×10^8 M$\odot$, which is consistent with the lower limit of 7×10^7 M$\odot$ inferred by Fischer *et al.* (2010), analyzing the absorption molecular lines detected by Herschel.

Indeed an unresolved P Cygni profile in the OH molecules at 65, 79 and 119 μm

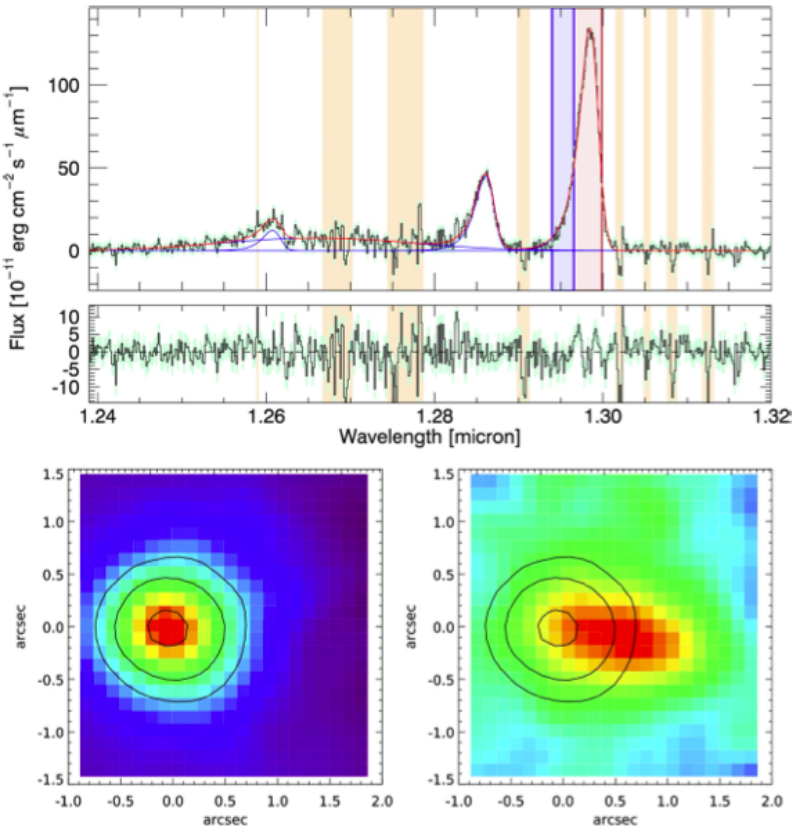

Figure 1.30. Upper panel: J-band SINFONI IFU spectrum of XID2028, integrated in a region of 1"×1" around the QSO. The red and blue shaded areas refer to the spectral channels in which the images shown in the bottom panels are collapsed. Bottom panels: [OIII]λ5007 images corresponding to the narrow [OIII] emission (left) and to the blue wing (right). Black contours refer to the position of the central QSO (Cresci *et al.* 2015).

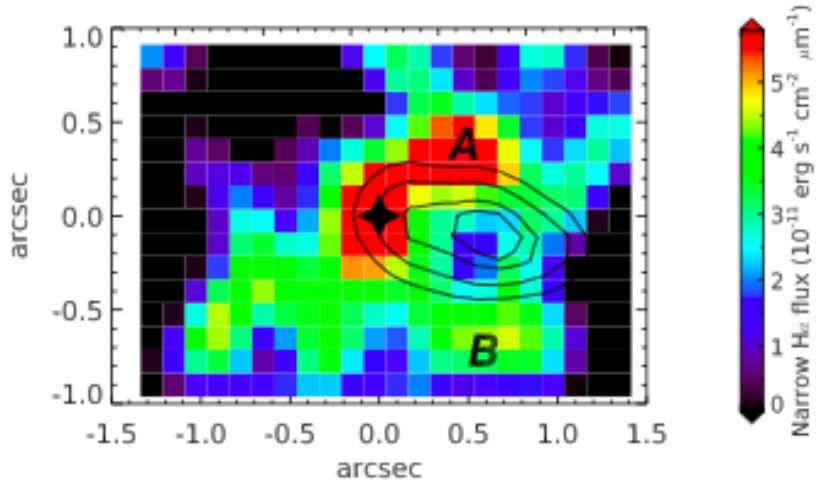

Figure 1.31. Narrow Hα map of XID2028. The contours indicates the [OIII] blue wing tracing the outflow position. A and B mark the position of two clumps of star formation. An anti-correlation between the outflow location and the star formation suggest that the outflowing gas is sweeping the material but also compressing the gas at its edge, triggering star formation in the marked position (Cresci *et al.* 2015).

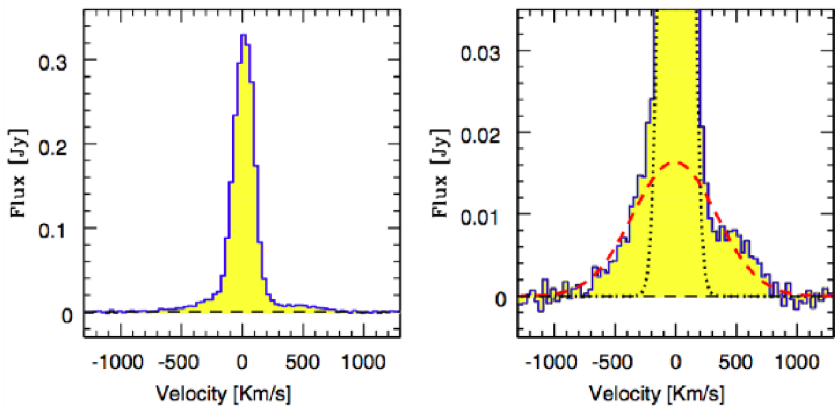

Figure 1.32. Continuum subtracted spectrum of the CO(1-0) transition in Mrk231. In the left panel the total profile is shown. In the right panel the zoom on the broad wing is presented (Feruglio *et al.* 2010).

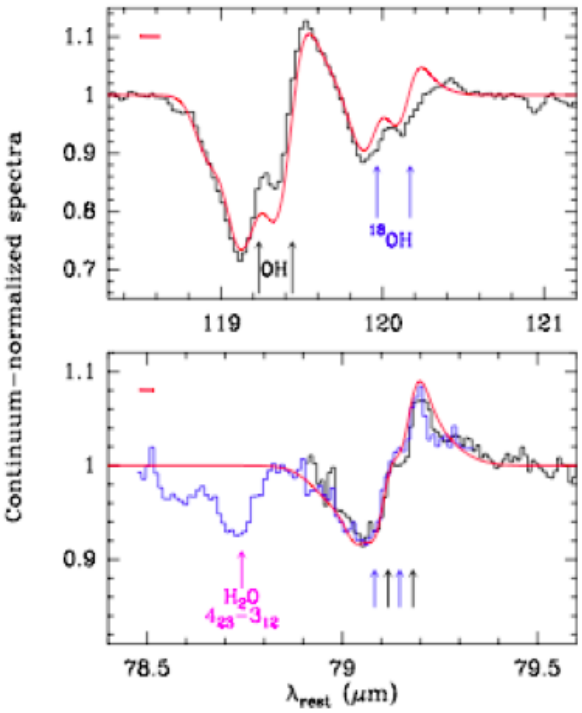

Figure 1.33. P-Cygni profiles of the OH 119 μm and OH μm molecules revealed in Mrk 231 by Hershel/PACS, observed by Fischer *et al.* (2010)

is also revealed in Mrk 231 by Herschel/PACS with a velocity shift of 1000 km s^{-1} (Fischer *et al.* 2010) as shown in Fig. 1.33.

Another important results concerning the properties of massive, galactic-scale molecular outflows has been provided by Cicone *et al.* 2014. They studied the CO(1-0) emission lines from IRAM/PdBI observations of local ultra-luminous infrared galaxies (ULIRGs) and quasar-hosts, discovering a clear signature of massive and energetic molecular outflows, extending on kpc scales, in four out of seven sources, with measured outflow rates of several 100 M$\odot$ yr^{-1}. More specifically, they found that the presence of an AGN can boost the outflow rate by a large factor with respect to the star formation rate (SFR) measured in their host galaxies. Furthermore, the $\dot{M}$ increases with the L_{AGN} / L_{bol} ratio, where L_{AGN} is the AGN luminosity and L_{bol} is the total galaxy bolometric luminosity. The gas depletion time scales due to molecular outflows (i.e. the time required by the outflow to completely remove the whole gas content in the host galaxy) are anti-correlated with the presence and luminosity of an AGN in these galaxies. In AGN hosts, the molecular gas depletion time scales due to the outflow are much shorter than the depletion time scales due to star formation. Cicone *et al.* (2014) derived an outflow kinetic power corresponding to about 5% of the AGN luminosity, as expected by models of AGN feedback (Di Matteo *et al.* 2005), and the outflow momentum rate of $\sim 20\ L_{Bol}/c$, which supports an energy-conserving expansion of these kpc-scale outflows.

1.5 The AGN outflow driving mechanism

As discussed by Proga (2007), considering an ideal gas, we can impose the conservation of momentum and write the equation of motion as follows:

$$\rho\frac{Dv}{Dt} + \rho\nabla\Phi = -\nabla P + \frac{1}{4\pi}(\nabla \times B) \times B + \rho F^{rad} \tag{1.40}$$

where ρ is the gas mass density, v is the velocity, P is the gas pressure, B is the magnetic field, Φ is the gravitational potential and F^{rad} is the radiation force. The right hand of the equation of motion is the sum of three forces:

- The gradient of gas pressure (∇P)
- The Lorentz force $\frac{1}{4\pi}(\nabla \times B) \times B$
- The radiation force ρF^{rad}.

In order to have a wind one of these forces have to dominate over gravitational force. Below i will review the driving mechanisms such as thermal driving, radiation driving and magnetic driving.

Thermal driving. Considering a Keplerian accretion disk in hydrostatic equilibrium, the radiation from the inner hotter disk can heat up the outer part of the disk to high temperature, with important consequences on the dynamics in the disks. The X-ray radiation can heat the gas to high temperature of $\sim 10^7$ K (e.g. the Compton temperature), as a consequence a hot corona forms or a thermal wind is produced depending on whether the thermal velocity exceeds the escape velocity (Proga & Kallman 2002). The thermal driving is expected to be more efficient at large radii where the escape velocity is small. The velocities reached by a thermal wind are very low velocities ($v_{max} = v_{sound} \sim 100$ km s^{-1}) and can explain the low velocity X-ray absorption features in AGN spectra (e.g. Chelouche & Netzer 2005). This mechanism is less important for temperature $< 10^7$ K, whereas the radiation and magnetic driven can be more important. In particular radiation-driven can dominate at temperature $<10^5$K.

Radiation driving. For a fully ionized gas, the radiation pressure is due to electron scattering and a near-Eddington source is expected in this case to have a dynamically important radiation driving. Therefore, the outflow is driven by a radiation pressure on electrons, such as those observed in UFOs (Pounds *et al.* 2016). However an outflow can also be driven even if the system is below the Eddington limit provided the gas opacity is higher than the electron scattering. An enhancement of the gas opacity is obtained via bound-free (photo-electric) and bound-bound (line-driving) transitions. The bound-free transitions are likely the mechanism by which the X-ray warm absorbers are accelerated near the BH.

For the case of line driving mechanism, its efficiency depends on the presence of bound electrons, i.e. it is most efficient when the gas is moderately ionized so that many UV transitions can occur (Castor *et al.* 1975). For a gas ionized by UV

radiation in the optically thin case the ratio between the line opacity and the electron scattering can be high of ∼ 2000-4000 (i.e. the so-called Force multiplier, Castor *et al.* 1975). When the gas is highly ionized, the ratio between the line opacity and the electron scattering drops to zero. Therefore the line driving requires a shielding mechanism in order to prevent overionization of the gas and see AGN outflows in UV absorption lines or UV disk winds (Murray *et al.* 1995; Proga & Kallman 2004).

In the radiation driven scenario for an outflow, it is expected a luminosity dependence of the outflow velocity (Laor & Brandt 2002 and reference therein). If that gas is moving with a Keplerian velocity ($v_{kep} \propto \sqrt{\frac{M_{BH}}{R}}$, where M_{BH} is the mass of the BH) at a certain radius R and then is launched driven by radiation, then the terminal velocity is defined as follows:

$$v_{ter} \simeq v_{kep} \sqrt{\frac{\Gamma L}{L_{Edd}}} \tag{1.41}$$

where Γ is the force multiplier which depends on the line opacity and it is assumed to be constant. From the definition of the Keplerian velocity we can rewritten the Eq. 1.41 as follows:

$$v_{ter} \propto \sqrt{\frac{\Gamma L}{R}} \tag{1.42}$$

with its maximum value at $R = R_{min}$ where R_{min} is the minimum launching radius. Considering the dust as the main opacity source of the gas, the R_{min} is the minimum radius where dust grains survive, which is just outside the BLR radius (see Sect. 1.2.b) (Laor & Draine 1993). In this case $R_{min} \propto L^{1/2}$.

If the bound-bound transitions (line-driven) are the source of opacity then $R_{min} = R_{BLR} \propto L^{1/2}$ as discussed in Sect. 1.2.b. The similar dependence of the outflow radius on luminosity for both dust and line driving mechanism indicates that it expected a similar outflow. If the force multiplier Γ is independent of L, which means that the gas ionization level, the dust/gas ratio and the grain size distribution are the same in all objects, then turns out that the maximum velocity of the outflow is given by:

$$v_{max} \propto L^{1/4} \tag{1.43}$$

i.e. the higher the AGN luminosity, the higher the outflow velocities (Arav *et al.* 1994; Scoville & Norman 1995).

Magnetic driving. Magnetic effects are important in AGNs, since they may be responsible for the angular momentum transport in disks (magneto-rotational instability). Two types of magnetic-driven winds can exists: magneto-centrifugal, with the magnetic tension as the major contribution to the Lorentz force and magnetic-pressure winds, with the magnetic pressure as the major contribution to the Lorentz force. Strong ordered and large-scale magnetic fields are required in order to produce such magneto-centrifugal winds. Magnetic winds can be effective in low luminosity

AGN and in those where the radiation overionized the gas, since they do not require radiation pressure. A difference of the magneto-centrifugal winds with respect to radiation driven winds is that they co-rotate with the disk, whereas radiation driven winds do not.

Magneto-centrifugal winds can reach high terminal velocity, close to the speed of light due to strong centrifugal force. Indeed they has been suggested as the mechanism responsible for the relativistic jets (Blandford & Payne 1982).

1.6 AGN Galaxy co-evolution and the role of AGN Feedback

Several theoretical and observational motivations lead to the idea that the BHs and their host galaxy are linked to each other, despite the difference of orders of magnitude in size between them. In this section i will present two observational results that imply a connection between BH and the host galaxy: (i) the cosmic evolution of BH growth and star formation, (ii) galaxy luminosity function and the colour of galaxies.

1.6.a The cosmic evolution of BH growth and star formation

The luminosity function (ϕ(L)) describes the space density of objects with different intrinsic luminosities. The number of sources per unit of volume with luminosity in the range L and L+dL can be written as dN=ϕ(L)dL . Defining the lower limit of the flux detection as S, the number of objects in a solid angle Ω can be written as follows:

$$N(>S) = \int \frac{\Omega}{3} r^3 \phi(L)\, dL \tag{1.44}$$

Taking into account the lower detection S, this implies that sources with luminosity L can be observed out to a certain distance r = $(L/4\pi S)^{0.5}$.

This leads to:

$$N(>S) = \frac{\Omega}{3(4\pi)^{3/2}} S^{-3/2} \int L^{3/2} \phi(L)\, dL \tag{1.45}$$

The change with time of the luminosity function and number density of AGN is fundamental to understand the nature of the BHs and their evolution with the galaxies. In 1970s Schmidt (1978) discovered that the AGN luminosity function evolves with time. This function can be therefore described by considering an evolution term:

$$\phi_L(L,z) = \frac{\phi(L)}{(L/L*)^a + (L/L*)^b} \tag{1.46}$$

where L* is the break luminosity, a and b are the slopes at low and high L, respectively. Two major problems affect the determination of this function: the bolometric

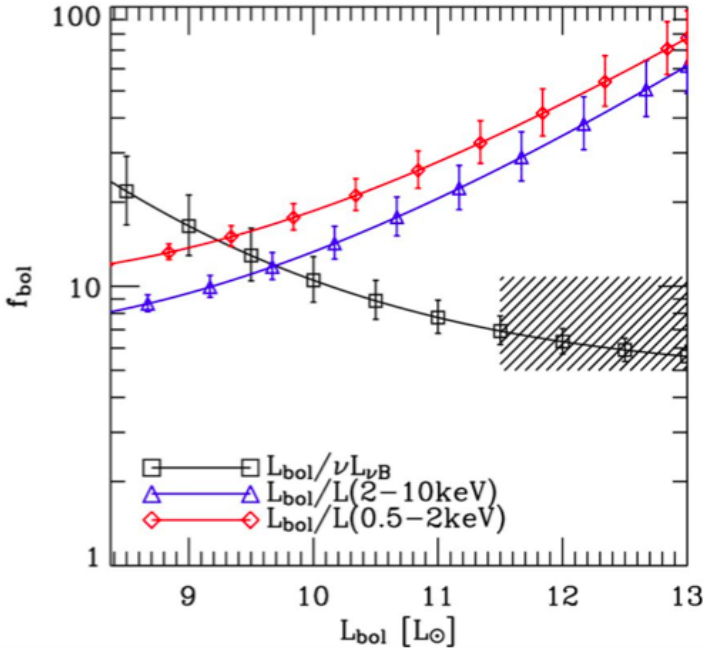

Figure 1.34. Bolometric corrections as a function of bolometric luminosity in the X-ray and optical band (hatched area) (Marconi *et al.* 2004)

correction applied to the AGN luminosity function observed in a specific band and the incompleteness due to obscuration.

Marconi *et al.* (2004) provided a bolometric correction based on the total intrinsic luminosity, defined as the luminosity directly produced by the accretion process. The luminosity of an AGN is the result of the luminosity arises by the accretion disc in the Optical-UV range and that from the hot corona in the X-ray band. As mentioned in Sect. 1.2.a, the IR radiation is the UV radiation reprocessed by dust, which emits in the IR band. Thus in order to retrieve the correct value of AGN luminosity, the IR contribution must be subtracted. In Fig. 1.34 the bolometric correction as a function of bolometric luminosity is shown, in the X-ray and optical band (Marconi *et al.* 2004).

Since most of the AGNs are obscured, because of the nucleus hidden by an absorbing material which may resides in the torus, the efficient way in localizing and identifying AGNs is to use X-ray observations. X-rays can penetrate the obscuring dust, leading to X-ray surveys to be less biased with respect to the Optical ones. Indeed the hard x-ray surveys provide the most complete census of AGN activity (Merloni & Heinz 2013), as it is shown in Fig. 1.35.

Taking into account the previous considerations for the luminosity function, the cosmic mass accretion history of massive BHs can be inferred using the Soltan argument (Soltan 1982) according to which from the integrated AGN bolometric luminosity function it is possible to obtain the density of mass accreted on BHs as a

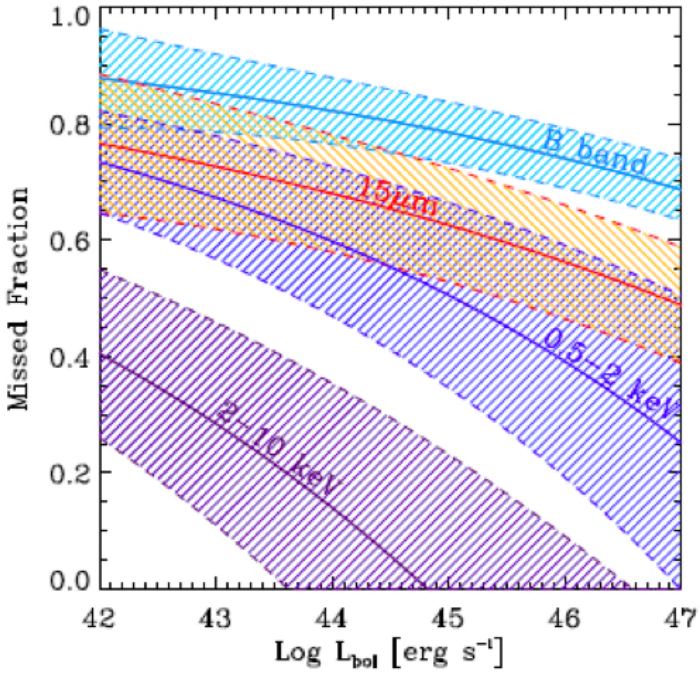

Figure 1.35. The fraction of AGN that are missed in a survey with a specific band as a function of bolometric luminosity. Red, cyan, blue and purple shaded areas correspond to the rest-frame mid-IR (15μm, UV (B-band), soft X-rays(0.5-2 keV) and hard X-rays (2-10 keV) (Merloni & Heinz 2013).

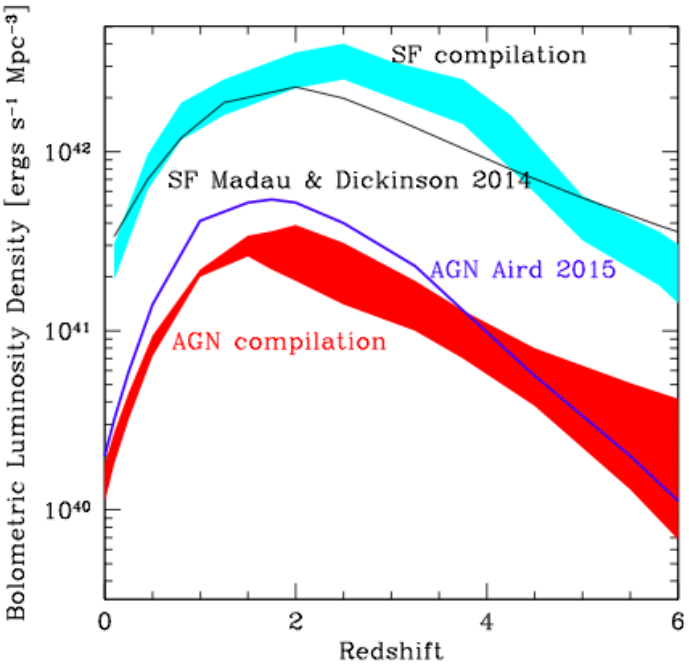

Figure 1.36. Bolometric luminosity density as a function of redshift computed from a compilation of X-ray luminosity function integrated in the range $\log L_X$ = 42-45 and assuming the Marconi *et al.* (2004) bolometric correction (red band) and compared with the similar determination of Aird *et al.* (2015) (blue line) and with the evolution of the UV luminosity density from Santini *et al.* (2009), Gruppioni *et al.* (2015), Bouwens *et al.* (2011, 2015)(cyan band). The comparison with the SF luminosity density as estimated by Madau & Dickinson (2014) is also shown (black curve) (Fiore *et al.* 2017).

function of redshift:

$$\rho_{BH}(z) = \frac{1-\eta}{\eta c^2} \int L\phi(L,z)dL \tag{1.47}$$

where η is the mass-energy conversion efficiency. The bolometric luminosity can be derived by X-ray, IR or Optical emissions using an appropriate bolometric correction.

In Fig. 1.36 the bolometric luminosity density is shown as a function of redshift computed from a compilation of X-ray luminosity function integrated in the range $\log L_X$ = 42-45 and assuming the Marconi *et al.* (2004) bolometric correction (red band) and compared with the similar determination of Aird *et al.* (2015) (blue line) and with the SF luminosity density from Santini *et al.* (2009), Gruppioni *et al.* (2015), Bouwens *et al.* (2011, 2015) (cyan band) and that estimated by Madau & Dickinson (2014) (black solid line). The AGN bolometric and SF luminosity density reveal a roughly similar shapes, with a peak at z = 1.5 - 2.5 and a drop to the present epoch, suggesting a co-evolution of BHs and their host-galaxies (Boyle & Terlevich 1998; Silverman *et al.* 2008).

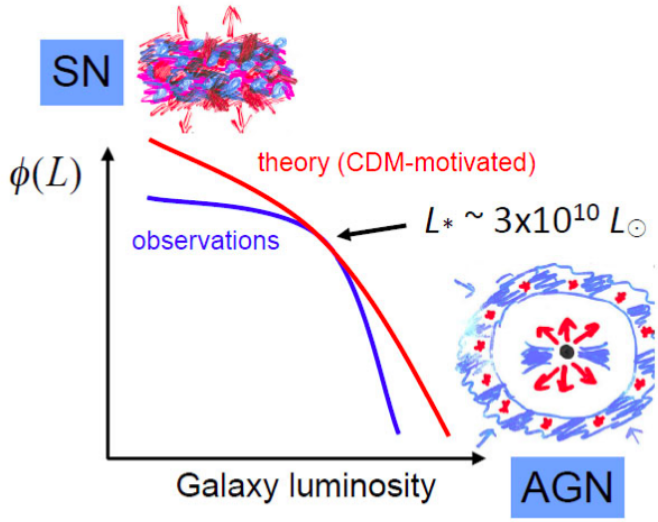

Figure 1.37. Role of feedback in modifying the galaxy luminosity function

1.6.b Galaxy luminosity function and the colour of galaxies

The luminosity function of the galaxies is usually fit by a Schechter function Schechter 1976. The shape of the luminosity function and scaled ΛCDM halo mass function are different, in particular the assumption that the stellar mass follows the halo mass leads to unseen many small galaxies and many big extremely bright galaxies, as shown in Fig. 1.37.

In order to reproduce the faint-end of the luminosity function winds from Supernovae and photoionization of pre-galactic gas are invoked. In the first case the cold gas is ejected from the galactic disk and the efficiency of star formation is reduced (Larson 1974). Observational evidences of supernova driven wind in dwarf galaxies (Ott *et al.* 2005) are in agreement with the model predictions (Croton *et al.* 2006).

For the bright-end of the luminosity function, the failed of a supernova superwind in reproducing the slope have required a different mechanism (Benson *et al.* 2003): the energy released by the accretion of matter onto the BH at the centre of the galaxy. Many semi-analytical models (SAMs) show how the central engine can be the responsible of the suppression of the cooling flow in massive galaxies. As an example, the SAM of Croton *et al.* (2006) takes into account the presence or not of AGN feedback. The AGN injects sufficient energy into the surrounding medium that can reduce or stop the cooling flow in more massive halos and allow to reproduce the high luminosity cut-off in the galaxy luminosity functions in the K and b_J bands as shown in Fig. 1.38.

The AGN feedback has also a significant effect on bright galaxy colours. The feedback model of Croton *et al.* (2006) shows how the colour distribution changes with or without the feedback. In particular the AGN feedback modifies the luminosities, colours and morphologies of high-mass galaxies. If no feedback acts, there are more massive, much bluer elliptical galaxies than to what is observed. Instead

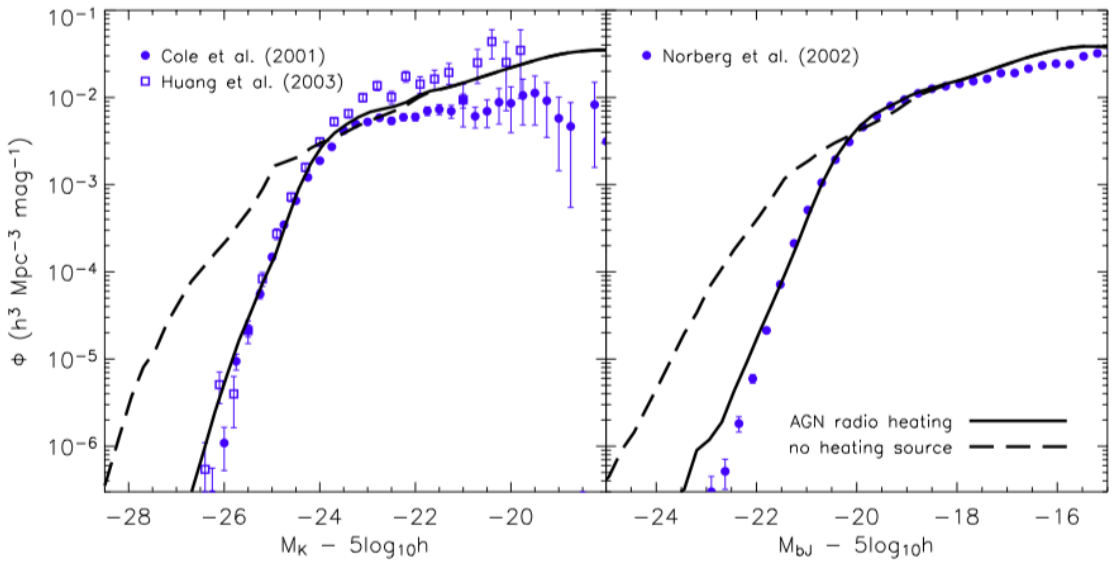

Figure 1.38. Galaxy luminosity function in the K (*left*) and b_J (*right*) photometric bands. The solid line represents the galaxy luminosity function with radio mode feedback; the long dashed line represents the galaxy luminosity function without feedback (Croton *et al.* 2006).

AGN heating cuts off the gas supply allowing the massive galaxies to redden. The B-V colours of model galaxies against stellar masses with and without radio mode feedback is shown in Fig. 1.39.

1.6.c The role of AGN feedback

As already stressed in the previous sections, it is now widely accepted that a SMBH is capable of controlling the growth of its host galaxy on scales much larger than its gravitational sphere of influence. The energy released by accretion in building a SMBH indeed considerably exceeds the bulge binding energy. The binding energy can be expressed as follows:

$$E_{gal} = M_{gal}\sigma^2 \tag{1.48}$$

where M_{gal} is the galaxy mass and σ is the velocity dispersion of the galaxy. The energy released by the growth of the BH is:

$$E_{BH} = \eta M_{BH} c^2 \tag{1.49}$$

where η is the radiative efficiency for the accretion process and, as found in Sect. 1.1 it is $\sim 10\%$.

The mass of the BH is observed to be $\sim 10^{-3}$ times the mass of the bulge (Kormendy & Gebhardt 2001; Merritt & Ferrarese 2001; Häring & Rix 2004) and that most galaxies have velocity dispersion of ~400 km s^{-1}. According to Eq. (1.48)

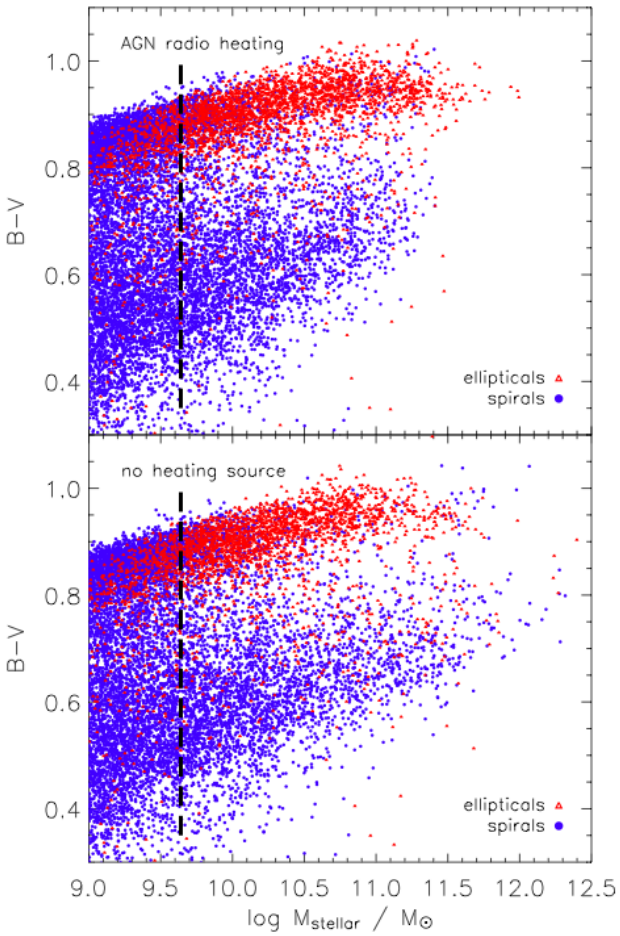

Figure 1.39. The B-V colours of model galaxies vs stellar masses with (*top*) and without (*bottom*) radio mode feedback. Red triangles and blues circles correspond to early and late morphological type respectively. The thick dashed lines mark the resolution limit to which morphology can be determined in the Millennium Run and it corresponds to the stellar mass of 4 x 10^9 $M_\odot$ (Croton *et al.* 2006).

and (1.49), the ratio E_{BH}/E_{gal} is greater than 80, implying that, despite the difference of orders of magnitude in size between a BH and a host galaxy, they are connected to each other.

Furthermore the mass of the BH is correlated with the mass of the bulge, which suggests that galaxies hosting classical spheroids grew in concert with their BHs. A connection between the growth of the BH (via accretion process) and the galaxy spheroid (via star formation) is expected since both processes are driven by a common fuel, i.e. the availability of cold gas.

The hierarchical galaxy evolution scenario support the idea that this fuel is the result of galaxy mergers which are a responsible to trigger both SF and AGN activity (Kauffmann & Haehnelt 2000; Di Matteo *et al.* 2005).

In this scenario the type-2 AGNs are likely an earlier phase triggered by gas-rich mergers, which moves from dust-enshrouded AGNs to type-1 AGNs, through powerful winds which clear out the environment (Sanders *et al.* 1988, Hopkins *et al.* 2006, Glikman *et al.* 2015). In particular, as presented by Hopkins *et al.* (2008) using a simulation of a galaxy evolution through a gas-rich major mergers, the galaxy evolution can be described as follows: (i) Gas-rich mergers are expected to produce massive inflows of gas to the galaxy center, triggering intense nuclear starbursts. The high gas densities feed a rapid growth of the BH which is obscured at optical wavelengths by dust and gas.

(ii) The obscured AGN activity ends when the nuclear gas is consumed by the starburst and the residual gas is dispersed by strong winds originated by SN explosions and by the black holes energy released into the ISM. This blow-out phase is associated with highly dust-reddened and/or IR-luminous quasars which represent ~20-40% of the quasar population (Hopkins *et al.* 2004). As the dust is removed, an unobscured phase of quasar occurs and the BH becomes. Finally, as no more fuel is available, star formation and quasar activity decline, and the galaxy is quiescent, evolving passively and satisfies observed correlations between black hole and its spheroid. This scenario is presented in Fig. 1.40.

1.6.d Quasar and Kinetic feedback

The energy released by the AGN accretion can be distinguished in two different modes, as shown in Fig. 1.41:

1. kinetic/maintenance/radio mode, which is usually associated with low Eddington ratios.

2. radiative/quasar mode, which is associated with high accreting BHs ($\lambda_{\rm Edd}\geq 0.01$)

Kinetic feedback. The kinetic mode or radio mode occurs when the BH is coupled with the hot gas via radiatively inefficient accretion, and the accretion energy is channeled into relativistic outflows, i.e. jets with narrow opening angle. Radio mode-dominated AGN are found in massive galaxies ($M_{stellar} \geq 10^{11}$ M$\odot$)

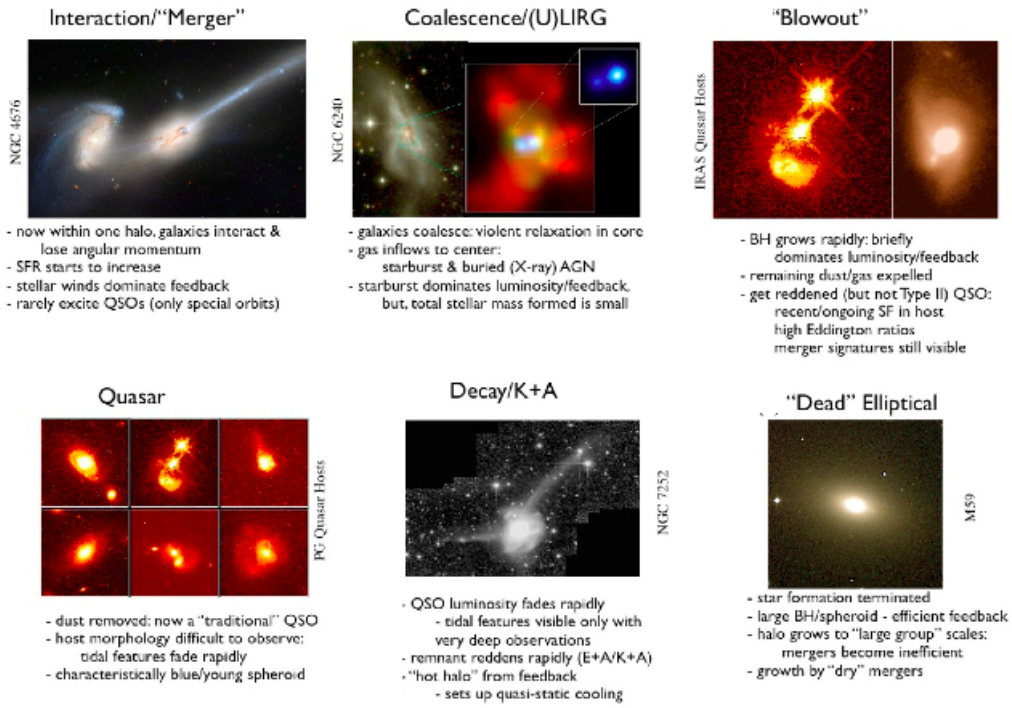

Figure 1.40. A scheme of the galaxy formation mechanism, which goes through a gas-rich major merger, adapted from Hopkins *et al.* (2008)

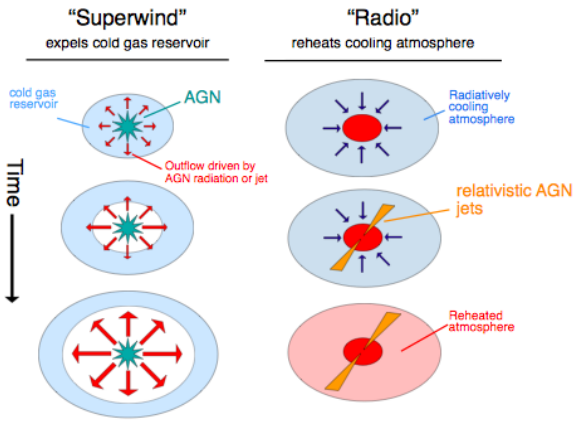

Figure 1.41. The two main modes of AGN outflows are illustrated: superwind-mode (i.e. quasar mode) outflows and radio-mode outflows.

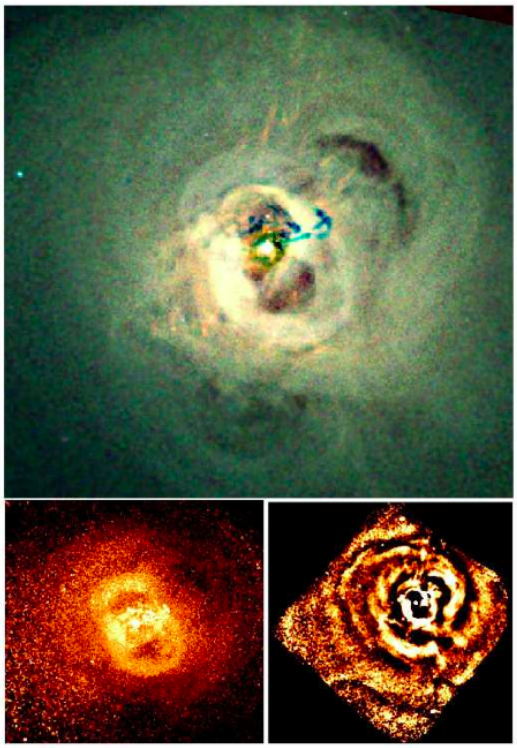

Figure 1.42. *(Top panel)* Chandra X-ray image of the Perseus cluster. Red-green-blue indicates soft to hard X-rays. The dark blue filaments in the center are likely due to a galaxy that is falling into NGC 1275, the giant galaxy that lies at the center of the cluster. *(Lower Left)* Pressure map derived from Chandra imaging X-ray spectroscopy of the Perseus cluster. Note the thick high pressure regions containing almost 4PV of energy surrounding each inner bubble, where V is the volume of the radio-plasma filled interior. *(Lower Right)*: unsharp-masked image showing the pressure ripples or sound waves (Fabian *et al.* 2006).

with old stellar populations in the local universe. The jets extend outward in a bipolar flow, inflating lobes of radio-emitting plasma. These lobes transfer energy to the surrounding X-ray emitting gas, leading to the formation of bubbles or X-ray cavities. The best-studied case for the radio mode is the Perseus cluster (Fig. 1.42), where spherical bubbles surrounded by a thick high-pressure region fronted by weak shock are present. These bubbles can transfer energy to the cluster gas, $\sim$ 4PV where P is the pressure and V is the volume of the lobe, which is the internal energy of a cavity dominated by relativistic plasma. This heating is often in balance with the radiative cooling of the hot gas (Rafferty *et al.* 2008), indeed no evidence of cooling flow is observed in massive galaxies in the center of clusters (Fabian 1994).

Radiative feedback. The radiative feedback consists on the coupling of the energy released by the growth of the BH and the surrounding material through the winds. These winds gives rise to wide-angle and sub-relativistic outflows in multiple gas phases, which are driven by the AGN radiation. This flavour of feedback is prevalent in high-accreted objects and has a typical timescale of $\sim 10^7$ years.

These outflows can evacuate the cold gas and suppress the star formation, as suggested by measurements of kinetic energy and mass outflow rates. However it is not clear the long-term impact of the winds on the host galaxies, where the efficiency of converting the available gas into stars may be reduced by AGN outflows, with no need of removing the gas (Harrison 2017).

Chapter 2

Systematic study of AGN winds in Quasars Surveys: the WISSH quasars Project

In this Chapter, i present the selection criteria and the general properties of the WISE-SDSS selected hyper-luminous (WISSH) quasars sample. Specifically i discuss about the discovery of powerful ionized winds in WISSH QSOs.

2.1 The WISSH survey

2.1.a Sample selection

As already mentioned, the energy released by the growth of the BH can be larger than the binding energy of the galaxy bulge, hence the AGN can have an important effect on the evolution of its host galaxy. Moreover powerful AGN-driven outflows are invoked as a viable mechanism for kinetic energy injection into the ISM, which can affect the evolution of their host galaxies. This scenario is expected to be more significant in the redshift interval $1< z <3$, i.e. the golden epoch of AGN and galaxy evolution, when the SMBHs of the most powerful QSOs have accreted most of their mass. Furthermore, from theory and observations we know that the efficiency in driving energetic winds increases with AGN luminosity (Menci *et al.* 2008; Faucher-Giguère & Quataert 2012; Cicone *et al.* 2014, Matzeu *et al.* 2017), which brings out that the most luminous QSOs are potentially the best targets to hunt for powerful AGN-driven outflows, especially at high redshift.

Weedman *et al.* (2012) presented the 100 most luminous quasars in $\nu L_\nu(7.8\ \mu m)$ (i.e.$\nu L_\nu(7.8\ \mu m) \geq 10^{47}$ erg s^{-1}) selected by cross-correlating the sample of SDSS DR7 Type-1 AGNs in the redshift range $1.5 < z < 5$ with the Wide-field Infrared Survey Explorer all-sky survey detections at 22μm, assuming a detection if $f_\nu(22\ \mu m) > 2$ mJy. The sample selection has been made from the mid-IR, because this band is less biased against dusty quasars than optical surveys, since the optical emission is

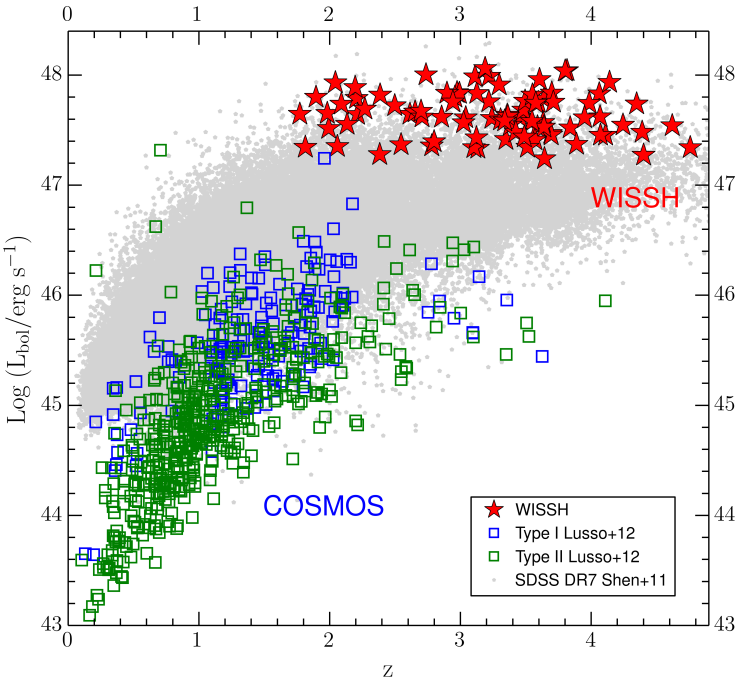

Figure 2.1. Bolometric luminosity as a function of redshift for the WISSH QSOs (red stars). The WISSH objects are compared with the Type I and Type II COSMOS AGNs from Lusso *et al.* (2012) sample (blue and green squares) and SDSS DR7 AGNs from Shen *et al.* (2011) sample (grey points)

absorbed in obscured quasars by dust and in fact re-emitted at IR wavelengths.

The objects analyzed in this Thesis work belong to the WISSH quasars sample, which has been obtained from the Weedman et al. sample after removing the lensed objects and those with a contaminated WISE photometry. The final sample consists of 86 hyper-luminous quasars at z ∼ 1.8 - 4.6.

In Fig. 2.1 the bolometric luminosity as a function of redshift is shown for the WISSH QSOs (red stars). The bolometric luminosity has been obtained from broad-band multi-component SED fitting for each WISSH object (Duras *et al.* 2017; Duras et al. in prep) and the redshift estimates are those from SDSS survey (Shen *et al.* 2011). The WISSH QSOs are compared with typical quasars such as the Type I and Type II COSMOS AGNs (blue and green squares, respectively) from Lusso *et al.* (2012) sample and with SDSS DR7 AGNs from Shen *et al.* (2011) sample (grey points). Fig. 2.1 clearly points out that the WISSH quasars are among the luminous AGNs in the Universe.

The WISSH survey was designed to determine the nuclear, host galaxy and AGN feedback properties in QSOs located at the brightest end of the AGN luminosity function. We are collecting data on the Hβ emission line of these sources in order to provide the best single-epoch estimate of the SMBH mass and accretion rate in units of the Eddington ratio, and hence characterize the nuclear properties. Indeed

as discussed in Sect. 1.2.b, it is worth noting that the CIV-based estimates of the BH mass deriving from the SDSS spectra are biased due to the presence of outflows which affect the CIV line profile.

There is on-going large multi-band observing program for the WISSH QSOs, based on ALMA, NOEMA, SINFONI, LBT, X-shooter, TNG, XMM-Newton and Chandra proprietary data. The project also benefits of public data as Herschel and 2MASS, in addition to WISE photometry and SDSS photometry and spectroscopy available for all the sources in the sample.

With the NIR coverage we were able to carefully infer accretion properties. Moreover thanks to the multi-wavelength coverage of the WISSH survey we are able to analyze the UV-mid-IR SED for each source and derive the bolometric luminosity of the AGNs. This enable us to investigate whether the AGN physical parameters such as BH mass, Eddington ratio and bolometric luminosity are correlated with the properties of outflows in different gas phases. Thanks to the huge luminosity of the WISSH QSOs, they are the ideal candidate for the AGN feedback and hence it is possible to probe the role of these outflows in the evolution of their host galaxies. Furthermore the AGN/galaxy co-evolution is linked to the SFR and consumption of the gas, therefore it is also crucial to study the star formation activity of the quasar host galaxies. Herschel/SPIRE data are available for $\sim 20\%$ of the WISSH QSOs which enabled us to study the host properties as the SFR, IR luminosities and dust masses. On-going follow-up with ALMA and NOEMA will also provide crucial information on the cold gas content and molecular outflows in these hyper-luminous QSOs.

2.1.b General properties

As previously mentioned, thanks to the multi-wavelength coverage of the WISSH survey we were able to analyze the UV-mid-IR SED for each source in the sample (Duras et al. in preparation) and, therefore, derive the extinction, the UV and mid-IR monochromatic luminosities (at 2500 Å and 6μm, respectively) and the bolometric luminosity of the AGNs. Furthermore, the availability of Herschel/SPIRE photometry in the Far-IR range for $\sim 20\%$ of the sample, enabled us to perform a broad-band SED fitting with a multi-component model, based on the combination of quasar and host galaxy emission in the IR, where the reprocessed stellar light is re-emitted by the dust, as described in Duras *et al.* (2017).

The quasar emission is the combination of power laws to describe the central source (Feltre *et al.* 2012) and the model by Stalevski *et al.* (2016) to characterize the reprocessed emission by a smooth and clumpy dusty torus. The galaxy cold dust emission in the IR was modeled with a modified black body, which accounts for the emission powered by star formation, absorbed by the dust grains and re-emitted in the MIR and FIR.

For some sources an additional component was added to reproduce the NIR emission, because of the peculiar feature not well reproduced by the standard modelization.

A small collection of broad-band SEDs of WISSH objects is shown in Fig. 2.2.

Through the SED multi-components method we derived robust measurements of Bolometric and monochromatic luminosities, dust mass and star formation rates (SFRs). In particular, integrating the best-fit modified blackbody in the range 8-1000 μm we derived the IR luminosity of the host galaxy and from the relation by Kennicutt (1998), i.e,

$$SFR(M_{\odot}/yr) = 10^{-10} L^{Host}_{IR\ 8-1000\mu m}(L_{\odot}) \quad (2.1)$$

we computed the SFR, assuming that all the FIR emission comes from young stars but keeping in mind that could be a contribution of the quasar to the FIR emission.

We found giant star nurseries in the WISSH quasars observed with Herschel, with SFRs up to 4500 $M_{\odot}$/yr. In Fig. 2.3 it is shown the SF luminosity as a function of bolometric luminosity for the WISSH quasars (blue stars), which populate the extreme region. We also plotted the SF luminosity corrected for the quasar contribution to the FIR (red asterisks). These findings are in agreement with those found for high-z sample in the same luminosity range presented by Netzer *et al.* (2014, 2016) (magenta pentagons and cyan triangles) and Fan *et al.* (2016) (orange squares). We also compared the WISSH samples with local sample of IR-selected galaxies from Gruppioni *et al.* (2016) (brown circles) and the quasar sample from the COSMOS survey (Bongiorno *et al.* 2012) (contours), in order to collect samples in a wide range of luminosity and redshift. We found a smaller dispersion at high luminosities than that found at the low luminosities.

We should keep in mind that the SF derived by FIR luminosity is the result of the integration of bursts of star formation that occurred over billions of years, thus we can not directly linked the SF luminosity with the on-going star formation in the host galaxy.

As presented in Martocchia *et al.* (2017), we have also investigated the nuclear properties of WISSH sources detected in the X-ray ($\sim$ 50 %, X-WISSH hereafter). They exhibit $L_{2-10\ keV} \approx 10^{45-46}$ erg s^{-1}, which extends the typical X-ray luminosity range of AGN investigated in previous X-ray spectroscopic studies. Furthermore, the MIR selection enables us to extend and complete the study of the nuclear properties of hyper-luminous quasars, which have been mainly based on X-ray and/or optically selected AGN samples so far. We found that the X-WISSH QSOs show a low level of X-ray absorption along the line of sight to the nucleus (see Fig. 2.4). The 70% of the X-WISSH shows an intrinsic obscuration $N_H \leq 5 \times 10^{22}$ cm^{-2}, as expected being classified as Type-1 QSOs.

In Martocchia *et al.* (2017) we also investigated the X-ray-to-Optical flux ratio (X/O) values for the X-WISSH QSOs, which is commonly used to provide a basic classification for X-ray sources without optical identification. The X-WISSH quasars show very low X/O values (< 0.1) compared to the typical AGN values of $0.1 <$ X/O < 10 measured for COSMOS, CDFS and PG samples, as shown in Fig. 2.5.

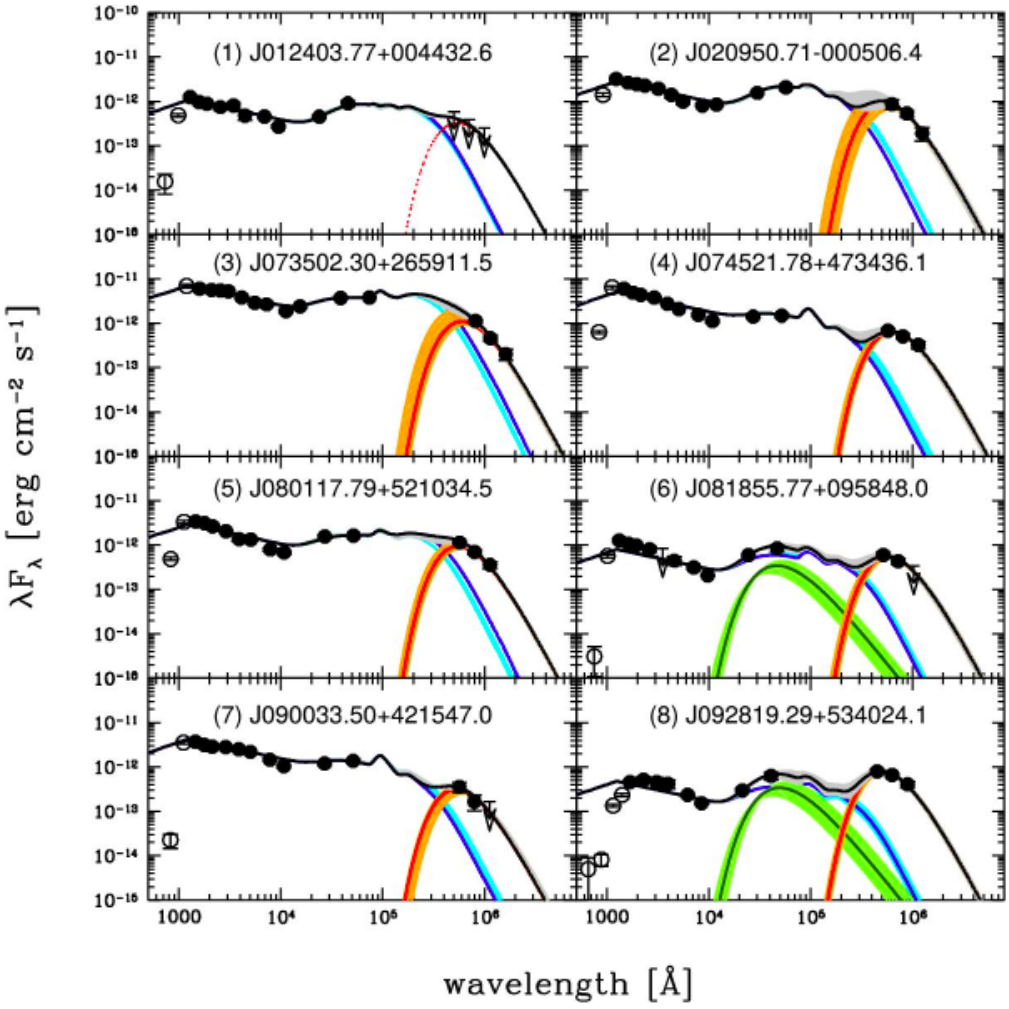

Figure 2.2. Resulting rest-frame SED decompositions for eight WISSH sources. Black circles are the rest-frame photometric points corresponding to the observed bands used to constrain the SED. Black open circles represent the photometric points not included in the fits (at $\lambda < 1216$ Å due to Ly-α absorption) while the black arrows correspond to upper limits on the observed flux densities at 1σ. Lines (and shaded areas) correspond to the model templates (and the 1σ error) found as best-fit solution to describe the photometric points through the χ^2 minimisation: blue is the accretion disc plus torus template, red is the cold dust component while dark green is the NIR excess when present. Finally, the black line shows the sum of all these contributions. Blue, orange, and light green shaded areas correspond to the accretion disc plus torus, the cold dust, and the NIR excess templates respectively, within 1σ of the best-fit template, and light grey shaded area to their sum (Duras *et al.* 2017).

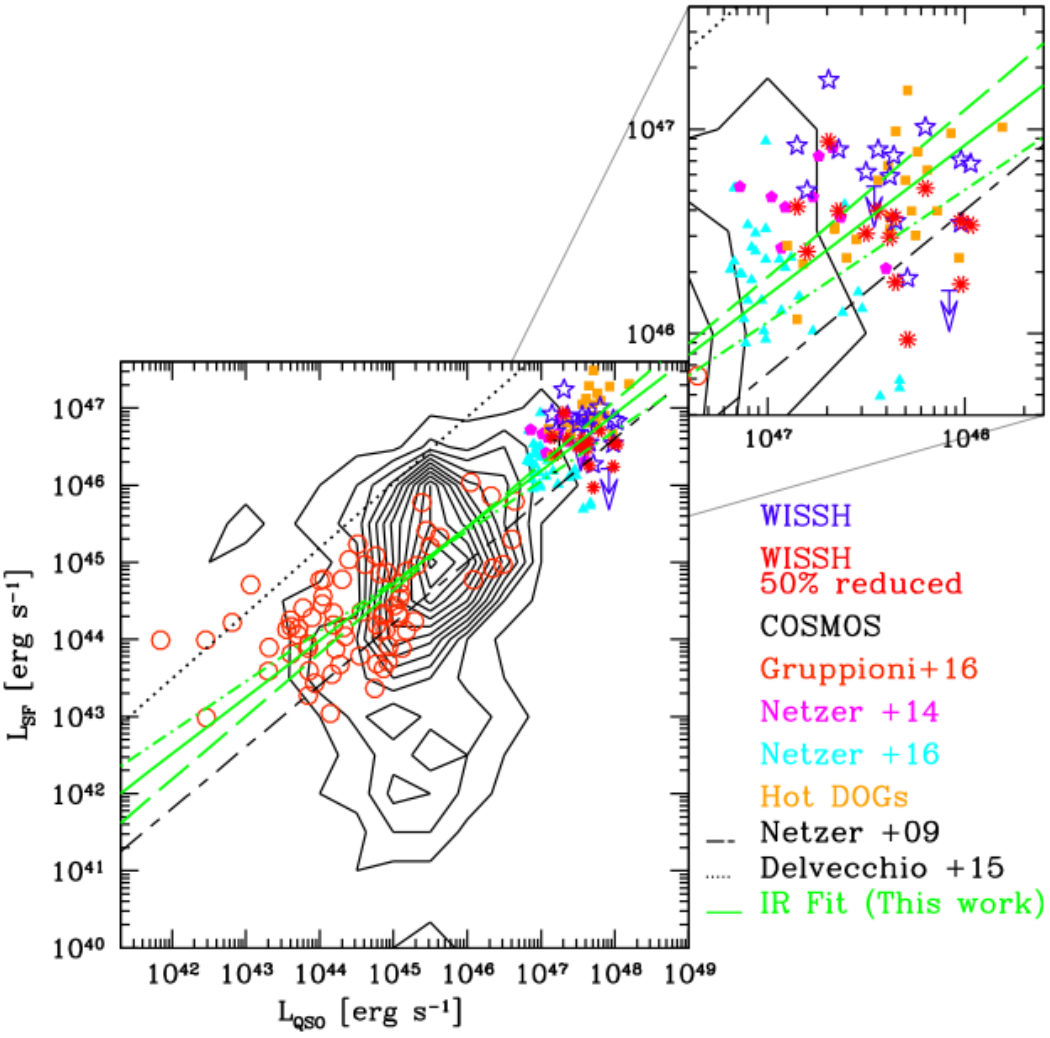

Figure 2.3. SF luminosity as a function of quasar bolometric luminosity for the WISSH quasars in comparison with other samples. The 16 WISSH quasars are shown as blue stars in the plot, while the red asterisks show SF luminosity values reduced by a factor of about 2 to account for the quasar contribution to the FIR. The same correction has been applied to the samples from Netzer *et al.* (2014, 2016) and Fan *et al.* (2016), which are of the same luminosity range (Duras *et al.* 2017).

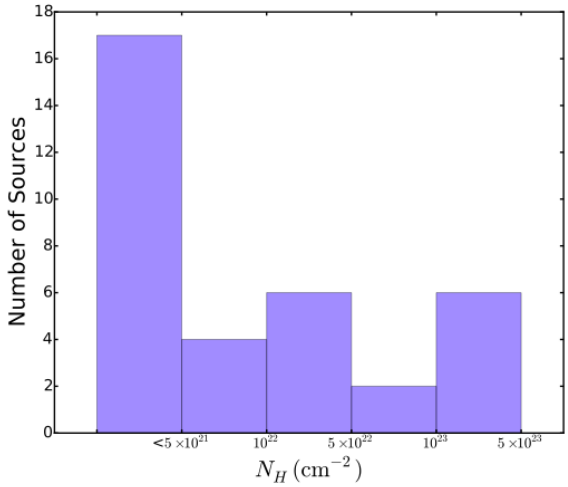

Figure 2.4. The distribution of absorption column densities for 35 X-ray detected WISSH quasars derived by the hardness ratio[1] or spectral analysis (Martocchia *et al.* 2017).

Thanks to the high-luminosities of the WISSH quasars, it was possible to investigate the bolometric correction in the X-ray (i.e. $k_{Bol,X} = L_{Bol}/L_{2-10\ keV}$ which quantifies the relative importance of the accretion disk and the corona to the total radiative output from an AGN) up to $L_{2-10\ keV} \geq 10^{45}$ erg s^{-1} and $L_{Bol} > 10^{47}$ erg s^{-1}, as shown in Fig. 2.6. The X-WISSH QSOs are compared with the Type-1 AGNs from XMM-Newton-COSMOS survey (Lusso *et al.* 2012) and PG quasars. The X-WISSH lie in the $k_{Bol,X}$ - L_{Bol} relation found by Lusso *et al.* (2012), which provides a good description for hyper-luminous quasars as the WISSH. The positive correlation observed between $k_{Bol,X}$ and L_{Bol} lends support to the scenario of a weaker corona radiative power with respect to the optical/UV disk emission at increasing L_{Bol}.

We also found that the X-WISSH quasars follow the well-known anti-correlation between αox - $L_{2500\ \text{Å}}$ (Vignali *et al.* 2003, Lusso *et al.* 2010). The αox provides an indication of the relative strength of the emission produced in the accretion disk at 2500 Å and that emitted via Compton up-scattering in the hot corona at 2 keV. We compared the X-WISSH sample with other Type 1 AGN at lower bolometric luminosities, such as those from the XMM-COSMOS survey (Lusso *et al.* 2010, blue open triangles) and PG quasars (yellow squares). The X-WISSH quasars populate the lower right corner of the plane, i.e the brightest end of the distribution with the steepest αox, as shown in Fig. 2.7, which implies that at high luminosities the X-ray emission is relatively weaker than the optical/UV contribution.

This finding suggests that the formation of radiation line driven winds from the accretion disk are favored in AGNs with strong UV luminosity and low-X ray level such as the WISSH quasars, where a soft ionizing continuum prevents the

[1]The hardness-ratio HR is defined as HR = $\frac{H-S}{H+S}$, where H is the number of counts in the hard band and S is the number of counts in the soft band

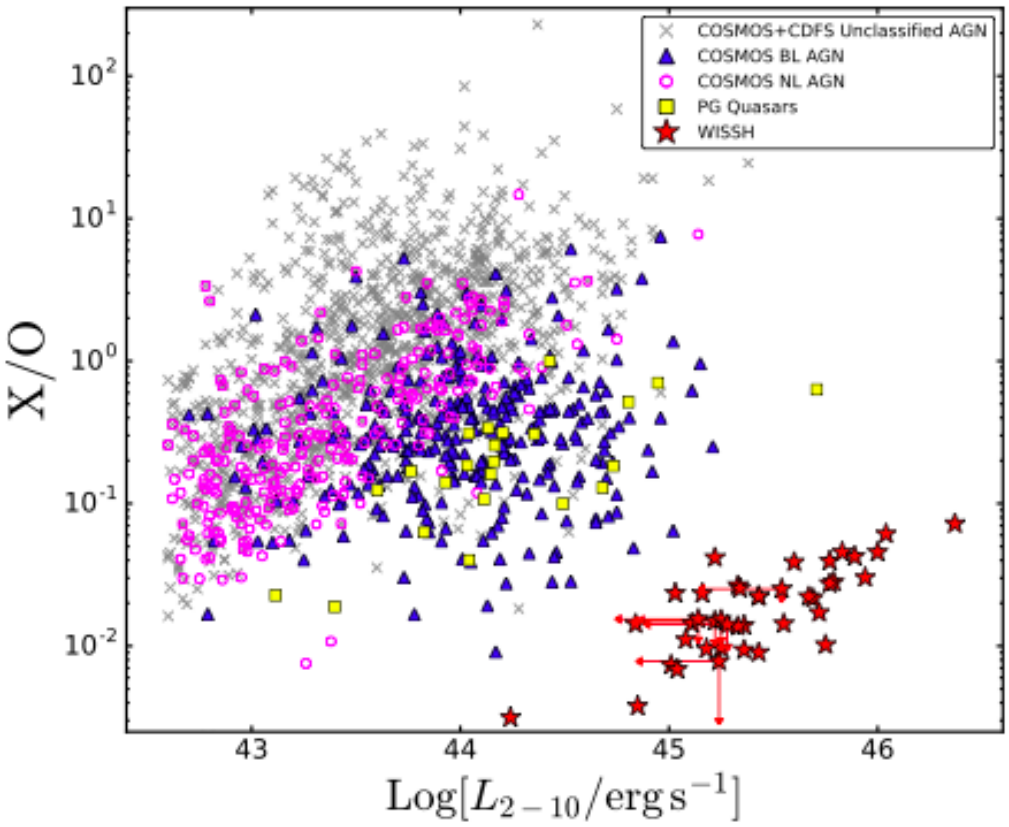

Figure 2.5. The X/O ratio as a function of the hard X-ray luminosity $L_{2-10\ keV}$. The X-WISSH quasars (red stars) are compared to Chandra COSMOS, CDFS and PG Quasars. Blue triangles indicate the X-ray selected broad line COSMOS AGN, while open circles indicate X-ray selected narrow-line COSMOS AGN. Unclassified X-ray selected AGN of both COSMOS and CDFS are represented with grey crosses. PG quasars are indicated with yellow squares (Martocchia *et al.* 2017).

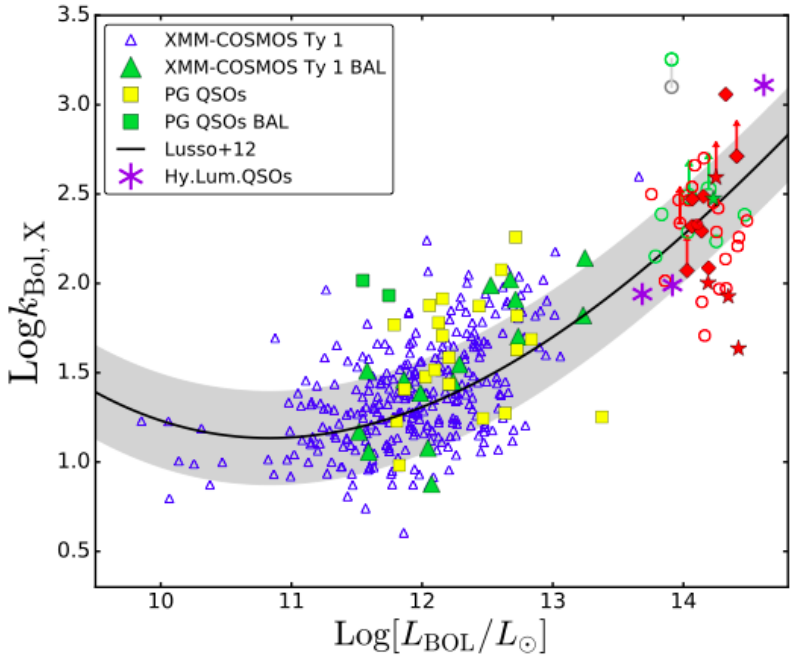

Figure 2.6. Bolometric correction $k_{Bol,X}$ as a function of the bolometric luminosity L_{Bol}. The X-WISSH QSOs are plotted as: BAL WISSH quasars are represented with green symbols while non-BAL WISSH are represented with red symbols. Filled symbols indicate objects which have LBT/LUCI optical spectrum. Star and diamond symbols indicate the presence of broad [OIII] emission lines and CIV shifts > 2000 km s^{-1} , respectively. Blue triangles indicate the Type-1 AGN sample from the XMM-Newton-COSMOS survey by Lusso *et al.* (2012). The yellow squares indicate PG quasars while green symbols represent BAL AGNs. Violet asterisks indicate the hyper luminous quasars ULASJ 1539+0557, ULASJ 2315+0143 and 2QZ0028-2830. The black solid curve represents the relation found by Lusso *et al.* (2012) for type 1 AGN, while the gray shaded area indicates the σ dispersion on the relation. The two values for the hard X-ray luminosity of J0045+1438 (i.e. the object with the lowest X-ray luminosity in the X-WISSH sample) are also reported and connected by a gray line. We calculated the $L_{2-10\ keV}$ by using the best fit value of N_H (i.e. 4×10^{22} cm^{-2}, green open circle) and the upper error (i.e. N_H =1.5×10^{23} cm^{-2}, gray open circle), respectively (Martocchia *et al.* 2017).

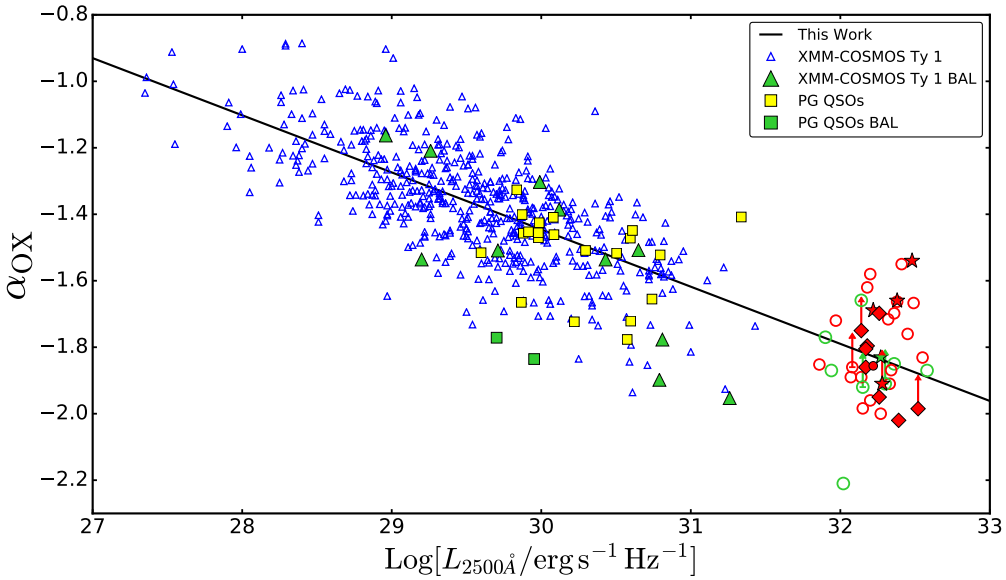

Figure 2.7. αox values as a function of extinction-corrected 2500 Å monochromatic luminosities. BAL WISSH quasars are plotted with green symbols while non-BAL WISSH are represented with red symbols. Blue triangles indicate the Broad-line AGN sample from the XMM-Newton-COSMOS survey by Lusso *et al.* (2010), while the yellow squares indicate PG quasars. Green symbols represent BAL AGN (Martocchia *et al.* 2017).

over-ionization of the gas in the wind (Leighly 2004, Proga 2003 and references therein). Further details about the relation of αox and the high-ionization lines winds will be discussed in Sect. 5.4.

2.2 Discovery of powerful ionized winds in WISSH QSOs: early results.

The first results of the WISSH quasars survey are presented in Bischetti *et al.* (2017), which is focused on the analysis of the LBT/LUCI1 optical rest-frame spectra of five WISSH quasars in the redshift z $\sim$ 2.5 - 3.5 showing prominent, broad [OIII] emission lines, observed during the Cycles 2014-2015 of the observing campaign at LBT.

In Fig. 2.8 an example of the Optical rest-frame LUCI1 spectrum of the WISSH QSOs J1326-0005 is shown. From the best-fitting decomposition of all the five WISSH spectra, we found the presence of very broad ($\mathrm{FWHM}_{[OIII]}$ up to 2200 km/s) [OIII] components (blue curve in Fig. 2.8), among the largest observed so far, which are blueshifted with respect to the systemic redshift (in all but one case, i.e. J1549 for which we found a broad redshifted [OIII] component), indicative of the presence

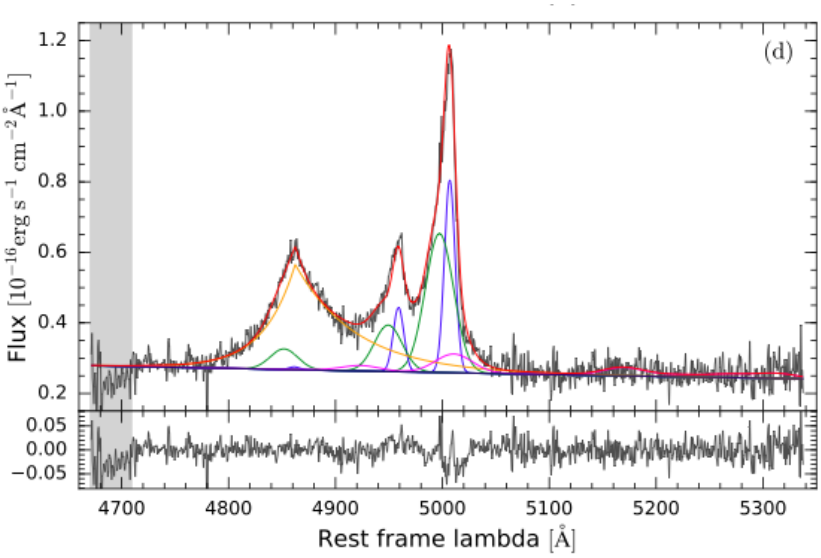

Figure 2.8. Example of LUCI1 spectrum of the WISSH quasar J1326-0005. Blue and green curves refer to the NLR core and broad emission of both [OIII] and Hβ, respectively. BLR Hβ emission line is indicated in orange and FeII emission is indicated in magenta. Gray bands indicate the regions excluded from the fit because of the presence of telluric features. (See Bischetti *et al.* 2017 for further details.)

of outflowing gas in the NLR.

We compared the results found for the WISSH quasars about the [OIII] properties of the broad emission line with previous studies, such as from the Type 1 and Type 2 objects both at low and high redshift, in Fig. 2.9. The WISSH quasars are in the top right corner of the plane exhibiting the highest [OIII] luminosities observed so far.

This clearly indicates that the WISSH selection gave the opportunity to extend the discovery of ionized outflows up to sources with [OIII] luminosity up to $\sim 10^{45}$ erg s^{-1}. Moreover it seems that a correlation between the FWHM$_{[OIII]}$ and [OIII] luminosity exists, with a lack of luminous AGNs with narrow [OIII] line profile.

We have been also able to retrieve spatial information from the LBT/LUCI spectra. As reported in Bischetti *et al.* (2017) we extracted 1D spectra at increasing offset distances from the central position from the 2D spectrum. With this technique the contamination from the nuclear emission is reduced and possible spatially extended [OIII] emission should be enhanced (Perna *et al.* 2015). We found that three out of five WISSH QSOs show possibly extended [OIII] emission.

In one case, namely J1201+1206, we found a blueshifted and redshifted components, extended up to $\sim$ 7 kpc and likely associated with a bipolar outflow. The velocity shift of the blue- and redshifted component with respect to the systemic redshift, at increasing distances from the central position, is shown in Fig. 2.10. The velocity shift between the two components ($\sim$ 1500 km s^{-1}) is too large to be associated with rotation ($\sim$ a factor of $\geq$ 4 larger than the typical value observed for a z$\sim$ 2-3 galaxy (Bouché *et al.* 2007)).

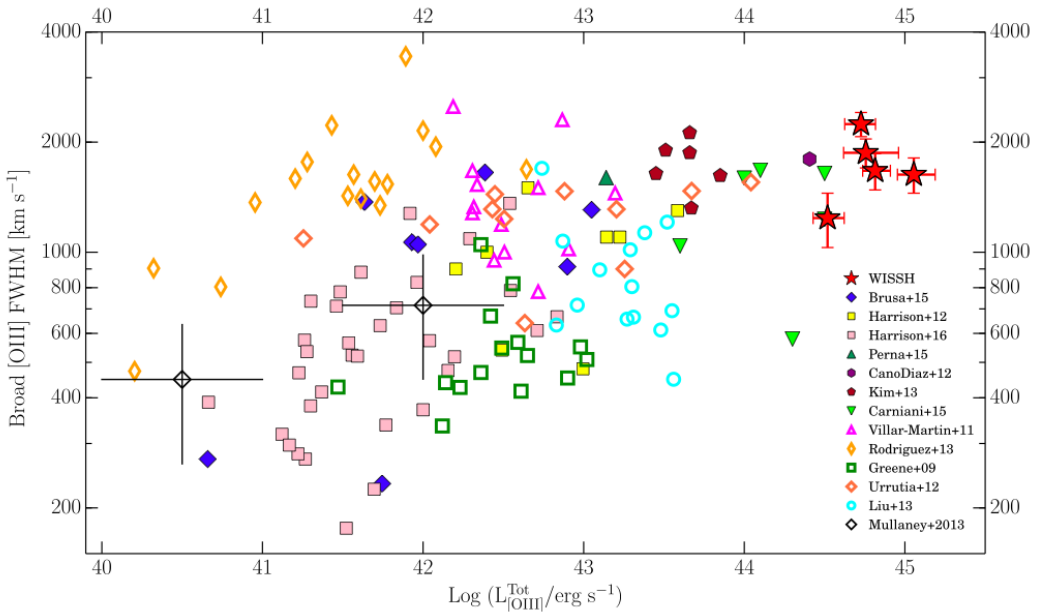

Figure 2.9. FWHM$^{[OIII]}_{broad}$ as a function of the total observed [OIII]λ5007 Å luminosity for the WISSH quasars (red stars) compared with other samples of Type 1 and Type 2 AGN both in low (empty symbols) and high redshift (filled symbols). We plot the values obtained for a sample of obscured (Greene *et al.* 2009; Brusa *et al.* 2015; Perna *et al.* 2015), red (Urrutia *et al.* 2012), Type 2 (Villar-Martín *et al.* 2011; Liu *et al.* 2013), luminous z ∼ 2.4 (Cano-Díaz *et al.* 2012; Carniani *et al.* 2015), KASHz at z ∼ 1.1-1.7 (Harrison *et al.* 2016), and radio quasars (Kim *et al.* 2013), and those obtained for the local and high-z ULIRGs by Rodríguez Zaurín *et al.* (2013) and Harrison *et al.* (2012), respectively. The average values in two L$^{Tot}_{[OIII]}$ bins for optically selected Type 2 AGN in Mullaney *et al.* 2013 are also shown (Bischetti *et al.* 2017).

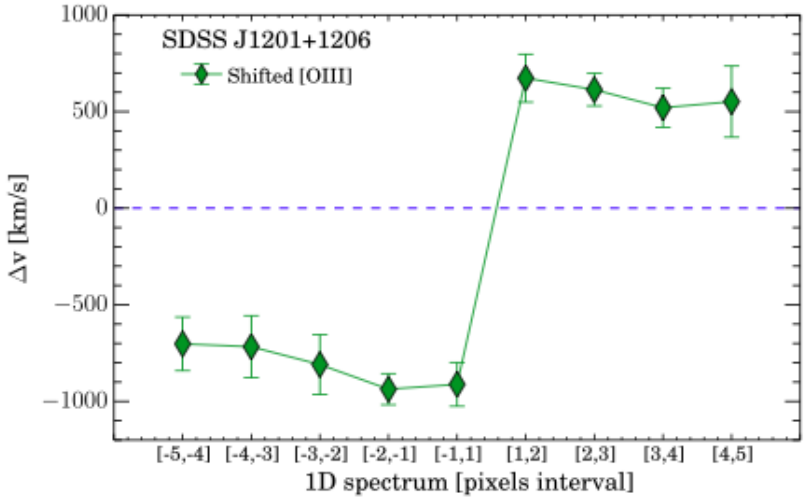

Figure 2.10. Velocity shift of the blue- and redshifted [OIII] component with respect to systemic redshift (at 5007 Å) (dashed line), detected in the off-nuclear Petra of J1201+1206 extracted from different apertures. Negative (positive) pixel values correspond to south (north) direction (1 pixel ∼ 1.9 kpc at the redshift of J1201+1206) (Bischetti *et al.* 2017).

By energetic consideration, the [OIII] outflows found in the WISSH QSOs exhibit huge values of mass outflow rate $\dot{M}$ (up to 7700 M$\odot$ yr^{-1}) and kinetic power $\dot{E}_{kin} \sim 10^{45-46}$ erg s^{-1}, indicating that WISSH quasars allow us to reveal extreme outflows. In Fig. 2.11 it is shown the mass outflow rate and the kinetic power as a function of bolometric luminosity, for the WISSH QSOs and other samples with ionized outflows from literature. Both $\dot{M}$ and $\dot{E}_{kin}$ seem to exhibit a correlation with the luminosity, in particular at increasing L_{Bol} the mass outflow rate increases, which is consistent with a theoretical scenario according to which the more luminous the AGN, the more the amount invested by a radiatively driven wind (Menci *et al.* 2008). Moreover it seems that the ionised outflows, revealed at the highest luminosities, may trace a larger fraction of the total outflowing gas than outflows in low luminosity AGN. Indeed at high luminosities the mass rate of the ionized and molecular outflow become comparable, as suggested considering the steeper best-fit relation of ionized outflow $\dot{M} \propto L_{bol}^{1.21}$ than to the best-fit relation of the molecular outflows $\dot{M}_{mol} \propto L_{bol}^{0.78}$. Most of $\dot{E}_{kin}$ values derived for these five WISSH quasars are broadly consistent with a fraction of ∼1% of bolometric luminosity, up to a value of ∼3%. These values are therefore very close to the predictions (i.e. $\dot{E}_{kin}/L_{Bol}$ ∼5%, see Sect. 1.3) of the vast majority of AGN feedback models (e.g. Di Matteo *et al.* 2005; Zubovas & King 2012) for an efficient feedback mechanism to be able to account for the M_{BH} - σ relation.

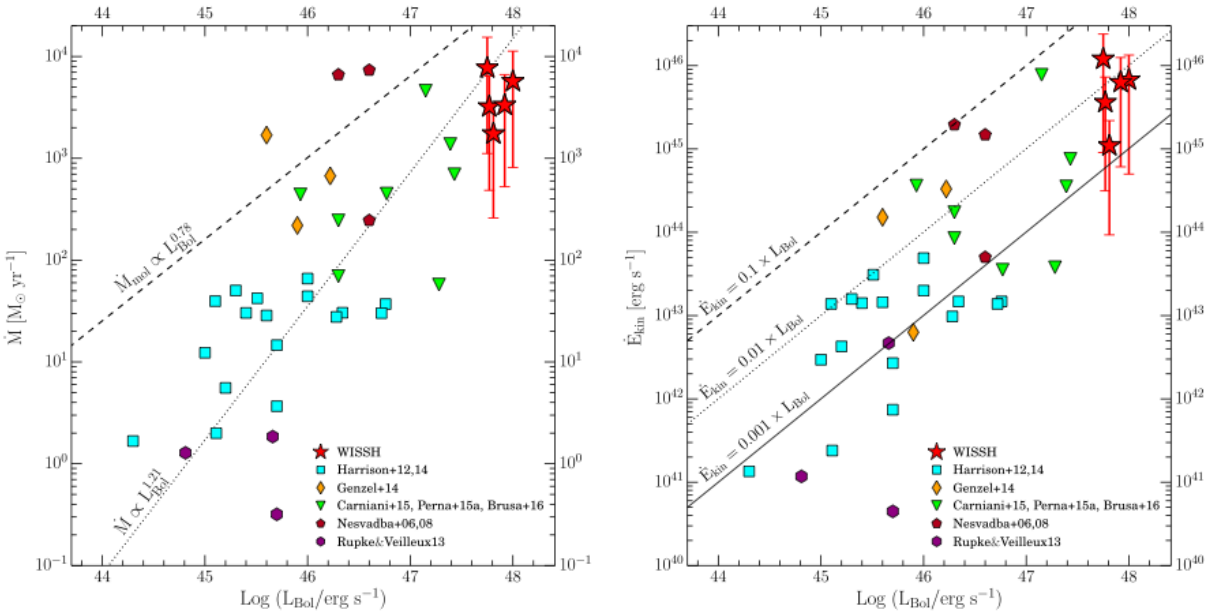

Figure 2.11. Kinetic power of the ionized outflows as a function of the bolometric luminosity. The WISSH quasars (red stars) are compared with others sample from literature (Harrison *et al.* 2012, 2014; Genzel *et al.* 2014; Carniani *et al.* 2015; Perna *et al.* 2015; Brusa *et al.* 2015; Nesvadba *et al.* 2006, 2008; Rupke & Veilleux 2013. Dashed, dotted and solid lines indicate an outflow kinetic power of 10%, 1% and 0.1% of the AGN luminosity, respectively (Bischetti *et al.* 2017).

Chapter 3

Observations and data reduction

One of the main goals of the WISSH survey is to determine the SMBH mass (via Hβ emission line) and the presence of AGN-driven outflows in sources at the brightest end of the AGN luminosity function, traced by the possibly broad blueshifted [OIII]λ5007Å emission line. Accordingly, we have collected Near-infrared (NIR) spectroscopic observations for 18 WISSH quasars with LUCI1 at LBT during the 2013-2015 campaigns and SINFONI at VLT during the period 093.A [1], according to the following selection criteria:

- sources with z > 3.7 and 1.6 < z < 2 have been excluded, because for these cases LBT/LUCI1 or VLT/SINFONI bandwidth does not cover the [OIII] spectral region.
- sources with no available 2MASS J H K magnitudes have been excluded, in order to estimate the expected S/N of the spectroscopic data without uncertainties.
- sources with a redshift for which telluric lines contaminate the [OIII] emission line or the LBT/LUCI1 or VLT/SINFONI bandwidth does not simultaneously cover both [OIII] and Hβ emission lines.

Furthermore, we obtained LUCI observing time for additional 18 WISSH objects in the Period 2016-2017 and 2017-2018 (observations are still on-going), which will give us the opportunity to double up the WISSH sample size with Hβ/[OIII] information and reach much more statistically sounder conclusions. In Table 3.1 it is listed the total number of WISSH QSOs for which we obtained spectroscopic observations in the rest-frame Optical range.

As discussed in Sect. 2.2, in Bischetti *et al.* (2017) we presented results about five WISSH objects with prominent broad [OIII] emission. In this Thesis I have analyzed additional 13 quasars with LUCI1/LBT (10 objects) and VLT/SINFONI (3 objects) observations and the rest-frame UV spectra of the 18 WISSH QSOs (see Table 3.1).

[1] Details on VLT/SINFONI and LBT/LUCI1 are given in Sect. 3.1 and 3.2

The coordinates, SDSS 12th data release (DR12) redshift, optical photometric data (Ahn *et al.* 2014), 2MASS NIR photometric data (Skrutskie *et al.* 2006) and colour excess E(B−V) (Duras et al 2017, in prep) of the 13 targets are listed in Table 3.2. In Appendix B are shown the LBT/LUCI1 and VLT/SINFONI rest-frame spectra of the WISSH quasars analyzed in this Thesis. In Appendix C are shown the SDSS spectra of the 18 WISSH QSOs considered here.

Table 3.1. The LBT/LUCI campaign of WISSH quasars. (The PI of the LBT/LUCI observations is E. Piconcelli, while F. Fiore is the PI of the SINFONI observations). Redshifts are from SDSS DR12.

Observing period	SDSS Name	RA	DEC	z	INSTRUMENT	
P13/14	J111119.10+133603.9	11 11 19.10	+13 36 03.9	3.481	LBT	
P13/14	J120147.90+120630.2	12 01 47.90	+12 06 30.2	3.484	LBT†	
P13/14	J123641.45+655442.1	12 36 41.45	+65 54 42.1	3.387	LBT	
P13/14	J132654.96-000530.1	13 26 54.96	-00 05 30.1	3.307	LBT†	
P13/14	J142123.97+463318.0	14 21 23.97	+46 33 18.0	3.363	LBT	
P13/14	J142243.02+441721.2	14 22 43.02	+44 17 21.2	3.545	LBT	Vietri et al. 2017, sub
P13/14	J152156.48+520238.5	15 21 56.48	+52 02 38.5	2.208	LBT	
P13/14	J154938.72+124509.1	15 49 38.72	+12 45 09.1	2.386	LBT†	
P14/15	J074521.78+473436.1	07 45 21.78	+47 34 36.1	3.214	LBT †	
P14/15	J080117.79+521034.5	08 01 17.79	+52 10 34.5	3.217	LBT†	
P14/15	J090033.50+421547.0	09 00 33.50	+42 15 47.0	3.295	LBT	
P14/15	J095841.21+282729.5	09 58 41.21	+28 27 29.5	3.382	LBT	
P14/15	J110610.72+640009.6	11 06 10.72	+64 00 09.6	2.205	LBT	
P14/15	J115747.99+272459.6	11 57 47.99	+27 24 59.6	2.214	LBT	
P14/15	J120144.36+011611.6	12 01 44.36	+01 16 11.6	3.240	LBT	
P14/15	J153830.55+085517.0	15 38 30.55	+08 55 17.0	3.551	LBT*	
P14/15	J212329.46-005052.9	21 23 29.46	-00 50 52.9	2.269	LBT*	
P14/15	J234625.66-001600.4	23 46 25.66	-00 16 00.4	3.489	LBT*	
P16/17	J041420.90+060914.2	04 14 20.90	+06 09 14.2	2.614	LBT	
P16/17	J081855.77+095848.0	08 18 55.77	+09 58 48.0	3.694	LBT	
P16/17	J094140.17+325703.2	09 41 40.17	+32 57 03.2	3.452	LBT	
P16/17	J101336.37+561536.3	10 13 36.37	+56 15 36.3	3.633	LBT	
P16/17	J101447.18+430030.1	10 14 47.18	+43 00 30.1	3.126	LBT	
P16/17	J102541.78+245424.2	10 25 41.78	+24 54 24.2	2.382	LBT	
P16/17	J102714.77+354317.4	10 27 14.77	+35 43 17.4	3.112	LBT	
P16/17	J111017.13+193012.5	11 10 17.13	+19 30 12.5	2.498	LBT	Data acquisition
P16/17	J120447.15+330938.7	12 04 47.15	+33 09 38.7	3.596	LBT	is still on-going
P16/17	J121027.62+174108.9	12 10 27.62	+17 41 08.9	3.640	LBT	
P16/17	J124957.23-015928.8	12 49 57.23	-01 59 28.8	3.638	LBT	
P16/17	J131011.60+460124.4	13 10 11.60	+46 01 24.4	2.133	LBT	
P16/17	J142656.18+602550.8	14 26 56.18	+60 25 50.8	3.189	LBT	
P16/17	J145125.31+144136.0	14 51 25.31	+14 41 36.0	3.102	LBT	
P16/17	J154446.34+412035.7	15 44 46.34	+41 20 35.7	3.548	LBT	
P16/17	J155912.34+482819.9	15 59 12.34	+48 28 19.9	3.423	LBT	
P16/17	J163300.13+362904.8	16 33 00.13	+36 29 04.8	3.576	LBT	
P16/17	J223808.07-080842.1	22 38 08.07	-08 08 42.1	3.122	LBT	

† Data presented in Bischetti *et al.* (2017)

* VLT/SINFONI spectroscopic data are also available for these QSOs.

Table 3.2. Properties of the 18 WISSH quasars considered in this work. The columns give the following information: (1) SDSS ID., (2–3) celestial coordinates, (4) redshift from SDSS DR12, (5–9) SDSS DR12 photometric data , (10–12) 2MASS photometric data, and (13) colour excess E(B−V) (Duras et al. 2017, in prep)

SDSS	RA	Dec	z_{SDSS}	u	g	r	i	z	J	H	K	E(B–V)
(1)	(2)	(3)	(4)	(5)	(6)	(7)	(8)	(9)	(10)	(11)	(12)	(13)
J0801+5210	08:01:17.79	+52:10:34.5	3.217	19.73	17.26	16.90	16.76	16.69	15.71	15.34	14.61	0.0
J0958+2827	09:58:41.21	+28:27:29.5	3.382	20.95	18.50	17.84	17.71	17.51	16.31	16.04	15.41	0 .0
J1106+6400	11:06:10.72	+64:00:09.6	2.205	16.44	16.11	16.01	15.98	15.81	15.06	14.55	13.95	0.0
J1111+1336	11:11:19.10	+13:36:03.9	3.462	22.26	18.11	17.30	17.18	17.05	15.89	15.51	15.03	0.0
J1157+2724	11:57:47.99	+ 27:24:59.6	2.214	19.98	19.11	18.25	17.77	17.31	16.14	15.43	14.48	0.2
J1201+0116	12:01:44.36	+01:16:11.6	3.240	19.50	17.72	17.39	17.32	17.27	15.90	15.88	14.84	0.0
J1236+6554	12:36:41.45	+65:54 :42.1	3.358	20.52	17.81	17.29	17.19	16.96	16.00	15.47	15.31	0.0
J1421+4633	14:21:23.97	+46:33:18.0	3.266	21.96	17.97	17.38	17.22	17.09	16.28	15.49	14.89	0.0
J1422+4417	14:22:43.02	+44:17:21.2	3.605	23.45	19.36	18.15	17.57	17.11	15.81	15.21	14.46	0.1
J1521+5202	15:21:56.48	+52:02:38.5	2.195	16.44	15.90	15.60	15.44	15.33	14.64	14.06	13.35	0.0
J1538+0855	15:38:30.55	+08:55:17.0	3.551	24.14	18.17	17.17	17.00	16.84	15.67	15.48	14.72	0.0
J2123−0050	21:23:29.46	−00:50:52.9	2.269	17.16	16.63	16.42	16.34	16.10	15.18	14.62	13.90	0.0
J2346−0016	23:46:25.66	−00:16:00.4	3.489	21.24	18.69	17.91	17.75	17.56	16.87	16.13	15.30	0.0
J0745+4734[†]	07:45:21.78	+47:34:36.1	3.214	19.56	16.63	16.35	16.29	16.19	15.08	14.61	13.95	0.0
J0900+4215[†]	09:00:33.50	+42:15:47.0	3.295	22.97	17.11	16.74	16.69	16.58	15.37	14.68	14.00	0.0
J1201+1206[†]	12:01:47.90	+12:06:30.3	3.484	20.77	18.31	17.41	17.31	17.18	15.87	15.25	14.61	0.0
J1326−0005[†]	13:26:54.95	−00:05:30.1	3.307	22.83	20.90	20.54	20.02	19.28	17.39	16.75	15.31	0.3
J1549+1245[†]	15:49:38.71	+12:45:09.1	2.386	20.23	18.67	17.84	17.38	16.90	15.86	14.56	13.52	0.1

[†] WISSH quasars analyzed in Bischetti *et al.* (2017)

Table 3.3. LUCI modes. Columns: (1) Type of Camera, (2) Pixel scale, (3) Field of view (4) Resolution, (5) Spectroscopic mode (LSS stands for Long SLIT Spectroscopy and MOS for Multi-Object Spectroscopy)

Camera (1)	Scale (2) "/pixel	FOV (3) arcmin	Resolution (4)	Spectroscopic mode (5)
N1.8	0.25	4×2.8	1900-8500	LSS & MOS
N3.75	0.12	4×2.8	3800-17000	LSS& MOS
N30	0.015	0.5×0.5	10000-40000	LSS

3.1 LUCI/LBT NIR spectroscopy

3.1.a LUCI spectrograph at LBT

The observations of WISSH quasars were carried out with LUCI1, a NIR spectrograph and imager for the Large Binocular Telescope (LBT) located in Mount Graham, Arizona. The spectrograph LUCI1 is mounted on the bent Gregorian focus of the SX mirror of LBT, together with an identical one, LUCI2, on the other side of the telescope (DX mirror). Both the spectrographs operate from 0.85 to 2.5 μm wavelength range, i.e. the bands z, J, H and K are covered, using a 2048 x 2048 element Hawaii II detector array from Rockwell. The observing modes currently available are:

- seeing-limited imaging
- seeing-limited longslit spectroscopy (LSS)
- seeing-limited multi object spectroscopy with slit masks (MOS)
- diffraction-limited imaging with LUCI1

The seeing-limited and the diffraction-limited modes are available over a 4 arc-minute square and 0.5 arc-minute square Field of View (FOV), respectively.

In Table 3.3 the LUCI spectroscopic observation modes and the relative cameras are summarized. The N1.8 and N3.75 cameras are used in seeing-limited mode for spectroscopy and imaging respectively, while the N30 camera is used in diffraction-limited mode.

Broad band filters in z-J-H-K_s-K bands, medium and narrow band filters are available for each LUCI instrument. For the WISSH QSOs we required medium resolution spectroscopic observations in longslit mode with a slit of 1 arcsec width, using the N1.8 camera. We chose as instrument setup the 150_K_s grating with the K_s filter and the 210_zJHK grating with the H filter, for objects at redshift bins $2.1 < z < 2.4$ and $3.1 < z < 3.6$, respectively. Table 3.4 summarizes the main characteristics of the gratings and the filters used during the LUCI1 observations.

Table 3.4. Characteristics of the gratings and filters used for the WISSH QSOs observations. Columns: (1) Grating, (2) Filter, (3) Minimum wavelength of the grating (micron), (4) Nominal center wavelength of the grating (micron), (5) Maximum wavelength of the grating (micron), (6) Spectral resolution (Angstrom), (7) Resolving Power

Grating	Filter	λ_{min}	λ_{cen}	λ_{max}	Spectral resolution	Resolving power
(1)	(2)	(3)	(4)	(5)	(6)	(7)
210_zJHK(2^{nd} order)	H	1.541	1.650	1.743	2.02	7838
150_K_s	K_s	1.890	2.170	2.423	5.33	4150

Table 3.5. Journal of the LBT/LUCI1 observations of the 13 WISSH QSOs analyzed for the first time in this Thesis. The columns give the following information: (1) SDSS ID (2) grating, (3) resolution power R, (4) exposure time (in units of s), (5) average seeing (in units of arcsec), (6) observation date, (7) standard star and (8) arc-lamps or sky lines.

SDSS	grating	R	t_{exp}	seeing	Obs date	Standard Star	Arclamp/Sky
(1)	(2)	(3)	(4)	(5)	(6)	(7)	(8)
J0801+5210	150 K_s	4150	2400	1.05	Feb 10^{th} 2015	HIP41798	ArNe
J0958+2827	150 K_s	4150	3600	0.75	Mar 21^{th} 2015	HIP41798	ArNe
J1106+6400	210 zJHK	7838	1800	0.69	Apr 17^{th} 2015	HIP52877	ArNe
J1111+1336	150 K_s	4150	2400	0.55	Apr 20^{th} 2014	HIP64231	OH sky
J1157+2724	210 zJHK	7838	1200	0.9	Mar 22^{th} 2015	HIP56736	ArNe
J1201+0116	150 K_s	4150	1440	0.78	Apr 27^{th} 2015	HIP75230	ArNe
J1236+6554	150 K_s	4150	2400	0.66	Apr 20^{th} 2014	HIP64231	OH sky
J1421+4633	150 K_s	4150	1500	0.52	Apr 20^{th} 2014	HIP71171	OH sky
J1422+4417	150 K_s	4150	800	0.55	Apr 20^{th} 2014	HIP64231	OH sky
J1521+5202	210 zJHK	7838	1200	1.01	Apr 20^{th} 2014	HIP68868	ArXe

3.1.b LUCI data reduction

The LUCI observations were performed from April 2014 to June 2015, in two different observing Periods (i.e. Period 2013-2014 and 2014-2015). The average seeing of both cycles is comparable, i.e. ~0.8 arcsec (See Table 3.5 for further details). I have performed the data reduction using IRAF tasks, ESO-MIDAS and IDL routines on both targets and standard stars.

The LUCI1 data reduction can be summarized as follows:

- Correction of the CCD response.
- Cosmic rays subtraction.
- Wavelength calibration.
- Sky emission lines subtraction.
- Spectrum extraction.
- Atmospheric correction and Flux calibration.

1) **Correction of the CCD response.** The pixels matrix which constitutes CCD detectors is characterized by a non-uniform response, with the resulting effect of elevating the counts in every pixel. To correct for this effect, several "zero" exposure time images are acquired with no light incident upon the detector, the so-called bias frames. These are used to subtract any accumulated charge electronic contamination to the scientific images.

Because the response of each pixel in the CCD may vary from one pixel to the next, a series of flat field frames are also taken in order to correct for any variations in the pixel-to-pixel sensitivity of the CCD. This is done by illuminating the CCD with a uniform radiation. Then a medium bias subtracted flat field has been computed and a normalized flat field with count values close to 1 has been created (see Fig. 3.1, upper panel). Finally, the science image has been divided for the normalized flat field. This procedure corrects the pixels to a uniform sensitivity level.

2) **Cosmic rays subtraction.** The CCD is sensitive to energetic charged particles such as cosmics rays, which produce bright spots on images. An approach to clean background pixels from cosmic rays is to detect pixels with a signal larger than a threshold value and replace them with a median level. This can be done by the task *crmedian* in the IRAF package.

3) **Wavelength calibration.** In order to perform wavelength calibration, the emission line spectrum of a well understood excited gas is used, i.e. the arc lamp. An arc spectrum should contain a number of spectral lines useful for the wavelength calibration, but in some cases other solutions are preferred. In the NIR band, the sky emission is strong overall the spectral range and it is measured simultaneously with the science observation. This leads to the sky background as a good calibrator with respect to the arc lamps. The wavelength identification is performed with the

IRAF task **identify**, using a list of wavelengths for the arc lamps or sky spectrum. Rousselot *et al.* (2000) provides a complete template of the nigh-sky OH emission lines. As a next step, bi-dimensional wavelength map is create with **fitcoords** and **transform** tasks, in order to calculate the geometric distortion solution for the instrument. Indeed may effects tend to curve the image as shown in Fig. 3.1(lower panel), with no univocal correspondence between the position on the x-direction and wavelength. A check on the goodness of the bi-dimensional wavelength map is done sampling three different horizontal part of the 2d images using MIDAS environment. If the wavelength solution is correctly done, it can be applied to the science image in an interactive mode using the IRAF task **transform**. We used Argon and Neon arc-lamps for the wavelength calibration of J0801+5210, J0958+2827, J1106+6400, J1157+2724 and J1201+0116; OH sky emission lines for the J1111+1336, J1236+6554, J1421+4633 and J1422+4417; finally, Argon and Xenon arc-lamps for J1521+5202.

4) **Sky emission lines subtraction** The sky subtraction has been done by subtracting frames corresponding to different telescope pointings along the slit, i.e. the ABBA method. The A-B and B-A images have been produced by subtracting the images at position A and B, as shown in Figure XX. In this way, the sky emission lines have been almost totally subtracted. The B-A images are shifted with respect to the A-B images, as shown in Fig. 3.2. The shift has been calculated and applied to B-A images, in order to re-align the positive emission of both images along the y-axis. As the next step, the aligned images have been summed using the IRAF task **imarith**.

5) **Extraction of the spectrum.** The one-dimensional spectrum has been then extracted from the wavelength calibrated and sky subtracted 2-dimensional image (see Fig. 3.5, left panel). The analyzed spectra have been extracted taking into account their maximum emission in the y-axis direction. It is worth noting that the extraction aperture width cannot be smaller than the slit width (1") or the seeing.

6) **Atmospheric correction and Flux calibration.** To account for telluric absorption and flux calibration, the observations of stars with known spectral type were taken during the observing nights (see Table 3.5). To remove the atmospheric absorption features we used the IDL routine XTELLCOR_GENERAL (Vacca *et al.* 2003). This routine makes use of (i) the observed standard stars spectra, which are affected by telluric absorption as the targets, and (ii) a Vega model spectrum, useful to build up an atmospheric absorption free spectrum. As the magnitudes of the standard stars are also known, we calibrated the target spectra in absolute flux, with the same IDL routine. The reduced final frames are sky lines and telluric absorption free, wavelength and flux calibrated (see Fig. 3.5, right panel).

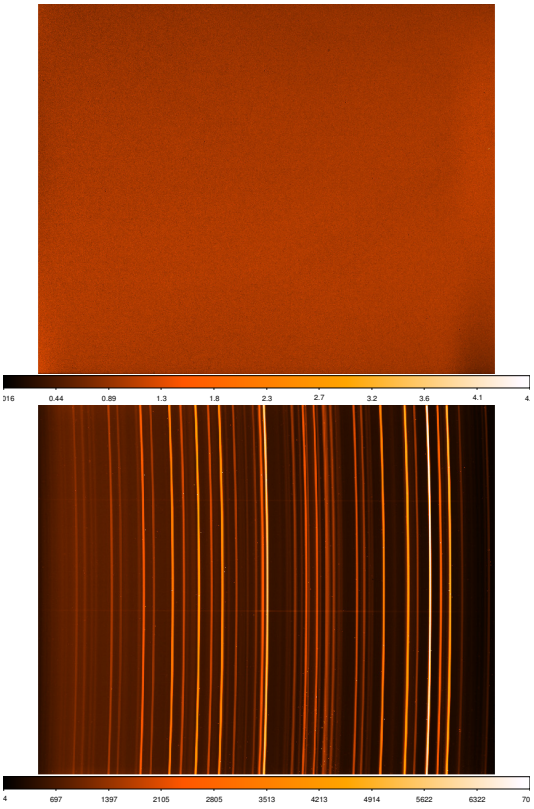

Figure 3.1. Normalized flat field (upper panel) and curved bi-dimensional spectroscopic image (lower panel) derived for the LUCI/LBT observations of J1326-0005

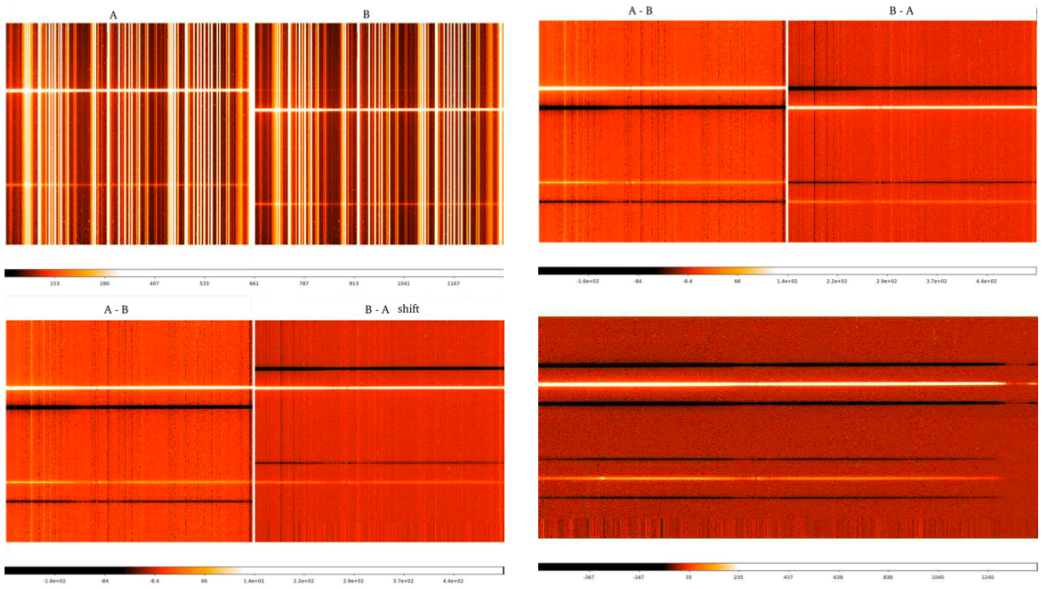

Figure 3.2. ABBA method for the subtraction of the sky emission lines in the NIR. It is evident the difference between the frames in the top left and the bottom right panels, where the frames are free from the sky emission lines

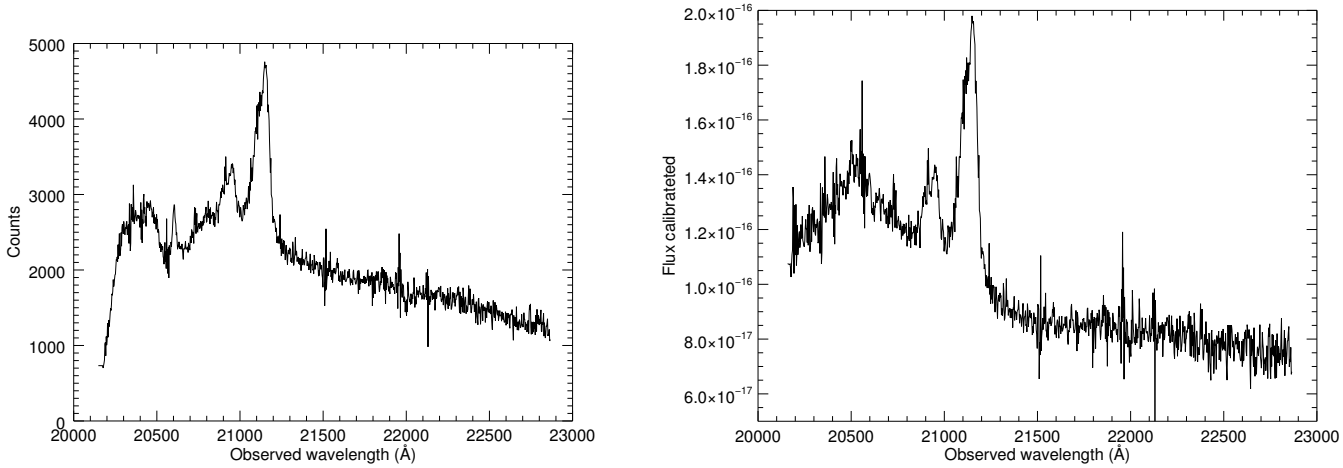

Figure 3.3. Integrated spectrum of WISSH QSO J0745+4734 before (left panel) and after (right panel) removing the absorption telluric feature in the Hβ wavelength range. The spectrum in the right panel is flux calibrated with respect to the that on the left panel (in counts)

3.2 SINFONI NIR spectroscopy

3.2.a SINFONI spectrograph at VLT

In addition to the long-slit LUCI1 observations, three quasars (namely J1538+0855, J2123-0050, J2346-0016) were observed with Spectrograph for INtegral Field Observations in the Near Infrared (SINFONI), at the VLT installed at the Cassegrain focus of Unit Telescope 4 (UT4). The observing program is 093.A-0175(A) with PI F. Fiore.

SINFONI is composed by two subsystems: the Multi-Application Curvature Adaptive Optics unit (MACAO) which allows diffraction and seeing limited observations; and the SPectrograph for Integral Faint Field Imaging (SPIFFI), a near-infrared (1.05 - 2.45 μm) integral field spectrograph.

The spectrograph operates with gratings such as J, H, K, H+K with a spectral resolution of 2000, 3000, 4000 and 1500 respectively. In the case of IFU, the SINFONI FOV is sliced into 32 slices by an image slicer of 32 plane mirrors, which disperse the light. It is possible to choose the slice height between 250, 100 and 25 mas/pixel, corresponding to a field of views of 8"×8", 3"×3" and 0.8"×0.8", respectively. SINFONI provides rectangular pixel which is then re-sampled to a square pixel, during the cube reconstruction. Another set of 32 mirrors is used to collect the light and forms a long pseudo-slit for each slice, which is dispersed according to a specific grating. Each slice corresponds to a detector slitlet and each of the 32 slitlets is imaged onto 64 pixels of the detector, resulting in 32x64 pixels and corresponding spectra of the imaged region on the sky. In Fig. 3.4 an overview

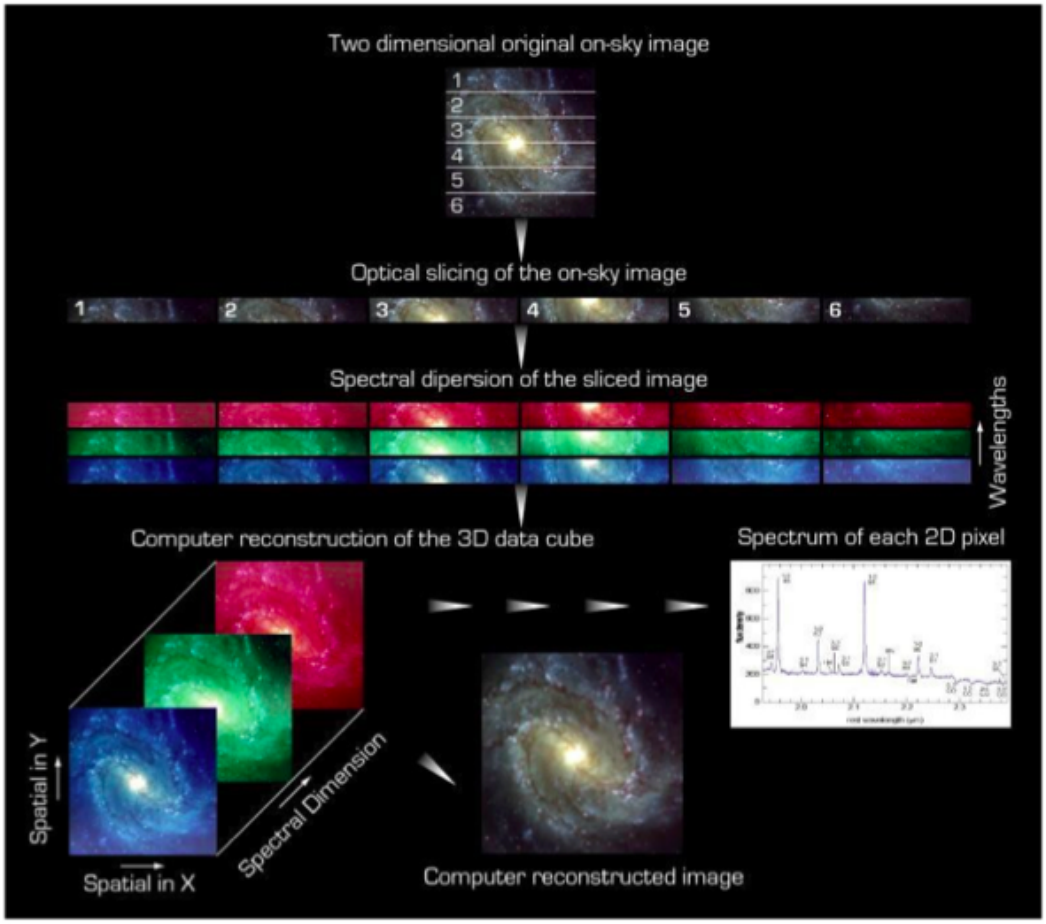

Figure 3.4. Overview of how a Integral Field Unity spectrometer works

of how a Integral Field Unity spectrometer works is shown. The data reduction software then reconstructs the 3D cube containing the spatial on-sky information in (x,y) direction and spectral information in z direction, as shown in the bottom-left corner of the Fig 3.4.

The MACAO optics offers the chance to partially correct the atmospheric turbulence. In general the light from a source which enters the atmosphere is distorted by atmospheric turbulence. An Adaptive Optics system (AO) tries to compensate the deformation of the wavefront by means of a wavefront sensor, which is able to measure the distortion. It is fundamental to measure the correct shape of the wavefront to perform its correction. For this purpose the light from a reference star, i.e. natural guide star (NGS), is used since it passed through the same turbulence as the science source. In order to provide the best correction, the guide star should be as close as possible to the science target. For SINFONI system can be also used a sodium laser guide star in the same way as the NGS.

For the WISSH QSOs, the SINFONI observations were performed in service mode during the period 093.A, with the adaptive optics (AO) - Laser Guide Star

mode. All the targets were observed within a FoV of 3"×3", with a spaxel scale of 0.05"×0.1". J1538+0855 and J2123-0050 were observed during the nights of Jul 19th-Jul 20th 2014, while J2346−0016 was observed during Aug 18th and Sept 1st 2014. Given the redshift range of the QSOs, we used K filters to target the Hβ - [OIII]λ5007Å spectral region with a spectral resolution of R~4000. The final spatial resolution obtained thanks to the LGS correction is 0.3" for J1538+0855 and J2346−0016, and 0.2" for J2123-0050, as derived by the Hβ broad emission line.

3.2.b Data reduction

The SINFONI data reduction has been performed using ESO pipelines, in Reflex environment (Freudling *et al.* 2013) and IDL routines. The data reduction procedure is quite similar to that applied to LUCI1/LBT data. The recipes used for the data reduction are summarized as follows:

- **sinfo_rec_delin**. The detector responsitivity as a function of the pixel intensity is computed in order to generate a non linear pixel map. For the identification of the non-linear pixels, linearity frames obtained by illuminating the detector for several exposure times are used. The grism and the filter used are the same as the science observations.

- **sinfo_rec_mdark**. A master dark frame is generated by stacking raw dark frames in order to correct for the accumulation of electrons in the pixels of the detector, which is related to the temperature of the detector itself. This also produce a bad pixels map flagging the hot-current pixels.

- **sinfo_rec_mflat**. A master flat is then created from the stacking of the input flat field frames. The intensity of this frame is normalized to that of the central pixel. A bad pixels mask is also created, identifying bad pixels which deviate too much from a certain threshold.

- **sinfo_rec_distortion**. The spatial distortion are computed using a set of 75 distortion fibres, which consist of an illuminated fibre along each slitlet position and a pair of arc lamp on/off. The distance between the individual slitlets is also retrieved.

- **sinfo_rec_wavecal**. The wavelength map is produced by means of arc lamp frames. The distortion products are used in order to assign a wavelength value to each pixel on the detector.

- **sinfo_rec_jitter**. Wavelength calibrated frames, corrected for the flat-field and distortion, are built. At this stage, it is also possible to choose to subtract or not the sky emission. The background sky emission subtraction for the WISSH QSOs was removed with the IDL routine SKYSUB, using object frames taken at different telescope pointings (Davies 2007).

Table 3.6. Journal of the SINFONI observations. The columns give the following information: (1) SDSS ID, (2) observation date, (3) exposure time (in units of s), (4) grating, (5) resolution power R, (6) the final spatial resolution thanks to AO observations (in units of arcsec) and (7) the telluric standard stars

SDSS	Obs date	t_{exp}	grating	R	spatial resolution	Telluric Standard
(1)	(2)	(3)	(4)	(5)	(6)	(7)
J1538+0855	Jul 19th 2014	2400	K	4000	0.3	HIP074546
J2123-0050	Jul 20th 2014	600	H	3000	0.2	HIP099193
J2346-0016	Aug18th - Sept 1st 2014	4800	K	4000	0.3	HIP022061

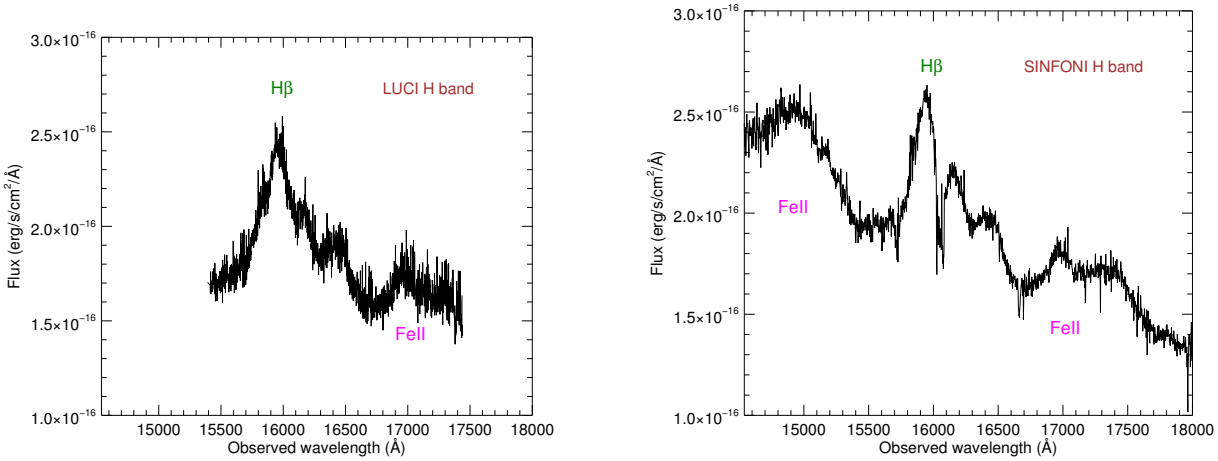

Figure 3.5. LBT/LUCI (left) and VLT/SINFONI (right) integrated spectra of the WISSH QSO J2123-0050 in the H band. The nominal wavelength range in the H band for LUCI is 15500-17400 Å and for SINFONI 14500-18500 Å. Thanks to the large bandwidth the FeII emission lines are well sampled, which allows to model properly all the features in the spectrum.

- **sinfo_utl_cube_combine**. The reconstruction of the image FOV from the 32 image slices and the coaddition of different science frame is performed, applying the relative offset to each science frame.

  After the cube reconstruction, the flux calibration has been performed with my own IDL routines, by means of telluric spectra acquired during the same nights as the targets. As a final step, I extracted a 1D spectrum for each source. This procedure does not allow to have the spatial information, but at this stage we are interested in the integrated emission from AGN. Information about SINFONI observation epochs, standard stars used for the telluric correction and flux calibration are listed in Table 3.6.

Table 3.7. Optical spectroscopic information: SDSS vs BOSS spectrograph

	SDSS spectrograph	BOSS spectrograph
Area covered	9274 square degrees	6373 square degrees
Plate area	1.49 deg radius, 6.97 deg^2	1.49 deg radius, 6.97 deg^2
Fibers per plate	640	1000
Wavelength coverage	3800 to 9200 Å	3600 to 10400 Å
Resolution	1800 to 2000	1400 to 2600

3.3 Sloan digital sky survey

The Sloan Digital Sky Survey (SDSS) is a multi-filter imaging and spectroscopic redshift survey, aiming to make a map of one quarter of the sky (10000 square degrees), centered on the North Galactic Pole. The SDSS survey uses a dedicated wide-field 2.5m telescope (Gunn *et al.* 2006) at Apache Point Observatory in Southern New Mexico. The project consists of four phases up to now: SDSS-I (2000-2005), SDSS-II (2005-2008), SDSS-III (2008-2014) and SDSS-IV (2014-2020).

We retrieved the rest-frame UV spectrum of the 18 WISSH quasars with NIR spectroscopic data, from the SDSS Data Release 12 (DR12) public archive, in order to derive the properties of the CIV emission line. The SDSS-III DR12 offers the final data from the SDSS-III, which include the complete dataset of the BOSS survey. The spectra are obtained with two spectrographs, SDSS-I with 640 fibers per plate and BOSS with 1000 fibers per plate. Both have a spectral resolution of 1500 at 3800 Å and 2500 at 9000 Å. There are two cameras for each spectrograph, one red and one blue. The red cameras cover at least 5650-10000 Angstroms, blue cameras cover at least 3600-6350 Angstroms. The optical imaging and spectroscopic information are listed in the Table 3.7.

Chapter 4

Spectral analysis

4.1 Modeling of the Hβ and [OIII] emission

Bischetti *et al.* (2017) report the results of LBT/LUCI1 spectroscopy of five WISSH QSOs with the prominent broad [OIII] emission line observed in 2014. We present here the results of the analysis of the spectra of additional 13 WISSH QSOs taken at LUCI1 during the 2013-14 and 2014-15 observing campaign at LBT. Furthermore, three quasars (namely J1538+0855, J2123-0050, J2346-0016) also benefit of VLT/SINFONI spectroscopy, we report for them the results of the analysis of these data (see Table 4.1).

The visual inspection of the rest-frame optical spectra of the 13 WISSH quasars taken with LBT/LUCI or VLT/SINFONI revealed the weakness of the [OIII] 5007/4959 Å doublet emission lines and the presence of a strong and complex FeII emission (see Appendix B). This combination makes the determination of [OIII] spectral parameters an extremely challenging task. In one case, i.e. J1422, the LBT/LUCI1 bandwidth does not cover the [OIII] spectral region. We developed a model based on the IDL package MPFIT (Markwardt 2009), in order to accurately infer the properties of the [OIII] and Hβ emission in these hyper-luminous quasars. The NIR spectra were fitted with a spectral model which consists on:

- **Hβ/[OIII] core components associated with the Narrow line region (NLR)**. Specifically, one Gaussian component has been adopted for fitting the core of Hβ4861 Å line with $\mathrm{FWHM}^{\mathrm{core}}_{\mathrm{H}\beta} \leq 1000$ km s^{-1} [1] plus one Gaussian profile for each component of the [OIII]$\lambda\lambda$4959,5007 Å doublet. The FWHM of the [OIII] doublet was forced to be the same as that of the Hβ core component. Moreover, we assumed the theoretical flux ratio for [OIII]$\lambda\lambda$4959, 5007 Å equal to 1:3 and the separation between [OIII]λ4959-5007 Å and Hβ fixed to 98–146 Å in the rest-frame, respectively.

[1] The limit of 1000 km s^{-1} for the FWHM has been set in order to account for a possible subtle Hβ outflow component.

- **[OIII] outflow components**. Specifically, one Gaussian profile with the same σ for each component of the [OIII] has been adopted in order to accurately constrain the possible presence of subtle broad/shifted components associated to outflows. Furthermore, we left free to vary the values of the FWHM ($FWHM^{broad}_{[OIII]}$) and centroids ($\lambda^{broad}_{[OIII]}$) in the range 500–2500 km s^{-1} and 4980–5034 Å, respectively, which are based on the values derived for these spectral parameters from the analysis of the [OIII] broad features in Bischetti *et al.* (2017). Given the weakness of the outflow in our objects, we do not included any outflow component in the Hβ line, corresponding to the [OIII] outflow component, as it will be irrelevant with respect to the dominant broad component from the BLR.

- **Hβ broad component associated with the Broad line region (BLR)**. We used one Gaussian profile with width free to vary or a broken power-law component convolved with a Gaussian curve (e.g. Nagao *et al.* 2006, Carniani *et al.* 2015, Bischetti *et al.* 2017).

Similarly to Bischetti *et al.* (2017), in order to fit the prominent FeII emission, we included one or two Fe II templates depending on the complexity of the iron emission (see Sect. 1.2.b for a detailed discussion about the FeII). Specifically, we chose among a library consisting of the three observational templates by Boroson & Green (1992), Véron-Cetty *et al.* (2004), Tsuzuki *et al.* (2006) and twenty synthetic FeII templates obtained with the CLOUDY plasma simulation code (Ferland *et al.* 2013), which takes into account different hydrogen densities, ionizing photon densities and turbulence. The FeII template was then convolved with a Gaussian function with a σ in the range 500-4000 km s^{-1}. Finally, the continuum was fitted by a power law component with the normalization left free to vary and the slope derived from the best-fit SED in the wavelength range of the observations. This parametrization worked well for all but two sources, i.e. J1538 and J2123, for which we used a slope left free to vary. We estimated the statistical noise from the line-free continuum emission and assumed to be constant over the entire wavelength bandwidth.

This fit yielded a good description of the observed NIR spectrum of the WISSH quasars. The results of our spectral analysis and of Bischetti *et al.* (2017) for the Hβ and [OIII]λ5007 emission lines are listed in Table 4.1 and Table 4.2, respectively. From the [OIII]-Hβ core component, we estimated the spectroscopic redshift.

The bulk of the Hβ emission is provided by the BLR component, well fitted by a broken power-law for all but four cases (J0801, J0958, J1422, J1521), which are better fitted by a Gaussian component. The FWHM of Hβ associated with the BLR has a range of 4000-7000 km s^{-1}, with a rest-frame equivalent width of 20–100 Å .

The normalization of the [OIII] emission line associated to the NLR is consistent with zero in all but three quasars (namely J0958, J1106 and J1236) for which the rest-frame equivalent width (**REW** hereafter) of the core component of the [OIII] emission line is $\approx$ 1 Å, confirming the weakness of this feature in the LUCI spectra considered here.

Table 4.1. Properties of NLR and BLR components of the Hβ emission line derived from parametric model fits (see Sect. 4.1 for details)

SDSS Name	z[a]	FWHM$^{\rm NLR}_{\rm H\beta}$ (Å)	REW$^{\rm NLR}_{\rm H\beta}$ (km s^{-1})	$\lambda^{\rm BLR}_{\rm H\beta}$ (Å)	FWHM$^{\rm BLR}_{\rm H\beta}$	REW$^{\rm BLR}_{\rm H\beta}$	Flux H$\beta^{\rm BLR}$/ Flux H$\beta^{\rm Tot}$
J0801+5210	3.257±0.002	1000*	2	4862±1	6100^{+100}_{-200}	$43.8^{+0.2}_{-0.7}$	$0.95^{+0.05}_{-0.09}$
J0958+2827	3.434±0.001	1000*	1	4859±1	5100^{+100}_{-200}	39±1	0.95±0.05
J1106+6400	$2.221^{+0.002}_{-0.003}$	1000*	1	4850^{+1}_{-2}	7900^{+300}_{-200}	92±3	0.99±0.01
J1111+1336	$3.490^{+0.004}_{-0.005}$	1000*	1	4871^{+1}_{-2}	7400±100	71^{+2}_{-1}	$0.99^{+0.01}_{-0.02}$
J1157+2724	2.217±0.001	1000*	3	4849±1	4200±100	56±1	0.95±0.03
J1201+0116	$3.248^{+0.002}_{-0.001}$	1000*	7	4855±2	4700^{+100}_{-300}	55±2	$0.89^{+0.05}_{-0.04}$
J1236+6554	3.424±0.001	1000*	1	4848±2	5300±200	64±2	$0.98^{+0.02}_{-0.03}$
J1421+4633	3.454±0.002	1000*	2	4838±3	6500±300	55^{+2}_{-1}	$0.96^{+0.04}_{-0.03}$
J1422+4417	3.648±0.001	1000*	3	4851±2	4400^{+300}_{-200}	21±1	0.89±0.20
J1521+5202	2.218±0.001	1000*	1	4861±1	7200±100	26±1	$0.96^{+0.04}_{-0.06}$
J1538+0855	$3.567^{+0.003}_{-0.002}$	1000*	2	4843±2	5500^{+400}_{-200}	104^{+4}_{-3}	0.98±0.02
J2123-0050	2.282±0.001	1000*	1	4850±2	4900±200	41±1	$0.97^{+0.01}_{-0.02}$
J2346-0016	$3.511^{+0.001}_{-0.002}$	1000*	4	4864^{+4}_{-7}	5800^{+300}_{-600}	66^{+6}_{-5}	$0.94^{+0.06}_{-0.09}$
J0745+4734†	3.225±0.001	500±200	-	4862±1	8600±200	86^{+3}_{-2}	$0.98^{+0.02}_{-0.08}$
J0900+4215†	3.294±0.001	300±100	<1	4861±1	3200±200	55±1	0.98±0.02
J1201+1206†	3.512±0.002	1700±200	10±2	4865±2	6200±300	68±1	0.86±0.07
J1326-0005†	3.303±0.001	700±200	<2	4862±1	3700±200	96±1	$0.93^{+0.07}_{-0.09}$
J1549+1245†	2.365±0.001	300±200	<1	4871±2	8300±300	64±2	$0.98^{+0.02}_{-0.09}$

[a] Redshifts are based on the core component of Hβ emission line from NIR spectroscopy.

* Best fit value corresponding to the maximum allowed value of FWHM (see Sect. 4). For these objects we only report the REW$^{NLR}_{[H\beta]}$ and FWHM$^{\rm NLR}_{[\rm H\beta]}$ corresponding to the best-fit values.

† WISSH quasars with LUCI1 spectra analyzed in Bischetti *et al.* (2017). For these objects the redshifts are based on the core component of the [OIII] emission line.

Table 4.2. Properties of the core (C) and broad (B) components of the [OIII]λ5007 emission line derived from parametric model fits. (see Sect. 4.1 for details)

SDSS Name	Component	$FWHM_{[OIII]}$ (km s^{-1})	$\lambda_{[OIII]}$ (Å)	$REW_{[OIII]}$ (Å)	$L_{[OIII]}$ (10^{42} erg s^{-1})
J0801+5210	C	1000*	5007±1	<0.1	<2.3
	B	1200±300	5026±5	$0.7^{+0.3}_{-0.2}$	15±7
J0958+2827	C	1000*	5007±2	1	13
	B	2500*	4980*	4	44
J1106+6400	C	1000*	5007±4	1	10
	B	500*	5022±2	0.3	5
J1111+1336	C	1000*	5007^{+3}_{-2}	<0.04	<1
	B	1000±200	5029±2	0.9±0.2	16±4
J1157+2724	C	1000*	5007±1	<0.1	<2
	B	500*	4995±2	1	6
J1201+0116	C	1000*	5006±1	<0.2	<3
	B	500*	5022^{+7}_{-35}	0.2	5
J1236+6554	C	1000*	5007±2	1	16
	B	800^{+300}_{-200}	5022±2	$1.0^{+0.4}_{-0.3}$	12±4
J1421+4633	C	1000*	5007±2	<0.01	<1
	B	700±100	5027±2	1.4±0.2	26±6
J1521+5202	C	1000*	5007±1	<0.1	<0.1
	B	1300±100	5033±1	1.5±0.1	46.0±4.0
J1538+0855	C	1000*	5007±3	<1	<16
	B	2000±300	4987^{+3}_{-2}	8±1	210^{+40}_{-30}
J2123-0050	C	1000*	5007±2	<0.01	<0.3
	B	2300	4980*	3	60
J2346-0016	C	1000*	5007±2	<0.2	<4
	B	1500±400	5030^{+4}_{-3}	3±1	50±20
J0745+4734†	C	500±200	5007±1	4±1	200±100
	B	1600±200	4999±1	25±1	1100±300
J0900+4215†	C	300±100	5007±1	1±1	50^{+100}_{-30}
	B	2200±200	4999±1	13±1	500±100
J1201+1206†	C	1700±200	5007±2	19±1	500±100
	B	900±200	4990±2	6±1	200±100
J1326-0005†	C	700±200	5007±1	27±1	600±300
	B	1900±200	4997±1	50±1	1100±300
J1549+1245†	C	300±200	5007±1	1±1	20^{+40}_{-10}
	B	1200±200	5012±1	14±1	500±100

† WISSH quasars analyzed in Bischetti *et al.* (2017)

* Best fit value corresponding to the minimum or maximum allowed value of FWHM or centroid (see Sect. 4). For these we only report the $REW_{[OIII]}$ and $L_{[OIII]}$ corresponding to the best-fit values.

Regarding the spectral components associated to a wind, for all but one (J1538) QSOs the best value of their FWHMs or centroids is equal to the maximum or minimum value allowed by our model (500–2500 km/s and 4980Å, respectively), or the centroids fall extremely redward to 5007 Å (i.e. > 5020 Å). The combination of these findings strongly suggests that this weak ($REW^{broad}_{[OIII]} \leq 3$ Å) Gaussian component is likely accounting for additional FeII emission not properly fitted by the templates, instead of being due to a wind. In the case of J1538, we measure a broad ($FWHM^{broad}_{[OIII]} = 1980$ km s^{-1}), blueshifted ($v^{broad}_{[OIII]} \sim 1200$ km s^{-1}) component with a $REW^{broad}_{[OIII]} = 7.7$ Å, making us highly confident to associate this spectral feature with blueshifted [OIII] emission. Hereafter, we refer to **"*[OIII]* sample"** as the group of WISSH quasars showing a REW of the [OIII] emission line (narrow+broad components) ≥ 5 Å, while quasars with $REW_{[OIII]} < 5$ Å are included in the **"*Weak [OIII]* sample"**.

4.2 Modeling of the CIV emission

We shifted the SDSS UV rest-frame spectra of the 18 WISSH QSOs with Optical rest-frame spectroscopy (i.e. 13 QSOs analyzed this Thesis work plus 5 from Bischetti *et al.* (2017), see Table 4.3) to the systemic rest-frame using the redshift measured from Hβ/[OIII] core component. The analysis of the SDSS spectra was focused in the spectral region of CIV emission line at 1549 Å, including spectral ranges free of emission/absorption features at both sides of the CIV line centroid, in order to constrain the underlying continuum.

The CIV emission was fitted using a combination of up to three Gaussian profiles with spectral parameters (centroid, width and normalization) left free to vary. We found that for all but three quasars the best-fit model consists on a combination of two Gaussian components. For the BAL quasars J1157+2724 and J1549+1245, for which the blue side of CIV line profile is heavily affected by absorption, the CIV is modeled by one Gaussian component (see Fig. C.4(left) for J1157 and Fig. C.8(right) for J1549 in the Appendix C) and for the quasar J0745+4734, showing a very prominent peak at 1549 Å , the best-fit model of the CIV profile is the combination of three Gaussian components (see Fig. C.1(left) in the Appendix C).

We considered in our fits the presence of FeII emission by using UV FeII templates from Vestergaard & Wilkes (2001), although FeII is not particularly strong in the CIV region. These templates were convolved with Gaussian profiles of different widths to account for the observed FeII-related emission features in the spectra. If requested, we also included in the model one or two Gaussian components to account for HeIIλ1640 Å and/or OIII]λ1664 Å emissions.

The resulting physical parameters of the CIV emission for the 18 WISSH quasars are listed in Table 4.3. We found a median value of $REW_{CIV} = 21$ Å with the lowest value for the object J1521 ($REW_{CIV} = 8$ Å), confirming its WLQ nature (Just *et al.* 2007; see Sect. 1.4.a for more details about WLQs). The CIV emission profile is broad with a median value of $FWHM_{CIV} = 7800$ km s^{-1} and, in four cases,

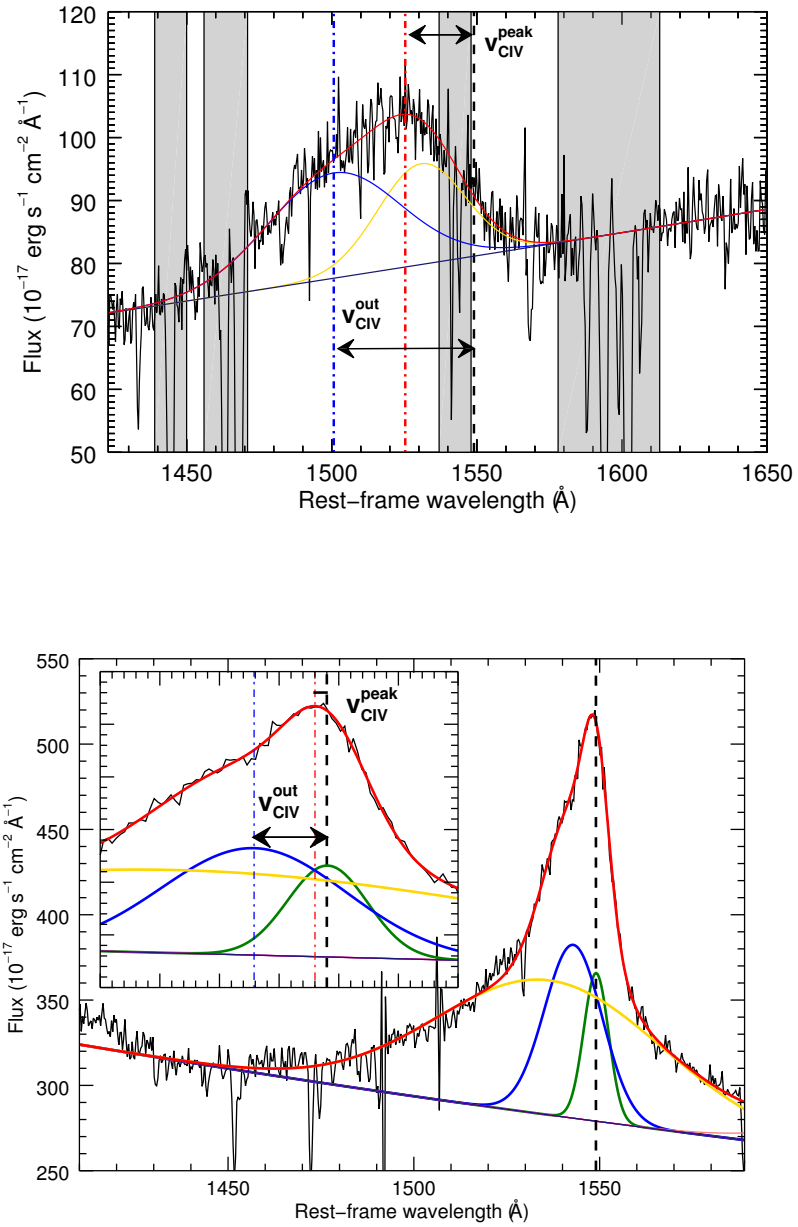

Figure 4.1. Parametrization of the CIV emission line profile of a *Weak [OIII]* quasar (Upper panel) and a *[OIII]* quasar (lower panel). In both panels the red, yellow and blue curves refer to the best-fit of the spectrum, virialized component and outflow component of the CIV emission line, respectively. The black dashed line indicates the λ_{CIV} at 1549 Å . The red dotted-dashed line denotes the peak of the CIV emission line and v_{CIV}^{peak} represent its velocity shift with respect to the systemic λ1549 Å . The blue dotted-dashed line indicates the peak of the outflow component and v_{CIV}^{out} is its velocity shift with respect to the systemic redshift. In the lower panel the green curve refers to component required by the fit, in order to better described the CIV profile.

exceptional values of $FWHM_{CIV}$ (> 10000 km s^{-1}) are detected. Moreover we found that the peak of the CIV profile is blueshifted with respect to the systemic redshift with a velocity shift (v_{CIV}^{peak} hereafter) in the range of v_{CIV}^{peak} = 200 – 7500 km s^{-1} in all cases but J1326 (v_{CIV}^{peak} = -50 km s^{-1}) [2].

The CIV emission line in the *Weak [OIII]* quasars shows broad, strongly blue and asymmetric profiles, with v_{CIV}^{peak} in the range of v_{CIV}^{peak} = 2500 – 7500 km s^{-1} . This clearly indicates the presence of an outflowing component associated with this transition. According to the best-fit model, we refer to the Gaussian line with the most blueshifted centroid as the outflow component with v_{CIV}^{out} indicating its velocity shift with respect to the systemic (see Fig. 4.1 upper panel).

The *[OIII]* sample exhibits the $FWHM_{CIV}$ in the range of 2000-5000 km s^{-1}, and lower blueshifts than those of the *Weak [OIII]* QSOs , i.e. $v_{CIV}^{peak} \gtrsim$ 2000 km s^{-1}. The profile of the CIV line in *[OIII]* QSOs typically is more symmetric than in *Weak [OIII]* objects, indicating a dominant contribution from emission of virialized gas. We therefore consider in this case the Gaussian component with the largest FWHM as the virialized one of the CIV emission line, while the second Gaussian component with a smaller FWHM is assumed to represent the emission associated to the wind (see Fig. 4.1 lower panel). It is worth noting that for the vast majority of our objects we measure a virialized component with a centroid not consistent (> 2σ) with 1549 Å (see Appendix C). This can be interpreted in terms of a low-velocity component likely associated to a virialized flow in a rotating accretion disk wind (Young *et al.* 2007; Kashi *et al.* 2013). Finally, in case of J1538, an *[OIII]* object that also exhibits some distinctive properties of *Weak [OIII]* sources (e.g. Appendix A), the virialized and outflow components of the CIV emission are assumed as for *Weak [OIII]* sources.

[2] It is important to bear in mind the presence of BAL features affecting the CIV line profile in this quasar

Table 4.3. Properties of CIVλ1549 emission line derived from parametric model fits (see Sect. 4.2 for details)

SDSS Name	$\lambda_{CIV\,peak}$ (Å)	$v_{CIV}^{peak,\dagger}$ (km s^{-1})	REW_{CIV} (Å)	$FWHM_{CIV}$ (km s^{-1})	L_{CIV} (10^{45} erg s^{-1})
J0745+4734	1548±1	200±100	$31.0^{+0.2}_{-4.5}$	4300±100	$8.3^{+0.2}_{-0.1}$
J0801+5210	1535±1	2700±200	17±1	10900^{+100}_{-200}	2.9±0.1
J0900+4215	1546±1	600±10032±1	4200±200	$6.4^{+0.3}_{-0.2}$	
J0958+2827	1520±1	5600±280	19±4	10000±500	1.7±0.2
J1106+6400	1534±1	2900±200	20.6±0.3	7800±200	2.8±0.1
J1111+1336	1540±1	1900±100	20±1	8200±200	3.0±0.2
J1157+2724[a]	1529^{+4}_{-3}	3800^{+700}_{-600}	71^{+12}_{-14}	7600^{+700}_{-800}	0.9±0.1
J1201+0116	1531±1	3400±100	17±1	8500±300	1.8±0.1
J1201+1206	1544±1	1000±100	37^{+3}_{-2}	5100±100	$4.4^{+0.2}_{-0.1}$
J1236+6554	1532±1	3400±100	$19.9^{+0.3}_{-0.4}$	7400±100	2.9±0.1
J1326-0005[a]	1549±1	-50^{+200}_{-100}	82^{+6}_{-7}	2100±200	17±2
J1421+4633	1523±1	5000^{+300}_{-100}	16±2	10200^{+200}_{-300}	2.1±0.2
J1422+4417	1525±1	4700±200	20±3	12400±200	5.9±0.1
J1521+5202	1511±1	7400±200	8±1	11500±400	2.1±0.1
J1538+0855	1538±1	2200±100	20.8±0.2	5160^{+60}_{-30}	4.0±0.1
J1549+1245[a]	1547±1	400^{+300}_{-200}	23±1	5700^{+300}_{-200}	$3.8^{+0.2}_{-0.3}$
J2123-0050	1537±1	2300±200	12±1	6700±200	1.7±0.1
J2346-0016	1532±1	3400^{+100}_{-200}	13±2	8600^{+100}_{-200}	1.2±0.1

[†] Velocity shifts of the CIV emission line are calculated from the peak of the multiple Gaussians modeling the CIV profile, with respect to the systemic redshift. See Fig. 4.1.

[a] Sources J1157+2724 and J1549+1245 are classified as BAL quasars according to the Balnicity Index (BI, Weymann *et al.* 1991) while J1326-0005 according to the modified absorption index ($AI_{1000} > 100$, Bruni *et al.* 2012), a more conservative version of the Hall *et al.* (2002) AI definition. The detailed analysis of the BAL properties of the WISSH QSOs will be presented in a forthcoming paper (Bruni et al. in prep). For these objects the strong absorption in the CIV emission line affects the spectral parameters.

Chapter 5

Results

5.1 Properties of the [OIII] emission: REW$_{[OIII]}$ and orientation

As discussed in Sect. 1.2.c, the observed equivalent width of the total profile of the [OIII] emission line (REW$_{[OIII]}$) can be used as indicator of the line of sight inclination as found by Risaliti *et al.* (2011) and Bisogni *et al.* (2017), i.e. REW$_{[OIII]}$ = REW$_{intrinsic}/cos(\theta)$ (with θ as the angle between the disc axis and the line of sight). In these works they showed that the distribution of REW$_{[OIII]}$ of a large sample of SDSS DR7 AGN with $0.001 < z < 0.8$, hereafter SDSS distribution, shows a power-law tail with $\Gamma \sim -3.5$ at the largest REW$_{[OIII]}$ values, which is well reproduced by assuming an isotropic [OIII] emission (which is proportional to the intrinsic disc luminosity) and a random inclination of the disc with respect to the line of sight. This demonstrates that the inclination effect is the likely responsible of the large-REW$_{[OIII]}$ power-law tail, whereby the higher REW$_{[OIII]}$ the higher inclination.

The *[OIII]* sample of the WISSH quasars exhibits REW$_{[OIII]} \approx$ 7-80 Å, which is mostly due to the broad blueshifted component of the [OIII] emission. Risaliti *et al.* (2011) and Bisogni *et al.* (2017) reported that REW$_{[OIII]} \geq$ 25-30 Å are associated to nearly edge-on AGN. Half of *[OIII]* sources populate the high-tail of the SDSS REW$_{[OIII]}$ distribution with REW$_{[OIII]} \gtrsim$ 25 Å (Fig. 5.1 *top*). Therefore, a high inclination, i.e. $\theta \approx 28° - 73°$ (Bisogni et al. in prep.), can likely explain such large REW$_{[OIII]}$.

For all but four quasars in the *Weak [OIII]* sample we estimated the REW$_{[OIII]}$ <2 Å, i.e. a range not covered by the SDSS distribution, which indeed includes objects having REW$_{[OIII]} > 2$. Given their high bolometric luminosities, weak [OIII] emission is expected in WISSH quasars due to over-ionization of the circumnuclear gas as found in Shen & Ho (2014) by analyzing the rest-frame optical spectra of $\sim$ 20000 Type-1 SDSS quasars (see Sect. 1.4.b). Another explanation for the reduced [OIII] emission could be linked to geometrical factors: if the ionization cone is indeed more perpendicular to the galaxy disk it would intercept a lower amount of ISM, resulting in a [OIII] line with a lower REW.

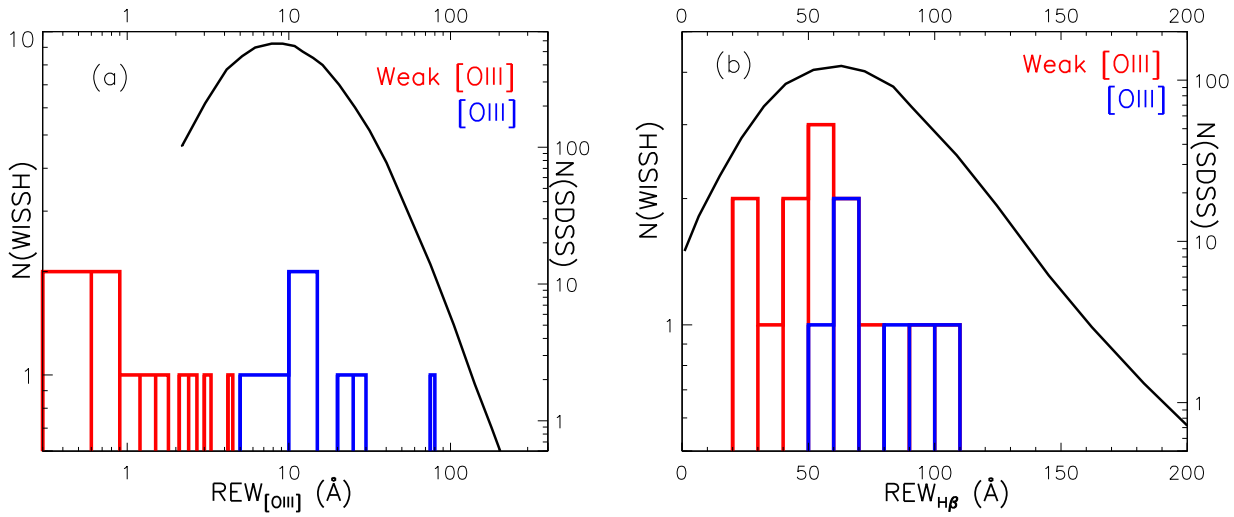

Figure 5.1. Observed distribution of the WISSH quasars for the *[OIII]* and *Weak [OIII]* samples of *(a)* $\mathrm{REW}_{[\mathrm{OIII}]}$ and *(b)* $\mathrm{REW}_{H\beta}$, compared to the best-fit of the $\mathrm{REW}_{[\mathrm{OIII}]}$ and $\mathrm{REW}_{H\beta}$ observed distributions of SDSS DR7 AGNs of Bisogni *et al.* (2017) (black solid line).

Furthermore, the *[OIII]* WISSH quasars typically have higher $\mathrm{REW}_{H\beta}$ values than the *Weak [OIII]* sources (Fig. 5.1, *bottom*), supporting a larger inclination scenario which leads to an observed lower underlying continuum. We also note that the $\mathrm{REW}_{H\beta}$ distribution of the WISSH quasar is consistent with SDSS $\mathrm{REW}_{H\beta}$ distribution.

If the inclination plays a role to explain the large differences in $\mathrm{REW}_{[\mathrm{OIII}]}$ between *[OIII]* and *Weak [OIII]* WISSH quasars, we also expect differences in the near- and mid-IR SED, as found by Bisogni et al. 2017 (in preparation) in a large SDSS sample of quasars. Face-on quasars offer a direct view of the hottest dust component located in the innermost part of the torus, while in case of high-inclination sources the view of this region can be partially blocked. This is consistent with the result obtained by comparing the average near- to mid-IR SEDs corresponding to *WISE* photometry of the quasars in the *[OIII]* and *Weak [OIII]* samples (Fig. 5.2) where sources with high $\mathrm{REW}_{[\mathrm{OIII}]}$ show a flux deficit in the NIR part of the SED around 3 μm with respect to *Weak [OIII]* sources.

5.2 Single epoch Hβ-based SMBH masses and Eddington ratios

In Sect. 1.2.b i presented the common method of measuring the black hole mass ($\mathrm{M_{BH}}$), i.e. the so-called Single Epoch technique (SE), which depends on BLR size estimated from the continuum luminosity of the quasar and on the velocity dispersion of the BLR, derived from the FWHM of a specific broad emission line, i.e

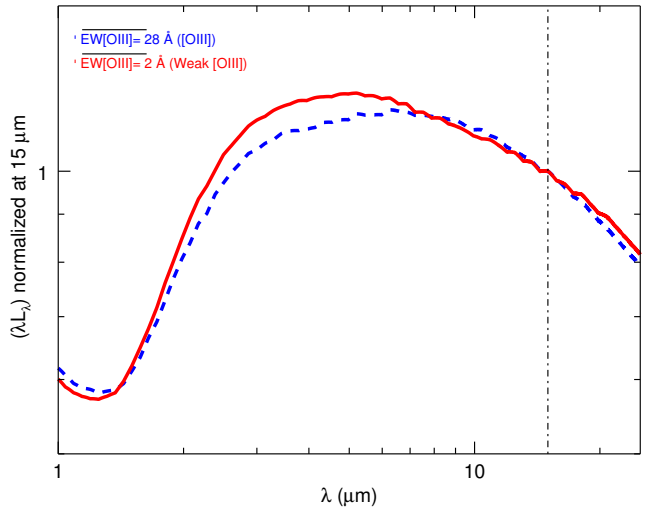

Figure 5.2. Average near- to mid-IR SEDs corresponding to WISE photometry of the WISSH *[OIII]* (dashed blue line) and *Weak [OIII]* samples (red line), normalized at 15μm (dot-dashed line).

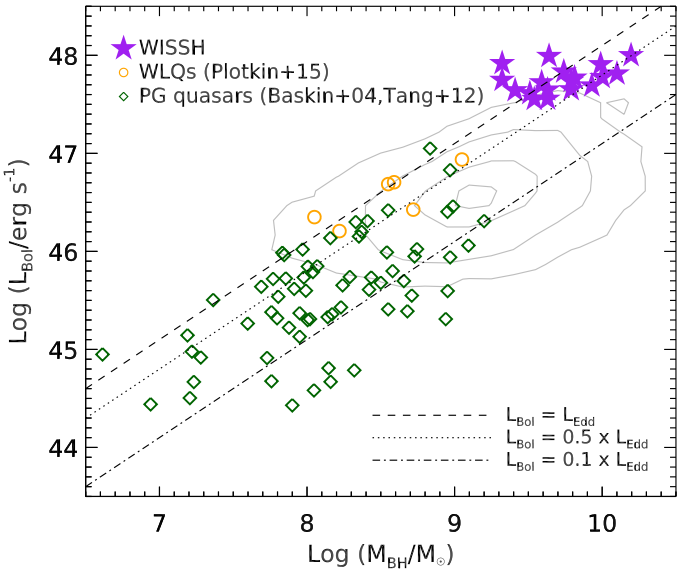

Figure 5.3. Bolometric luminosity as a function of BH mass for the WISSH sample, compared to PG quasars from Tang *et al.* (2012) and Baskin & Laor (2004) and WLQs from Plotkin *et al.* (2015). Luminosity in fractions of 0.1, 0.5 and 1 Eddington Luminosity are respectively indicated with dot-dashed, dotted and dashed lines. Contours levels (0.01, 0.1, 0.5, and 0.9 relative to the peak) refer to SDSS DR7 quasars from Shen *et al.* (2011).

Hα, Hβ, MgII or CIV, depending on the redshift (McGill *et al.* 2008; Trakhtenbrot & Netzer 2012; Matsuoka *et al.* 2013). As mentioned in Sect. 4.2, the CIV emission line is affected by the presence of non virialized components (Baskin & Laor 2005; Richards *et al.* 2011) which can bias the BH mass estimation. The Hβ clouds are mostly dominated by virial motions, ascribing this emission line as the best estimator of the SMBH mass (Denney 2012). In order to estimate M_{BH}, we used SE relation for Hβ reported in Bongiorno *et al.* (2014), i.e.

$$\mathrm{Log}(M_{BH}/M_{\odot}) = 6.7 + 2 \times \mathrm{Log}\left(\frac{\mathrm{FWHM}}{10^3\ \mathrm{km\ s^{-1}}}\right) + 0.5 \times \mathrm{Log}\left(\frac{\lambda L_{\lambda}}{10^{44}\ \mathrm{erg\ s^{-1}}}\right) \quad (5.1)$$

For each quasar, we used the best-fit value of the FWHM of the broad component of Hβ line derived in Sect. 4 (see Table 4.1) and the continuum luminosity at 5100 Å obtained from broad-band multi-component SED fitting (Duras et al. in prep). We list the results of Hβ-based M_{BH} for all the WISSH quasars with rest-frame optical spectroscopy in Table 5.1. [1]

We found that all the BHs have masses larger than 10^9 $M_{\odot}$, with 9 out of 18 quasars hosting SMBHs with $M_{BH} \gtrsim 5 \times 10^9$ $M_{\odot}$. Based on these Hβ-based M_{BH} values and bolometric luminosities, derived from broad-band multi-component SED fitting (Duras et al. in prep), we derived Eddington ratios $\lambda_{edd} = 0.4 - 3.1$ (with a median value of 1). Fig. 5.3 shows the comparison of the M_{BH}, L_{Bol} and λ_{edd} measured for WISSH quasars with those derived from (i) a sample of ~23,000 SDSS quasars with $1.5 \leq z \leq 2.2$ with MgII-based M_{BH} (Shen *et al.* 2011, contour lines), hereafter "SDSS sample", (ii) the $z < 0.5$, bright PG quasars with Hβ-based M_{BH} (Tang *et al.* 2012; Baskin & Laor 2004, green diamonds) and (iii) the WLQs with Hβ-based M_{BH} from Plotkin *et al.* (2015) (orange circles). The luminosity in fraction of 0.1, 0.5 and 1 Eddington Luminosity is reported. The WISSH quasars are therefore powered by highly accreting SMBHs at the heaviest end of the M_{BH} function and allow to probe the extreme AGN accretion regime and the impact of this huge radiative output on the properties of the nuclear region and the surrounding host galaxy.

5.3 Properties of the CIV emission line

5.3.a CIV velocity shift

Previous works have found that the CIV emission line typically shows a velocity blueshift with respect to the systemic redshift (Gaskell 1982), suggesting it is associated with outflowing gas in the BLR (see Sect. 1.4.a for a discussion about the CIV winds). As already mentioned in Sect. 4.2, for the WISSH objects we

[1] The error associated to the $M_{BH}^{H\beta}$ and M_{BH}^{CIV} includes both the statistical uncertainties and the systematic uncertainty in the virial relation itself (~ 0.3 dex, see Bongiorno *et al.* , 2014, for a complete discussion)

Table 5.1. The following information is listed: (1) SDSS ID, (2) Logarithm of intrinsic luminosity at 5100 Å , (3) Hβ-based SMBH mass (in units of 10^9 $M_\odot$), (4) CIV-based SMBH mass listed in Shen *et al.* (2011) (in units of 10^9 $M_\odot$), (5) Logarithm of bolometric luminosity (Duras et al. 2017, in prep), and (6) Eddington ratio

SDSS Name	Log L_{5100}	$M_{BH}^{H\beta}$	M_{BH}^{CIV}	Log L_{Bol}	λ_{Edd}
(1)	(2)	(3)	(4)	(5)	(6)
J0745+4734	47.3	15.7±10.8	8.7±6.0	48.0[48.2][a]	$0.5^{+0.5}_{-0.3}$
J0801+5210	47.1	6.2±4.3	38.9±26.9	47.8	0.7±0.5
J0900+4215	47.2	2.1±1.5	6.6±4.6	48.0[48.1][a]	$3.1^{+0.6}_{-2.2}$
J0958+2827	46.9	3.5±2.4	33.9±23.4	47.6	0.8±0.6
J1106+6400	47.0	10.0±6.9	19.1±13.2	47.8	0.5±0.3
J1111+1336	47.0	8.5±5.9	21.9±15.1	47.7	0.5±0.3
J1157+2724	47.0	2.6±1.8	2.1±1.5	47.6	1.3±0.9
J1201+0116	47.0	3.2±2.3	19.9±13.8	47.6	1.0±0.7
J1201+1206	47.1	6.5±4.5	6.2±4.3	47.8[47.9][a]	$0.7^{+0.3}_{-0.5}$
J1236+6554	47.0	4.3±3.0	22.9±15.8	47.7	0.8±0.6
J1326-0005	47.0	2.1±1.6	0.11±0.08	47.8[48.3][a]	$2.1^{+0.7}_{-1.6}$
J1421+4633	47.0	6.2±4.3	25.1±17.4	47.7	0.6±0.4
J1422+4417	47.3	4.4±3.1	28.2±19.5	48.0	1.8±1.3
J1521+5202	47.2	9.98±6.8	9.9±6.8	47.9	0.7±0.5
J1538+0855	47.1	5.5±3.8	10.5±7.3	47.8[47.8][a]	$1.0^{+0.8}_{-0.7}$
J1549+1245	47.1	12.6±8.7	1.9±1.3	47.8[47.9][a]	$0.4^{+0.9}_{-0.3}$
J2123-0050	47.0	3.9±2.7	20.4±14.1	47.7	1.1±0.7
J2346-0016	46.8	4.3±3.0	17.4±12.0	47.5	0.7±0.2

[a] [..] refers to Bolometric Luminosity corrected for orientation effect

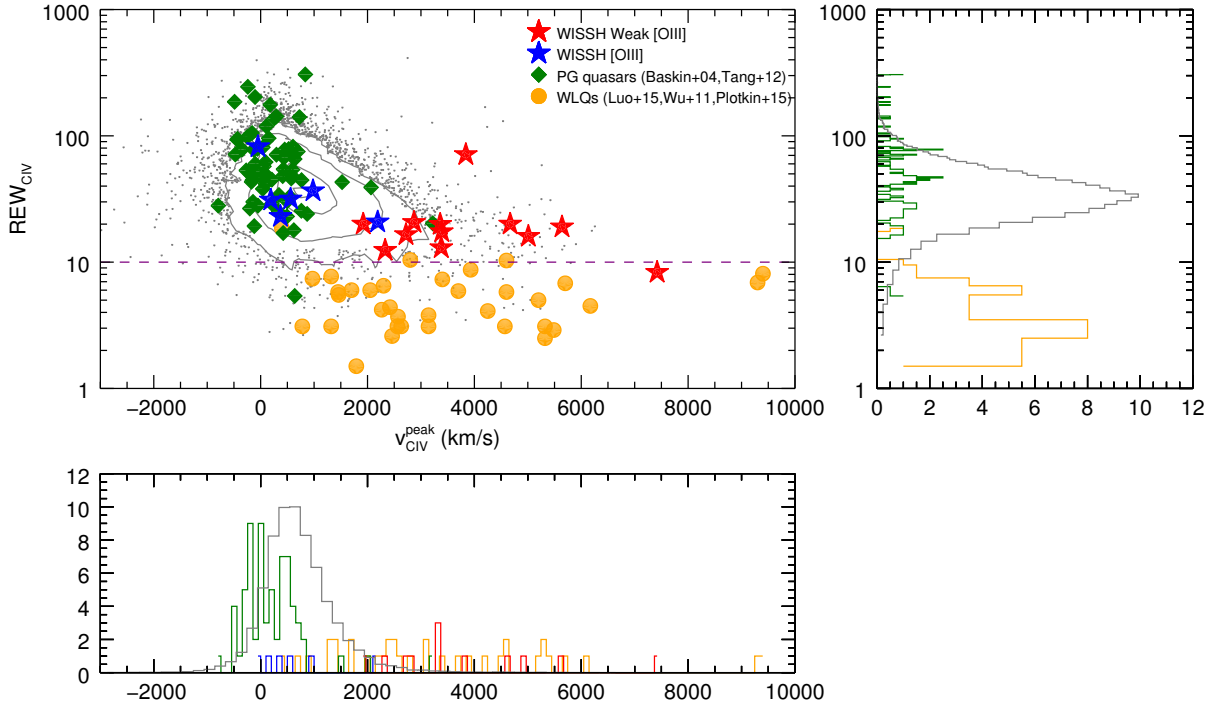

Figure 5.4. REW$_{CIV}$ as a function of v_{CIV}^{peak} for different samples. The WISSH quasars are indicated by blue and red stars, for *[OIII]* and *Weak [OIII]* samples respectively. Contours levels (0.03, 0.1, 0.5, and 0.9 relative to the peak) refer to the SDSS DR7 sample from Shen *et al.* (2011). The green diamonds indicate the PG quasars from Baskin & Laor (2004) and Tang *et al.* (2012). The orange circles refer to the sample of WLQs from Plotkin *et al.* (2015), Luo *et al.* (2015) and Wu *et al.* (2011). The purple dashed line marks the REW$_{CIV}$ = 10 Å , which is the threshold for the WLQs. The distribution of the REW$_{CIV}$ and v_{CIV}^{peak} are on the right and on the bottom, respectively.

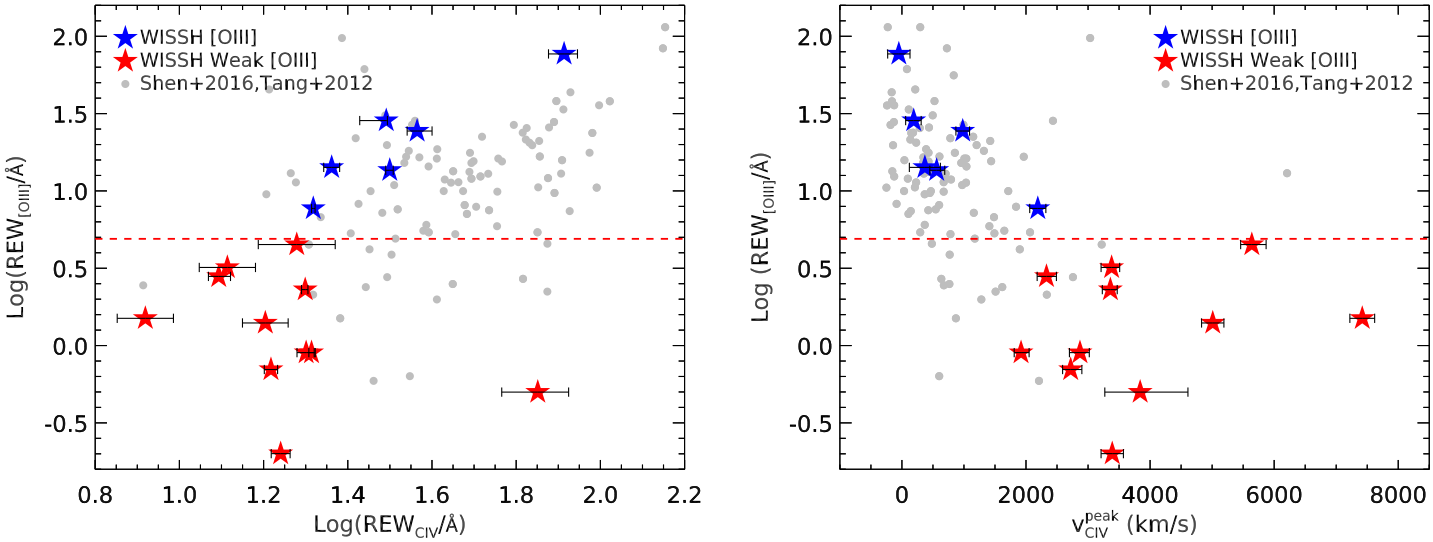

Figure 5.5. Rest-frame EW of [OIII]λ5007 as a function of REW$_{CIV}$ (*left*) and v$_{\rm CIV}^{\rm peak}$ (*right*) for the WISSH targets (i.e. blue stars for the *[OIII]* sample and red stars for the *Weak [OIII]* sample), compared to the Shen (2016a) and Tang *et al.* (2012) samples. The dashed red line refers to the WISSH [OIII] dichotomy, with REW$_{[OIII]}$ boundary value of 5 Å.

measured the CIV velocity shifts (v$_{\rm CIV}^{\rm peak}$) from the peak of the entire CIV emission line model fit with respect to the systemic redshift (similar approach is used in the work of Shen *et al.* (2011) for "SDSS sample").

Fig. 5.4 indicates an anti-correlation between the v$_{\rm CIV}^{\rm peak}$ and the strength of the CIV emission line for the WISSH quasars. This result was already reported by previous studies, e.g. Corbin & Boroson (1996); Richards *et al.* (2002).

We compare our findings with those derived for the SDSS sample [2] (contours), PG quasars (Tang *et al.* 2012; Baskin & Laor 2004), and WLQs and PHL1811-analogs (Plotkin *et al.* 2015, Luo *et al.* 2015 and Wu *et al.* 2011). Remarkably, *Weak [OIII]* WISSH quasars show extreme velocity shifts, comparable to the largest v$_{\rm CIV}^{\rm peak}$ reported so far in WLQs. Interestingly, while WLQs show the distinctive property of a REW$_{CIV} \leq$ 10 Å, the WISSH sample have a REW$_{CIV} \geq$ 10 Å, demonstrating the existence of high-velocity outflows traced by high-ionization species also in sources with higher REW$_{CIV}$ than those of the WLQs.

In Fig. 5.5 the REW$_{\rm [OIII]}$ as a function of the REW$_{CIV}$ (*left*) and v$_{\rm CIV}^{\rm peak}$ (*right*) is shown for the WISSH QSOs. We considered the core and broad components of the [OIII] emission line for the WISSH sources with fixed values of REW$_{[OIII]}$ and the broad component alone for the WISSH objects having upper limits on the [OIII] core component (see Sect. 4.1 about results of [OIII] spectral analysis).

[2] We used the improved redshift estimates of Hewett & Wild (2010), derived using emission lines not including the CIV.

We discovered an intriguing dichotomy between *[OIII]* sample, which shows small values of v_{CIV}^{peak} ($\lesssim$ 2000 km s^{-1}) with REW$_{CIV} \geq$ 20 Å and *Weak [OIII]* sample, exhibiting v_{CIV}^{peak} $\gtrsim$ 2000 km s^{-1} with REW$_{CIV} \leq$ 20 Å. This is also supported by the same behaviour shown by the quasars in the Shen (2016a) and Tang *et al.* (2012) samples, which populate the same region of the plane REW$_{[OIII]} - v_{CIV}^{peak}$. This dichotomy can be likely interpreted assuming a polar geometry for the CIV winds, where the bulk of the emission is along the polar direction, against *[OIII]* quasars which are supposed to be viewed at high inclination.

We also investigated the possible relation between the v_{CIV}^{peak} with the FWHM of the broad emission lines, i.e. CIV and Hβ, by combining WISSH quasars with other samples in Fig. 5.6 (*top*) . For this purpose we used 84 SDSS quasars at 1.5 < z < 3.5 with available Hβ information (67 sources from Shen 2016b, Shen & Liu 2012 and 17 objects from Coatman *et al.* 2016), 44 radio-quiet non-BAL PG quasars from Baskin & Laor (2004) and Tang *et al.* (2012), 6 WLQs from Plotkin *et al.* (2015) with z ∼ 1.4 – 1.7. All these objects cover a luminosity range Log(L$_{bol}$/erg s^{-1}) = 44.5 – 48. We refer to these samples as "Hβ sample". As expected, sources with large v_{CIV}^{peak} ($\gtrsim$ 2,000 km s^{-1}) show a CIV emission line with a broad profile ($\gtrsim$ 6,000 km s^{-1}). This suggests that for these sources the line profile is likely the result of the combination of virialized component plus a strongly outflowing one. Fig. 5.6 (*bottom panel*) shows the behaviour of the FWHM of the outflow component of the CIV emission line resulting from our multi-component fit (see Sect. 4.2) as a function of the v_{CIV}^{peak} . Performing the Spearman rank correlation we found r = 0.6 and P-value = 5.2× 10^{-3}, indicating that a large width of this spectral component can be indeed considered as a proxy of the presence of high velocity outflows.

No clear trend is found between the FWHM$_{H\beta}$ and the v_{CIV}^{peak}, as shown in Fig. 5.7. Interestingly, the WISSH QSOs show the FWHM$_{H\beta} \geq$ 4000 km s^{-1}, even for those sources with large v_{CIV}^{peak}, while previous works claimed the presence of large v_{CIV}^{peak} in quasars with FWHM$_{H\beta}$ < 4000 km s^{-1}, i.e. the so-called Population A (Sulentic *et al.* 2011, 2007; Marziani *et al.* 2010, 2016) and WLQs (Plotkin *et al.* 2015). This indicates that the inclusion of quasars with extreme luminosities as the WISSH ones put no limits on the FWHM$_{H\beta}$ for the presence of large CIV blueshifts.

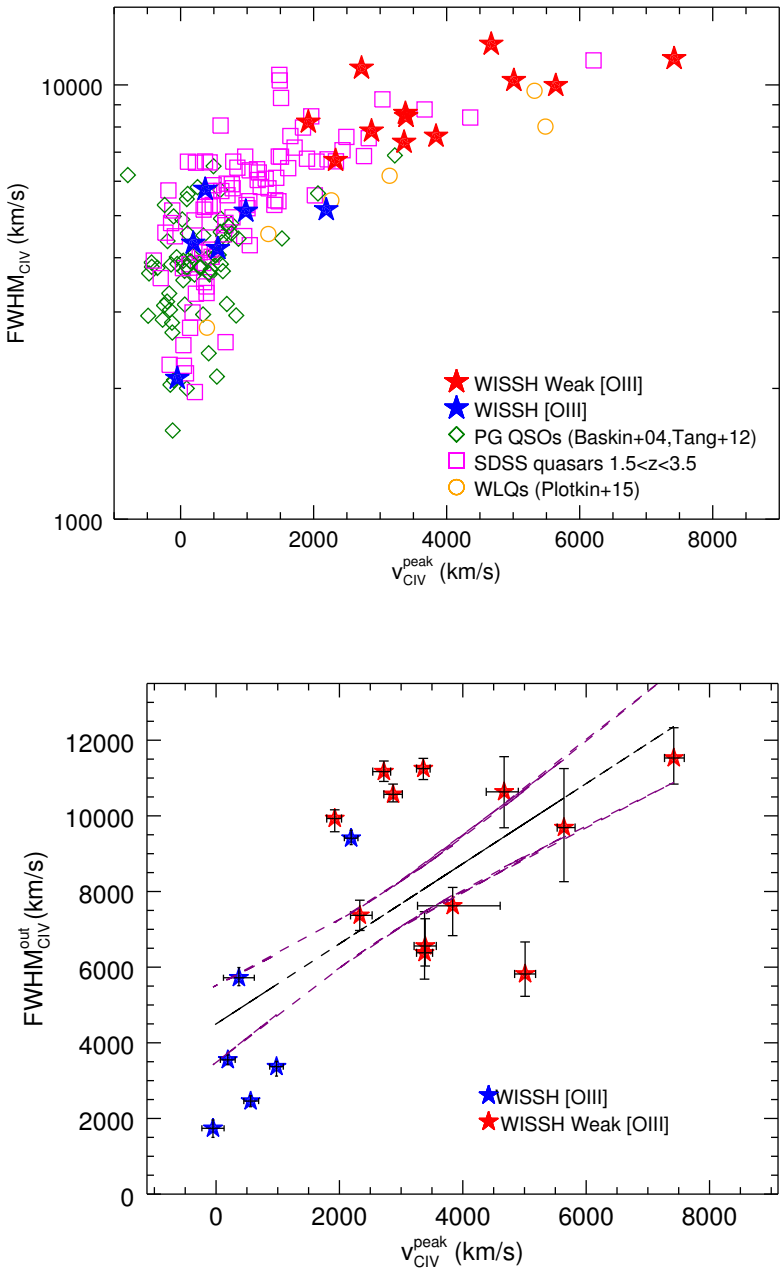

Figure 5.6. (*top*) FWHM$_{CIV}$ of the entire emission line profile as a function of v_{CIV}^{peak} for the WISSH sample, compared to PG QSOs from Baskin & Laor (2004) and Tang *et al.* (2012) (green diamonds), WLQs from Plotkin et al 2015 (orange circles) and SDSS quasars from Shen (2016a) and Coatman *et al.* (2016) (magenta squares). (*bottom*) FWHM(CIV) of the outflow component , as a function of v_{CIV}^{peak} for the WISSH sample. The black line indicates the best linear fits to the data and the purple lines are its 1 standard deviation error.

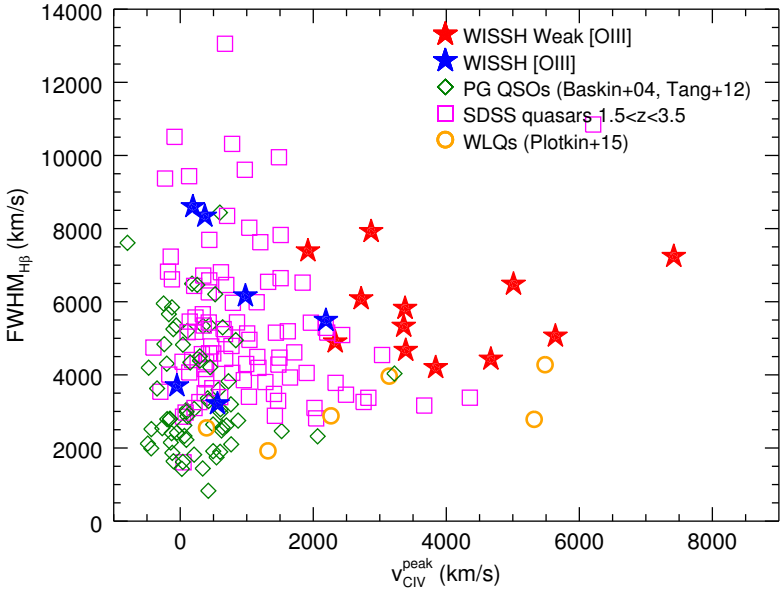

Figure 5.7. FWHM(Hβ) as a function of v_{CIV}^{peak} for the WISSH sample, compared to PG QSOs from Baskin & Laor (2004) and Tang et al. 2012 (green diamonds), WLQs from Plotkin et al 2015 (orange circles) and SDSS quasars from Shen (2016a) and Coatman *et al.* (2016) (magenta squares).

5.3.b Mass and kinetic power of CIV winds

We estimated the ionized gas mass (M_{out}^{ion}) of the outflow associated to the outflow component of the CIV emission line for the *Weak [OIII]* sources according to the following formula from Marziani *et al.* (2016). This relation assumes a constant density scenario for the CIV emitting gas (i.e., $n(C^{3+})/n(C) = 1$) and takes into account the carbon abundance:

$$M_{ion} = 9.5 \times 10^2 \times L_{45}(CIV) \times Z_5^{-1} \times n_9^{-1}\ (M_\odot) \tag{5.2}$$

where L_{45}(CIV) is the luminosity of the outflow component in units of 10^{45} erg s^{-1}, Z_5 is the metallicity in units of 5 $Z_\odot$ (i.e. the typical value measured for the BLR in high-z luminous quasars, Nagao *et al.* 2006) and n_9 is the gas density in units of 10^9 cm^{-3}. For the *Weak [OIII]* sample we estimated M_{ion} =150 – 1100 $M_\odot$, assuming $Z = 5\ Z_\odot$ and $n = 10^{9.5}$ cm^{-3} (see Table 5.2). From equation (5.2) it is possible to derive the mass outflow rate ($\dot{M}_{out}^{ion}$), i.e. the mass of ionized gas passing through a sphere of radius R:

$$\dot{M}_{ion} = 3 \times (M_{ion} \times v)/R_1\ (M_\odot\ yr^{-1}) \tag{5.3}$$

where $v = v_{CIV}^{out}$ and R_1 is the outflow radius in units of 1 pc. The BLR radius-luminosity relation ($R_{BLR} \propto L_{5100}^{0.5}$, e.g. Bentz *et al.* 2009), indicates a typical radius of $\sim$ 1 pc for the WISSH quasars with luminosity $L_{5100} > 6 \times 10^{46}$ erg s^{-1}. We inferred $\dot{M}_{out}^{ion}$ in the range $\approx$ 3 – 30 $M_\odot\ yr^{-1}$, which is similar to the accretion rate for a quasar with L_{Bol} corresponding to the median L_{Bol} of the WISSH range, i.e. $\sim$ 70 $M_\odot yr^{-1}$ for $L_{Bol} = 4 \times 10^{47}$ erg s^{-1}, assuming a radiative efficiency of 10%. Accordingly, the kinetic power of the outflow can be expressed as:

$$\dot{E}_{kin} = \frac{1}{2}\,\dot{M} \times v^2\ (erg\ s^{-1}) \tag{5.4}$$

The resulting values of $\dot{E}_{kin}$ associated to the outflow component as a function of L_{Bol} are plotted in Fig. 5.8 as red filled symbols for objects in the *Weak [OIII]* sample.

Since the *[OIII]* quasars also show an outflow component of the CIV emission (see Fig. 4.1), we were able to provide an estimate of M_{out}^{ion}, $\dot{M}_{out}^{ion}$ and $\dot{E}_{kin}$ also for them. Moreover, as discussed in Sect. 5.1, *[OIII]* quasars are supposed to be viewed at high inclination. Accordingly, we estimated $\dot{M}_{out}^{ion}$ and $\dot{E}_{kin}$ by assuming the so-called maximum velocity $v_{CIV}^{max} = v_{CIV}^{out} + 2\times\sigma_{CIV}^{out}$, where σ_{CIV}^{out} is the velocity dispersion of the outflow component, taking into account projection effects and can be indeed considered representative of the bulk velocity of the outflow in case of biconically symmetric outflowing gas (see Bischetti *et al.* (2017) and references therein). In Fig. 5.8 the $\dot{E}_{kin}$ values associated to the outflow component in *[OIII]* sources are plotted as blue filled stars.

As mentioned in Sect. 4.2, the bulk of virialized component of the CIV emission line is located bluewards 1549 Å in our fits for both the *Weak [OIII]* and (even

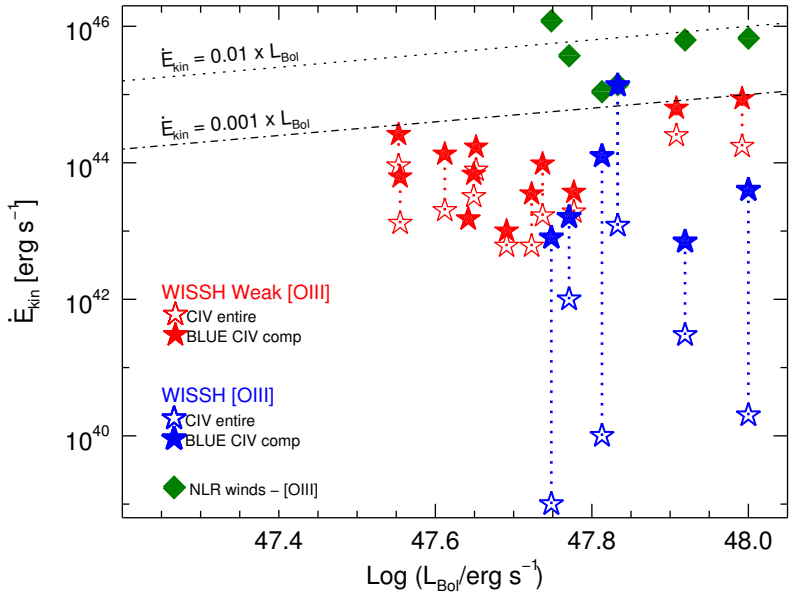

Figure 5.8. Kinetic power of the BLR winds as a function of L_{Bol} . Red filled stars refer to values of $\dot{E}_{kin}$ of the *Weak [OIII]* quasars derived from the CIV outflow component using v_{CIV}^{out}. Blue filled stars refer to values of $\dot{E}_{kin}$ of the *[OIII]* quasars derived from the entire CIV profile using v_{max} . Blue and red empty stars refer to values of $\dot{E}_{kin}$ derived from the entire CIV profile using v_{CIV}^{peak} , for the *[OIII]* and *Weak [OIII]* QSOs, respectively. BLR winds are compared with WISSH NLR ionized outflows from Bischetti *et al.* (2017) (green diamonds).

slightly) *[OIII]* quasars. This means that it can be also associated with an outflow and, therefore, we also derived M_{out}^{ion}, $\dot{M}_{out}^{ion}$ and $\dot{E}_{kin}$ using the formula (2), (3), (4), considering its luminosity in addition to that of the outflow component and adopting v_{CIV}^{peak} in the calculations of the outflow rates (see Table 5.3). The kinetic power derived by considering the entire profile of the CIV emission line are shown in Fig. 5.8 as red and blue empty symbols for the *Weak [OIII]* and *[OIII]* samples, respectively. In the case of *Weak [OIII]* sources they are a factor of $\approx$ 2-10 smaller than the values based only on the luminosity and velocity of the outflow component ($v_{CIV}^{peak} < v_{CIV}^{out}$), due to the $\dot{E}_{kin} \propto v^3$ dependence. In the case of *[OIII]*, the $\dot{E}_{kin}$ calculated in this way are a factor of $\gtrsim$ 100-1000 smaller than those derived by using v_{max}. Accordingly, they can be considered as very conservative estimates of $\dot{E}_{kin}$.

As shown in Fig. 5.8 the bulk of kinetic power of the BLR winds discovered in WISSH quasars is $\dot{E}_{kin} \sim 10^{-5} \times L_{Bol}$ for both *Weak [OIII]* and *[OIII]* quasars. It is instructive to compare these $\dot{E}_{kin}$ with those inferred for ionized NLR winds traced by [OIII]. The 20% of the BLR winds detected in WISSH quasars shows kinetic powers comparable (i.e. $10^{-3} < \dot{E}_{kin} < 10^{-2} \times L_{Bol}$) to those estimated for

Table 5.2. Properties of the CIV outflows derived from the outflow component. The following information are listed: (1) SDSS ID, (2) CIV luminosity (in units of 10^{45} erg s^{-1}), (3) ionized gas mass, (4) velocity of the outflow component, (5) ionized gas mass rate and (6) kinetic power (units of 10^{42} erg s^{-1})

SDSS Name	L_{CIV}	M_{out}^{ion}	$v_{CIV}^{out/max*}$	$\dot{M}_{out}^{ion}$	$\dot{E}_{kin}$
	(10^{45}erg s^{-1})	($M_\odot$)	(km s^{-1})	($M_\odot$ yr^{-1})	(10^{42}erg s^{-1})
(1)	(2)	(3)	(4)	(5)	(6)
J0745+4734†	$1.90^{+0.05}_{-0.03}$	570	4200±100	7.3	40
J0801+5210	2.6±0.1	770	5100^{+200}_{-100}	11.9	100
J0900+4215†	1.4±0.1	420	2600^{+100}_{-200}	3	7
J0958+2827	0.7±0.2	220	10700^{+1400}_{-1000}	7	260
J1106+6400	2.3±0.1	690	3800±200	8	40
J1111+1336	2.6±0.2	780	2400±200	6	10
J1157+2724	0.9±0.1	270	3800^{+700}_{-600}	3	15
J1201+0116	0.5±0.1	150	9800^{+500}_{-300}	4	130
J1201+1206†	1.1±0.1	340	3600^{+100}_{-200}	4	20
J1236+6554	2.4±0.1	710	4600^{+200}_{-100}	10	68
J1326-0005†	6.9±0.1	2090	1600±200	10	8
J1421+4633	0.5±0.1	160	10400^{+500}_{-300}	5	170
J1422+4417	3.7±0.1	1100	9400^{+400}_{-700}	31	870
J1521+5202	1.1±0.1	330	12600^{+1500}_{-700}	13	630
J1538+0855†	1.9±0.1	585	13400±300	24	1360
J1549+1245†	$3.8^{+0.2}_{-0.3}$	1070	5200^{+300}_{-200}	16	125
J2123-0050	1.2±0.1	350	4700^{+300}_{-200}	5	35
J2346-0016	0.5±0.1	150	7600^{+500}_{-300}	3	62

* We used v_{CIV}^{out} and v_{CIV}^{max} in the calculation of the outflow properties of the *Weak [OIII]* and *[OIII]* quasars respectively (see Sect. 5.3.b).

† *[OIII]* WISSH quasars

Table 5.3. Properties of the CIV outflows derived from the CIV entire profile. The following information are listed: (1) SDSS ID, (2) CIV luminosity (in units of 10^{45} erg s^{-1}), (3) ionized gas mass, (4) velocity shift, (5) ionized gas mass rate and (6) kinetic power (units of 10^{42} erg s^{-1})

SDSS Name	L_{CIV} (10^{45}erg s^{-1})	M_{out}^{ion} ($M_\odot$)	v_{CIV}^{peak} (km s^{-1})	$\dot{M}_{out}^{ion}$ ($M_\odot$ yr^{-1})	$\dot{E}_{kin}$ (10^{42}erg s^{-1})
(1)	(2)	(3)	(4)	(5)	(6)
J0745+4734	$8.3^{+0.2}_{-0.1}$	2500	200±100	2	0.02
J0801+5210	2.9±0.1	860	2700±200	7	17
J0900+4215	$6.4^{+0.3}_{-0.2}$	1940	600±100	3	0.3
J0958+2827	1.7±0.2	520	5600±200	9	90
J1106+6400	2.8±0.1	840	2900±200	7	19
J1111+1336	3.0±0.2	900	1900±100	5	6
J1157+2724	0.9±0.1	270	3800^{+700}_{-600}	3	15
J1201+0116	1.8±0.1	540	3400±100	6	20
J1201+1206	$4.4^{+0.2}_{-0.1}$	1350	1000±100	4	1
J1236+6554	2.9±0.1	870	3400±100	9	32
J1326-0005	17±2	4990	-50^{+200}_{-100}	1	0.001
J1421+4633	2.1±0.2	640	5000^{+300}_{-100}	10	78
J1422+4417	5.9±0.1	1780	4700±200	25	174
J1521+5202	2.1±0.1	620	7400±200	14	250
J1538+0855	4.0±0.1	1210	2200±100	8	12
J1549+1245	$3.8^{+0.2}_{-0.3}$	1130	400^{+300}_{-200}	1	0.01
J2123-0050	1.7±0.1	520	2300±200	4	6
J2346-0016	1.2±0.1	350	3400^{+100}_{-200}	4	13

NLR winds in *[OIII]* sources (green diamonds). Remarkably, in one case, i.e. J1538, the outflows associated to CIV and [OIII] have consistent $\dot{E}_{kin}$ values (see Appendix A). This would suggest that we are possibly revealing the same outflow in two different gas phases at increasing distance from the AGN (in an energy conserving scenario). This further supports the idea that this object represents a hybrid showing a mixture of the distinctive properties of the two populations of *Weak* and *[OIII]* quasars, suggesting not a clear dichotomy between the two samples but a continuous correlation.

Hereafter, we consider the outflow parameters derived by using v_{CIV}^{out} and v_{max} for the *Weak [OIII]* and the *[OIII]* quasars, respectively, as the most representative ones. Fig 5.9 shows a comparison of $\dot{E}_{kin}$ as a function of L_{Bol} between the NLR and BLR winds revealed in WISSH quasars and a large collection of [OIII]-based NLR winds from a heterogeneous AGN sample reported in Fiore *et al.* (2017). A sizable fraction of BLR winds in *Weak [OIII]* and *[OIII]* quasars are as powerful as NLR winds in less luminous quasars, with $\dot{E}_{kin} < 10^{43-44}$ erg s^{-1}. This suggests that BLR winds should be taken into account to obtain a complete census of strong AGN-driven winds and comprehensively evaluate their effects of depositing energy and momentum into the ISM.

In order to give an idea of the possible uncertainties affecting the calculations of $\dot{E}_{kin}$, in Fig. 5.9 we show the maximum and minimum values obtained by considering a very large range of variation for the two fundamental parameters n_e and Z. More specifically, the lower bound corresponds to the assumption of $n_e = 10^{10}$ cm^{-3} based on the presence of the semiforbidden line CIII]λ1909 Å (Ferland & Elitzur 1984), and $Z = 8\ Z_\odot$ (Nagao *et al.* 2006), while the upper bound corresponds to the assumption of n_e=10^9 cm^{-3}, based on the absence of forbidden lines such as [OIII]λ4363 Å (Ferland & Elitzur 1984) and $Z = 3\ Z_\odot$ (Nagao *et al.* 2006).

Fig. 5.10(upper panel) displays the outflow momentum load (i.e. the outflow momentum rate $\dot{P}_{out}$ ($\equiv \dot{M}_{out} \times v_{out}$) normalized to the AGN radiation momentum rate $\dot{P}_{AGN} \equiv L_{Bol}/c$) as a function of outflows velocity for different classes of outflow derived by Fiore *et al.* (2017), compared to those measured for the winds traced by the blueshifted CIV emission line in WISSH. The BLR winds in WISSH show velocities between those measured for X-ray Ultra-Fast ($v > 10^4$ km s^{-1}) outflows (UFOs, crosses) and [OIII]-based outflows ($v < 2000$ km s^{-1}, triangles). This matches well with interpreting the outflow velocity distribution as a proxy of the distribution in radial distance from the AGN, i.e. from the innermost region of the accretion disk (tens of gravitational radii for the UFOs, e.g. Nardini *et al.* 2015; Tombesi *et al.* 2012, 2013b; Gofford *et al.* 2015) up to kpc-scale in case the [OIII] winds (e.g. Harrison *et al.* 2012; Carniani *et al.* 2015; Cresci *et al.* 2015; Bischetti *et al.* 2017). In Fig. 5.10(lower panel) a schematic representation of different AGN regions at different physical scales is shown.

The BLR winds typically exhibit a low momentum load, i.e $\dot{P}_{out}/\dot{P}_{AGN} \lesssim 0.1$, which is a range poorly sampled by other ionized winds. Furthermore, the BLR winds seem to represent the low-power, low-velocity analogs of UFOs. The latter show $\dot{P}_{out}/\dot{P}_{AGN} \sim 1$, as expected in case of quasi-spherical winds with electron

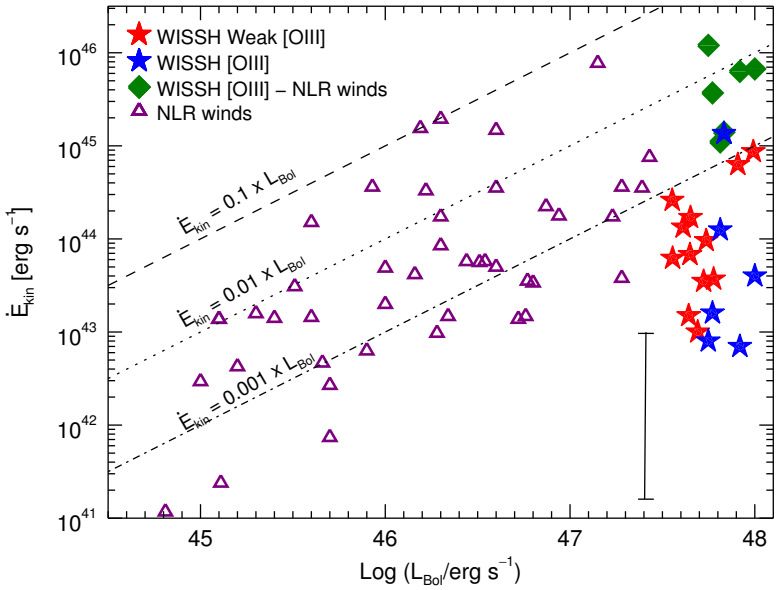

Figure 5.9. Kinetic power of the CIV outflow component as a function of L_{Bol} for the WISSH quasars (red and blue stars) compared with WISSH NLR ionized outflows from Bischetti *et al.* (2017) (green diamonds) and other samples from literature (purple triangles). The error bar (bottom right corner) is calculated as described in Sect. 5.3.b

scattering optical depth $\tau \sim 1$ produced by systems accreting at $\lambda_{Edd} \sim 1$ (e.g. King 2010). UFOs are found to have a large covering factor (Nardini *et al.* 2015; King & Pounds 2015). BLR clouds in luminous AGN are expected to have a covering factor of ~ 0.1 (Netzer 1990). We can thus speculate that the low $\dot{P}_{out}/\dot{P}_{AGN}$ of BLR winds with respect to that of UFOs may be due to both a lower N_H and a lower covering factor of the CIV outflowing gas with respect to the fast highly ionized gas responsible for the UFOs.

5.4 What is the physical driver of the CIV velocity shift?

In order to shed light on the main physical driver of the large blueshifts of the CIV emission line observed in quasars, we investigated the dependence of CIV velocity shift on fundamental AGN parameters such as L_{Bol}, λ_{Edd} and the UV-to-X-ray continuum slope (α_{OX}). Previous studies indeed found that v_{CIV}^{peak} is correlated with all these three quantities (Marziani *et al.* 2016, Richards *et al.* 2011), but it still unclear which is the fundamental dependency. We proceeded as follows: we initially identified the main driver of v_{CIV}^{peak} between L_{Bol} and λ_{Edd} and then we studied the dependency of v_{CIV}^{peak} on this parameter with that on α_{OX}.

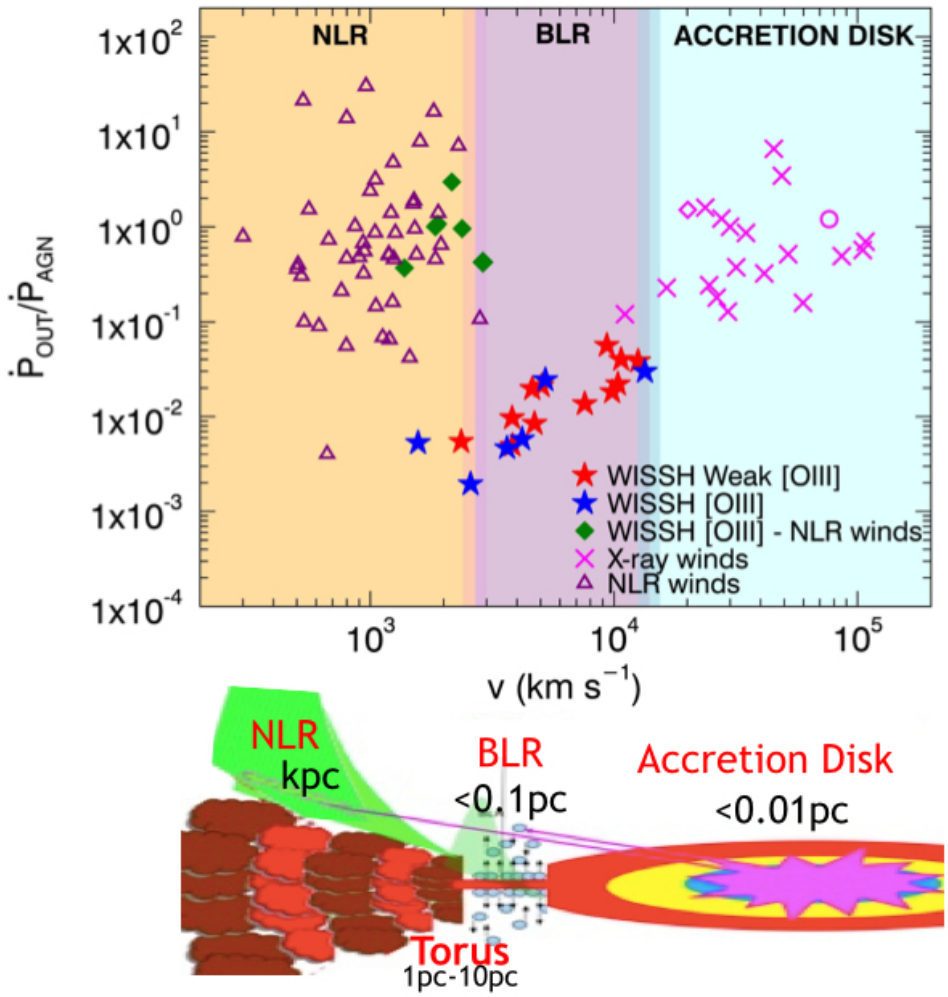

Figure 5.10. (Top panel) Wind momentum load as a function of the outflow velocity. The BLR winds traced by the CIV outflow components from the WISSH quasars (red and blue stars) are compared with X-ray winds (magenta crosses) and Ionized winds (green triangle). X-ray winds for Markarian 231 and IRASF11119+13257 are drawn with magenta square and circle, respectively. (Bottom panel) Schematic representation of different AGN regions at different physical scales (Courtesy by Chris Done)

5.4.a Velocity shifts vs. L_{Bol}, λ_{Edd} and α_{ox}

We compared the WISSH sample to quasars for which the BH mass and Eddington ratio are derived from the Hβ emission line, the "Hβ sample", because of the large uncertainties of BH mass estimation from CIV emission line, affected by non-virialized component. All these sources therefore have reliable SMBH masses and λ_{edd}.

Fig. 5.11 shows v_{CIV}^{peak} as a function of L_{Bol} (a) and λ_{Edd} (b) for the WISSH and the "Hβ sample" quasars. The blueshifts are clearly correlated with both L_{Bol} and λ_{Edd}. Specifically, we found a stronger correlation with L_{Bol} (Spearman rank r = 0.35 and P-value = 8.6×10^{-6}) than with λ_{Edd} (Spearman rank r = 0.23 and P-value= 3.9×10^{-3}), bearing in mind the large scatter affecting both relations.

Moreover, performing a least squares fit, we found that $v_{CIV}^{peak} \propto L_{Bol}^{0.24\pm0.05}$. This is consistent with a radiation-driven wind scenario (Laor & Brandt 2002), for which we indeed expect a terminal outflow velocity $v_t \propto \sqrt{L/R_{\geq BLR}} \propto L^{0.25}$ (Netzer & Laor 1993; Kaspi *et al.* 2000; Bentz *et al.* 2009, see Sect. 1.5 for further details), which is consistent with the slope we measured. A similar dependence is also found for v_{CIV}^{peak} as a function of M_{BH}. This lends further support to the radiative wind scenario and rule out the hypothesis that v_{CIV}^{peak} could be consistent with the Keplerian velocity at the launching radius of the wind, for which a dependence of $\propto M_{BH}^{0.5}$ is expected.

In order to determine which is the fundamental variable between L_{Bol} and λ_{Edd}, we studied correlations between the residuals from (i) λ_{Edd}-L_{Bol} and v_{CIV}^{peak}-L_{Bol} relations and (ii) L_{Bol}-λ_{Edd} and v_{CIV}^{peak}-λ_{Edd} relations (see Appendix B in Bernardi *et al.* 2005 for further details about residuals analysis). More specifically, we tested the hypothesis that the bolometric luminosity is the fundamental variable. In this case we expect that: (i) no significant correlation between the residuals obtained from the λ_{Edd}-L_{Bol} ($\Delta_{\lambda,L}$) and v_{CIV}^{peak}-L_{Bol} ($\Delta_{v,L}$) relations; (ii) a correlation between residuals obtained from L_{Bol}-λ_{Edd} ($\Delta_{L,\lambda}$) and v_{CIV}^{peak}-λ_{Edd} ($\Delta_{v,\lambda}$) relations; (iii) the slope of this correlation should be the same as the v_{CIV}^{peak}-L_{Bol} relation.

The $\Delta_{\lambda,L}$–$\Delta_{v,L}$ residuals are plotted in Fig. 5.11c. In this case we derived a Spearman rank r = 0.07 and P-value = 4.0×10^{-1}, which indicates no correlation between parameters as expected from (i). In Fig. 5.11d the $\Delta_{L,\lambda}$ and $\Delta_{v,\lambda}$ residuals are plotted. In this case we found a strong correlation with a Spearman rank r = 0.31 and P-value = 8.2×10^{-5}, with a slope consistent (2σ) with that we measured for v_{CIV}^{peak}-L_{Bol} relation.

By combining these results, we conclude that L_{Bol} is the fundamental variable with respect to the λ_{Edd} and it can be considered as the main driver of the observed CIV blueshifts with respect to λ_{Edd}.

We have performed the same analysis between L_{Bol} and α_{OX}, to investigated the primary driver of the CIV blueshifts. Fig. 5.12 shows the v_{CIV}^{peak} as a function of L_{Bol} and α_{OX} for 14 WISSH quasars with both Hβ and X-ray detection. The α_{OX} is defined as :

$$\alpha_{OX} = \frac{\mathrm{Log}(L_{2keV}/L_{2500\text{Å}})}{\mathrm{Log}(\nu_{2keV}/\nu_{2500\text{Å}})} \tag{5.5}$$

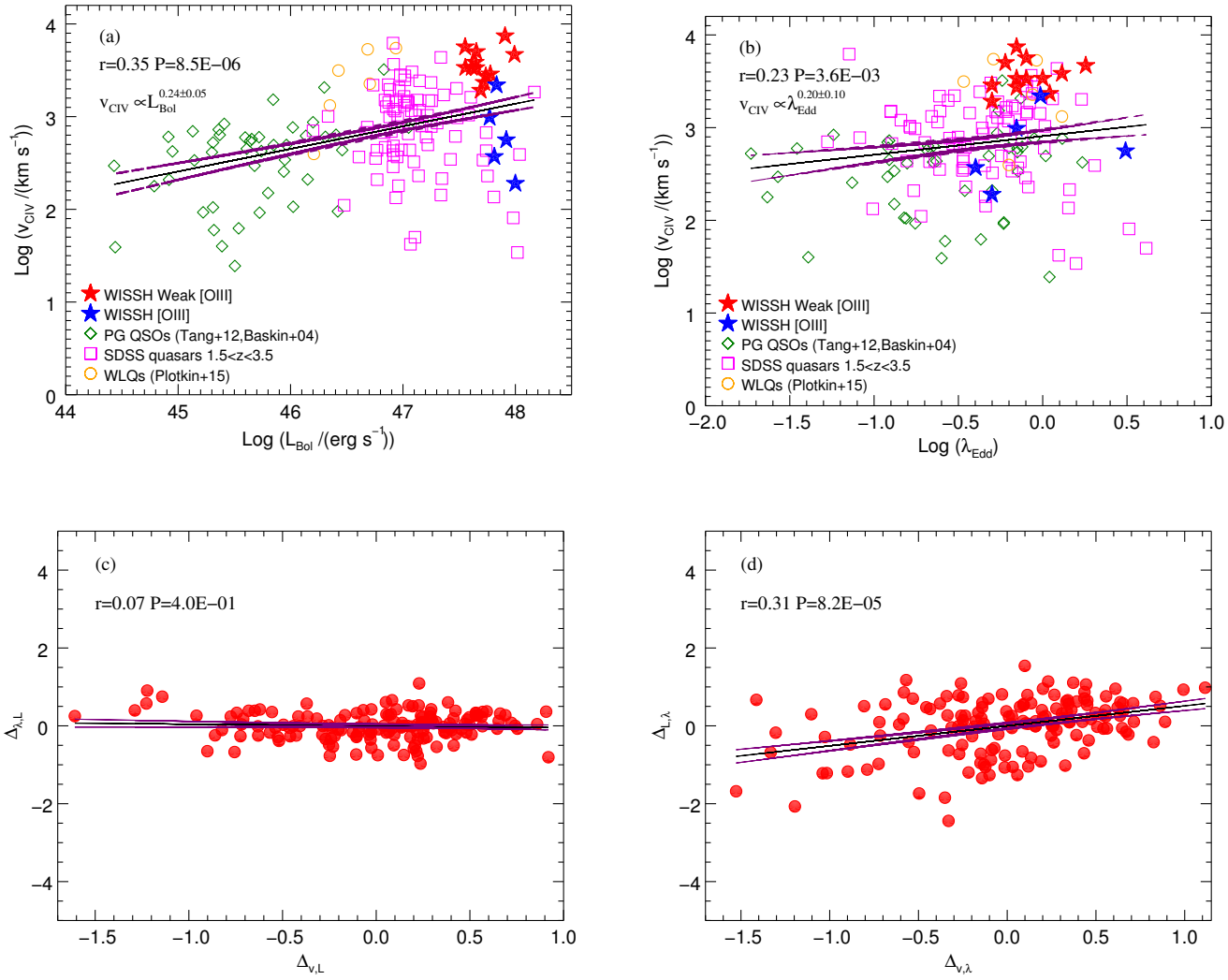

Figure 5.11. v_{CIV}^{peak} as a function of L_{Bol} *(a)* and as a function of λ_{Edd} *(b)*, for the WISSH sample (*blue/red stars*) compared to the PG QSOs from Baskin & Laor (2004) and Tang *et al.* (2012) (green diamonds), WLQs from Plotkin *et al.* (2015) (orange circles) and SDSS quasars from Shen (2016a) and Coatman *et al.* (2016) (magenta squares).*(c)* Residuals plot of λ_{Edd} - L_{Bol} and v_{CIV}^{peak} - L_{Bol} relations. *(d)* Residuals plot of L_{Bol} - λ_{Edd} and v_{CIV}^{peak} - λ_{Edd} relations. The black lines indicates the best linear fits to the data and the purple lines are their 1 standard deviation errors

where L_{2keV} and $L_{2500Å}$ are the luminosities at 2 keV and 2500 Å, respectively. For the WISSH QSOs the α_{OX} was derived using the monochromatic luminosities at 2500 Å obtained from broad-band multi-component SED fitting and the absorption-corrected luminosities at 2 keV (Martocchia *et al.* 2017). We compare our findings with those derived for 187 radio-quiet, broad-line quasars from the Wu *et al.* (2009) sample and 29 WLQs (Luo *et al.* 2015; Wu *et al.* 2011) with available UV and X-ray information.

Performing a least-square fit also for this large sample, we confirm the results about the presence of correlation between v_{CIV}^{peak} and L_{Bol}, deriving a dependence $v_{CIV}^{peak} \propto L_{Bol}^{0.25\pm0.06}$ (Spearman rank r = 0.30 and P-value = 1.1×10^{-5}; see Fig. 5.12a).

As already reported by Richards *et al.* (2011), we found a very strong anti-correlation between the v_{CIV}^{peak} and α_{OX} (Fig. 5.12b), i.e. $v_{CIV}^{peak} \propto \alpha_{OX}^{-1.07\pm0.16}$ (Spearman rank r = -0.46 and P-value = 8.7×10^{-13}).

We also performed the correlations analysis between the residuals from (i) v_{CIV}^{peak}-L_{Bol} ($\Delta_{v,L}$) and α_{OX}-L_{Bol} ($\Delta_{\alpha ox,L}$) relations and (ii) v_{CIV}^{peak}-α_{OX} ($\Delta_{v,\alpha ox}$) and L_{Bol}-α_{OX} ($\Delta_{L,\alpha ox}$) relations, based on the hypothesis that L_{Bol} is the fundamental parameter. However, the results reported in Fig. 5.12c,d are at odds with this hypothesis, indicating a clear anti-correlation between $\Delta_{v,L}$ and $\Delta_{\alpha ox,L}$, and no correlation between $\Delta_{v,\alpha ox}$ and $\Delta_{L,\alpha ox}$. Furthermore the slope of the residuals $\Delta_{v,L}$-$\Delta_{\alpha ox,L}$ is consistent with that found for α_{OX} - v_{CIV}^{peak} relation. From a statistical point of view, this points to α_{OX} as the primary driver of the blueshifts of the CIV emission line observed in these quasars.

We note that there is a well-known strong anti-correlation between α_{OX} and the UV luminosity ($\sim L_{Bol}$ for Type I quasars), (e.g. Vignali *et al.* 2003; Steffen *et al.* 2006; Lusso *et al.* 2010; Martocchia *et al.* 2017) according to which the steeper the α_{OX} the higher the luminosity. Therefore both selecting steep αox or high L_{Bol} allows to pick up fast outflows.

In Table 5.4 a summary of correlations of the CIV velocity shifts with physical quantities as L_{Bol}, λ_{Edd} , M_{BH} and α_{OX} is reported. Results from residuals correlations are also listed.

The dependence of the velocity shift on L_{Bol} and hence on α_{OX} is in agreement with our scenario of radiation driven wind, according to which a strong UV continuum is necessary to launch the wind but the level of Extreme UV (EUV) and X-ray emission (i.e. up to 2 kev) is crucial to determine its existence, since strong X-ray radiation can easily overionize the gas and hamper an efficient line-driving mechanism. On the contrary, an X-ray weaker emission with respect to the optical/UV accretion disk emission can allow UV line opacity (Leighly 2004; Richards *et al.* 2011). Furthermore, as suggested by Wu *et al.* (2009), the increasing steepness of the α_{OX} (i.e. the soften of EUV - X-ray emission) at progressively higher UV luminosities may also explain the weakness of the CIV emission line (ionization potential 64.45 eV) in luminous quasars: the strength of the line indeed depends on the number of the photons available to produce it, whereby a deficit of such ionizing photons leads to CIV weaker emission lines, as typically observed in *Weak [OIII]*

Table 5.4. Correlations of v_{CIV}^{peak} with L_{Bol}, λ_{Edd}, M_{BH} and α_{OX}. Results from residuals correlations are also listed.

Correlation	slope	Spearman Rank	null hyphotesis probability
v_{CIV}^{peak} vs. L_{Bol} [a]	0.24±0.05	0.35	8.5×10^{-6}
v_{CIV}^{peak} vs. λ_{Edd} [a]	0.20±0.10	0.23	3.6×10^{-3}
v_{CIV}^{peak} vs. M_{BH} [a]	0.26±0.06	0.32	7.3×10^{-5}
$\Delta_{\lambda,L}$ vs. $\Delta_{v,L}$ [a]	-0.04±0.06	0.07	4.0×10^{-1}
$\Delta_{L,\lambda}$ vs. $\Delta_{v,\lambda}$ [a]	0.51±0.11	0.31	8.2×10^{-5}
v_{CIV}^{peak} vs. L_{Bol} [b]	0.25±0.06	0.30	1.1×10^{-5}
v_{CIV}^{peak} vs. α_{OX} [b]	-1.07±0.16	-0.46	8.7×10^{-13}
$\Delta_{v,L}$ vs. $\Delta_{\alpha ox,L}$ [b]	-0.97±0.18	-0.38	1.2×10^{-8}
$\Delta_{v,\alpha ox}$ vs. $\Delta_{L,\alpha ox}$ [b]	0.09±0.06	0.07	3.0×10^{-1}

[a] Correlations derived for the WISSH quasars and samples from literature with Hβ detection.

[b] Correlations derived for the WISSH quasars with both Hβ and X-ray detection and samples from literature with available UV and X-ray information.

quasars and WLQs.

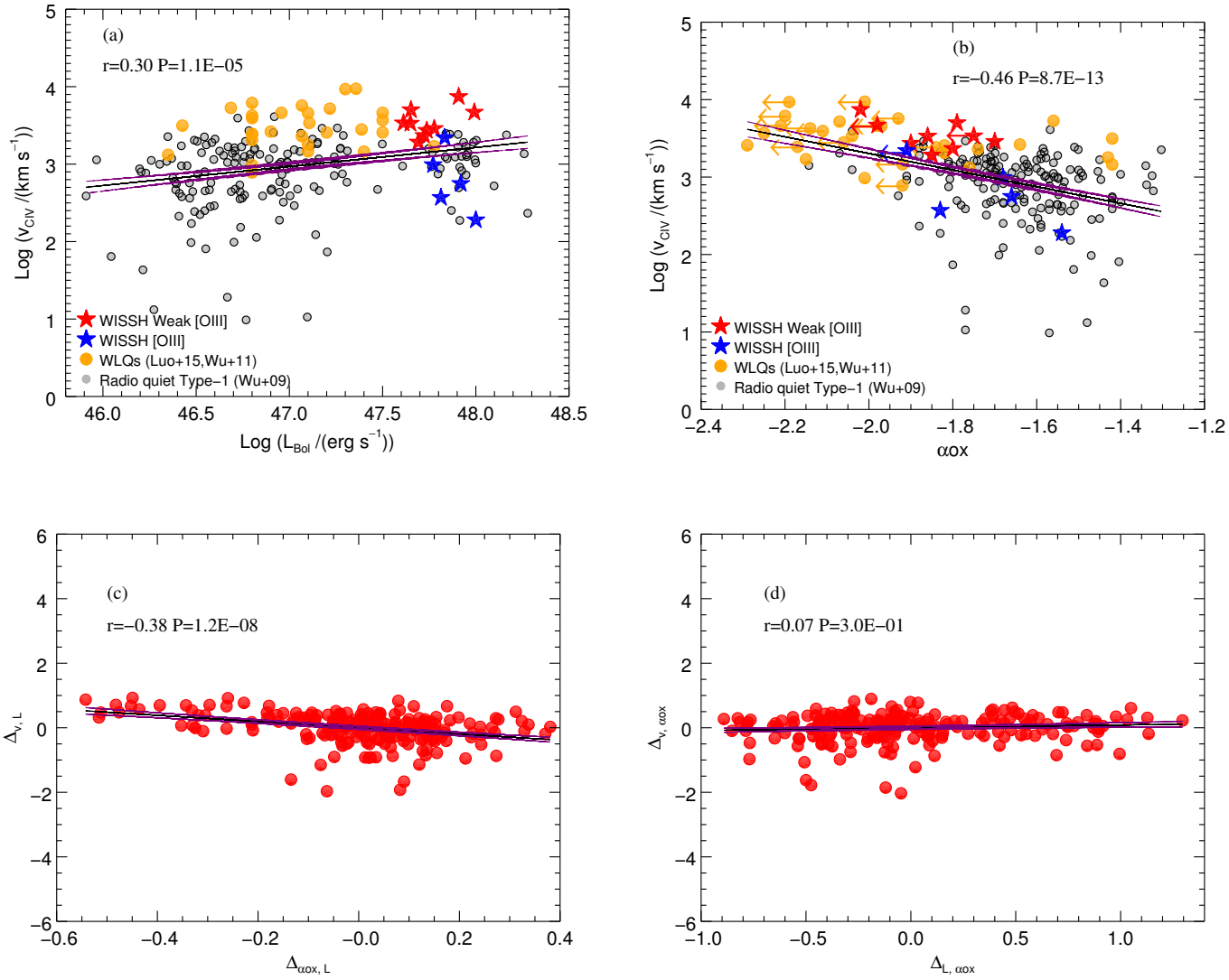

Figure 5.12. v_{CIV}^{peak} as a function of L_{Bol} *(a)* and α_{OX} *(b)*, for the WISSH sample (*blue/red stars*) compared to Radio quiet Type-1 quasars from Wu *et al.* (2009) (black circles) and WLQs from Wu *et al.* (2011) and Luo *et al.* (2015) (orange circles). The BAL quasars in WISSH sample are indicated with circles. *(c)* Residuals plot of v_{CIV}^{peak} - L_{Bol} and α_{OX} - L_{Bol} relations. *(d)* Residuals plot of bolometric v_{CIV}^{peak} - α_{OX} and L_{Bol} - α_{OX} relations. The black lines represent the best linear fits to the data and the purple lines are their 1 standard deviation errors.

Chapter 6

The SUPER survey

6.1 Goals of the project

As discussed in the previous sections, we focus our attention on the most luminous quasars of the WISSH survey, where, according to theoretical models, the efficiency of AGN feedback is maximized. This clearly leads to a selection bias towards those sources which are expected to exhibit powerful outflows.

The *Sinfoni Survey for Unveiling the Physics and Effect of Radiative feedback* (SUPER) was designed to overcome most of selection biases affecting previous studies by a blind search of AGN-driven outflows not selecting a-priori AGNs with already known outflows or with high chances for being in an outflowing phase. This will provide us to have a more comprehensive picture of the general AGN population at high redshift.

This project is based on a VLT-SINFONI large observing program (PI: V. Mainieri (ESO)) with AO capabilities, aimed at carrying out the first statistically-sound investigation of ionized outflows in AGN host galaxy at the peak epoch of AGN and galaxy assembly, i.e. z $\approx$ 2.

The sample has been selected combining the X-ray catalogues from the deep observations in the CDFS (Xue *et al.* 2011) and COSMOS (Brusa *et al.* 2010; Civano *et al.* 2016) with the larger area XMM-XXL survey (Pierre *et al.* 2007). This survey consists on 41 objects both Type I and Type II equally divided in number, with confirmed spectroscopic redshifts and the available multi-wavelength data, which allow to estimate bolometric luminosities, black hole masses, Eddington ratio, SFR and stellar mass.

The targets have bolometric luminosity $L_{Bol} = 10^{44-47.5}$ erg s^{-1} in the redshift range z = 2.12 - 2.49. Specifically it was designed to map the ionized kinematics and the on-going star formation using the Hβ, [OIII]λ5007 (in the H band) and Hα (in the K band) emission lines, with $\sim$ 1 kpc spatial resolution, and if possible, to constrain electron densities using [SII]λ6716,6731.

The L_{Bol} and the column density N_H cover almost four orders of magnitudes as shown in Fig. 6.2. In the right top panel of Fig. 6.1 it is also evident the wide range

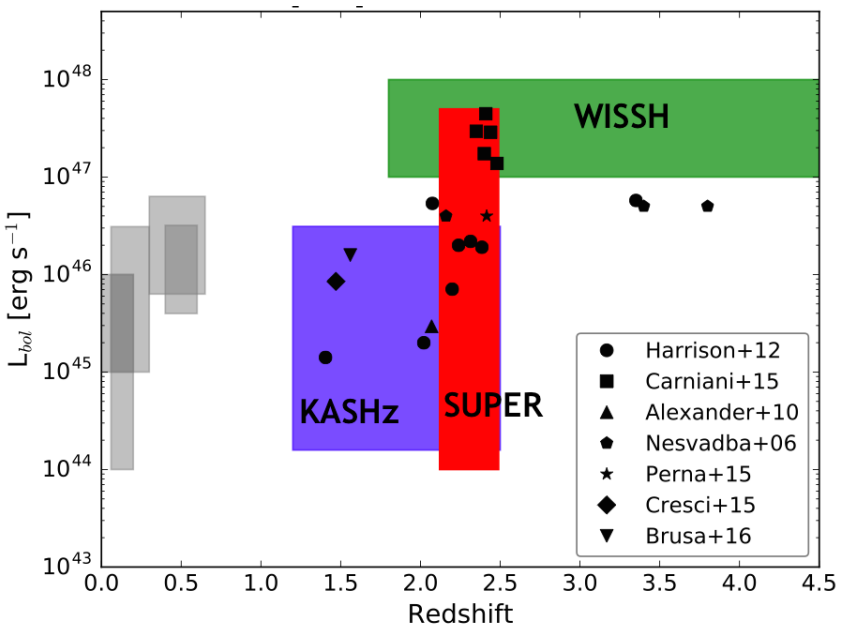

Figure 6.1. Bolometric luminosity as a function of redshift. The red rectangle indicates the SUPER survey location. The WISSH survey is indicated with a green rectangle and the violet rectangle refers to the KMOS AGN survey at high redshift (KASHz, Harrison *et al.* 2016). The samples at z < 1 (grey rectangles) are from Harrison *et al.* (2014), Husemann *et al.* (2013), Liu *et al.* (2013)

of accretion rate probed by SUPER survey for Type-1 quasars, from which it is possible to investigate the outflow properties as a function of $\lambda_{\rm Edd}$. For Type-2 AGNs we have reliable estimates of the stellar masses and SFR thanks to the excellent multi-wavelength coverage, from the UV to the Herschel PACS bands, therefore we can consider this sub-sample when looking at the average properties of the outflows in the SFR-stellar mass plane, as shown in the bottom panel of Fig. 6.2. The area covered by SUPER AGNs is similar to that of covered by the IFU AO observations of inactive galaxies at z ∼ 2 (grey filled squares, Forster et al. in prep.), which will serve as a comparison sample.

The SUPER survey has the aim of deliver tight scaling relations between the frequency, mass, mass outflow rate and momentum rate of ionized outflows, and AGN bolometric luminosity and Eddington ratio, which can be directly plugged into models of galaxy evolution. It represents a major advance in the understanding of the origin of AGN-driven winds and their real impact on the evolution of the host galaxy.

On-going follow-up with Atacama Pathfinder Experiment Telescope (APEX) and ALMA will also provide information about the dense and the diffuse molecular gas, using [CI](2-1), CO(7-6) and CO(3-2) transitions, which allow to make very significant progress in understanding the origin of any difference in the gas content of AGN hosts compared to inactive galaxies.

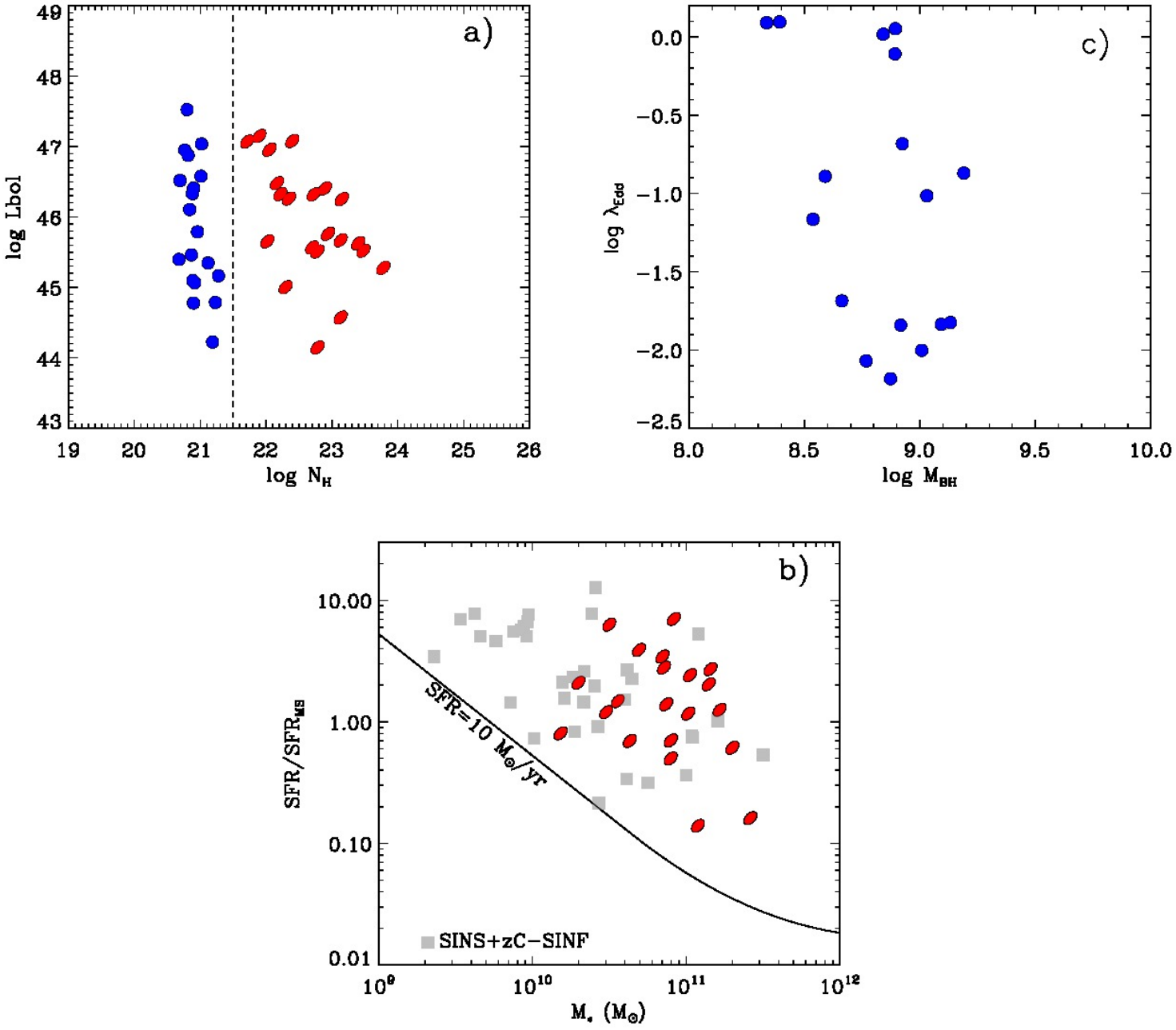

Figure 6.2. (a) Bolometric luminosity as a function of the column density for the SUPER survey. The SUPER AGNs are equally divided in Type 1 and Type 2 and cover almost four orders of magnitudes. (b) Eddington ratio as a function of black hole mass. It is evident the wide range of accretion rate probed by SUPER survey for Type-1 quasars. (c) SFR normalized to the one on the main-sequence as a function of stellar masses for Type 2 quasars of SUPER survey, for which we have reliable estimate of the both quantities. The SUPER targets covered similar area to that covered by IFU AO observations of inactive galaxies at z ∼ 2 (Forster Schreiber et al in prep), which is used as a comparison sample.

6.2 Spatial extension of the NLR outflows with SINFONI: the case of J1549+1245

As a part of the SUPER observing program, the WISSH quasar J1549+1245 was observed with the IFU spectrograph SINFONI at VLT, using the AO capabilities of SINFONI on June 23rd 2016 for the H band and on July 29th 2017 for the K band.

This object has a redshift of z = 2.365, as found by Bischetti *et al.* (2017) analyzing its rest-frame optical LBT/LUCI1 spectrum. From its SDSS spectrum (see 1.23), we know that it is a BAL QSO, with strong absorption through blueward CIV and SiIV emission lines. Moreover this source also shows absorption from metastable iron species as FeII and FeIII, i.e. FeLoBAL QSO, a rare class of BAL quasars which constitute only ∼1% of the BAL quasars and ∼0.3% of the total quasar population (Urrutia *et al.* 2009 and reference therein).

Furthermore it is also a red quasar (Glikman *et al.* 2012), i.e. a class of quasars defined to have NIR colors R - K > 4 and J - K > 1.7. In the context of merger-driven AGN/galaxy co-evolution, this kind of sources are thought to be undergoing a dust-enshrouded phase preceding the standard blue, optically-bright phase. The reddening properties of these types of quasars were analyzed by Glikman *et al.* (2012). They applied four different dust laws in order to find the appropriate one to use for the red quasars by fitting the spectra with the SMC dust law, LMC dust law from Misselt *et al.* (1999), Milky Way dust law of Cardelli *et al.* (1989) and Calzetti *et al.* (1994) dust law for starburst galaxies. In Fig. 6.4 it is shown the UV-to-Optical spectrum of J1549+1245 , with different dust laws superimposed. It it evident the discrepancy between the fits, whereas the SMC dust law produces the most reliable fit to the spectrum.

The NIR/Optical rest-frame SINFONI observations in H and K bands allow us to target both the Hβ+[OIII] and Hα regions. Details about the SINFONI data reduction can be found in Sect. 3.2.b. We extracted a 1D spectrum in the H band with a circular aperture of 1" diameter, which clearly shows the presence of a red wing of the [OIII] emission line (see Fig. 6.5), as previously reported by Bischetti *et al.* (2017). Specifically from the spectral decomposition, a redshifted component ($\sim$ 360 km s^{-1}) with a FWHM[OIII] $\sim$ 1100 km s^{-1}, suggests the presence of a receding outflow in the opposite side with respect to the observer.

We collapsed the datacube in the H band on spectral channels corresponding to the line core. The resulting map is shown in bottom left panel of Fig. 6.5.

In order to look at the extension of this receding outflow, we performed an analysis based on the deblending of the QSO and host galaxy emission using a dedicated software, i.e. QDeblend3D (Husemann *et al.* 2013). The underlying idea of this tool is to treat the spaxels (i.e. spectral pixel) at different location of the datacube as a set of independent spectra. In the absence of atmospheric dispersion, the spectral shape of a point source is the same in each spaxel and the brightness is a function of position with a certain scale factor, which depends on the point spread function (PSF) of the observations. It is possible to derive these scale factors from

the broad line emission profiles, since they trace the central region of the QSOs.

After the PSF subtraction, we collapsed the datacube on the spectral channels corresponding to the redward line wing of the 1D spectrum, as shown in medium right panel of Fig. 6.5. It is clear the detection of ionized material located away from the position of the central quasar (black contours) of up to 5 kpc (1 pixel $\approx$ 0.1 " $\approx$ 0.8 kpc at z =2.365). Furthermore, the gas associated to the wind has a very extended morphology, being very different from that of the core [OIII] emission.

We extracted 1D spectrum at two different position in the datacube, namely A and B in Fig. 6.5, medium and bottom panels. It is evident that the [OIII] emission line with a peak at 5011 Å and 5015 Å, respectively, i.e. redshifted with respect to the systemic redshift with a velocity of 240 km s^{-1} and 480 km s^{-1}.

In Fig. 6.6 is reported the K-band integrated spectrum, extracted with a circular aperture of 1" diameter, where the Hα emission line is the prominent line. The profile is dominated by the broad component due to the BLR emission. We do not find a properly core component, which usually allows to map the star formation. However we collapsed the datacube in the wavelength range corresponding to the Hα peak as shown in Fig. 6.6. As contours indicate, it seems that the narrow Hα, likely tracing the SF, is not affected by the presence of [OIII] outflow. However a more accurate analysis is required in order to assess any strong conclusions. The analysis of the SINFONI data is still preliminary, and will be refined in the next months (Vietri et al. in prep.). Nonetheless, these SINFONI observations clearly emphasize the power of IFU spectroscopy in shedding light how ionized outflows expand into the host galaxy ISM.

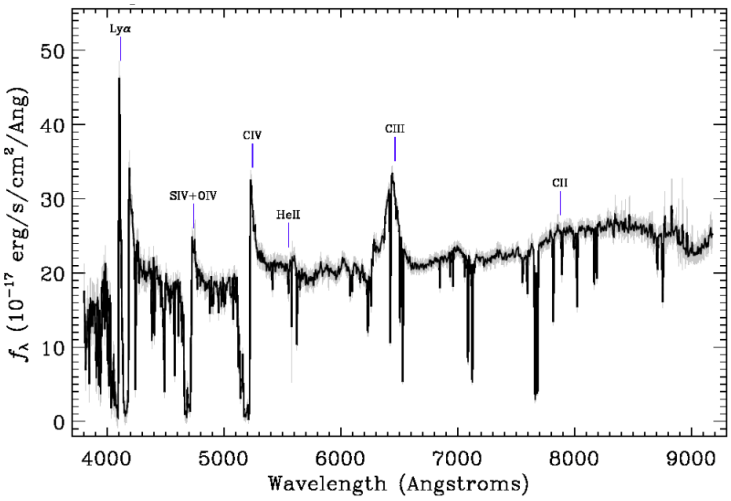

Figure 6.3. The rest-frame UV spectrum of the WISSH QSO SDSSJ1549+1245 from SDSS DR12.

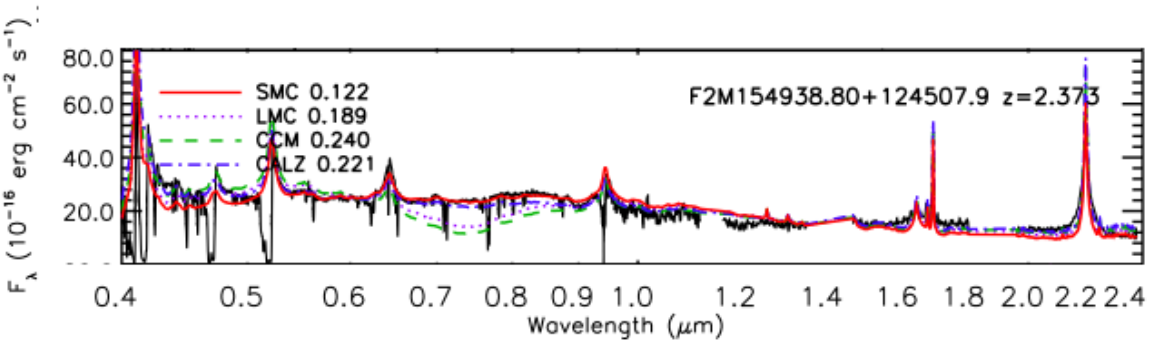

Figure 6.4. UV/Optical spectrum of the WISSH QSO J1549+1245, showing the comparison between four dust laws, i.e. SMC dust law, LMC dust law from Misselt *et al.* (1999), Milky Way dust law of Cardelli *et al.* (1989) and Calzetti *et al.* (1994) dust law for starburst galaxies. (Glikman *et al.* 2012).

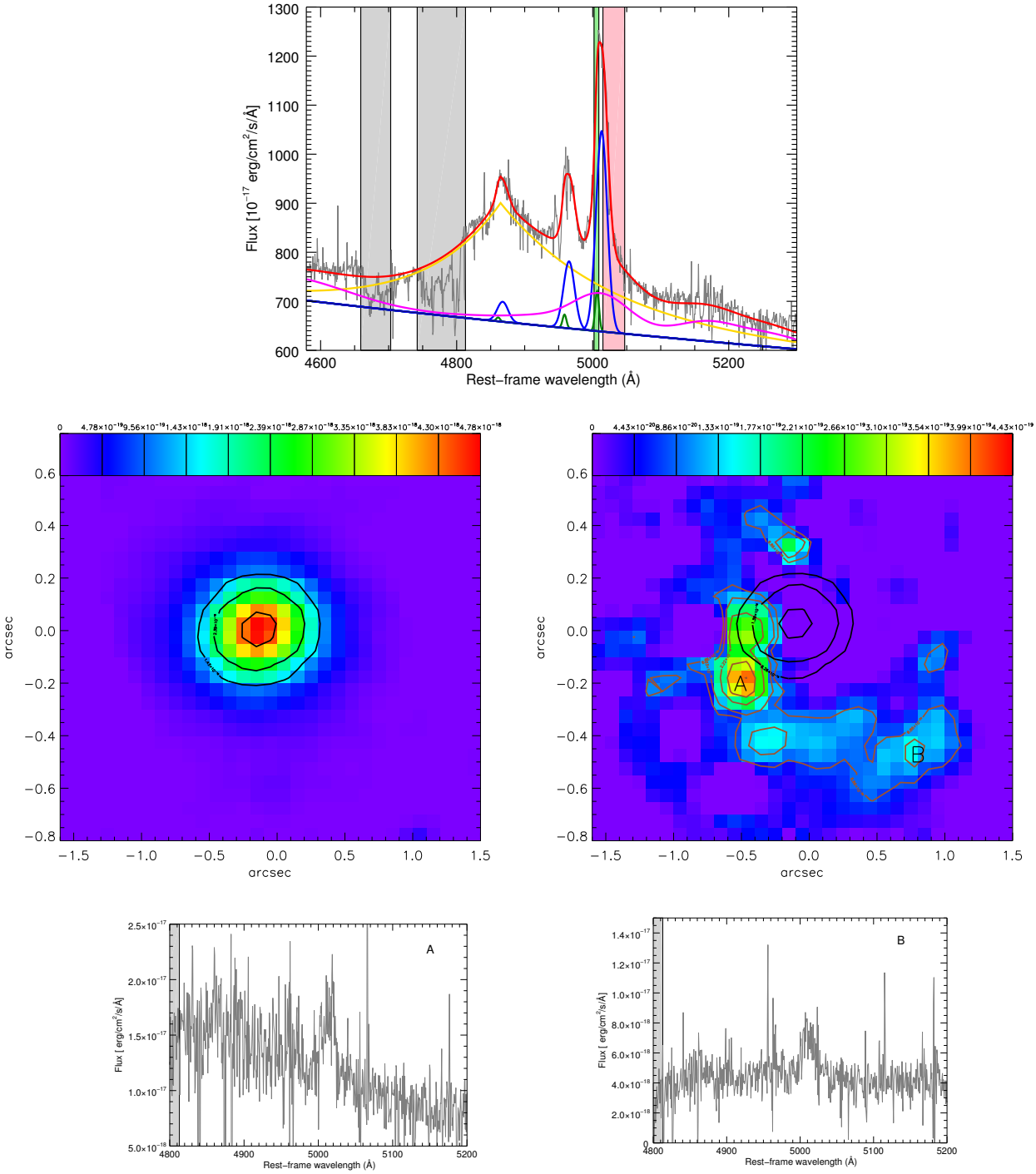

Figure 6.5. (Upper panel) SINFONI spectrum in the H band of J1549+1245, integrated in a region with 1" diameter. The best fit to the data is indicated with the red curve.The yellow curve indicates the Hβ component of the BLR. The red curves indicate the core component associated with the NLR. The blue curves indicate the outflow components. The shaded area indicate the telluric absorption, which are excluded from the fit. The FeII emission is shown with magenta curve. The green and pink regions show the wavelength interval in which the maps in the bottom panels are collapsed. (Left medium panel) Collapsed map of the core [OIII]λ5007 emission line continuum subtracted (black contours levels 0.3, 0.5 and 0.9 relative to the peak). (Right medium panel) Collapsed map of the [OIII]λ5007 red wing, from the cube PSF subtracted. The black contours of the QSO central position are superimposed and the brown contours denoted the [OIII] red wing extension (at 0.2, 0.3, 0.5, 0.7 and 0.9 relative to the peak). A and B denote two regions from which we extracted the 1D spectrum shown in the bottom panels, left and right respectively.

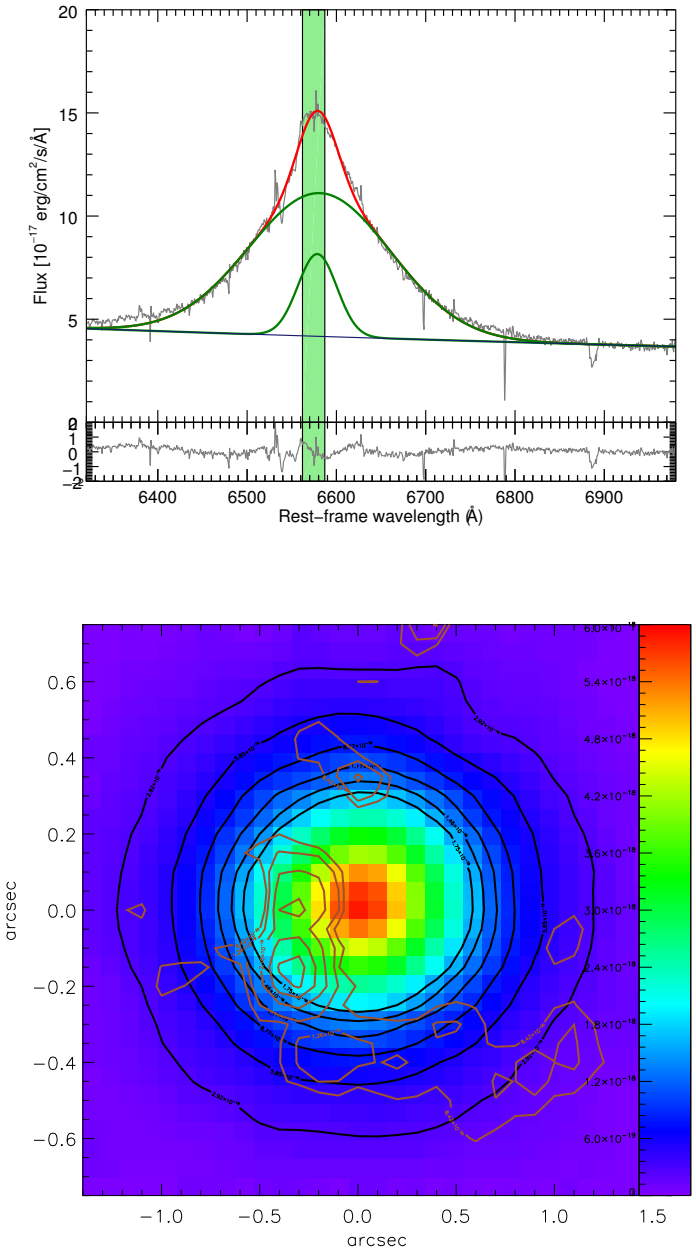

Figure 6.6. (Upper panel) Integrated spectrum of J1549+1245 in the SINFONI K-band. Hα emission is the prominent emission line. The best fit to the data is indicated in red, as a result of two combination of Gaussians (in green). The green band indicates the wavelength region of the collapsed image shown in the bottom panel. (Bottom panel) Hα map of the Hα narrow component with superimposed black contours level at 0.05, 0.1, 0.15, 0.20, 0.25 and 0.30 relative to the peak.

Chapter 7

Summary and Conclusions

We have presented the results of the analysis of NIR spectroscopy from LBT/LUCI and VLT/SINFONI observations of thirteen sources in the WISSH quasar sample, in addition to five sources already discussed in Bischetti *et al.* (2017). For each quasars the analysis of the profile of the CIV emission line from the SDSS spectra has been also performed.

Our analysis has been designed with the goal of deriving the properties of (i) Hβ and [OIII] emission lines from the optical rest-frame spectra, and (ii) CIV emission line by using rest-frame UV SDSS spectra. Our main findings can be summarised as follows:

- All the randomly-selected 18 WISSH quasars considered here exhibit SMBHs with mass larger than 10^9 $M_\odot$, with 50% of them hosting very massive SMBHs with $M_{BH} \gtrsim 5 \times 10^9$ $M_\odot$. Based on these Hβ-based M_{BH} values, we derived Eddington ratios $0.4 < \lambda_{edd} < 3.1$. This supports the scenario where the WISSH quasars are powered by highly accreting SMBHs at the massive end of the SMBH mass function.

- According to the REW([OIII]) > or < 5 Å the WISSH quasars can be divided into two groups: the *[OIII]* and *Weak [OIII]* sub-samples, respectively. More specifically 6 sources exhibit REW([OIII])≈7-70 Å and [OIII] profile dominated by a broad blueshifted component, while 11 sources have REW([OIII])≈0.3-3 Å(*Weak [OIII]* sub-sample) .

  As reported in Sect. 5.1, there is more than one explanation to ascribe to the WISSH $REW_{[OIII]}$ distribution. One is in terms of orientation effect, with the *[OIII]* sample likely seen at high (≈ 25° - 73°) inclination. This leads to a lower continuum luminosity and, hence, high $REW_{[OIII]}$ values. On the contrary, the *Weak [OIII]* sources are likely associated to nearly face-on AGNs. But the weak [OIII] emission for the WISSH quasars is expected due to the high bolometric luminosities of these sources. Indeed the [OIII] emission tends to decrease because of the over-ionization from the central engine, as found by Shen & Ho (2014). A further explanation for the difference

in $REW_{[OIII]}$ between the *[OIII]* and *Weak [OIII]* may be ascribed by the presence of a kpc-scale ionization cone oriented along the galaxy disk for the *[OIII]* objects, leading to a larger amount of gas to be ionized, while a ionization cone oriented more perpendicular to the galaxy disk in the case of *Weak [OIII]* sample may lead to a lower content of [OIII] gas to be ionized.

- Most of the WISSH quasars exhibits a $REW_{CIV} < 20$ Å with the peak of the entire CIV profile blueshifted with respect to the systemic redshift ($v_{CIV}^{peak} \sim$ 200–8000 km s^{-1}), indicating that the emitting gas is outflowing. This suggests that the luminosity-based selection criterion of WISSH is very effective in collecting the strong CIV winds. In particular quasars belonging to the *Weak [OIII]* sample, representing the 70% of the WISSH sample, show a broad asymmetric blueward and relatively weak (i.e. REW(CIV) < 20 Å) CIV line profile (see Fig 5.5), with the peak of the entire CIV profile extremely blueshifted ($v_{CIV}^{peak} \geq 2000$ km s^{-1} up to 8000 km s^{-1}). On the contrary, 30% of the WISSH QSOs (i.e. the *[OIII]* sample) shows peaky CIV profile with $REW_{CIV} > 20$ Å and $v_{CIV}^{peak} \leq 2000$ km s^{-1}. This highlights a dichotomy in the detection of BLR and NLR winds in the WISSH quasars, which could be likely due to inclination effects in a polar geometry scenario for the CIV winds, as suggested in Sect. 5.3. However one object, namely J1538, exhibits both NLR and BLR winds, suggesting a possible continuous distribution in BLR-NLR plane.

- We found that a sizable fraction of WISSH quasars exhibit BLR winds traced by CIV blueshifted emission with $\dot{M}_{out}^{ion} \approx$ 3-30 $M_\odot$ yr^{-1}, similar to the median accretion rate of WISSH quasars. The 20% of the BLR winds detected in WISSH shows kinetic powers $10^{-3} < \dot{E}_{kin} < 10^{-2} \times L_{Bol}$, i.e. comparable to those measured for the powerful NLR winds associated to [OIII] broad/blueshifted emission lines detected in the *[OIII]* sample (Bischetti *et al.* 2017). 80% of the BLR winds in WISSH shows kinetic powers comparable to [OIII] winds revealed in less luminous AGN. This suggests that the BLR winds should be taken into account to obtain a complete census of strong AGN-driven outflows and comprehensively evaluate their effects of depositing energy and momentum into the ISM.

- The BLR winds discovered here exhibit a velocity range between those measured for UFO (at sub-pc scale) and NLR winds (at kpc-scale), interpreting the outflow velocity distribution as a proxy of the distribution in radial distance for different classes of outflows (see fig 5.10). Moreover, the BLR winds have a $\dot{P}_{OF}/\dot{P}_{AGN} \lesssim 0.1$, which is lower than that found for UFOs (i.e. $\dot{P}_{OF}/\dot{P}_{AGN} \sim$ 1). In this case the momentum rate of the outflow is comparable to that of the AGN, suggesting a covering factor for the UFOs of the order of unity. Since the covering factor for the BLR is expected to be ~ 0.1, we can thus speculate that the momentum load of the nuclear winds may reflect the covering factor of the outflowing gas in the BLR.

- We investigated the dependence of v_{CIV}^{peak} on fundamental AGN physical parameters such as L_{Bol}, λ_{Edd} and α_{OX} . We found a stronger correlation with L_{Bol} than the λ_{Edd} (see Fig. 5.11), with a dependence consistent with a radiatively driven winds scenario ($v_{CIV}^{peak} \propto L^{0.24\pm0.05}$). Moreover, we further studied the dependence of v_{CIV}^{peak} on α_{OX}, finding a stronger correlation with α_{OX} than L_{Bol}. This relation is expected due to the dependence of α_{OX} on L_{Bol} (Vignali *et al.* 2003), i.e. the steeper α_{OX} the larger L_{Bol}. Therefore both selecting sources with steep αox or, equivalently, high L_{Bol} allows to pick up fast outflows in the BLR.

- Finally, for one source, i.e. J1549+1245, IFU spectroscopic data with VLT/SINFONI have been collected in the framework of the SUPER survey (PI: V. Mainieri). Unlike the three WISSH QSOs observed with SINFONI analyzed in this Thesis work, preliminary results about J1549 reveal the presence of an ionized wind traced by redshifted [OIII] emission up to $\sim$ 5 kpc from the nucleus. This emission has an arc-like morphology, very different from that of the core [OIII] emission. The complete analysis of these data will be published in a forthcoming paper (Vietri et al. 2018, in prep).

Appendix A

SDSSJ 1538+0855

We present here a detailed analysis of the source J1538 since is the only object exhibiting both NLR and BLR winds.

As reported in Sect. 5.3.b we measured the CIV outflow properties based on the so-called outflow component. We estimate the gas mass of the outflow M_{ion} = 590 $M_{\odot}$, the maximum velocity of the outflow as representative of the bulk velocity of the outflow v_{CIV}^{max} = 13400 km s^{-1}, the ionized gas mass rate $\dot{M}_{ion}$ = 24 $M_{\odot}$ yr^{-1} and the kinetic power $\dot{E}_{kin} \sim 1.4 \times 10^{45}$ erg s^{-1}. We have also measured the properties of the CIV outflow considering the entire CIV profile, with the v_{CIV}^{peak} as representative of the outflow velocity. We estimate M_{ion} = 1210 $M_{\odot}$, a ionized gas mass rate $\dot{M}_{ion}$ = 8 $M_{\odot}$ yr^{-1} and a kinetic power $\dot{E}_{kin} = 12 \times 10^{42}$ erg s^{-1}.

As mentioned in Sect. 4.1, for J1538 we found a broad (~2000 km s^{-1}) blueshifted (4987 Å) [OIII] component, indicative of outflow. In order to characterize the ionized outflowing gas, we calculated the mass rate $\dot{M}$ and the kinetic power $\dot{E}_{kin}$, assuming the outflow model discussed in Bischetti *et al.* (2017) and using the [OIII] emission line. According to the equations (2), (5) and (6) in Bischetti *et al.* (2017), we derived $M_{ion} = 4.2 \times 10^8$ $M_{\odot}$, $\dot{M}_{ion}$ = 530 $M_{\odot}$ yr^{-1} and $\dot{E}_{kin}$ = 1.4×10^{45} erg s^{-1} of the ionized outflow, assuming an electron density of n_e = 200 cm^{-3}, a solar metallicity and an outflow velocity defined as $v_{max} = |\Delta v| + 2\sigma_{[OIII]}^{broad}$, where Δv is the velocity shift between the broad [OIII] component and the systemic [OIII] assumed at 5007 Å and $\sigma_{[OIII]}^{broad}$ is the velocity dispersion of the broad [OIII] component (v_{max} = 2900 km s^{-1}). We refer to Bischetti *et al.* (2017) for more details about the assumptions used in the calculation of the outflow parameters.

We investigated how the values of $\dot{M}_{ion}^{[OIII]}$ and $\dot{E}_{kin}^{[OIII]}$ are sensitive to different assumed parameters. As in Bischetti *et al.* (2017), the upper bound corresponds to the assumption of n_e = 80 cm^{-3}, (as in Genzel *et al.* 2014) and we determined the $\dot{M}_{ion}^{[OIII]}$ = 1330 $M_{\odot}$ yr^{-1} and $\dot{E}_{kin}^{[OIII]} = 3.5 \times 10^{45}$ erg s^{-1}, while the lower bound corresponds to n_e = 1000 cm^{-3} (typical value for the NLR, Peterson 1997) and velocity of W_{80}/1.3 (as in Harrison *et al.* 2014), where W_{80} is the velocity width of the line at the 80% of the line flux. We derived a lower bound of $\dot{M}_{ion}^{[OIII]}$ = 60 $M_{\odot}$ yr^{-1} and $\dot{E}_{kin}^{[OIII]} = 5 \times 10^{43}$ erg s^{-1}.

Appendix B

Optical rest-frame spectra of 13 WISSH quasars

We present the LBT/LUCI and VLT/SINFONI (i.e. J1538+0855, J2123-0050 and J2346-0016) Optical rest-frame spectra in the wavelength range of the Hβ-[OIII] emission lines for the 13 WISSH quasars analyzed in this Thesis work (see Table 3.2). The red lines show the best-fit of the spectra. Green curves refer to the core component associated with the NLR emission of Hβ emission line. If present, blue curves refer to the broad blueshifted emission of [OIII]λ5007/4959 Å, indicative of outflow. Gold curves indicate the broad component of Hβ associated with BLR emission. FeII emission is indicated in magenta. Grey band indicates the region excluded from the fit because of the presence of sky line residual. Lower panels show the fit residuals.

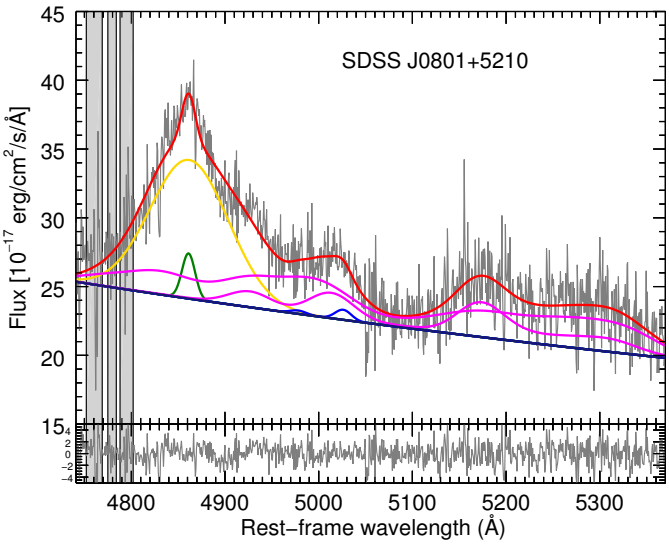

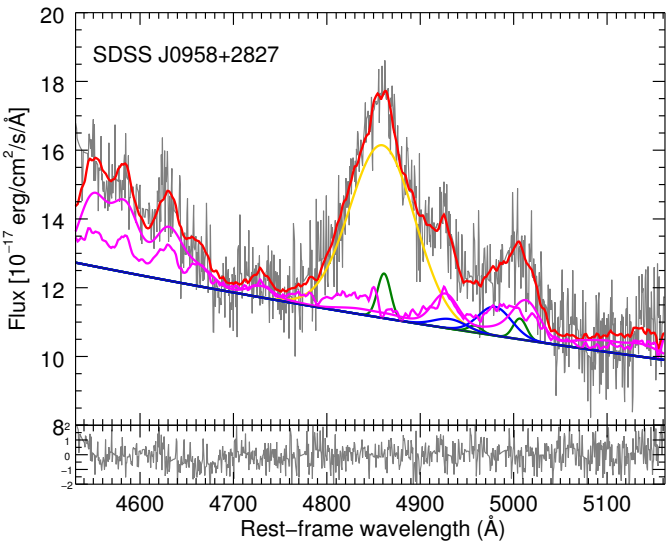

Figure B.1

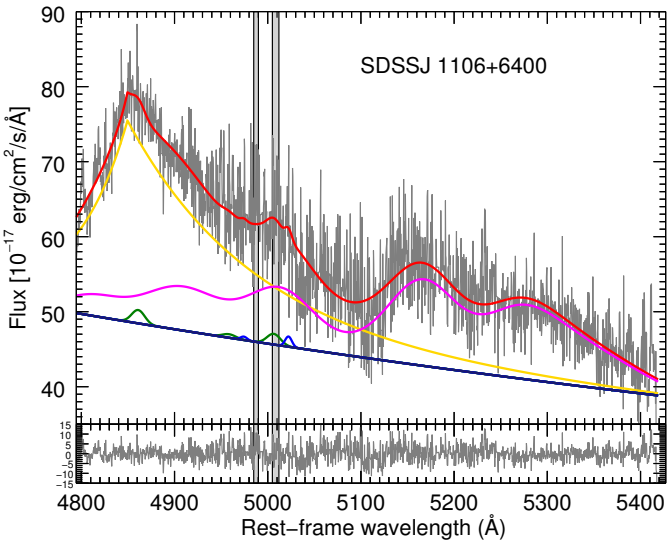

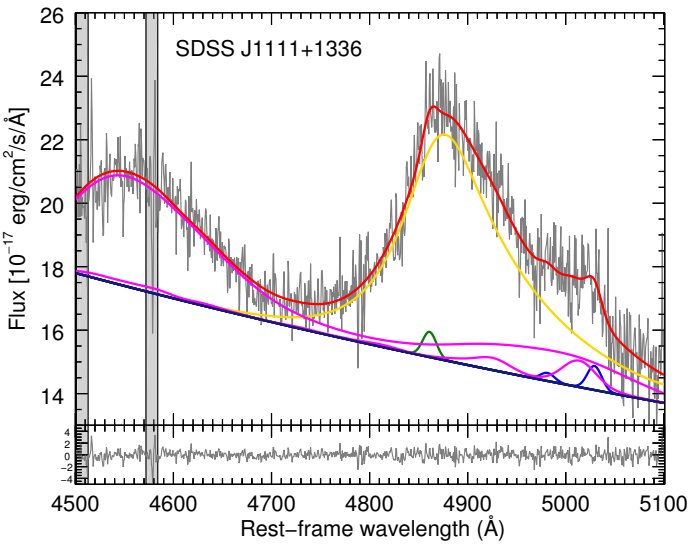

Figure B.2

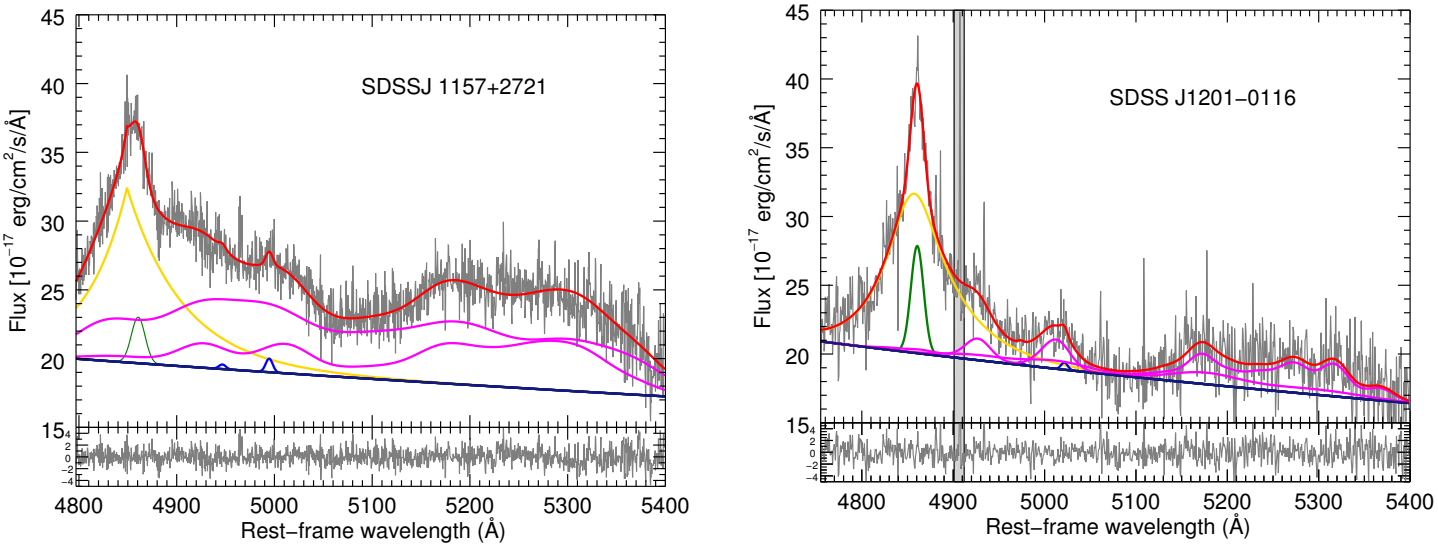

Figure B.3

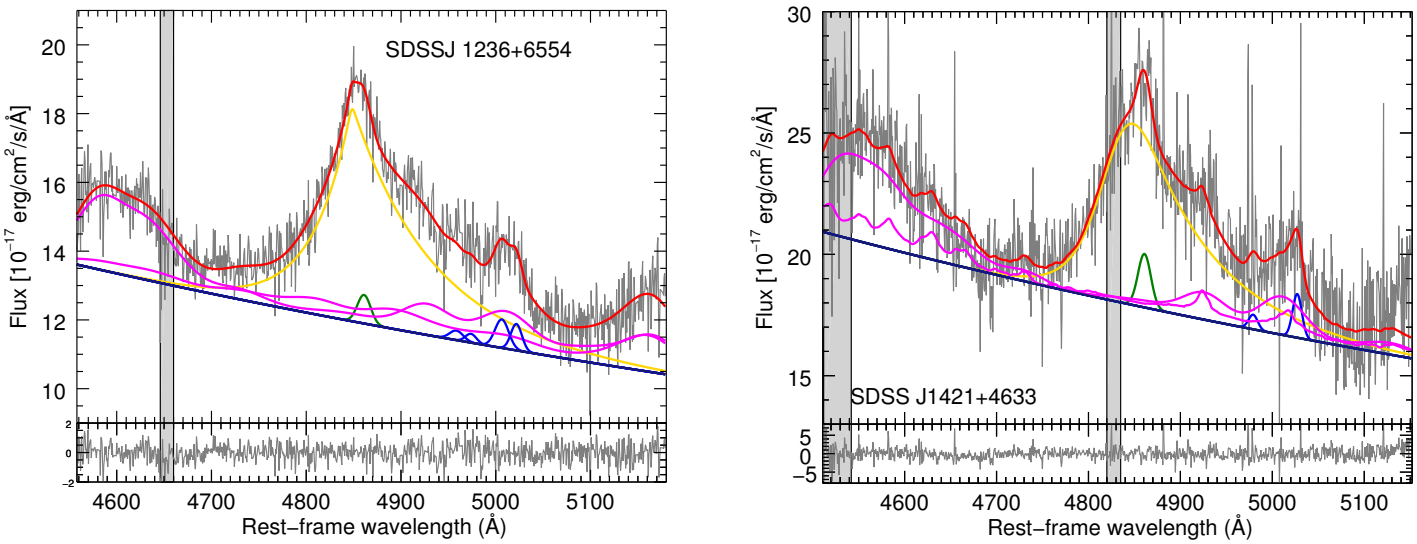

Figure B.4

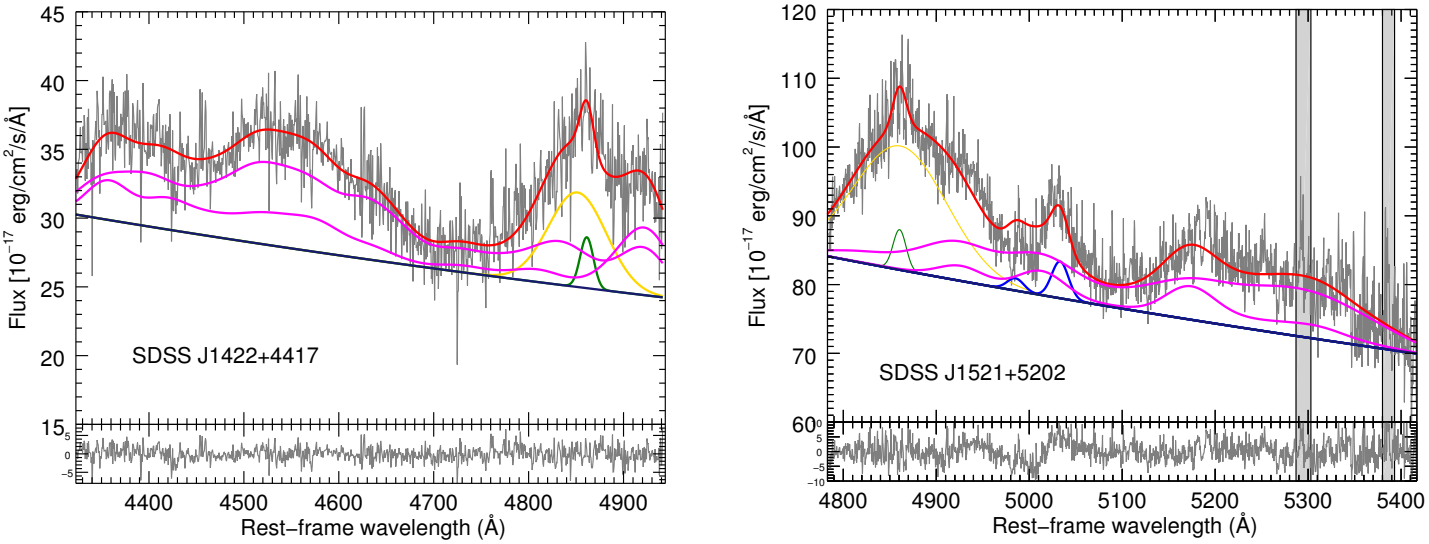

Figure B.5

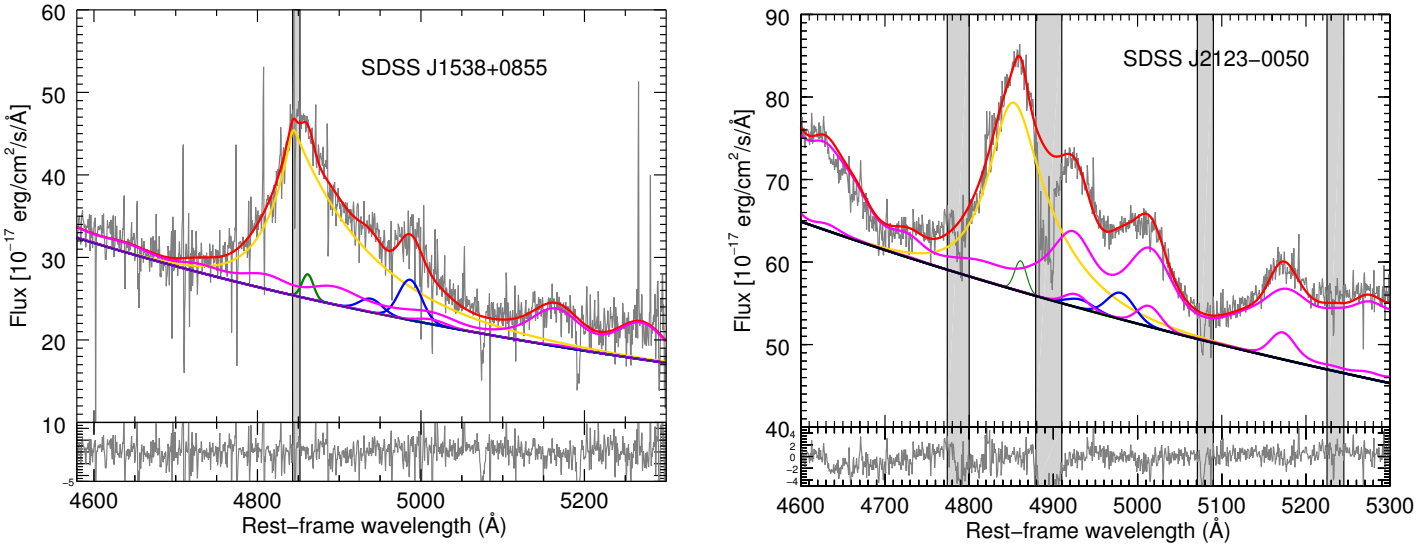

Figure B.6

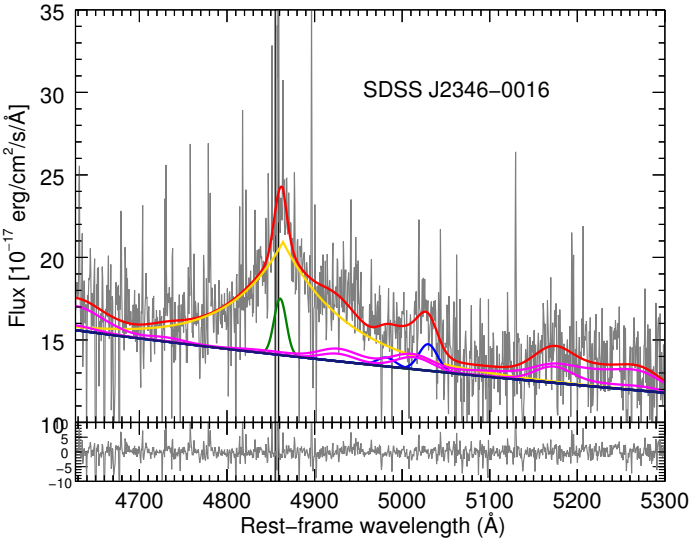
SDSS J2346−0016
Flux [10^{-17} erg/cm^2/s/Å]
Rest−frame wavelength (Å)
35
30
25
20
15
10
5
0
−5
−10
4700
4800
4900
5000
5100
5200
5300

Figure B.7

Appendix C

SDSS Optical/UV rest-frame spectra of 18 WISSH quasars

We present the SDSS DR12 UV rest-frame spectra of the 18 WISSH quasars analyzed in this Thesis work. The red lines show the best-fit of the spectra. If present, green curves refer to the core component likely associated with the NLR emission of the CIV emission. Blue curves refer to the broad blueshifted emission of CIV emission line, indicative of outflow. Gold curves indicate the broad virialized component associated with the BLR emission. FeII emission is indicated in magenta. Grey bands indicate the region excluded from the fit because of the presence of absorption lines. The dashed lines denote the CIV λ1549 Å rest-frame wavelength. Lower panels show the fit residuals.

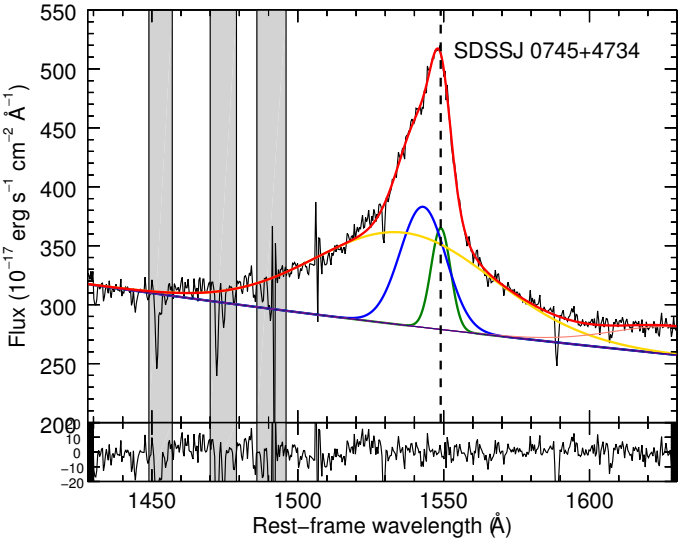

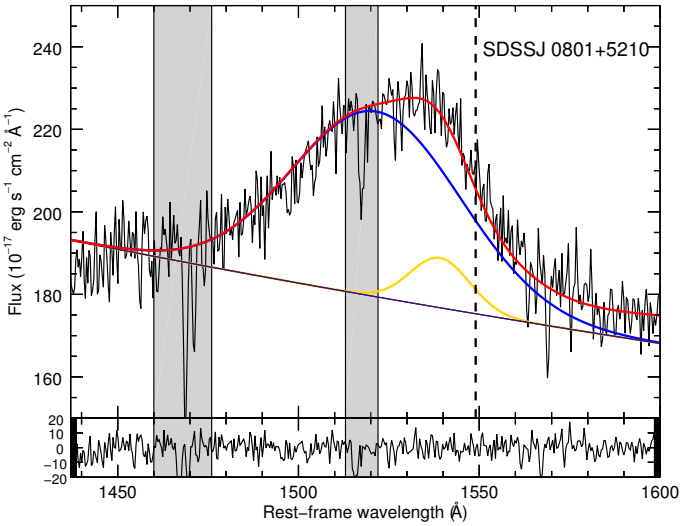

Figure C.1

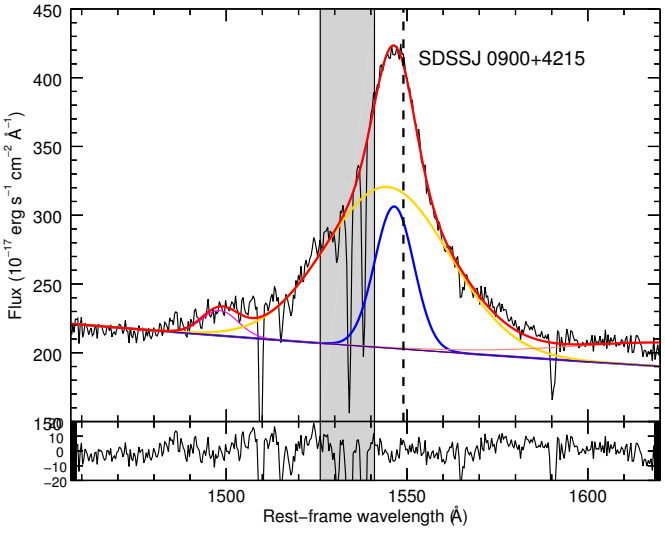

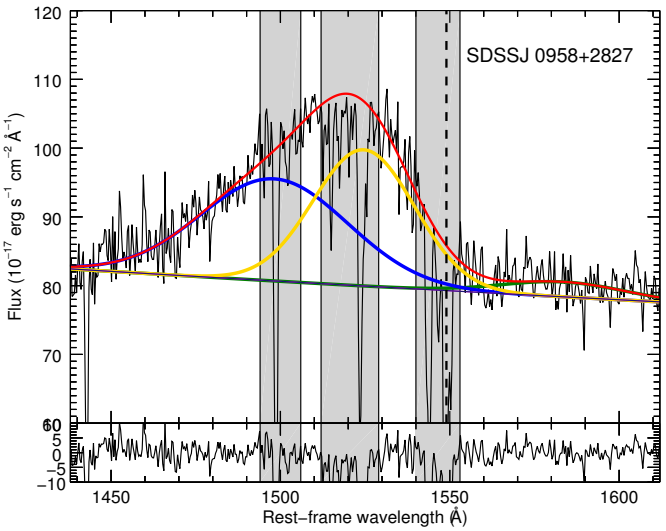

Figure C.2

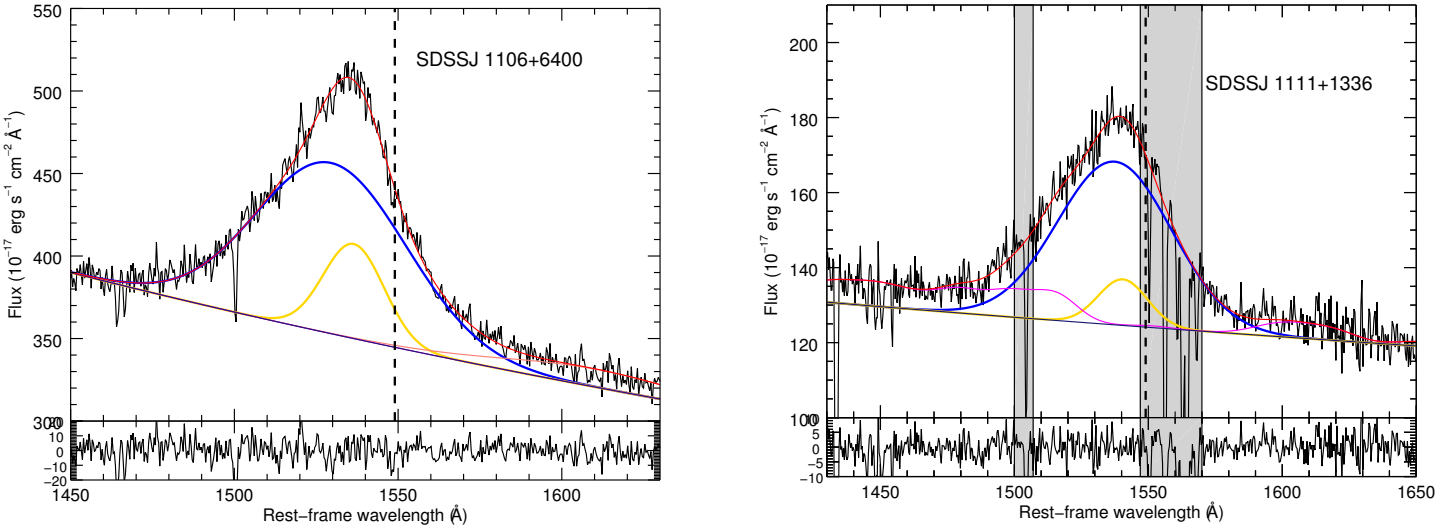

Figure C.3

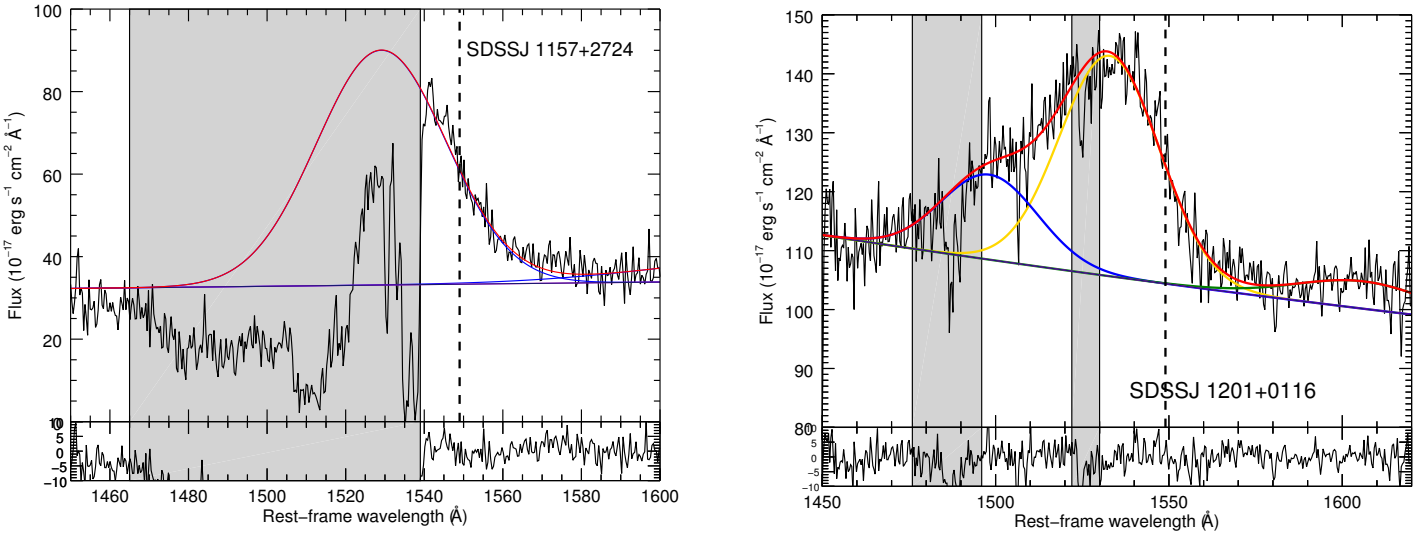

Figure C.4

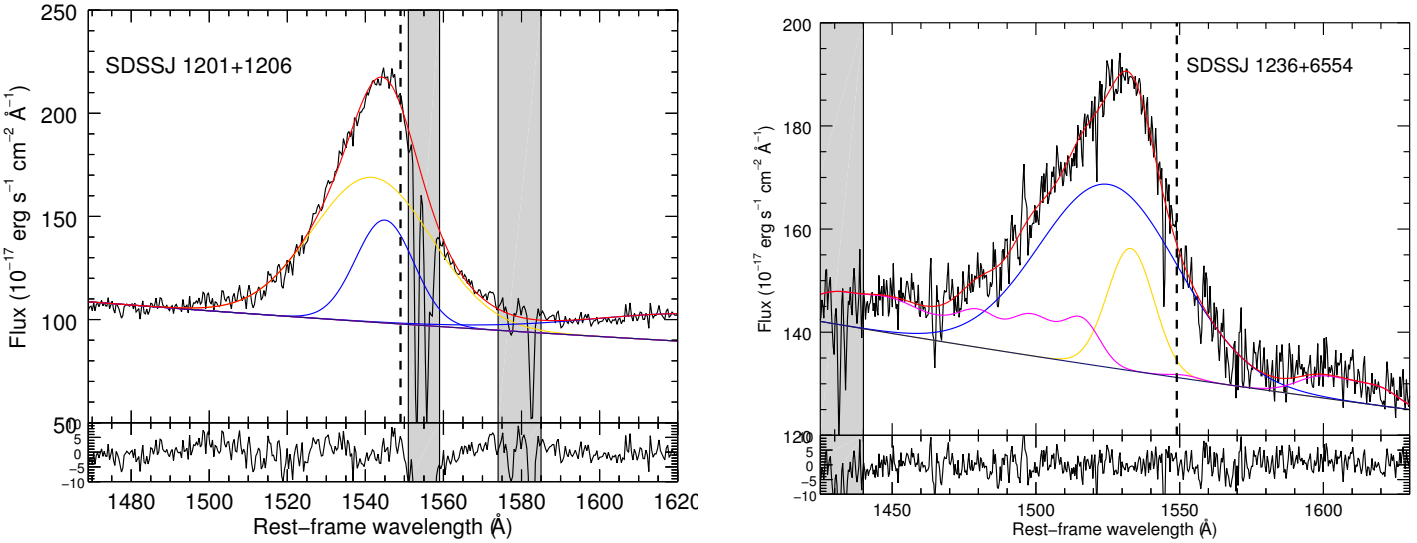

Figure C.5

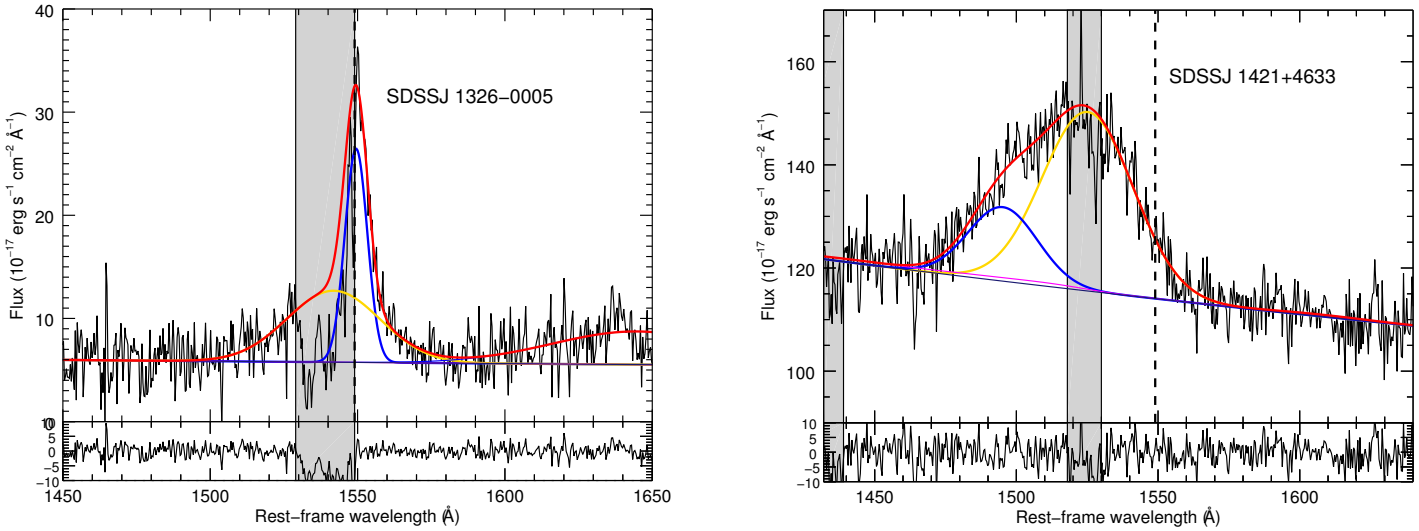

Figure C.6

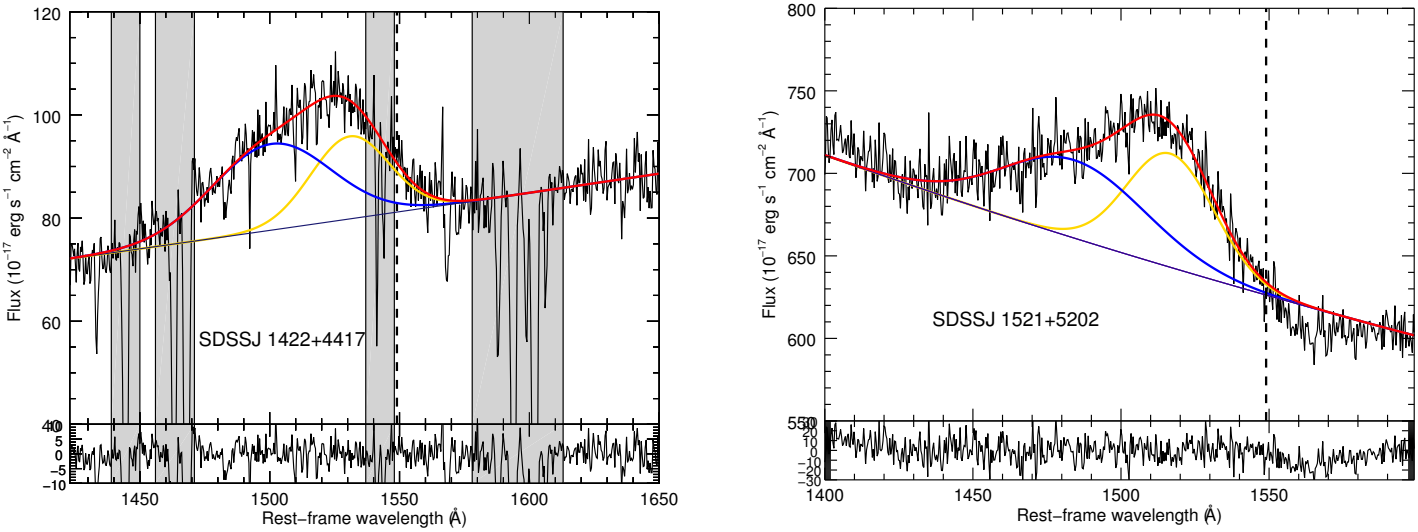

Figure C.7

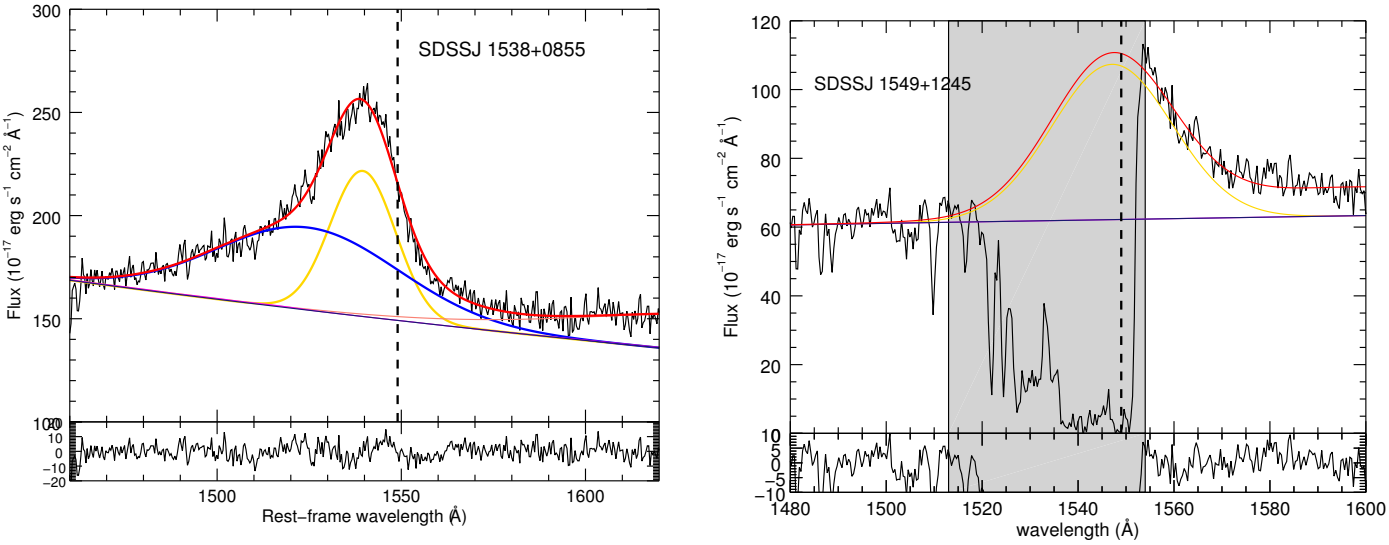

Figure C.8

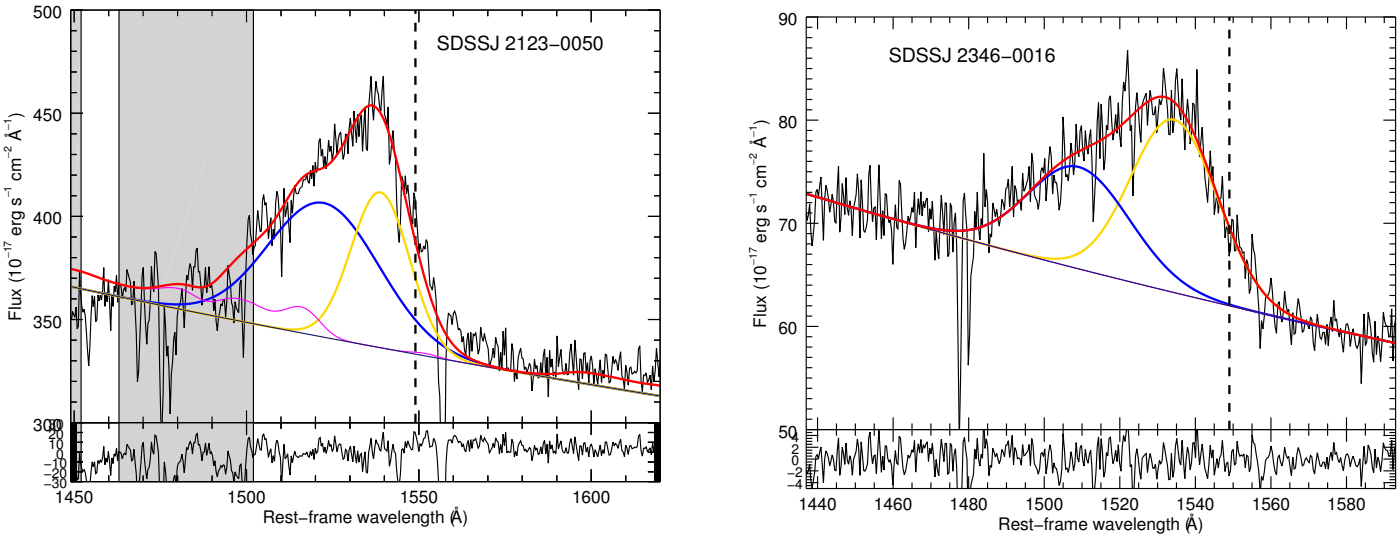
SDSSJ 2123−0050
SDSSJ 2346−0016
Flux (10^{-17} erg s^{-1} cm^{-2} Å^{-1})
Rest−frame wavelength (Å)

Figure C.9

Bibliography

Abramowicz, M. A., Czerny, B., Lasota, J. P., & Szuszkiewicz, E. 1988. Slim accretion disks. ApJ, **332**(Sept.), 646–658.

Ahn, C. P., Alexandroff, R., Allende Prieto, C., Anders, F., Anderson, S. F., Anderton, T., Andrews, B. H., Aubourg, É., Bailey, S., Bastien, F. A., & et al. 2014. The Tenth Data Release of the Sloan Digital Sky Survey: First Spectroscopic Data from the SDSS-III Apache Point Observatory Galactic Evolution Experiment. ApJS, **211**(Apr.), 17.

Aird, J., Coil, A. L., Georgakakis, A., Nandra, K., Barro, G., & Pérez-González, P. G. 2015. The evolution of the X-ray luminosity functions of unabsorbed and absorbed AGNs out to z∼ 5. MNRAS, **451**(Aug.), 1892–1927.

Alexander, D. M., & Hickox, R. C. 2012. What drives the growth of black holes? New A Rev., **56**(June), 93–121.

Antonucci, R. 1993. Unified models for active galactic nuclei and quasars. ARA&A, **31**, 473–521.

Arav, N., Li, Z.-Y., & Begelman, M. C. 1994. Radiative acceleration in outflows from broad absorption line quasi-stellar objects. 2: Wind models. ApJ, **432**(Sept.), 62–74.

Balbus, S. A., & Hawley, J. F. 1991. A powerful local shear instability in weakly magnetized disks. I - Linear analysis. II - Nonlinear evolution. ApJ, **376**(July), 214–233.

Baldwin, J. A. 1977. Luminosity Indicators in the Spectra of Quasi-Stellar Objects. ApJ, **214**(June), 679–684.

Barnes, J. E., & Hernquist, L. 1992. Dynamics of interacting galaxies. ARA&A, **30**, 705–742.

Baskin, A., & Laor, A. 2004. On the origin of the C IV Baldwin effect in active galactic nuclei. MNRAS, **350**(May), L31–L35.

Baskin, A., & Laor, A. 2005. What controls the CIV line profile in active galactic nuclei? MNRAS, **356**(Jan.), 1029–1044.

Bennert, N., Falcke, H., Schulz, H., Wilson, A. S., & Wills, B. J. 2002. Size and Structure of the Narrow-Line Region of Quasars. ApJ, **574**(Aug.), L105–L109.

Benson, A. J., Bower, R. G., Frenk, C. S., Lacey, C. G., Baugh, C. M., & Cole, S. 2003. What Shapes the Luminosity Function of Galaxies? ApJ, **599**(Dec.), 38–49.

Bentz, M. C., Peterson, B. M., Netzer, H., Pogge, R. W., & Vestergaard, M. 2009. The Radius-Luminosity Relationship for Active Galactic Nuclei: The Effect of Host-Galaxy Starlight on Luminosity Measurements. II. The Full Sample of Reverberation-Mapped AGNs. ApJ, **697**(May), 160–181.

Bernardi, M., Sheth, R. K., Nichol, R. C., Schneider, D. P., & Brinkmann, J. 2005. Colors, Magnitudes, and Velocity Dispersions in Early-Type Galaxies: Implications for Galaxy Ages and Metallicities. AJ, **129**(Jan.), 61–72.

Bian, W.-H., Fang, L.-L., Huang, K.-L., & Wang, J.-M. 2012. The C IV Baldwin effect in quasi-stellar objects from Seventh Data Release of the Sloan Digital Sky Survey. MNRAS, **427**(Dec.), 2881–2888.

Bischetti, M., Piconcelli, E., Vietri, G., Bongiorno, A., Fiore, F., Sani, E., Marconi, A., Duras, F., Zappacosta, L., Brusa, M., Comastri, A., Cresci, G., Feruglio, C., Giallongo, E., La Franca, F., Mainieri, V., Mannucci, F., Martocchia, S., Ricci, F., Schneider, R., Testa, V., & Vignali, C. 2017. The WISSH quasars project. I. Powerful ionised outflows in hyper-luminous quasars. A&A, **598**(Feb.), A122.

Bisogni, S., Marconi, A., & Risaliti, G. 2017. Orientation effects on spectral emission features of quasars. MNRAS, **464**(Jan.), 385–397.

Blandford, R. D., & Payne, D. G. 1982. Hydromagnetic flows from accretion discs and the production of radio jets. MNRAS, **199**(June), 883–903.

Bongiorno, A., Merloni, A., Brusa, M., Magnelli, B., Salvato, M., Mignoli, M., Zamorani, G., Fiore, F., Rosario, D., Mainieri, V., Hao, H., Comastri, A., Vignali, C., Balestra, I., Bardelli, S., Berta, S., Civano, F., Kampczyk, P., Le Floc'h, E., Lusso, E., Lutz, D., Pozzetti, L., Pozzi, F., Riguccini, L., Shankar, F., & Silverman, J. 2012. Accreting supermassive black holes in the COSMOS field and the connection to their host galaxies. MNRAS, **427**(Dec.), 3103–3133.

Bongiorno, A., Maiolino, R., Brusa, M., Marconi, A., Piconcelli, E., Lamastra, A., Cano-Díaz, M., Schulze, A., Magnelli, B., Vignali, C., Fiore, F., Menci, N., Cresci, G., La Franca, F., & Merloni, A. 2014. The M_{BH}-M_* relation for X-ray-obscured, red QSOs at $1.2 < z < 2.6$. MNRAS, **443**(Sept.), 2077–2091.

Boroson, T. A., & Green, R. F. 1992. The emission-line properties of low-redshift quasi-stellar objects. ApJS, **80**(May), 109–135.

Bouché, N., Cresci, G., Davies, R., Eisenhauer, F., Förster Schreiber, N. M., Genzel, R., Gillessen, S., Lehnert, M., Lutz, D., Nesvadba, N., Shapiro, K. L., Sternberg, A., Tacconi, L. J., Verma, A., Cimatti, A., Daddi, E., Renzini, A., Erb, D. K., Shapley, A., & Steidel, C. C. 2007. Dynamical Properties of z ˜ 2 Star-forming Galaxies and a Universal Star Formation Relation. ApJ, **671**(Dec.), 303–309.

Bouwens, R. J., Illingworth, G. D., Oesch, P. A., Labbé, I., Trenti, M., van Dokkum, P., Franx, M., Stiavelli, M., Carollo, C. M., Magee, D., & Gonzalez, V. 2011. Ultraviolet Luminosity Functions from 132 z ˜ 7 and z ˜ 8 Lyman-break Galaxies in the Ultra-deep HUDF09 and Wide-area Early Release Science WFC3/IR Observations. ApJ, **737**(Aug.), 90.

Bouwens, R. J., Illingworth, G. D., Oesch, P. A., Trenti, M., Labbé, I., Bradley, L., Carollo, M., van Dokkum, P. G., Gonzalez, V., Holwerda, B., Franx, M., Spitler, L., Smit, R., & Magee, D. 2015. UV Luminosity Functions at Redshifts z ∼ 4 to z ∼ 10: 10,000 Galaxies from HST Legacy Fields. ApJ, **803**(Apr.), 34.

Boyle, B. J., & Terlevich, R. J. 1998. The cosmological evolution of the QSO luminosity density and of the star formation rate. MNRAS, **293**(Jan.), L49–L51.

Braibant, L., Hutsemékers, D., Sluse, D., Anguita, T., & García-Vergara, C. J. 2014. Microlensing of the broad-line region in the quadruply imaged quasar HE0435-1223. A&A, **565**(May), L11.

Bruhweiler, F., & Verner, E. 2008. Modeling Fe II Emission and Revised Fe II (UV) Empirical Templates for the Seyfert 1 Galaxy I Zw 1. ApJ, **675**(Mar.), 83–95.

Bruni, G., Mack, K.-H., Salerno, E., Montenegro-Montes, F. M., Carballo, R., Benn, C. R., González-Serrano, J. I., Holt, J., & Jiménez-Luján, F. 2012. Radio spectra and polarisation properties of a bright sample of radio-loud broad absorption line quasars. A&A, **542**(June), A13.

Brusa, M., Civano, F., Comastri, A., Miyaji, T., Salvato, M., Zamorani, G., Cappelluti, N., Fiore, F., Hasinger, G., Mainieri, V., Merloni, A., Bongiorno, A., Capak, P., Elvis, M., Gilli, R., Hao, H., Jahnke, K., Koekemoer, A. M., Ilbert, O., Le Floc'h, E., Lusso, E., Mignoli, M., Schinnerer, E., Silverman, J. D., Treister, E., Trump, J. D., Vignali, C., Zamojski, M., Aldcroft, T., Aussel, H., Bardelli, S., Bolzonella, M., Cappi, A., Caputi, K., Contini, T., Finoguenov, A., Fruscione, A., Garilli, B., Impey, C. D., Iovino, A., Iwasawa, K., Kampczyk, P., Kartaltepe, J., Kneib, J. P., Knobel, C., Kovac, K., Lamareille, F., Leborgne, J.-F., Le Brun, V., Le Fevre, O., Lilly, S. J., Maier, C., McCracken, H. J., Pello, R., Peng, Y.-J., Perez-Montero, E., de Ravel, L., Sanders, D., Scodeggio, M., Scoville, N. Z., Tanaka, M., Taniguchi, Y., Tasca, L., de la Torre, S., Tresse, L., Vergani, D., & Zucca, E. 2010. The XMM-Newton Wide-field Survey in the Cosmos Field (XMM-COSMOS): Demography and Multiwavelength Properties of Obscured and Unobscured Luminous Active Galactic Nuclei. ApJ, **716**(June), 348–369.

Brusa, M., Bongiorno, A., Cresci, G., Perna, M., Marconi, A., Mainieri, V., Maiolino, R., Salvato, M., Lusso, E., Santini, P., Comastri, A., Fiore, F., Gilli, R., La Franca, F., Lanzuisi, G., Lutz, D., Merloni, A., Mignoli, M., Onori, F., Piconcelli, E., Rosario, D., Vignali, C., & Zamorani, G. 2015. X-shooter reveals powerful outflows in z ∼ 1.5 X-ray selected obscured quasi-stellar objects. MNRAS, **446**(Jan.), 2394–2417.

Calzetti, D., Kinney, A. L., & Storchi-Bergmann, T. 1994. Dust extinction of the stellar continua in starburst galaxies: The ultraviolet and optical extinction law. ApJ, **429**(July), 582–601.

Cano-Díaz, M., Maiolino, R., Marconi, A., Netzer, H., Shemmer, O., & Cresci, G. 2012. Observational evidence of quasar feedback quenching star formation at high redshift. A&A, **537**(Jan.), L8.

Cappi, M., Panessa, F., Bassani, L., Dadina, M., Di Cocco, G., Comastri, A., della Ceca, R., Filippenko, A. V., Gianotti, F., Ho, L. C., Malaguti, G., Mulchaey, J. S., Palumbo, G. G. C., Piconcelli, E., Sargent, W. L. W., Stephen, J., Trifoglio, M., & Weaver, K. A. 2006. X-ray spectral survey with XMM-Newton of a complete sample of nearby Seyfert galaxies. A&A, **446**(Feb.), 459–470.

Cardelli, J. A., Clayton, G. C., & Mathis, J. S. 1989. The relationship between infrared, optical, and ultraviolet extinction. ApJ, **345**(Oct.), 245–256.

Carniani, S., Marconi, A., Maiolino, R., Balmaverde, B., Brusa, M., Cano-Díaz, M., Cicone, C., Comastri, A., Cresci, G., Fiore, F., Feruglio, C., La Franca, F., Mainieri, V., Mannucci, F., Nagao, T., Netzer, H., Piconcelli, E., Risaliti, G., Schneider, R., & Shemmer, O. 2015. Ionised outflows in z ˜ 2.4 quasar host galaxies. A&A, **580**(Aug.), A102.

Castor, J. I., Abbott, D. C., & Klein, R. I. 1975. Radiation-driven winds in Of stars. ApJ, **195**(Jan.), 157–174.

Chelouche, D., & Netzer, H. 2005. Dynamical and Spectral Modeling of the Ionized Gas and Nuclear Environment in NGC 3783. ApJ, **625**(May), 95–107.

Cicone, C., Maiolino, R., Sturm, E., Graciá-Carpio, J., Feruglio, C., Neri, R., Aalto, S., Davies, R., Fiore, F., Fischer, J., García-Burillo, S., González-Alfonso, E., Hailey-Dunsheath, S., Piconcelli, E., & Veilleux, S. 2014. Massive molecular outflows and evidence for AGN feedback from CO observations. A&A, **562**(Feb.), A21.

Ciotti, L., & Ostriker, J. P. 1997. Cooling Flows and Quasars: Different Aspects of the Same Phenomenon? I. Concepts. ApJ, **487**(Oct.), L105–L108.

Civano, F., Marchesi, S., Comastri, A., Urry, M. C., Elvis, M., Cappelluti, N., Puccetti, S., Brusa, M., Zamorani, G., Hasinger, G., Aldcroft, T., Alexander,

D. M., Allevato, V., Brunner, H., Capak, P., Finoguenov, A., Fiore, F., Fruscione, A., Gilli, R., Glotfelty, K., Griffiths, R. E., Hao, H., Harrison, F. A., Jahnke, K., Kartaltepe, J., Karim, A., LaMassa, S. M., Lanzuisi, G., Miyaji, T., Ranalli, P., Salvato, M., Sargent, M., Scoville, N. J., Schawinski, K., Schinnerer, E., Silverman, J., Smolcic, V., Stern, D., Toft, S., Trakhtenbrot, B., Treister, E., & Vignali, C. 2016. The Chandra Cosmos Legacy Survey: Overview and Point Source Catalog. ApJ, **819**(Mar.), 62.

Coatman, L., Hewett, P. C., Banerji, M., & Richards, G. T. 2016. C IV emission-line properties and systematic trends in quasar black hole mass estimates. MNRAS, **461**(Sept.), 647–665.

Coatman, L., Hewett, P. C., Banerji, M., Richards, G. T., Hennawi, J. F., & Prochaska, J. X. 2017. Correcting C IV-based virial black hole masses. MNRAS, **465**(Feb.), 2120–2142.

Collin-Souffrin, S., Joly, M., Dumont, S., & Heidmann, N. 1980. Formation of permitted lines in the spectrum of type 1 Seyfert galaxies and quasars. II - Fe II lines and the low excitation region. A&A, **83**(Mar.), 190–198.

Corbin, M. R., & Boroson, T. A. 1996. Combined Ultraviolet and Optical Spectra of 48 Low-Redshift QSOs and the Relation of the Continuum and Emission-Line Properties. ApJS, **107**(Nov.), 69.

Crenshaw, D. M., Schmitt, H. R., Kraemer, S. B., Mushotzky, R. F., & Dunn, J. P. 2010. Radial Velocity Offsets Due to Mass Outflows and Extinction in Active Galactic Nuclei. ApJ, **708**(Jan.), 419–426.

Cresci, G., Mainieri, V., Brusa, M., Marconi, A., Perna, M., Mannucci, F., Piconcelli, E., Maiolino, R., Feruglio, C., Fiore, F., Bongiorno, A., Lanzuisi, G., Merloni, A., Schramm, M., Silverman, J. D., & Civano, F. 2015. Blowin' in the Wind: Both "Negative" and "Positive" Feedback in an Obscured High-z Quasar. ApJ, **799**(Jan.), 82.

Croom, S. M., Rhook, K., Corbett, E. A., Boyle, B. J., Netzer, H., Loaring, N. S., Miller, L., Outram, P. J., Shanks, T., & Smith, R. J. 2002. The correlation of line strength with luminosity and redshift from composite quasi-stellar object spectra. MNRAS, **337**(Nov.), 275–292.

Croton, D. J., Springel, V., White, S. D. M., De Lucia, G., Frenk, C. S., Gao, L., Jenkins, A., Kauffmann, G., Navarro, J. F., & Yoshida, N. 2006. The many lives of active galactic nuclei: cooling flows, black holes and the luminosities and colours of galaxies. MNRAS, **365**(Jan.), 11–28.

Davies, R. I. 2007. A method to remove residual OH emission from near-infrared spectra. MNRAS, **375**(Mar.), 1099–1105.

Denney, K. D. 2012. Are Outflows Biasing Single-epoch C IV Black Hole Mass Estimates? ApJ, **759**(Nov.), 44.

Di Matteo, T., Springel, V., & Hernquist, L. 2005. Energy input from quasars regulates the growth and activity of black holes and their host galaxies. Nature, **433**(Feb.), 604–607.

Diamond-Stanic, A. M., Fan, X., Brandt, W. N., Shemmer, O., Strauss, M. A., Anderson, S. F., Carilli, C. L., Gibson, R. R., Jiang, L., Kim, J. S., Richards, G. T., Schmidt, G. D., Schneider, D. P., Shen, Y., Smith, P. S., Vestergaard, M., & Young, J. E. 2009. High-redshift SDSS Quasars with Weak Emission Lines. ApJ, **699**(July), 782–799.

Dietrich, M., Hamann, F., Shields, J. C., Constantin, A., Vestergaard, M., Chaffee, F., Foltz, C. B., & Junkkarinen, V. T. 2002. Continuum and Emission-Line Strength Relations for a Large Active Galactic Nuclei Sample. ApJ, **581**(Dec.), 912–924.

Duras, F., Bongiorno, A., Piconcelli, E., Bianchi, S., Pappalardo, C., Valiante, R., Bischetti, M., Feruglio, C., Martocchia, S., Schneider, R., Vietri, G., Vignali, C., Zappacosta, L., La Franca, F., & Fiore, F. 2017. The WISSH quasars project. II. Giant star nurseries in hyper-luminous quasars. A&A, **604**(Aug.), A67.

Elvis, M. 2000. A Structure for Quasars. ApJ, **545**(Dec.), 63–76.

Elvis, M., Wilkes, B. J., McDowell, J. C., Green, R. F., Bechtold, J., Willner, S. P., Oey, M. S., Polomski, E., & Cutri, R. 1994. Atlas of quasar energy distributions. ApJS, **95**(Nov.), 1–68.

Eracleous, M., & Halpern, J. P. 1994. Doubled-peaked emission lines in active galactic nuclei. ApJS, **90**(Jan.), 1–30.

Fabian, A. C. 1994. Cooling Flows in Clusters of Galaxies. ARA&A, **32**, 277–318.

Fabian, A. C. 2012. Observational Evidence of Active Galactic Nuclei Feedback. ARA&A, **50**(Sept.), 455–489.

Fabian, A. C., Sanders, J. S., Taylor, G. B., Allen, S. W., Crawford, C. S., Johnstone, R. M., & Iwasawa, K. 2006. A very deep Chandra observation of the Perseus cluster: shocks, ripples and conduction. MNRAS, **366**(Feb.), 417–428.

Fan, L., Han, Y., Nikutta, R., Drouart, G., & Knudsen, K. K. 2016. Infrared Spectral Energy Distribution Decomposition of WISE-selected, Hyperluminous Hot Dust-obscured Galaxies. ApJ, **823**(June), 107.

Fan, X., Strauss, M. A., Gunn, J. E., Lupton, R. H., Carilli, C. L., Rupen, M. P., Schmidt, G. D., Moustakas, L. A., Davis, M., Annis, J., Bahcall, N. A., Brinkmann, J., Brunner, R. J., Csabai, I., Doi, M., Fukugita, M., Heckman, T. M., Hennessy, G. S., Hindsley, R. B., Ivezić , Ž., Knapp, G. R., Lamb, D. Q., Munn,

J. A., Pauls, A. G., Pier, J. R., Rockosi, C. M., Schneider, D. P., Szalay, A. S., Tucker, D. L., & York, D. G. 1999. The Discovery of a High-Redshift Quasar without Emission Lines from Sloan Digital Sky Survey Commissioning Data. ApJ, **526**(Dec.), L57–L60.

Faucher-Giguère, C.-A., & Quataert, E. 2012. The physics of galactic winds driven by active galactic nuclei. MNRAS, **425**(Sept.), 605–622.

Feltre, A., Hatziminaoglou, E., Fritz, J., & Franceschini, A. 2012. Smooth and clumpy dust distributions in AGN: a direct comparison of two commonly explored infrared emission models. MNRAS, **426**(Oct.), 120–127.

Ferland, G. J., & Elitzur, M. 1984. Radiation pressure and the stability of broad-line region clouds. ApJ, **285**(Oct.), L11–L14.

Ferland, G. J., Porter, R. L., van Hoof, P. A. M., Williams, R. J. R., Abel, N. P., Lykins, M. L., Shaw, G., Henney, W. J., & Stancil, P. C. 2013. The 2013 Release of Cloudy. Rev. Mexicana Astron. Astrofis., **49**(Apr.), 137–163.

Feruglio, C., Maiolino, R., Piconcelli, E., Menci, N., Aussel, H., Lamastra, A., & Fiore, F. 2010. Quasar feedback revealed by giant molecular outflows. A&A, **518**(July), L155.

Feruglio, C., Fiore, F., Carniani, S., Piconcelli, E., Zappacosta, L., Bongiorno, A., Cicone, C., Maiolino, R., Marconi, A., Menci, N., Puccetti, S., & Veilleux, S. 2015. The multi-phase winds of Markarian 231: from the hot, nuclear, ultra-fast wind to the galaxy-scale, molecular outflow. A&A, **583**(Nov.), A99.

Fiore, F., Feruglio, C., Shankar, F., Bischetti, M., Bongiorno, A., Brusa, M., Carniani, S., Cicone, C., Duras, F., Lamastra, A., Mainieri, V., Marconi, A., Menci, N., Maiolino, R., Piconcelli, E., Vietri, G., & Zappacosta, L. 2017. AGN wind scaling relations and the co-evolution of black holes and galaxies. A&A, **601**(May), A143.

Fischer, J., Sturm, E., González-Alfonso, E., Graciá-Carpio, J., Hailey-Dunsheath, S., Poglitsch, A., Contursi, A., Lutz, D., Genzel, R., Sternberg, A., Verma, A., & Tacconi, L. 2010. Herschel-PACS spectroscopic diagnostics of local ULIRGs: Conditions and kinematics in Markarian 231. A&A, **518**(July), L41.

Freudling, W., Romaniello, M., Bramich, D. M., Ballester, P., Forchi, V., García-Dabló, C. E., Moehler, S., & Neeser, M. J. 2013. Automated data reduction workflows for astronomy. The ESO Reflex environment. A&A, **559**(Nov.), A96.

García-Burillo, S., Combes, F., Schinnerer, E., Boone, F., & Hunt, L. K. 2005. Molecular gas in NUclei of GAlaxies (NUGA). IV. Gravitational torques and AGN feeding. A&A, **441**(Oct.), 1011–1030.

Gaskell, C. M. 1982. A redshift difference between high and low ionization emission-line regions in QSOs - Evidence for radial motions. ApJ, **263**(Dec.), 79–86.

Gaskell, C. M. 2009. What broad emission lines tell us about how active galactic nuclei work. New A Rev., **53**(July), 140–148.

Gaskell, C. M., & Sparke, L. S. 1986. Line variations in quasars and Seyfert galaxies. ApJ, **305**(June), 175–186.

Gaskell, C. M., Klimek, E. S., & Nazarova, L. S. 2007. NGC 5548: The AGN Energy Budget Problem and the Geometry of the Broad-Line Region and Torus. *ArXiv e-prints*, Nov.

Genzel, R., Förster Schreiber, N. M., Rosario, D., Lang, P., Lutz, D., Wisnioski, E., Wuyts, E., Wuyts, S., Bandara, K., Bender, R., Berta, S., Kurk, J., Mendel, J. T., Tacconi, L. J., Wilman, D., Beifiori, A., Brammer, G., Burkert, A., Buschkamp, P., Chan, J., Carollo, C. M., Davies, R., Eisenhauer, F., Fabricius, M., Fossati, M., Kriek, M., Kulkarni, S., Lilly, S. J., Mancini, C., Momcheva, I., Naab, T., Nelson, E. J., Renzini, A., Saglia, R., Sharples, R. M., Sternberg, A., Tacchella, S., & van Dokkum, P. 2014. Evidence for Wide-spread Active Galactic Nucleus-driven Outflows in the Most Massive z ˜ 1-2 Star-forming Galaxies. ApJ, **796**(Nov.), 7.

Gibson, R. R., Jiang, L., Brandt, W. N., Hall, P. B., Shen, Y., Wu, J., Anderson, S. F., Schneider, D. P., Vanden Berk, D., Gallagher, S. C., Fan, X., & York, D. G. 2009. A Catalog of Broad Absorption Line Quasars in Sloan Digital Sky Survey Data Release 5. ApJ, **692**(Feb.), 758–777.

Glikman, E., Urrutia, T., Lacy, M., Djorgovski, S. G., Mahabal, A., Myers, A. D., Ross, N. P., Petitjean, P., Ge, J., Schneider, D. P., & York, D. G. 2012. FIRST-2MASS Red Quasars: Transitional Objects Emerging from the Dust. ApJ, **757**(Sept.), 51.

Glikman, E., Simmons, B., Mailly, M., Schawinski, K., Urry, C. M., & Lacy, M. 2015. Major Mergers Host the Most-luminous Red Quasars at z ˜ 2: A Hubble Space Telescope WFC3/IR Study. ApJ, **806**(June), 218.

Gofford, J., Reeves, J. N., Tombesi, F., Braito, V., Turner, T. J., Miller, L., & Cappi, M. 2013. The Suzaku view of highly ionized outflows in AGN - I. Statistical detection and global absorber properties. MNRAS, **430**(Mar.), 60–80.

Gofford, J., Reeves, J. N., McLaughlin, D. E., Braito, V., Turner, T. J., Tombesi, F., & Cappi, M. 2015. The Suzaku view of highly ionized outflows in AGN - II. Location, energetics and scalings with bolometric luminosity. MNRAS, **451**(Aug.), 4169–4182.

Greene, J. E., & Ho, L. C. 2005. Estimating Black Hole Masses in Active Galaxies Using the Hα Emission Line. ApJ, **630**(Sept.), 122–129.

Greene, J. E., Zakamska, N. L., Liu, X., Barth, A. J., & Ho, L. C. 2009. The Growth of Black Holes: Insights from Obscured Active Galaxies. ApJ, **702**(Sept.), 441–459.

Gruppioni, C., Calura, F., Pozzi, F., Delvecchio, I., Berta, S., De Lucia, G., Fontanot, F., Franceschini, A., Marchetti, L., Menci, N., Monaco, P., & Vaccari, M. 2015. Star formation in Herschel's Monsters versus semi-analytic models. MNRAS, **451**(Aug.), 3419–3426.

Gruppioni, C., Berta, S., Spinoglio, L., Pereira-Santaella, M., Pozzi, F., Andreani, P., Bonato, M., De Zotti, G., Malkan, M., Negrello, M., Vallini, L., & Vignali, C. 2016. Tracing black hole accretion with SED decomposition and IR lines: from local galaxies to the high-z Universe. MNRAS, **458**(June), 4297–4320.

Gunn, J. E., Siegmund, W. A., Mannery, E. J., Owen, R. E., Hull, C. L., Leger, R. F., Carey, L. N., Knapp, G. R., York, D. G., Boroski, W. N., Kent, S. M., Lupton, R. H., Rockosi, C. M., Evans, M. L., Waddell, P., Anderson, J. E., Annis, J., Barentine, J. C., Bartoszek, L. M., Bastian, S., Bracker, S. B., Brewington, H. J., Briegel, C. I., Brinkmann, J., Brown, Y. J., Carr, M. A., Czarapata, P. C., Drennan, C. C., Dombeck, T., Federwitz, G. R., Gillespie, B. A., Gonzales, C., Hansen, S. U., Harvanek, M., Hayes, J., Jordan, W., Kinney, E., Klaene, M., Kleinman, S. J., Kron, R. G., Kresinski, J., Lee, G., Limmongkol, S., Lindenmeyer, C. W., Long, D. C., Loomis, C. L., McGehee, P. M., Mantsch, P. M., Neilsen, Jr., E. H., Neswold, R. M., Newman, P. R., Nitta, A., Peoples, Jr., J., Pier, J. R., Prieto, P. S., Prosapio, A., Rivetta, C., Schneider, D. P., Snedden, S., & Wang, S.-i. 2006. The 2.5 m Telescope of the Sloan Digital Sky Survey. AJ, **131**(Apr.), 2332–2359.

Hall, P. B., Anderson, S. F., Strauss, M. A., York, D. G., Richards, G. T., Fan, X., Knapp, G. R., Schneider, D. P., Vanden Berk, D. E., Geballe, T. R., Bauer, A. E., Becker, R. H., Davis, M., Rix, H.-W., Nichol, R. C., Bahcall, N. A., Brinkmann, J., Brunner, R., Connolly, A. J., Csabai, I., Doi, M., Fukugita, M., Gunn, J. E., Haiman, Z., Harvanek, M., Heckman, T. M., Hennessy, G. S., Inada, N., Ivezić, Ž., Johnston, D., Kleinman, S., Krolik, J. H., Krzesinski, J., Kunszt, P. Z., Lamb, D. Q., Long, D. C., Lupton, R. H., Miknaitis, G., Munn, J. A., Narayanan, V. K., Neilsen, E., Newman, P. R., Nitta, A., Okamura, S., Pentericci, L., Pier, J. R., Schlegel, D. J., Snedden, S., Szalay, A. S., Thakar, A. R., Tsvetanov, Z., White, R. L., & Zheng, W. 2002. Unusual Broad Absorption Line Quasars from the Sloan Digital Sky Survey. ApJS, **141**(Aug.), 267–309.

Häring, N., & Rix, H.-W. 2004. On the Black Hole Mass-Bulge Mass Relation. ApJ, **604**(Apr.), L89–L92.

Harrison, C., Alexander, D., Mullaney, J., Stott, J., Swinbank, M., Arumugam, V., Bauer, F., Bower, R., Bunker, A., & Sharples, R. 2016. The KMOS AGN Survey at High Redshift (KASHz). *The Messenger*, **163**(Mar.), 35–38.

Harrison, C. M. 2017. Impact of supermassive black hole growth on star formation. *Nature Astronomy*, **1**(July), 0165.

Harrison, C. M., Alexander, D. M., Swinbank, A. M., Smail, I., Alaghband-Zadeh, S., Bauer, F. E., Chapman, S. C., Del Moro, A., Hickox, R. C., Ivison, R. J., Menéndez-Delmestre, K., Mullaney, J. R., & Nesvadba, N. P. H. 2012. Energetic galaxy-wide outflows in high-redshift ultraluminous infrared galaxies hosting AGN activity. MNRAS, **426**(Oct.), 1073–1096.

Harrison, C. M., Alexander, D. M., Mullaney, J. R., & Swinbank, A. M. 2014. Kiloparsec-scale outflows are prevalent among luminous AGN: outflows and feedback in the context of the overall AGN population. MNRAS, **441**(July), 3306–3347.

Hewett, P. C., & Foltz, C. B. 2003. The Frequency and Radio Properties of Broad Absorption Line Quasars. AJ, **125**(Apr.), 1784–1794.

Hewett, P. C., & Wild, V. 2010. Improved redshifts for SDSS quasar spectra. MNRAS, **405**(July), 2302–2316.

Hopkins, P. F., Strauss, M. A., Hall, P. B., Richards, G. T., Cooper, A. S., Schneider, D. P., Vanden Berk, D. E., Jester, S., Brinkmann, J., & Szokoly, G. P. 2004. Dust Reddening in Sloan Digital Sky Survey Quasars. AJ, **128**(Sept.), 1112–1123.

Hopkins, P. F., Hernquist, L., Cox, T. J., Di Matteo, T., Robertson, B., & Springel, V. 2006. A Unified, Merger-driven Model of the Origin of Starbursts, Quasars, the Cosmic X-Ray Background, Supermassive Black Holes, and Galaxy Spheroids. ApJS, **163**(Mar.), 1–49.

Hopkins, P. F., Hernquist, L., Cox, T. J., & Kereš, D. 2008. A Cosmological Framework for the Co-Evolution of Quasars, Supermassive Black Holes, and Elliptical Galaxies. I. Galaxy Mergers and Quasar Activity. ApJS, **175**(Apr.), 356–389.

Hu, C., Wang, J.-M., Ho, L. C., Chen, Y.-M., Zhang, H.-T., Bian, W.-H., & Xue, S.-J. 2008. A Systematic Analysis of Fe II Emission in Quasars: Evidence for Inflow to the Central Black Hole. ApJ, **687**(Nov.), 78–96.

Husemann, B., Wisotzki, L., Sánchez, S. F., & Jahnke, K. 2013. The properties of the extended warm ionised gas around low-redshift QSOs and the lack of extended high-velocity outflows. A&A, **549**(Jan.), A43.

Hutsemekers, D., Braibant, L., Sluse, D., Anguita, T., & Goosmann, R. 2017. New constraints on quasar broad absorption and emission line regions from gravitational microlensing. *Frontiers in Astronomy and Space Sciences*, **4**(Sept.), 18.

Ishibashi, W., & Fabian, A. C. 2015. AGN feedback: galactic-scale outflows driven by radiation pressure on dust. MNRAS, **451**(July), 93–102.

Just, D. W., Brandt, W. N., Shemmer, O., Steffen, A. T., Schneider, D. P., Chartas, G., & Garmire, G. P. 2007. The X-Ray Properties of the Most Luminous Quasars from the Sloan Digital Sky Survey. ApJ, **665**(Aug.), 1004–1022.

Kashi, A., Proga, D., Nagamine, K., Greene, J., & Barth, A. J. 2013. On the Virialization of Disk Winds: Implications for the Black Hole Mass Estimates in Active Galactic Nuclei. ApJ, **778**(Nov.), 50.

Kaspi, S., Smith, P. S., Netzer, H., Maoz, D., Jannuzi, B. T., & Giveon, U. 2000. Reverberation Measurements for 17 Quasars and the Size-Mass-Luminosity Relations in Active Galactic Nuclei. ApJ, **533**(Apr.), 631–649.

Kauffmann, G., & Haehnelt, M. 2000. A unified model for the evolution of galaxies and quasars. MNRAS, **311**(Jan.), 576–588.

Kelly, B. C. 2007. Some Aspects of Measurement Error in Linear Regression of Astronomical Data. ApJ, **665**(Aug.), 1489–1506.

Kennicutt, Jr., R. C. 1998. Star Formation in Galaxies Along the Hubble Sequence. ARA&A, **36**, 189–232.

Kim, M., Ho, L. C., Lonsdale, C. J., Lacy, M., Blain, A. W., & Kimball, A. E. 2013. Evidence for Active Galactic Nucleus Driven Outflows in Young Radio Quasars. ApJ, **768**(May), L9.

King, A., & Pounds, K. 2015. Powerful Outflows and Feedback from Active Galactic Nuclei. ARA&A, **53**(Aug.), 115–154.

King, A. R. 2010. Black hole outflows. MNRAS, **402**(Mar.), 1516–1522.

King, A. R., & Pounds, K. A. 2003. Black hole winds. MNRAS, **345**(Oct.), 657–659.

Kormendy, J., & Gebhardt, K. 2001 (Oct.). Supermassive black holes in galactic nuclei. *Pages 363–381 of:* Wheeler, J. C., & Martel, H. (eds), *20th Texas Symposium on relativistic astrophysics*. American Institute of Physics Conference Series, vol. 586.

Kormendy, J., & Ho, L. C. 2013. Coevolution (Or Not) of Supermassive Black Holes and Host Galaxies. ARA&A, **51**(Aug.), 511–653.

Laor, A., & Brandt, W. N. 2002. The Luminosity Dependence of Ultraviolet Absorption in Active Galactic Nuclei. ApJ, **569**(Apr.), 641–654.

Laor, A., & Draine, B. T. 1993. Spectroscopic constraints on the properties of dust in active galactic nuclei. ApJ, **402**(Jan.), 441–468.

Larson, R. B. 1974. Effects of supernovae on the early evolution of galaxies. MNRAS, **169**(Nov.), 229–246.

Leighly, K. M. 2004. Hubble Space Telescope STIS Ultraviolet Spectral Evidence of Outflow in Extreme Narrow-Line Seyfert 1 Galaxies. II. Modeling and Interpretation. ApJ, **611**(Aug.), 125–152.

Liu, G., Zakamska, N. L., Greene, J. E., Nesvadba, N. P. H., & Liu, X. 2013. Observations of feedback from radio-quiet quasars - II. Kinematics of ionized gas nebulae. MNRAS, **436**(Dec.), 2576–2597.

Luo, B., Brandt, W. N., Hall, P. B., Wu, J., Anderson, S. F., Garmire, G. P., Gibson, R. R., Plotkin, R. M., Richards, G. T., Schneider, D. P., Shemmer, O., & Shen, Y. 2015. X-ray Insights into the Nature of PHL 1811 Analogs and Weak Emission-line Quasars: Unification with a Geometrically Thick Accretion Disk? ApJ, **805**(June), 122.

Lusso, E., Comastri, A., Vignali, C., Zamorani, G., Brusa, M., Gilli, R., Iwasawa, K., Salvato, M., Civano, F., Elvis, M., Merloni, A., Bongiorno, A., Trump, J. R., Koekemoer, A. M., Schinnerer, E., Le Floc'h, E., Cappelluti, N., Jahnke, K., Sargent, M., Silverman, J., Mainieri, V., Fiore, F., Bolzonella, M., Le Fèvre, O., Garilli, B., Iovino, A., Kneib, J. P., Lamareille, F., Lilly, S., Mignoli, M., Scodeggio, M., & Vergani, D. 2010. The X-ray to optical-UV luminosity ratio of X-ray selected type 1 AGN in XMM-COSMOS. A&A, **512**(Mar.), A34.

Lusso, E., Comastri, A., Simmons, B. D., Mignoli, M., Zamorani, G., Vignali, C., Brusa, M., Shankar, F., Lutz, D., Trump, J. R., Maiolino, R., Gilli, R., Bolzonella, M., Puccetti, S., Salvato, M., Impey, C. D., Civano, F., Elvis, M., Mainieri, V., Silverman, J. D., Koekemoer, A. M., Bongiorno, A., Merloni, A., Berta, S., Le Floc'h, E., Magnelli, B., Pozzi, F., & Riguccini, L. 2012. Bolometric luminosities and Eddington ratios of X-ray selected active galactic nuclei in the XMM-COSMOS survey. MNRAS, **425**(Sept.), 623–640.

Madau, P., & Dickinson, M. 2014. Cosmic Star-Formation History. ARA&A, **52**(Aug.), 415–486.

Madau, P., Haardt, F., & Dotti, M. 2014. Super-critical Growth of Massive Black Holes from Stellar-mass Seeds. ApJ, **784**(Apr.), L38.

Marconi, A., Risaliti, G., Gilli, R., Hunt, L. K., Maiolino, R., & Salvati, M. 2004. Local supermassive black holes, relics of active galactic nuclei and the X-ray background. MNRAS, **351**(June), 169–185.

Markwardt, C. B. 2009 (Sept.). Non-linear Least-squares Fitting in IDL with MPFIT. *Page 251 of:* Bohlender, D. A., Durand, D., & Dowler, P. (eds), *Astronomical Data Analysis Software and Systems XVIII*. Astronomical Society of the Pacific Conference Series, vol. 411.

Martocchia, S., Piconcelli, E., Zappacosta, L., Duras, F., Vietri, G., Vignali, C., Bianchi, S., Bischetti, M., Bongiorno, A., Brusa, M., Lanzuisi, G., Marconi, A., Mathur, S., Miniutti, G., Nicastro, F., Bruni, G., & Fiore, F. 2017. The WISSH Quasars Project III. X-ray properties of hyper-luminous quasars. *ArXiv e-prints*, Aug.

Marziani, P., & Sulentic, J. W. 1993. Evidence for a very broad line region in PG 1138+222. ApJ, **409**(June), 612–616.

Marziani, P., Zamanov, R. K., Sulentic, J. W., & Calvani, M. 2003. Searching for the physical drivers of eigenvector 1: influence of black hole mass and Eddington ratio. MNRAS, **345**(Nov.), 1133–1144.

Marziani, P., Sulentic, J. W., Negrete, C. A., Dultzin, D., Zamfir, S., & Bachev, R. 2010. Broad-line region physical conditions along the quasar eigenvector 1 sequence. MNRAS, **409**(Dec.), 1033–1048.

Marziani, P., Martínez Carballo, M. A., Sulentic, J. W., Del Olmo, A., Stirpe, G. M., & Dultzin, D. 2016. The most powerful quasar outflows as revealed by the Civ λ1549 resonance line. Ap&SS, **361**(Jan.), 29.

Matsuoka, K., Silverman, J. D., Schramm, M., Steinhardt, C. L., Nagao, T., Kartaltepe, J., Sanders, D. B., Treister, E., Hasinger, G., Akiyama, M., Ohta, K., Ueda, Y., Bongiorno, A., Brandt, W. N., Brusa, M., Capak, P., Civano, F., Comastri, A., Elvis, M., Lilly, S. J., Mainieri, V., Masters, D., Mignoli, M., Salvato, M., Trump, J. R., Taniguchi, Y., Zamorani, G., Alexander, D. M., & Schawinski, K. 2013. A Comparative Analysis of Virial Black Hole Mass Estimates of Moderate-luminosity Active Galactic Nuclei Using Subaru/FMOS. ApJ, **771**(July), 64.

Matzeu, G. A., Reeves, J. N., Braito, V., Nardini, E., McLaughlin, D. E., Lobban, A. P., Tombesi, F., & Costa, M. T. 2017. Evidence for a radiatively driven disc-wind in PDS 456? *ArXiv e-prints*, Aug.

McGill, K. L., Woo, J.-H., Treu, T., & Malkan, M. A. 2008. Comparing and Calibrating Black Hole Mass Estimators for Distant Active Galactic Nuclei. ApJ, **673**(Feb.), 703–714.

McLure, R. J., & Dunlop, J. S. 2004. The cosmological evolution of quasar black hole masses. MNRAS, **352**(Aug.), 1390–1404.

McLure, R. J., & Jarvis, M. J. 2002. Measuring the black hole masses of high-redshift quasars. MNRAS, **337**(Nov.), 109–116.

Menci, N., Fiore, F., Puccetti, S., & Cavaliere, A. 2008. The Blast Wave Model for AGN Feedback: Effects on AGN Obscuration. ApJ, **686**(Oct.), 219–229.

Merloni, A., & Heinz, S. 2013. *Evolution of Active Galactic Nuclei*. Page 503.

Merritt, D., & Ferrarese, L. 2001. The M$_?$-σ Relation for Supermassive Black Holes. ApJ, **547**(Jan.), 140–145.

Misselt, K. A., Clayton, G. C., & Gordon, K. D. 1999. A Reanalysis of the Ultraviolet Extinction from Interstellar Dust in the Large Magellanic Cloud. ApJ, **515**(Apr.), 128–139.

Motta, V., Mediavilla, E., Rojas, K., Falco, E. E., Jiménez-Vicente, J., & Muñoz, J. A. 2017. Probing the Broad-Line Region and the Accretion Disk in the Lensed Quasars HE 0435-1223, WFI 2033-4723, and HE 2149-2745 Using Gravitational Microlensing. ApJ, **835**(Feb.), 132.

Mulchaey, J. S., Koratkar, A., Ward, M. J., Wilson, A. S., Whittle, M., Antonucci, R. R. J., Kinney, A. L., & Hurt, T. 1994. Multiwavelength tests of the dusty torus model for Seyfert galaxies. ApJ, **436**(Dec.), 586–598.

Mullaney, J. R., Alexander, D. M., Fine, S., Goulding, A. D., Harrison, C. M., & Hickox, R. C. 2013. Narrow-line region gas kinematics of 24 264 optically selected AGN: the radio connection. MNRAS, **433**(July), 622–638.

Murray, N., & Chiang, J. 1997. Disk Winds and Disk Emission Lines. ApJ, **474**(Jan.), 91–103.

Murray, N., Chiang, J., Grossman, S. A., & Voit, G. M. 1995. Accretion Disk Winds from Active Galactic Nuclei. ApJ, **451**(Oct.), 498.

Nagao, T., Marconi, A., & Maiolino, R. 2006. The evolution of the broad-line region among SDSS quasars. A&A, **447**(Feb.), 157–172.

Nardini, E., Reeves, J. N., Gofford, J., Harrison, F. A., Risaliti, G., Braito, V., Costa, M. T., Matzeu, G. A., Walton, D. J., Behar, E., Boggs, S. E., Christensen, F. E., Craig, W. W., Hailey, C. J., Matt, G., Miller, J. M., O'Brien, P. T., Stern, D., Turner, T. J., & Ward, M. J. 2015. Black hole feedback in the luminous quasar PDS 456. *Science*, **347**(Feb.), 860–863.

Nesvadba, N. P. H., Lehnert, M. D., Eisenhauer, F., Gilbert, A., Tecza, M., & Abuter, R. 2006. Extreme Gas Kinematics in the z=2.2 Powerful Radio Galaxy MRC 1138-262: Evidence for Efficient Active Galactic Nucleus Feedback in the Early Universe? ApJ, **650**(Oct.), 693–705.

Nesvadba, N. P. H., Lehnert, M. D., De Breuck, C., Gilbert, A. M., & van Breugel, W. 2008. Evidence for powerful AGN winds at high redshift: dynamics of galactic outflows in radio galaxies during the "Quasar Era". A&A, **491**(Nov.), 407–424.

Netzer, H. 1990. AGN emission lines. *Pages 57–160 of:* Blandford, R. D., Netzer, H., Woltjer, L., Courvoisier, T. J.-L., & Mayor, M. (eds), *Active Galactic Nuclei*.

Netzer, H., & Laor, A. 1993. Dust in the narrow-line region of active galactic nuclei. ApJ, **404**(Feb.), L51–L54.

Netzer, H., & Wills, B. J. 1983. Broad emission features in QSOs and active galactic nuclei. I - New calculations of Fe II line strengths. ApJ, **275**(Dec.), 445–460.

Netzer, H., Laor, A., & Gondhalekar, P. M. 1992. Quasar discs. III - Line and continuum correlations. MNRAS, **254**(Jan.), 15–20.

Netzer, H., Shemmer, O., Maiolino, R., Oliva, E., Croom, S., Corbett, E., & di Fabrizio, L. 2004. Near-Infrared Spectroscopy of High-Redshift Active Galactic Nuclei. II. Disappearing Narrow-Line Regions and the Role of Accretion. ApJ, **614**(Oct.), 558–567.

Netzer, H., Mor, R., Trakhtenbrot, B., Shemmer, O., & Lira, P. 2014. Star Formation and Black Hole Growth at z ˜= 4.8. ApJ, **791**(Aug.), 34.

Netzer, H., Lani, C., Nordon, R., Trakhtenbrot, B., Lira, P., & Shemmer, O. 2016. Star Formation Black Hole Growth and Dusty Tori in the Most Luminous AGNs at z=2-3.5. ApJ, **819**(Mar.), 123.

Osterbrock, D. E. 1978. Observational Model of the Ionized Gas in Seyfert and Radio-Galaxy Nuclei. *Proceedings of the National Academy of Science*, **75**(Feb.), 540–544.

Ott, J., Walter, F., & Brinks, E. 2005. A Chandra X-ray survey of nearby dwarf starburst galaxies - II. Starburst properties and outflows. MNRAS, **358**(Apr.), 1453–1471.

Padovani, P. 2017. On the two main classes of active galactic nuclei. *Nature Astronomy*, **1**(Aug.), 0194.

Padovani, P., Alexander, D. M., Assef, R. J., De Marco, B., Giommi, P., Hickox, R. C., Richards, G. T., Smolčić, V., Hatziminaoglou, E., Mainieri, V., & Salvato, M. 2017. Active galactic nuclei: what's in a name? A&A Rev., **25**(Aug.), 2.

Perez, E., Mediavilla, E., Penston, M. V., Tadhunter, C., & Moles, M. 1988. An accretion disc in the broad-line radio galaxy 3C 390.3? MNRAS, **230**(Feb.), 353–362.

Perna, M., Brusa, M., Cresci, G., Comastri, A., Lanzuisi, G., Lusso, E., Marconi, A., Salvato, M., Zamorani, G., Bongiorno, A., Mainieri, V., Maiolino, R., & Mignoli, M. 2015. Galaxy-wide outflows in z ˜ 1.5 luminous obscured quasars revealed through near-IR slit-resolved spectroscopy. A&A, **574**(Feb.), A82.

Peterson, B. M. 1997. *An Introduction to Active Galactic Nuclei*.

Peterson, B. M., Ferrarese, L., Gilbert, K. M., Kaspi, S., Malkan, M. A., Maoz, D., Merritt, D., Netzer, H., Onken, C. A., Pogge, R. W., Vestergaard, M., & Wandel, A. 2004. Central Masses and Broad-Line Region Sizes of Active Galactic Nuclei. II. A Homogeneous Analysis of a Large Reverberation-Mapping Database. ApJ, **613**(Oct.), 682–699.

Pettini, M., & Pagel, B. E. J. 2004. [OIII]/[NII] as an abundance indicator at high redshift. MNRAS, **348**(Mar.), L59–L63.

Phillips, M. M. 1979. A compilation of Oscillator Strengths for selected Fe II Transitions. ApJS, **39**(Mar.), 377–388.

Piconcelli, E., Jimenez-Bailón, E., Guainazzi, M., Schartel, N., Rodríguez-Pascual, P. M., & Santos-Lleó, M. 2005. The XMM-Newton view of PG quasars. I. X-ray continuum and absorption. A&A, **432**(Mar.), 15–30.

Pierre, M., Chiappetti, L., Pacaud, F., Gueguen, A., Libbrecht, C., Altieri, B., Aussel, H., Gandhi, P., Garcet, O., Gosset, E., Paioro, L., Ponman, T. J., Read, A. M., Refregier, A., Starck, J.-L., Surdej, J., Valtchanov, I., Adami, C., Alloin, D., Alshino, A., Andreon, S., Birkinshaw, M., Bremer, M., Detal, A., Duc, P.-A., Galaz, G., Jones, L., Le Fèvre, J.-P., Le Fèvre, O., Maccagni, D., Mazure, A., Quintana, H., Röttgering, H. J. A., Sprimont, P.-G., Tasse, C., Trinchieri, G., & Willis, J. P. 2007. The XMM-Large Scale Structure catalogue: X-ray sources and associated optical data. Version I. MNRAS, **382**(Nov.), 279–290.

Plotkin, R. M., Anderson, S. F., Brandt, W. N., Diamond-Stanic, A. M., Fan, X., MacLeod, C. L., Schneider, D. P., & Shemmer, O. 2010. Multiwavelength Observations of Radio-quiet Quasars with Weak Emission Lines. ApJ, **721**(Sept.), 562–575.

Plotkin, R. M., Shemmer, O., Trakhtenbrot, B., Anderson, S. F., Brandt, W. N., Fan, X., Gallo, E., Lira, P., Luo, B., Richards, G. T., Schneider, D. P., Strauss, M. A., & Wu, J. 2015. Detection of Rest-frame Optical Lines from X-shooter Spectroscopy of Weak Emission Line Quasars. ApJ, **805**(June), 123.

Popović, L. Č., Mediavilla, E., Bon, E., & Ilić, D. 2004. Contribution of the disk emission to the broad emission lines in AGNs: Two-component model. A&A, **423**(Sept.), 909–918.

Pounds, K., Lobban, A., Reeves, J., & Vaughan, S. 2016. Detection of a second high-velocity component in the highly ionized wind from PG 1211+143. MNRAS, **457**(Apr.), 2951–2957.

Pounds, K. A., Reeves, J. N., King, A. R., Page, K. L., O'Brien, P. T., & Turner, M. J. L. 2003. A high-velocity ionized outflow and XUV photosphere in the narrow emission line quasar PG1211+143. MNRAS, **345**(Nov.), 705–713.

Proga, D. 2003. Numerical Simulations of Mass Outflows Driven from Accretion Disks by Radiation and Magnetic Forces. ApJ, **585**(Mar.), 406–417.

Proga, D. 2007 (Oct.). Theory of Winds in AGNs. *Page 267 of:* Ho, L. C., & Wang, J.-W. (eds), *The Central Engine of Active Galactic Nuclei*. Astronomical Society of the Pacific Conference Series, vol. 373.

Proga, D., & Kallman, T. R. 2002. On the Role of the Ultraviolet and X-Ray Radiation in Driving a Disk Wind in X-Ray Binaries. ApJ, **565**(Jan.), 455–470.

Proga, D., & Kallman, T. R. 2004. Dynamics of Line-driven Disk Winds in Active Galactic Nuclei. II. Effects of Disk Radiation. ApJ, **616**(Dec.), 688–695.

Rafferty, D. A., McNamara, B. R., & Nulsen, P. E. J. 2008. The Regulation of Cooling and Star Formation in Luminous Galaxies by Active Galactic Nucleus Feedback and the Cooling-Time/Entropy Threshold for the Onset of Star Formation. ApJ, **687**(Nov.), 899–918.

Reichert, G. A., Rodriguez-Pascual, P. M., Alloin, D., Clavel, J., Crenshaw, D. M., Kriss, G. A., Krolik, J. H., Malkan, M. A., Netzer, H., Peterson, B. M., Wamsteker, W., Altamore, A., Altieri, B., Anderson, K. S., Blackwell, Jr., J. H., Boisson, C., Brosch, N., Carone, T. E., Dietrich, M., England, M. N., Evans, I. N., Filippenko, A. V., Gaskell, C. M., Goad, M., Gondhalekar, P. M., Horne, K., Kazanas, D., Kollatschny, W., Koratkar, A. P., Korista, K. T., MacAlpine, G. M., Maoz, D., Mazeh, T., McCollum, B., Miller, H. R., Mendes de Oliveira, C., O'Brien, P. T., Pastoriza, M. G., Pelat, D., Perez, E., Perola, G. C., Pogge, R. W., Ptak, R. L., Recondo-Gonzalez, M. C., Rodriguez-Espinosa, J., Rosenblatt, E. I., Sadun, A. C., Santos-Lleo, M., Shields, J. C., Shrader, C. R., Shull, J. M., Simkin, S. M., Sitko, M. L., Snijders, M. A. J., Sparke, L. S., Stirpe, G. M., Stoner, R., Storchi-Bergmann, T., Sun, W.-H., Wang, T., Welsh, W. F., White, R. J., Winge, C., & Zheng, W. 1994. Steps toward determination of the size and structure of the broad-line region in active galactic nuclei. 5: Variability of the ultraviolet continuum and emission lines of NGC 3783. ApJ, **425**(Apr.), 582–608.

Richards, G. T., Vanden Berk, D. E., Reichard, T. A., Hall, P. B., Schneider, D. P., SubbaRao, M., Thakar, A. R., & York, D. G. 2002. Broad Emission-Line Shifts in Quasars: An Orientation Measure for Radio-Quiet Quasars? AJ, **124**(July), 1–17.

Richards, G. T., Keeton, C. R., Pindor, B., Hennawi, J. F., Hall, P. B., Turner, E. L., Inada, N., Oguri, M., Ichikawa, S.-I., Becker, R. H., Gregg, M. D., White, R. L., Wyithe, J. S. B., Schneider, D. P., Johnston, D. E., Frieman, J. A., & Brinkmann, J. 2004. Microlensing of the Broad Emission Line Region in the Quadruple Lens SDSS J1004+4112. ApJ, **610**(Aug.), 679–685.

Richards, G. T., Lacy, M., Storrie-Lombardi, L. J., Hall, P. B., Gallagher, S. C., Hines, D. C., Fan, X., Papovich, C., Vanden Berk, D. E., Trammell, G. B., Schneider, D. P., Vestergaard, M., York, D. G., Jester, S., Anderson, S. F., Budavári, T., & Szalay, A. S. 2006. Spectral Energy Distributions and Multiwavelength Selection of Type 1 Quasars. ApJS, **166**(Oct.), 470–497.

Richards, G. T., Kruczek, N. E., Gallagher, S. C., Hall, P. B., Hewett, P. C., Leighly, K. M., Deo, R. P., Kratzer, R. M., & Shen, Y. 2011. Unification of Luminous Type 1 Quasars through C IV Emission. AJ, **141**(May), 167.

Risaliti, G., Salvati, M., & Marconi, A. 2011. [O III] equivalent width and orientation effects in quasars. MNRAS, **411**(Mar.), 2223–2229.

Rodríguez Zaurín, J., Tadhunter, C. N., Rose, M., & Holt, J. 2013. The importance of warm, AGN-driven outflows in the nuclear regions of nearby ULIRGs. MNRAS, **432**(June), 138–166.

Rousselot, P., Lidman, C., Cuby, J.-G., Moreels, G., & Monnet, G. 2000. Night-sky spectral atlas of OH emission lines in the near-infrared. A&A, **354**(Feb.), 1134–1150.

Rupke, D. S. N., & Veilleux, S. 2013. The Multiphase Structure and Power Sources of Galactic Winds in Major Mergers. ApJ, **768**(May), 75.

Rupke, D. S. N., & Veilleux, S. 2015. Spatially Extended Na I D Resonant Emission and Absorption in the Galactic Wind of the Nearby Infrared-Luminous Quasar F05189-2524. ApJ, **801**(Mar.), 126.

Sanders, D. B., Soifer, B. T., Elias, J. H., Madore, B. F., Matthews, K., Neugebauer, G., & Scoville, N. Z. 1988. Ultraluminous infrared galaxies and the origin of quasars. ApJ, **325**(Feb.), 74–91.

Santini, P., Fontana, A., Grazian, A., Salimbeni, S., Fiore, F., Fontanot, F., Boutsia, K., Castellano, M., Cristiani, S., de Santis, C., Gallozzi, S., Giallongo, E., Menci, N., Nonino, M., Paris, D., Pentericci, L., & Vanzella, E. 2009. Star formation and mass assembly in high redshift galaxies. A&A, **504**(Sept.), 751–767.

Schechter, P. 1976. An analytic expression for the luminosity function for galaxies. ApJ, **203**(Jan.), 297–306.

Schmidt, M. 1978. The cosmological evolution of quasars. Phys. Scr, **17**(Mar.), 329–332.

Schmitt, H. R., Donley, J. L., Antonucci, R. R. J., Hutchings, J. B., & Kinney, A. L. 2003. A Hubble Space Telescope Survey of Extended [O III] λ5007 Emission in a Far-Infrared Selected Sample of Seyfert Galaxies: Observations. ApJS, **148**(Oct.), 327–352.

Scoville, N., & Norman, C. 1995. Stellar Contrails in Quasi-stellar Objects: The Origin of Broad Absorption Lines. ApJ, **451**(Oct.), 510.

Scoville, N. Z., Sargent, A. I., Sanders, D. B., & Soifer, B. T. 1991. Dust and gas in the core of ARP 220 (IC 4553). ApJ, **366**(Jan.), L5–L9.

Shakura, N. I., & Sunyaev, R. A. 1973. Black holes in binary systems. Observational appearance. A&A, **24**, 337–355.

Shen, Y. 2016a. Rest-frame Optical Properties of Luminous 1.5 < Z < 3.5 Quasars: The Hβ-[O iii] Region. ApJ, **817**(Jan.), 55.

Shen, Y. 2016b. Rest-frame Optical Properties of Luminous 1.5 < Z < 3.5 Quasars: The Hβ-[O III] Region. ApJ, **817**(Jan.), 55.

Shen, Y., & Ho, L. C. 2014. The diversity of quasars unified by accretion and orientation. Nature, **513**(Sept.), 210–213.

Shen, Y., & Liu, X. 2012. Comparing Single-epoch Virial Black Hole Mass Estimators for Luminous Quasars. ApJ, **753**(July), 125.

Shen, Y., Greene, J. E., Strauss, M. A., Richards, G. T., & Schneider, D. P. 2008. Biases in Virial Black Hole Masses: An SDSS Perspective. ApJ, **680**(June), 169–190.

Shen, Y., Richards, G. T., Strauss, M. A., Hall, P. B., Schneider, D. P., Snedden, S., Bizyaev, D., Brewington, H., Malanushenko, V., Malanushenko, E., Oravetz, D., Pan, K., & Simmons, A. 2011. A Catalog of Quasar Properties from Sloan Digital Sky Survey Data Release 7. ApJS, **194**(June), 45.

Silk, J., & Rees, M. J. 1998. Quasars and galaxy formation. A&A, **331**(Mar.), L1–L4.

Silverman, J. D., Green, P. J., Barkhouse, W. A., Kim, D.-W., Kim, M., Wilkes, B. J., Cameron, R. A., Hasinger, G., Jannuzi, B. T., Smith, M. G., Smith, P. S., & Tananbaum, H. 2008. The Luminosity Function of X-Ray-selected Active Galactic Nuclei: Evolution of Supermassive Black Holes at High Redshift. ApJ, **679**(May), 118–139.

Skrutskie, M. F., Cutri, R. M., Stiening, R., Weinberg, M. D., Schneider, S., Carpenter, J. M., Beichman, C., Capps, R., Chester, T., Elias, J., Huchra, J., Liebert, J., Lonsdale, C., Monet, D. G., Price, S., Seitzer, P., Jarrett, T., Kirkpatrick, J. D., Gizis, J. E., Howard, E., Evans, T., Fowler, J., Fullmer, L., Hurt, R., Light, R., Kopan, E. L., Marsh, K. A., McCallon, H. L., Tam, R., Van Dyk, S., & Wheelock, S. 2006. The Two Micron All Sky Survey (2MASS). AJ, **131**(Feb.), 1163–1183.

Soltan, A. 1982. Masses of quasars. MNRAS, **200**(July), 115–122.

Spoon, H. W. W., Farrah, D., Lebouteiller, V., González-Alfonso, E., Bernard-Salas, J., Urrutia, T., Rigopoulou, D., Westmoquette, M. S., Smith, H. A., Afonso, J., Pearson, C., Cormier, D., Efstathiou, A., Borys, C., Verma, A., Etxaluze, M., & Clements, D. L. 2013. Diagnostics of AGN-Driven Molecular Outflows in ULIRGs from Herschel-PACS Observations of OH at 119 μm. ApJ, **775**(Oct.), 127.

Stalevski, M., Ricci, C., Ueda, Y., Lira, P., Fritz, J., & Baes, M. 2016. The dust covering factor in active galactic nuclei. MNRAS, **458**(May), 2288–2302.

Steffen, A. T., Strateva, I., Brandt, W. N., Alexander, D. M., Koekemoer, A. M., Lehmer, B. D., Schneider, D. P., & Vignali, C. 2006. The X-Ray-to-Optical Properties of Optically Selected Active Galaxies over Wide Luminosity and Redshift Ranges. AJ, **131**(June), 2826–2842.

Sulentic, J., Marziani, P., & Zamfir, S. 2011. The Case for Two Quasar Populations. *Baltic Astronomy*, **20**(Aug.), 427–434.

Sulentic, J. W., Marziani, P., & Dultzin-Hacyan, D. 2000. Phenomenology of Broad Emission Lines in Active Galactic Nuclei. ARA&A, **38**, 521–571.

Sulentic, J. W., Bachev, R., Marziani, P., Negrete, C. A., & Dultzin, D. 2007. C IV λ1549 as an Eigenvector 1 Parameter for Active Galactic Nuclei. ApJ, **666**(Sept.), 757–777.

Tang, B., Shang, Z., Gu, Q., Brotherton, M. S., & Runnoe, J. C. 2012. The Optical and Ultraviolet Emission-line Properties of Bright Quasars with Detailed Spectral Energy Distributions. ApJS, **201**(Aug.), 38.

Tombesi, F., Cappi, M., Reeves, J. N., Palumbo, G. G. C., Yaqoob, T., Braito, V., & Dadina, M. 2010. Evidence for ultra-fast outflows in radio-quiet AGNs. I. Detection and statistical incidence of Fe K-shell absorption lines. A&A, **521**(Oct.), A57.

Tombesi, F., Cappi, M., Reeves, J. N., & Braito, V. 2012. Evidence for ultrafast outflows in radio-quiet AGNs - III. Location and energetics. MNRAS, **422**(May), L1–L5.

Tombesi, F., Cappi, M., Reeves, J. N., Nemmen, R. S., Braito, V., Gaspari, M., & Reynolds, C. S. 2013a. Unification of X-ray winds in Seyfert galaxies: from ultra-fast outflows to warm absorbers. MNRAS, **430**(Apr.), 1102–1117.

Tombesi, F., Cappi, M., Reeves, J. N., Nemmen, R. S., Braito, V., Gaspari, M., & Reynolds, C. S. 2013b. Unification of X-ray winds in Seyfert galaxies: from ultra-fast outflows to warm absorbers. MNRAS, **430**(Apr.), 1102–1117.

Tombesi, F., Tazaki, F., Mushotzky, R. F., Ueda, Y., Cappi, M., Gofford, J., Reeves, J. N., & Guainazzi, M. 2014. Ultrafast outflows in radio-loud active galactic nuclei. MNRAS, **443**(Sept.), 2154–2182.

Trakhtenbrot, B., & Netzer, H. 2012. Black hole growth to z = 2 - I. Improved virial methods for measuring M_{BH} and L/L_{Edd}. MNRAS, **427**(Dec.), 3081–3102.

Tsuzuki, Y., Kawara, K., Yoshii, Y., Oyabu, S., Tanabé, T., & Matsuoka, Y. 2006. Fe II Emission in 14 Low-Redshift Quasars. I. Observations. ApJ, **650**(Oct.), 57–79.

Urrutia, T., Becker, R. H., White, R. L., Glikman, E., Lacy, M., Hodge, J., & Gregg, M. D. 2009. The FIRST-2MASS Red Quasar Survey. II. An Anomalously High Fraction of LoBALs in Searches for Dust-Reddened Quasars. ApJ, **698**(June), 1095–1109.

Urrutia, T., Lacy, M., Spoon, H., Glikman, E., Petric, A., & Schulz, B. 2012. Spitzer Observations of Young Red Quasars. ApJ, **757**(Oct.), 125.

Urry, C. M., & Padovani, P. 1995. Unified Schemes for Radio-Loud Active Galactic Nuclei. PASP, **107**(Sept.), 803.

Vacca, W. D., Cushing, M. C., & Rayner, J. T. 2003. A Method of Correcting Near-Infrared Spectra for Telluric Absorption. PASP, **115**(Mar.), 389–409.

Vanden Berk, D. E., Richards, G. T., Bauer, A., Strauss, M. A., Schneider, D. P., Heckman, T. M., York, D. G., Hall, P. B., Fan, X., Knapp, G. R., Anderson, S. F., Annis, J., Bahcall, N. A., Bernardi, M., Briggs, J. W., Brinkmann, J., Brunner, R., Burles, S., Carey, L., Castander, F. J., Connolly, A. J., Crocker, J. H., Csabai, I., Doi, M., Finkbeiner, D., Friedman, S., Frieman, J. A., Fukugita, M., Gunn, J. E., Hennessy, G. S., Ivezić, Ž., Kent, S., Kunszt, P. Z., Lamb, D. Q., Leger, R. F., Long, D. C., Loveday, J., Lupton, R. H., Meiksin, A., Merelli, A., Munn, J. A., Newberg, H. J., Newcomb, M., Nichol, R. C., Owen, R., Pier, J. R., Pope, A., Rockosi, C. M., Schlegel, D. J., Siegmund, W. A., Smee, S., Snir, Y., Stoughton, C., Stubbs, C., SubbaRao, M., Szalay, A. S., Szokoly, G. P., Tremonti, C., Uomoto, A., Waddell, P., Yanny, B., & Zheng, W. 2001. Composite Quasar Spectra from the Sloan Digital Sky Survey. AJ, **122**(Aug.), 549–564.

Verner, E. M., Verner, D. A., Korista, K. T., Ferguson, J. W., Hamann, F., & Ferland, G. J. 1999. Numerical Simulations of Fe II Emission Spectra. ApJS, **120**(Jan.), 101–112.

Véron-Cetty, M.-P., Joly, M., & Véron, P. 2004. The unusual emission line spectrum of I Zw 1. A&A, **417**(Apr.), 515–525.

Véron-Cetty, M.-P., Joly, M., Véron, P., Boroson, T., Lipari, S., & Ogle, P. 2006. The emission spectrum of the strong Fe II emitter BAL Seyfert 1 galaxy IRAS 07598+6508. A&A, **451**(June), 851–858.

Vestergaard, M. 2002. Determining Central Black Hole Masses in Distant Active Galaxies. ApJ, **571**(June), 733–752.

Vestergaard, M., & Wilkes, B. J. 2001. An Empirical Ultraviolet Template for Iron Emission in Quasars as Derived from I Zwicky 1. ApJS, **134**(May), 1–33.

Vignali, C., Brandt, W. N., & Schneider, D. P. 2003. X-Ray Emission from Radio-Quiet Quasars in the Sloan Digital Sky Survey Early Data Release: The α_{ox} Dependence upon Ultraviolet Luminosity. AJ, **125**(Feb.), 433–443.

Villar-Martín, M., Humphrey, A., Delgado, R. G., Colina, L., & Arribas, S. 2011. Ionized outflows in SDSS type 2 quasars at z $\sim$ 0.3-0.6. MNRAS, **418**(Dec.), 2032–2042.

Wang, J.-G., Dong, X.-B., Wang, T.-G., Ho, L. C., Yuan, W., Wang, H., Zhang, K., Zhang, S., & Zhou, H. 2009. Estimating Black Hole Masses in Active Galactic Nuclei Using the Mg II λ2800 Emission Line. ApJ, **707**(Dec.), 1334–1346.

Weedman, D., Sargsyan, L., Lebouteiller, V., Houck, J., & Barry, D. 2012. Infrared Classification and Luminosities for Dusty Active Galactic Nuclei and the Most Luminous Quasars. ApJ, **761**(Dec.), 184.

Weymann, R. J., Morris, S. L., Foltz, C. B., & Hewett, P. C. 1991. Comparisons of the emission-line and continuum properties of broad absorption line and normal quasi-stellar objects. ApJ, **373**(May), 23–53.

Wills, B. J., & Browne, I. W. A. 1986. Relativistic beaming and quasar emission lines. ApJ, **302**(Mar.), 56–63.

Wills, B. J., Netzer, H., & Wills, D. 1985. Broad emission features in QSOs and active galactic nuclei. II - New observations and theory of Fe II and H I emission. ApJ, **288**(Jan.), 94–116.

Wu, J., Vanden Berk, D. E., Brandt, W. N., Schneider, D. P., Gibson, R. R., & Wu, J. 2009. Probing The Origins of the C IV and Fe Kα Baldwin Effects. ApJ, **702**(Sept.), 767–778.

Wu, J., Brandt, W. N., Hall, P. B., Gibson, R. R., Richards, G. T., Schneider, D. P., Shemmer, O., Just, D. W., & Schmidt, S. J. 2011. A Population of X-Ray Weak Quasars: PHL 1811 Analogs at High Redshift. ApJ, **736**(July), 28.

Xue, Y. Q., Luo, B., Brandt, W. N., Bauer, F. E., Lehmer, B. D., Broos, P. S., Schneider, D. P., Alexander, D. M., Brusa, M., Comastri, A., Fabian, A. C., Gilli, R., Hasinger, G., Hornschemeier, A. E., Koekemoer, A., Liu, T., Mainieri, V., Paolillo, M., Rafferty, D. A., Rosati, P., Shemmer, O., Silverman, J. D., Smail, I., Tozzi, P., & Vignali, C. 2011. The Chandra Deep Field-South Survey: 4 Ms Source Catalogs. ApJS, **195**(July), 10.

Young, S., Axon, D. J., Robinson, A., Hough, J. H., & Smith, J. E. 2007. The rotating wind of the quasar PG 1700+518. Nature, **450**(Nov.), 74–76.

Zhang, X.-G., Dultzin-Hacyan, D., & Wang, T.-G. 2006. SDSS J2125-0813: the evidence for the origination of optical FeII emission lines from an accretion disc near a central black hole. MNRAS, **372**(Oct.), L5–L8.

Zubovas, K., & King, A. 2012. Clearing Out a Galaxy. ApJ, **745**(Feb.), L34.